

UNIVERSIDAD DE CANTABRIA  
Departamento de Física Moderna

y

C.S.I.C. - U.C.  
Instituto de Física de Cantabria

**Invariancia de escala en el crecimiento  
de superficies e interfases**



**José Javier Ramasco Sukia**  
**Tesis doctoral**  
2002



UNIVERSIDAD DE CANTABRIA  
Departamento de Física Moderna  
y  
C.S.I.C. - U.C.  
Instituto de Física de Cantabria

## Invariancia de escala en el crecimiento de superficies e interfases

Memoria presentada por el Licenciado  
**José Javier Ramasco Sukia**  
para optar al título de Doctor en Ciencias Físicas

Realizada bajo la supervisión del  
Dr. **Miguel Ángel Rodríguez Díaz**  
y del  
Dr. **Juan Manuel López Martín**  
2002



*a mis padres*



## Agradecimientos

Me gustaría, lo primero de todo, agradecer a mis padres su constante apoyo y comprensión durante todo este tiempo. El resultado de estos años de trabajo está dedicado a ellos. Me gustaría también mencionar a mis dos "jefes": a Miguel y a Juanma. Muchas gracias por todo lo que me habéis enseñado, y por toda la paciencia que habéis invertido en el proceso. A Luis Pesquera, sin quien esta tesis nunca hubiera empezado. A Alejandro y a Ángel Valle; al primero he de agradecer, entre otras cosas, una paciente lectura de este documento, y al segundo la ayuda prestada durante cuatro años como compañeros de despacho. Y a José Revuelta por todo lo que me enseñó de ese *terrible* mundo de los computadores.

Aunque sin escribir todos sus nombres, me gustaría también mencionar a mis compañeros de pasillo que han contribuido a formar un maravilloso ambiente de trabajo. A pesar de no ser astrofísico no es poco lo que he aprendido de ellos, y estoy convencido que dicho ambiente ayudará a desarrollar grandes proyectos científicos (o de otro tipo [Vielva y Herranz 2002]). Querría también agradecer a Knut Jørgen Måløy la hospitalidad que me brindó durante mi estancia en Oslo. Por último, mencionar a mis amigos/as de L.D.S. de Reinosá, mi vida hubiese sido mucho más aburrida sin ellos/as.



*Physics is finished, young man. It's a dead-end street.*

Max Planck's Teacher (unknown name)



# Scale Invariance in Surface Growth

A dissertation submitted in partial fulfillment of the requirements for the degree of Philosophy Doctor in  
Physics

by

**José Javier Ramasco Sukia**

Departamento de Física Moderna  
Universidad de Cantabria

&

Instituto de Física de Cantabria  
Consejo Superior de Investigaciones  
Científicas-Universidad de Cantabria

2002



# Contents

<b>1</b>	<b>Introduction</b>	<b>1</b>
1.1	Fractals . . . . .	2
1.1.1	Self-similar fractals . . . . .	2
1.1.2	Self-affine fractals . . . . .	5
1.1.3	Scaling of Interfaces . . . . .	7
1.2	Molecular Beam Epitaxy . . . . .	8
1.3	Fire fronts . . . . .	11
1.4	Fluid flow through porous media . . . . .	13
1.5	Cosmological distribution of matter . . . . .	15
1.6	Conclusions . . . . .	17
<b>2</b>	<b>Theoretical models</b>	<b>19</b>
2.1	Characterization of interfaces . . . . .	19
2.2	Models and equations with annealed disorder . . . . .	24
2.2.1	The Edwards-Wilkinson equation . . . . .	25
2.2.2	The Kardar-Parisi-Zhang equation . . . . .	27
2.2.3	The MBE growth equations . . . . .	32
2.3	Models with quenched disorder . . . . .	36
2.3.1	The quenched EW equation . . . . .	37
2.3.2	The quenched KPZ equation . . . . .	39
2.3.3	Self-Organized Depinning models . . . . .	43
2.4	Non-local models . . . . .	45
2.5	Conclusions . . . . .	47
<b>3</b>	<b>Anomalous scaling</b>	<b>49</b>
3.1	Why is a new scaling needed? . . . . .	49
3.2	The anomalous scaling ansatz . . . . .	51
3.3	Scaling in direct space . . . . .	53

3.3.1	Family-Vicsek scaling . . . . .	54
3.3.2	Intrinsic Anomalous roughening . . . . .	56
3.3.3	Super-roughness . . . . .	57
3.3.4	Faceted surfaces . . . . .	59
3.4	How to predict the presence of anomalous scaling . . . . .	61
3.5	Conclusions . . . . .	64
<b>4</b>	<b>Inside heterogeneous media</b>	<b>67</b>
4.1	Other way to get depinned . . . . .	67
4.2	The model . . . . .	69
4.3	What we found . . . . .	70
4.3.1	The depinning transition . . . . .	71
4.3.2	Which universality does this transition belong to? . . .	72
4.3.3	Searching for a phase diagram . . . . .	74
4.4	Finite size scaling and phase transitions . . . . .	76
4.5	Conclusions . . . . .	80
<b>II</b>	<b>Some experimental examples</b>	<b>81</b>
<b>5</b>	<b>Fracture fronts</b>	<b>83</b>
5.1	Introduction . . . . .	83
5.2	Experimental setup . . . . .	86
5.3	Results . . . . .	87
5.3.1	The microphone . . . . .	89
5.3.2	The strain gage . . . . .	90
5.3.3	The camera . . . . .	93
5.4	Conclusions . . . . .	101
<b>6</b>	<b>Fluid flow in porous media</b>	<b>103</b>
6.1	Introduction . . . . .	103
6.2	Experimental setup . . . . .	105
6.3	Analysis of the results . . . . .	106
6.3.1	The velocity of the fronts . . . . .	106
6.3.2	Width and correlations . . . . .	107
6.3.3	Power spectrum . . . . .	109
6.3.4	A phase diagram . . . . .	109

6.4	A first step towards a theoretical framework . . . . .	111
6.5	Conclusions . . . . .	113
<b>A</b>	<b>Detailed calculation of direct space functions</b>	<b>115</b>
A.1	Global magnitudes . . . . .	115
A.2	Local estimators . . . . .	116
A.2.1	Early time regime, $t \ll l^z$ . . . . .	117
A.2.2	Intermediate regime, $l^z \ll t \ll L^z$ . . . . .	117
A.2.3	Saturation regime, $t \gg L^z$ . . . . .	119
<b>B</b>	<b>Resumen en castellano</b>	<b>121</b>
B.1	Introducción . . . . .	121
B.1.1	Experimentos con interfases . . . . .	122
B.1.2	Modelos teóricos . . . . .	124
B.2	Escalado anómalo . . . . .	130
B.3	Crecimiento debido a no-linealidades . . . . .	134
B.4	Experimentos de fractura . . . . .	137
B.5	Frentes de fluidos . . . . .	140
<b>C</b>	<b>Publication list</b>	<b>147</b>
<b>D</b>	<b>Reprints</b>	<b>149</b>



# Chapter 1

## Introduction

Sometime before writing this paragraph, I was reading Weinberg's book about the discovery of the subatomic particles [Weinberg 1990]. In this book, when a new topic is introduced, the author reviews the subject from a historical point of view. So, when he arrives to the question of why a cathodic ray is deviated by a capacitor, a flashback on the history of electric and magnetic forces is included. Concerning electricity, it was known since the times of ancient Greece that when a piece of amber is rubbed with an animal skin, the amber acquires the strange property of attracting other objects, e.g. hair. More recently, many school children play a similar game in which a plastic pen or comb is rubbed with a woolen sweater. The pen, treated in this way, is able to attract small pieces of paper or even to deviate the water poured from a glass.

Nowadays, electric forces are pretty well characterized. During the 70's and 80's the theory called Quantum Electro-Dynamics (QED) was developed and tested. The final result is more than incredible: the QED is able to predict experimental results with more accuracy than any other physical theory. Despite of that, the way in which the amber piece or the plastic pen get charged remains still a mystery. The exact Weinberg's words were: *the reader may well also wonder why when amber is rubbed with fur the electrons go from the fur to the amber [...]?* *Oddly enough, we still don't know. The question involves the physics of surfaces of complex solids as silk or hair, and this branch of physics has still not reached a point where we can make definite predictions with any certainty.* I suppose this to be a good reason for writing a thesis on this subject.

This thesis deals with interfaces, the way to characterize them and how

they appear and grow in heterogeneous media. I have even included the word *surface* explicitly in the title. I consider important to explain the meaning of this concept. This is a formal definition:

**Interface:** *surface separating two phases of matter, each of which may be solid, liquid, or gaseous. An interface is not a geometric surface but a thin layer that has properties differing from those of the bulk material on either side of the interface. A common interface is that between a body of water and the air, which exhibits such properties as surface tension, by which the interface acts somewhat like a stretched elastic membrane. Interfacial effects, or processes that occur at interfaces, include the evaporation of liquids, the action of detergents and chemical catalysts, and the absorption of gases on metals. [Encyclopædia Britannica].*

One of the main reasons to study interfaces is the importance that they have in transport processes. For instance, let us consider the cellular membrane: all the molecules used by the cell as food come into through the membrane. If something, energy or mass, is transferred through an interface, the total amount depends on the extension of that surface. Finally, the area of the interface is determined by its geometry.

Everybody knows what is felt when one touches a piece of polished marble. From those kind of experiences, we infer the idea of flatness. On the other hand, the opposite to the previous concept is the idea of roughness. Clearly, the extension of a surface is related to how rough it is. These intuitive concepts may be described within a mathematical framework called fractal geometry.

## 1.1 Fractals

### 1.1.1 Self-similar fractals

A fractal is a mathematical set that remains invariant under scale transformations. Fractals were discovered as a group of structures that presented a paradox for the theory of measure. This theory was developed during later 19th century and early 20th century by a group of mathematicians like Cantor, Peano, von Koch, Hausdorff and Besicovitch. Most of whom gave later their names to examples of fractal sets that they discovered.

The paradox consisted in the impossibility of measuring the size of some sets by a standard medium. When one wants to measure the length of a

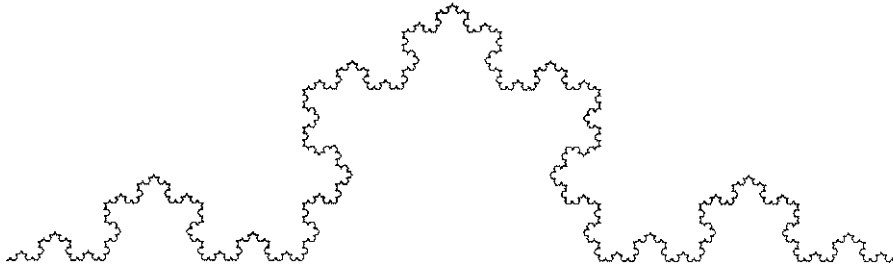


Figure 1.1: The Koch's curve, a fractal with Hausdorff dimension  $D = \log(4)/\log(3)$ . Ref. [Mandelbrot 1982]

circumference, the simplest way is to cover it with small segments of known size  $l$ . The sum of all segment sizes may be considered as an approximation to the circle perimeter. The shorter the segments are, the more exact this approximation is. In the limit  $l \rightarrow 0$ , the sum of all segment lengths must tend to  $2\pi r$ , where  $r$  is the radius of the circle. This procedure to measure the *size* of a set is known as the box-counting method. The paradox arises when one tries to employ the same procedure with a set as the one shown in the figure 1.1. That set, Koch's curve, has in the limit  $l \rightarrow 0$  an infinite length. This fact is not very surprising, there is a great number of simple non-selfcrossing curves with an infinite perimeter. However, none of them may be enclosed within a finite area as happens with Koch's set. This kind of problems won the fractals the appellative of a gallery of monsters.

The solution to the paradox arrived with the modification of the concept of dimension. Let us suppose that  $\mu$  is the magnitude to be measured; length, area or volume of a certain set. The method used to estimate it is to cover the original structure with small sets of known  $\mu$ , say  $\mu_i$ , and linear size  $l$ . If  $\mu(l) = \sum_i \mu_i$  is the approximation of  $\mu$  on the scale  $l$ , the Hausdorff dimension is defined as

$$D = \lim_{l \rightarrow 0} \frac{\log(\mu(l))}{\log(1/l)}. \quad (1.1)$$

The Hausdorff dimension is an integer for classical geometrical objects, as points ( $D=0$ ), lines ( $D=1$ ), squares ( $D=2$ ) or cubes ( $D=3$ ), and takes a non-integer value for fractals. In the case of Koch's curve, it is  $D = \log(4)/\log(3) = 1.2618$ , a value between the dimension of a line,  $D = 1$ , and

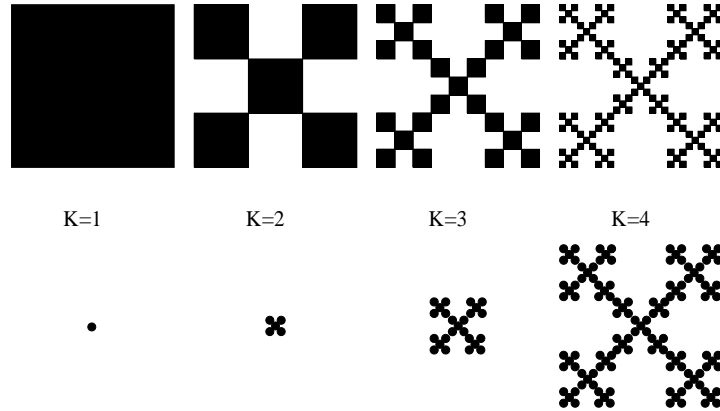


Figure 1.2: Two methods to grow a fractal. This is the Vicsek [Vicsek 1989] fractal.

that of a surface,  $D = 2$ .

The reason why  $D$  is expected to be a finite number is the particular functional form of  $\mu(l)$ . If we consider a segment of length  $L$ , the *mass*,  $\mu(l)$ , is the number of small segments of length  $l$  needed to cover  $L$ . This quantity is:  $\mu(l) = L/l$ . So, the function  $\mu(l)$  behaves as a power law with  $l$ . In this case, the exponent of the power law is  $-1$ , coinciding with the  $-D$  for a segment. The important feature of power laws is that they are the only functions whose form is scale invariant. As was previously mentioned, this is the symmetry which defines fractal geometry. Therefore, most properties of fractals are expressed via power laws.

A fractal set may be constructed by two different methods, as is shown in fig. 1.2. In the first procedure the set *grows*: i.e. a unit figure is chosen and copies of it are added to the set maintaining some pre-established symmetries. There are many real-world systems that use a similar technique of growth, examples are electro-deposition, bacteria colonies or crystal growth, with ions, cells and atoms playing the role of units of growth, respectively. As a result, most of those systems produce fractal structures that will be further discussed later. On the other hand, the construction of a fractal may also start from a figure with a dimension  $d$  bigger than that of the future set,

and drill it producing holes of all sizes. If the distribution of hole hyper-volumes is a power law;  $P(s) \sim s^{-\gamma}$ , the final set is a fractal with a dimension  $D = d(\gamma - 1)$ . This process is similar to erosion in real rocks. The two methods give different kind of fractals. Those produced holing have a finite size in the host space (they may be enclosed within a finite hyper-volume), so upper a certain scale they loose their fractality. On the contrary, those generated by aggregation of small pieces present an infinite size, but also own a lower cutoff in resolution and scale invariance.

The fractals mentioned so far are isotropic. They remain invariant when the scale is changed equally in all directions. However, it is easy to find situations where two or more directions are not equivalent. For instance, in a fractal growth by aggregation a main direction can easily be introduced if the particles arrive to the set only from one side. The set, grown in this way, is not a classical self-similar fractal, but belongs to a different type named self-affine fractals.

### 1.1.2 Self-affine fractals

A self-affine fractal is a set that remains invariant under an anisotropic scale transformation. Despite their differences, in a scale transformation, directions are not completely independent. If one axis changes in a factor  $b$ ,  $x_1 \rightarrow bx_1$ , the others must be rescaled in a factor  $b^{\alpha_i}$ ,  $x_i \rightarrow b^{\alpha_i}x_i$ , in order to preserve the set invariant. The exponents  $\alpha_i$  are called Hurst exponents and give information about the degree of anisotropy of the set. There is a special case of the latter definition particularly important for this thesis. That is the case in which all the directions but one are equivalent. In interface growth, the special dimension corresponds to the growth direction. The existence of a privileged direction implies that there is only one nontrivial Hurst exponent, which is called roughness exponent  $\alpha$ . In figure 1.3, several surfaces with different values of the roughness exponent are plotted.

In some occasions, fractal sets may be expressed as single-valued functions depending only on the position  $h(x_1, x_2, \dots)$ . One of those functions represents a self-affine fractal whenever the following condition is satisfied

$$h(bx_1, b^{\alpha_2}x_2, \dots) = b^{-\alpha}h(x_1, x_2, \dots) . \quad (1.2)$$

If there is only one Hurst exponent different from one, the previous equation takes the simpler form:  $h(b\vec{x}) = b^{-\alpha}h(\vec{x})$ . This expression will appear

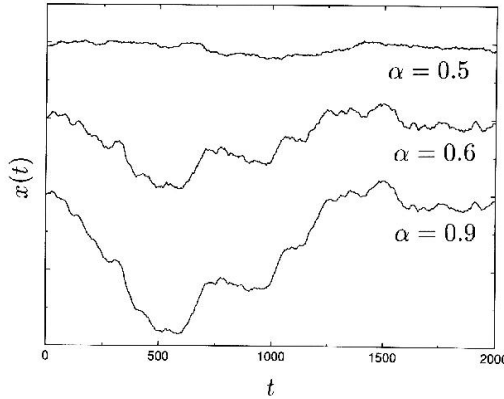


Figure 1.3: Self affine fractals with different roughness exponent. Ref [Barabási 1995]

profusely through out this work.

Apart from the height of a surface over the substrate, the function  $h(\vec{x})$  may correspond to many other different magnitudes . It can be a density of mass or charge, a magnetic or a electric field, the velocity of an element of mass in a fluid, etc. In general, a function  $F(x_1, x_2, \dots)$  that verifies the equation 1.2 is called a homogeneous function. It is easy to demonstrate that for a function  $F(\vec{x})$  to be homogeneous is necessary and sufficient that

$$F(x_1, x_2, x_3 \dots) = x_1^{-\alpha} g(x_2/x_1^{\alpha_2}, x_3/x_1^{\alpha_3}, \dots) . \quad (1.3)$$

The proof is as simple as substituting  $b$  in equation 1.2 by  $1/x_1$ . That change leads to  $g(\vec{u}) = F(1, \vec{u})$ . Homogeneous functions are very important to describe other kind of fractal sets.

All the fractal sets described till now are generated by the repetition, on different scales, of a unitary scheme. Namely, the addition of a certain number of particles, or the holling of a figure maintaining some prefixed symmetries. If the process includes the possibility of failures (the number of added particles fluctuates or directions are randomly chosen), the resulting set is a very particular fractal named random fractal. These sets do not fulfill scale invariance condition. If they are rescaled, the resulting set does not match exactly the original fractal. However, when they are viewed as

random variables, their probability density functions (PDF) do not contain characteristic scales apart from those shared by all fractals. The maximum size  $L$  in growth by aggregation (the size of the smallest hole  $a$  in fractals developed by holing), which are a consequence of the finite character of the construction process of real fractals. This supposes that those PDFs, and their moments, behave as homogeneous functions of two variables: the scale of observation  $l$  and the characteristic scale  $L$ , or  $a$ , of the system.

### 1.1.3 Scaling of Interfaces

Interfaces are considered as random self-affine fractals [Mandelbrot 1982]. Usually, the growth of an interface starts from a flat configuration. So, its width, defined as the variance of the height distribution, is initially zero. The width then increases in time as a power law,  $w(t) \sim t^\beta$ . The roughening goes on for a while, till it finally stops at a time  $t_\times$ . The value of  $t_\times$  is a function of the system size. From this moment on, the width depends on the system size,  $w \sim L^\alpha$ . The exponent  $\beta$  is called growth exponent and  $\alpha$  is the roughness exponent, already mentioned in the previous section. The functional dependence of  $w$  may be written in a compact form as

$$w(L, t) = t^\beta f(t/t_\times) = t^\beta f(t/L^{\alpha/\beta}) . \quad (1.4)$$

Where  $f()$  is a scaling function;  $f(u)$  is constant for small values of  $u$  and  $f(u) \sim u^{-\beta}$  when  $u \gg 1$ .

The width is a homogeneous function that depends on two variables: system size and time. Different values of  $\alpha$  and  $\beta$  are expected to classify interface growth phenomena in different universality classes, as happens in equilibrium phase transitions [Stanley 1971]. This scheme is purely phenomenological and is based on the presence of only one characteristic scale in the problem. This scale is the mean size of correlated clusters in the height profile,  $\xi$ . The value of  $\xi$  is expected to increase as  $\xi \sim t^{\beta/\alpha}$  till it reaches the system size  $\xi = L$ , and to be constant further on. This framework is known as scaling hypothesis and was firstly proposed by Family and Vicsek [Family 1985].

The utility of fractals to describe natural phenomena was firstly pointed out by Benoit Mandelbrot [Mandelbrot 1977, Mandelbrot 1982], and later studied in many other monographs [Feder 1988], [Vicsek 1989], [Barabási 1995] or [Meakin 1998]. In following sections, several experimental examples, where

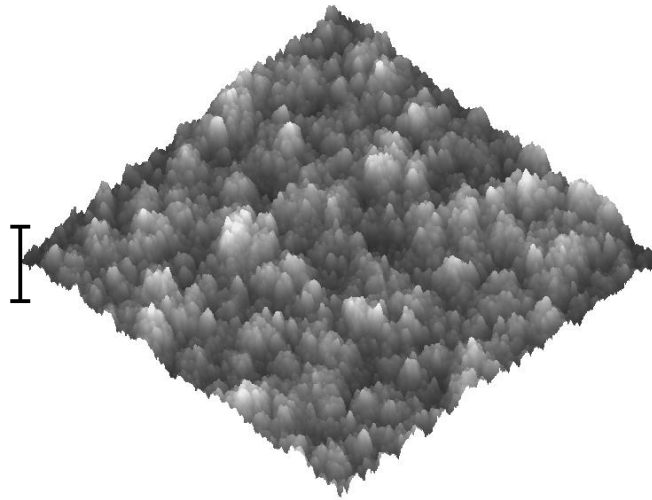


Figure 1.4: AFM image of amorphous  $\text{SiO}_2$  deposited by chemical vapor deposition at  $T = 723\text{k}$ . The scale of the side of the image is  $30000 \text{ \AA}$  and that of the vertical bar is  $4000 \text{ \AA}$ . Ref [Ojeda 2000].

interfaces play an important role, are reviewed.

## 1.2 Molecular Beam Epitaxy

In nature, solids may only appear in two kind of structures. They may be either amorphous -their atoms or molecules have a not defined spatial order-, or crystals -an atomic configuration is repeated periodically in space. In both cases, a solid grows from a solution or from its fluid (liquid or gaseous) phase. Inside the fluid, nucleation starts around a defect or a micro-crystal. This happens whenever a difference between the chemical potentials of solid and fluid phases exists. While non-equilibrium conditions are maintained, new atoms arrive to the surface and attach to it, increasing thus the size of the solid. The growth goes on till the system reaches an equilibrium state or till all the matter is in the solid phase.

Most of the modern technological devices, as computers chips or the smallest lasers, are based on the usage of high quality semiconductor crystals. There are several methods to grow a crystal. Essentially, the process of growth was described previously, but some external conditions may be

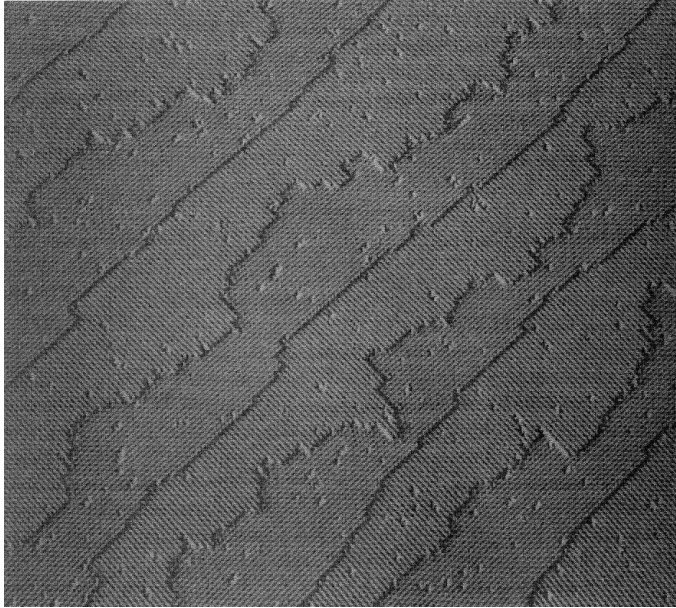


Figure 1.5: Silicon (001) vicinal surface, each side of the image is 100 Å long. In this case, the crystal surface is smooth though the limits between different terraces are rough. Ref. [Pimpinelli 1998]

changed. For instance, the simplest method is to prepare a solution with the elements that must form the crystal. When the liquid is evaporated the residue is the desired crystal. However, the quality of such crystals is not too high.

Molecular beam epitaxy (MBE) is the finest method to construct a solid. Inside a high vacuum chamber, atoms of selected elements are thermally evaporated from a source and deposited onto the surface of the growing crystal. Once atoms reach there, they diffuse over the surface till an energetically favorable position is found or till they are detached. Both processes, diffusion and desorption, are function of temperature and substrate material. Diffusion length,  $l_d$ , and the probability of desorption by unit of time,  $1/\tau$ , increase with temperature following Arrhenius laws;  $l_d \sim e^{-E_o/kT}$  and  $1/\tau \sim e^{-E_D/kT}$ , where  $k$  is the Boltzmann constant,  $T$  the temperature and  $E_D$  and  $E_o$  the activation energies for diffusion and desorption respectively.

Although desorption is usually negligible for most MBE processes, diffusion is of crucial importance for the properties of the crystal interface. The

lower the diffusion length is, the rougher the surface results. This is because the diffusion length represents the limit of atomic mobility. If the mobility is very high, all atoms may reach the most stable configuration, in which they are rounded by the largest number of neighbors. As a consequence, interfaces of crystals that are grown at temperatures with low value of the coefficient  $E_o/kT$  are smooth, their width does not depend on the observation scale  $l$  and they cannot be described with fractal geometry. On the other hand, interfaces produced with high values of the coefficient  $E_o/kT$  are rough. In the next table, roughness and growth exponents of some experiments on the latter category of growth are shown.

<i>Growing crystal/ Substrate</i>	<i>T(k)</i>	$\alpha$	$\beta$	<i>Ref.</i>
Fe/Fe(001)	343	0.79	0.22	[He-YL. 1992]
Au/Si(111)	220	0.42	0.42	[You 1993]
Ag/Si	300	0.70	0.26	[Thompson 1994]
Ag/quartz( <i>SiO</i> <sub>2</sub> )	300	0.82	0.29	[Palasantzas 1994]
Cu/Cu(001)	200 160	1 1	0.56 <sup>1</sup> 0.26	[Ernst 1994]
CuCl/CaF <sub>2</sub> (111)	383, 353	0.84	–	[Tong 1994]
Si/Si(111)	548	1	0.25	[Yang 1994]
Pt/glass	300	0.9	0.26	[Jeffries 1996]
Ag/Ag(111)	300	0.88 $\Rightarrow$ 1 <sup>2</sup>	–	[Heyvaert. 1996]
Ge <sub>1-x</sub> Sn <sub>x</sub> /Ge(001)	373	0.66 $\Leftrightarrow$ 0.45 <sup>3</sup>	–	[Desjardins 1999]
linear poly p-xylene (-C <sub>8</sub> H <sub>10</sub> -)/Si <sup>4</sup>	300, 243	0.72	0.25	[Zhao 2000]
SiO <sub>2</sub> /Si(100) <sup>4</sup>	723	0.75 $\Rightarrow$ 0.42	0.42 $\Rightarrow$ 0.26	[Ojeda 2000]

Such a detailed description of MBE phenomenon had not been possible without the experimental methods used to visualize crystal interfaces. Most of them are based on diffraction of electrons, x rays or atoms by a surface.

<sup>1</sup>An early unstable growth with pyramid-like surface profile for  $T = 200K$  is reported.

<sup>2</sup>The symbol " $\Rightarrow$ " represent a cross-over from one scaling regime to other with different exponents.

<sup>3</sup>The value of  $\alpha$  reduces with an increasing proportion of Sn ( $x$ ).

<sup>4</sup>In these experiments a technique known as chemical vapor deposition is used instead of classic MBE.

The rougher the interface is, the more abundant the radiation diffracted out of Bragg angles. There is, however, other technique worthy to mention apart. The scanning tunneling microscope (STM), firstly constructed by Binnig and Rohrer in 1985, consists of a metallic tip placed very close to a crystal interface and controlled using a group of piezoelectric resorts. If the interface corresponds to a metallic or a semiconductor material, some electrons are moving almost freely through out the conduction band. In these conditions, if an electric potential between the tip and the surface is applied, some electrons are able to escape from the interface due to tunnel effect. The number of *jumps* depends on the density of electrons, which is higher close to atoms. So, with this technique individual atoms may be resolved, and though it does not work for all materials, its applicability is wide enough to offer detailed information about interface morphology. The figure 1.4, for example, is produced using a STM. The figure 1.5 is acquired using other technique named atomic force microscope (ATM).

### 1.3 Fire fronts

Experiments with fire fronts take place on scales very different from those of MBE. Actually, the range of scales for fire fronts goes from burning of a paper sheet to a big forest fire, from centimeters to kilometers.

In this section, some experiments on paper burning are reviewed. In laboratories, conditions of experiments must be easier to handle and to reproduce. Following this idea, experiments on fire fronts must avoid uncontrollable elements as flames and turbulent air currents. Inside a well ventilated chamber a sheet of paper is lied down (to avoid the transport of heat by convention). The paper is, in many occasions, impregnated with some substance to prevent flame formation or to ensure uniform heat distribution (as  $KNO_3$ ). The sheet is fired from one of its extremes, starting the combustion front from a configuration as flat as possible. The advance of the front is recorded by a camera. Typical fronts are shown in figure 1.6.

The correlation function (which behaves as the width) is represented in figure 1.7. In both, the dependence on time ( $t$ ) and on observation scale ( $l$ ), there is a cross-over from a regime with high  $\alpha$  and  $\beta$  ( $\alpha = 0.8 - 0.71$  and  $\beta = 0.4$  [Zhang-J. 1992, Maunuksela 1997]) to other with values of the exponents  $\alpha = 0.48$  and  $\beta = 0.32$  [Maunuksela 1997, Mylly 2000, Mylly 2001]. The interpretation of this result is under debate [Amaral 1998, Maunuksela 1998,

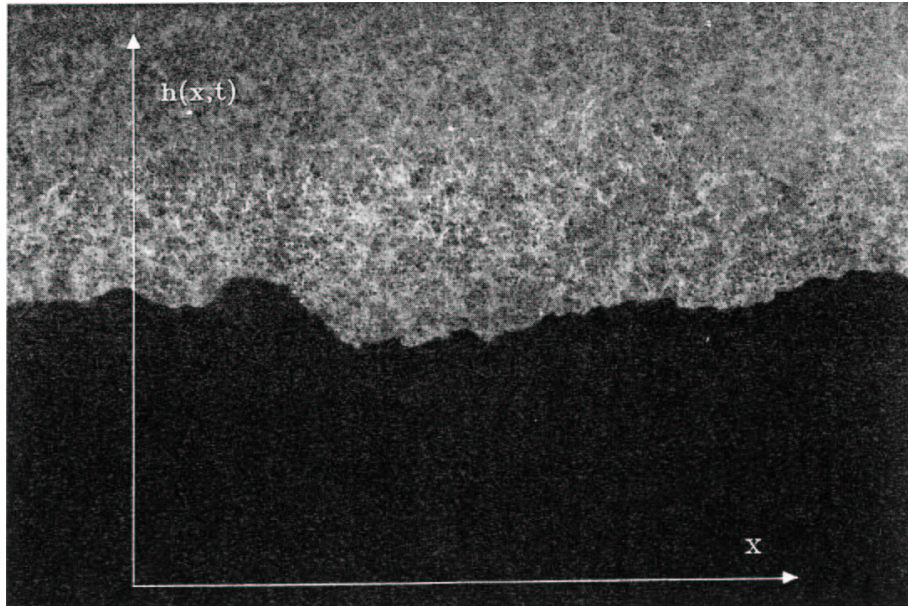


Figure 1.6: Fire front in a experiment of paper burning. Ref [Zhang-J. 1992]

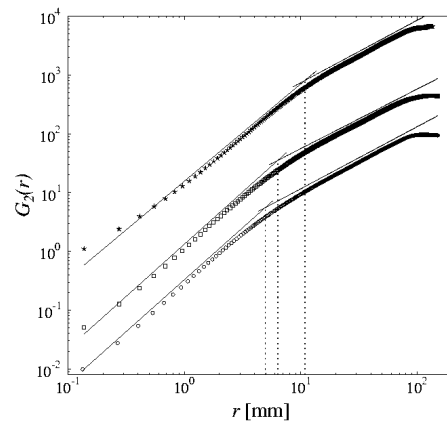


Figure 1.7: Correlation function vs observation scale in a paper burning experiment . The two regimes with different values of  $\alpha$  are clearly marked. Ref [Myllys 2001].

Myllys 2000, Myllys 2001]. Despite of that, what is not under suspicion is the utility of fractals to modelize those experiments.

## 1.4 Fluid flow through porous media

As in the previous section, the scale of this phenomenon coincides with our daily life experience. So, it is easy to find some well-known cases of this phenomenon. For instance, examples of a fluid flowing through a porous media are: watering a plant (water is absorbed by the ground), preparing an espresso (hot water percolates through coffee powder) or pouring that coffee on the tablecloths (coffee spot expands through the fibers of the cloths).

As happens with fire fronts, in the laboratory experimental conditions must be carefully controlled. The setup of these experiments consists usually of two transparent plates placed at a fixed distance. The space between the plates is filled with a heterogeneous medium. Examples of how to construct such a medium are: a pack of small balls with controlled size, a sheet of paper or even the copper strips of electronic circuits. In all cases, a wetting fluid (water, oil, glycerin, ...) displaces other with poorer wetting properties, very often air. If the experiment was performed in the opposite direction, e.g. air pushing oil, some instabilities quite similar to fingers would appear [Ben-Jacob 1983, Langer 1980]. Fronts are recorded by a camera outside the transparent plates, allowing an exhaustive study of its geometry. One of these experimental fronts may be seen in figure 1.8.

In the next table, some of the exponents measured in this type of experiments are shown. In these experiments, there are two possible operational modes depending on what is kept fixed during the experiment: either the volume of injected fluid by unit of time or the pressure. The first method produces experiments with constant velocity fronts, while in the second, fronts are decelerated,  $v \sim t^{-\gamma}$ .

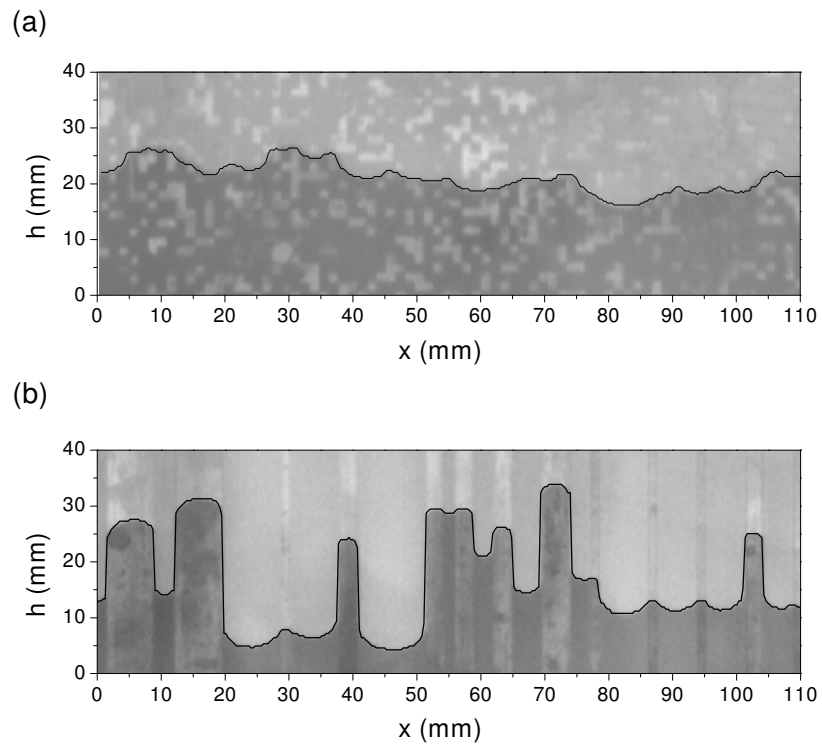


Figure 1.8: Two fluid flow experiments, the liquid is oil pushing air. The heterogeneous medium is formed by randomly distributed copper strips grown onto the lowest plate. In the figure b, the strip distribution is columnar. Ref. [Hernández-M 2001, Soriano 2002].

<i>Fluids</i>	<i>Disorder medium</i>	$\alpha$	$\beta$	<i>Ref.</i>
water/air	glass beads	0.73	–	[Rubio 1989]
water/air	glass beads	0.88	–	[Horváth 1990]
glycerol/air	glass beads	0.81 $\Rightarrow$ 0.49	0.65	[Horváth 1991]
ink(coffee)/air	paper	0.63	–	[Buldyrev 1992]
water/air	glass beads	0.65 $\Rightarrow$ 0.91 <sup>1</sup>	–	[He-S. 1992]
ink/air	a block of paper 3 dimen. (2+1)	0.5	–	[Buldyrev 1992b]
water/air	paper	–	0.56	[Horváth 1995]
water/air	paper	0.67	0.24	[Kwon 1996]
water/air	isotropic and anisotropic paper	0. 0.46	–	[Zik 1997]
ink/air	two papers of different density	0.74 0.64	0.86-0.47 <sup>2</sup> 0.61-0.35 <sup>2</sup>	[Balakin 2000]
silicone oil/air	copper strips	0.9 $\Rightarrow$ 0.6	0.47	[Hernández-M 2001]

## 1.5 Cosmological distribution of matter

Although this subject is still matter of a big controversy, I would like to finish this chapter saying a few words about it. If the distribution of mass in the universe is fractal (at least, it is fractal for some scales), this is an example of fractals at much larger scales than those of previous sections. Actually, the scale of described phenomena has increased along sections, from inter-atomic to cosmological distances. Secondly, a considerable effort is being spent on this question, showing thus the importance it has for cosmology.

This is a very old problem. In 17th century, Newton's concept of the universe as a static place was widely accepted. In that model, all stars were at fixed positions in the empty space and, though this distribution was gravitationally unstable (in a finite universe), there was no other alternative model for several centuries. This idea changed with the work carried out by E. Hubble at the early 20th century. He measured the departing velocities of several galaxies (most galaxies are moving away from us) and found a linear relation between velocity and distance. The universe expansion was the most likely

<sup>1</sup>The exponent  $\alpha$  varies with fluid injection velocity and, though not so clearly, with the capillary number

<sup>2</sup>The value of  $\beta$  depends on the orientation of the front respect to the fibers of paper.

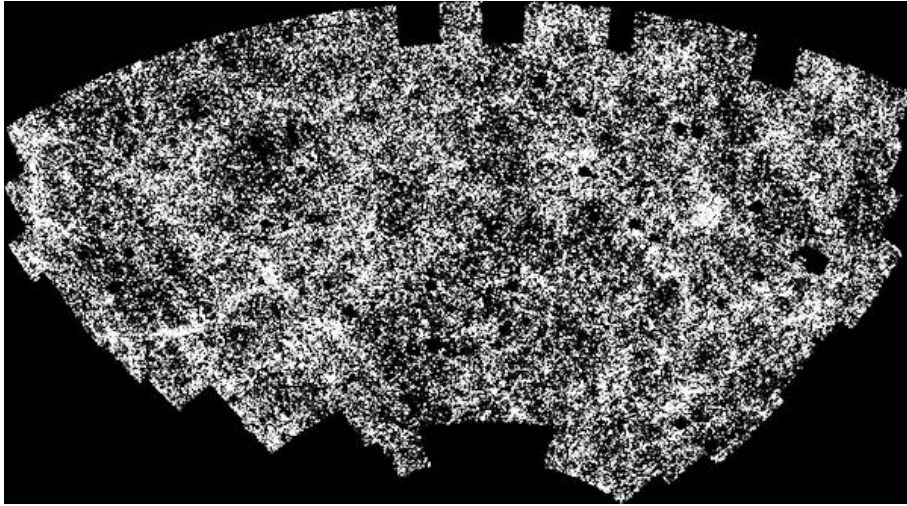


Figure 1.9: The distribution of galaxies on a sky sector centered in the south galactic pole. Ref. [Wu 1999]

explanation for this strange fact. That possibility had already been theoretically predicted several years before by Friedmann using Einstein's field equations of general relativity. One of the assumptions on which Friedmann's solutions are based is homogeneity and isotropy of mass distribution in the universe. Isotropy must be accepted to prevent the existence of privileged observers, but this is not the case for homogeneity.

On solar system scales, mass distribution is clearly heterogeneous. The density of mass in the space between the Earth and the Moon is almost zero, while it is, in average,  $5.5 \text{ tons/m}^3$  inside our planet. On the other hand, there is some evidence, as the monopole in the cosmic microwave background (CMB), pointing to a homogeneous mass distribution on very large scales. In figure 1.9, the distribution of galaxies, an intermediate scale between CMB and solar system, is plotted for a sky sector. There are some places with a high concentration of galaxies and also some randomly distributed areas which are almost empty. This kind of distribution is what would be expected for a fractal set. So, figures as the previous one could be analyzed using fractal tools. This analysis was carried out by several authors with different results. They measured the Hausdorff dimension:  $D = 1.2 \Rightarrow 2.2$  [Guzzo 1991],  $D = 2.25 \Rightarrow 2.77$  [Martínez 1994],  $D = 2$  [Lemson 1991, Labini 1998],  $D = 1 \Rightarrow 3$

[Martínez 1998],  $D = 2.93$  [Scaramella 1998] or  $D = 3$  expected from x rays and CMB.

This work deals with surfaces, hence it would be adequate to explain how this problem about the distribution of matter in universe may be mapped into a fractal interface. As was mentioned in section 1.1.2, the function  $h(\vec{x})$  may correspond to many magnitudes apart from the height of a point over a substrate. In particular, its value may represent the density of matter in each position ( $h(\vec{x}, t) = \rho(\vec{x}, t)$ ) of the space. Consequently, the density may be viewed, in time, as a surface within a four dimensional space. The dynamics of the system is then driven mainly by two opposite tendencies. Gravitational collapse increases the value of the density wherever it has a peak, and the expansion of the universe makes  $\rho$  smoother. The previous values for the Hausdorff dimension would correspond to roughness exponents  $\alpha = 3 - D$ , in the range from  $\alpha = 1.8$  to  $\alpha = 0$ .

All those different results in the measured dimensions have led to a strong debate. Are they due to a non fractality of the universe?. To the lack of better statistical samples?. Or to the methods used to measure  $D$ ?

## 1.6 Conclusions

In last sections, some experiments (and observations) where fractals were used to modelize a physical system have been presented. In all of them, the final aim was to measure a fractal dimension or the roughness and the growth exponents. This is because, as in the case of equilibrium Statistical Physics, those exponents are expected to inform about the underlying symmetries of the problem. As a consequence, it would be possible to classify physical systems that share the same microscopic symmetries in universality classes.



# Chapter 2

## Theoretical models

Mathematical models are the working tools for theoretical physicists. Models are simplified versions of real systems settled in the easier treatable field of mathematics. Surface growth, as a part of Statistical Physics, is not an exception to this general rule. The first step in a theoretical framework is not an equation. In classical mechanics, for instance, the final product is Newton's second law, but before reaching that point it is necessary to specify how particles, their positions, and forces enter in the model.

### 2.1 Characterization of interfaces

In order to simplify the theoretical work, interfaces are usually represented by single-valued functions,  $h(\vec{x}, t)$ , where  $h$  is the height of the surface over the substrate position  $\vec{x}$  at the time  $t$ . The procedure to define a  $h$  profile is not always well established. In many real situations, the surface may curve over itself, producing thus a very complicated multi-valued height distribution. Several solutions have been tested to solve this problem. The simplest possibility is to consider only the maximum of  $h$  at each position. While the overhangs have a characteristic size, this method or any other similar, may be valid.

The height profiles,  $h(\vec{x}, t)$ , are the basic ingredients of surface growth. Each experiment, either in a computer or in a laboratory, gives as result one of those profiles for each time of measurement. If that experiment is repeated, the resulting height profile will be obviously different. This fact add a certain complexity to the process of definition of mean quantities. Let

us consider, for instance, the simplest magnitude, the mean height. For a particular height profile, the average height is defined as

$$\langle h \rangle_x(t) = \frac{1}{L} \sum_i h_i(t) \approx \frac{1}{L} \int_0^\infty dx h(x, t) . \quad (2.1)$$

The second expression on the right hand is the continuous case approximation. This estimator for the average height is missing some crucial information that comes from the other realizations of  $h(x, t)$ . With it, only a determined value for a stochastic quantity that is actually characterized by a whole probability distribution is found. In order to obtain a more useful estimator, the average over different realizations must be taken. The definition of the mean height is then

$$\langle h \rangle(t) = \{ \langle h \rangle_x \} = \left\{ \frac{1}{L} \sum_i h_i(t) \right\} . \quad (2.2)$$

The symbols  $\{..\}$  represent the average over a set of different height profiles while  $\langle..\rangle_x$  correspond to an average over the space for a single disorder realization.

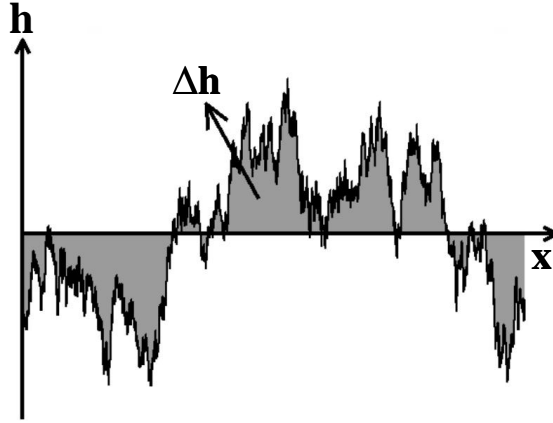


Figure 2.1: Representation of  $|\Delta h|$  for a rough interface. This is the quantity that takes the role of the *mass* of a fractal set.

The basic quantity to be studied is the fluctuations of each front from its mean height,  $\Delta h(x, t) = h(x, t) - \langle h \rangle_x(t)$ . This magnitude is expected to behave as the mass or hyper-volume in random fractals of the previous chapter. The main difference is that it can take positive or negative values. Indeed, the average of  $\Delta h$  in space is always zero by definition,  $\langle \Delta h(x, t) \rangle_x = 0$ . The first magnitude to be analyzed is then the second order momentum; the global width of the interface.

$$W(t, L) = \{ \langle [h(x, t) - \langle h \rangle_x]^2 \rangle_x \}^{1/2} = \{ \langle [\Delta h(x, t)]^2 \rangle_x \}^{1/2}. \quad (2.3)$$

Interfaces are supposed to be random self-affine fractals, but only in their final state. Typically, the initial condition of these systems is very far from that situation. For instance in many practical cases, a flat surface is taken as initial state  $h(x, t = 0) = 0$ . This means that the global width is zero at  $t = 0$ . Later, the system evolves and the interface becomes rougher. The lack of a characteristic scale imposes that the growth of the width happens as a power-law in time,  $W(t, L) \sim t^\beta$ . The roughening of the interface goes on till the system reaches a stationary state. Further on, the width of the surfaces depends on the only characteristic scale left; the system size,  $W(t > t_{sat}) \sim L^\alpha$ . These two asymptotical tendencies may be included in an unique compact expression,

$$W(t, L) = t^\beta f(t/t_\times) = t^\beta f(t/L^{\alpha/\beta}), \quad (2.4)$$

where  $\alpha$  is the roughness exponent,  $\beta$  the growth exponent,  $L$  the system size and  $f()$  a scaling function that asymptotically behaves as:

$$f(u) \sim \begin{cases} \text{const} & \text{if } u \ll 1 \\ u^{-\beta} & \text{otherwise.} \end{cases} \quad (2.5)$$

This ansatz for the width scaling is the so called Family-Vicsek scaling [Family 1985].

In many practical situations as, for example, in experiments, the width of the whole front cannot be estimated. However, a local width may be defined considering only a fraction of the system with a lateral size  $l < L$ . In that case, the mean values  $\langle \dots \rangle_x$  are restricted to that small area. In order to distinguish them from the global averages, they will be denoted by  $\langle \dots \rangle_l$ . The definition of the local width is then

$$w(t, l) = \{ \langle [h(x, t) - \langle h \rangle_l]^2 \rangle_l \}^{1/2} = \{ \langle [\Delta_l h(x, t)]^2 \rangle_l \}^{1/2}. \quad (2.6)$$

The Family-Vicsek scaling for this function is assumed to be the same as for the global width, but substituting  $L$  by  $l$ :  $w(t, l) = t^\beta g(t/l^{\alpha/\beta})$ . The function  $g(\cdot)$  has the same asymptotic behaviour as  $f(\cdot)$ . The change from global to local scale is not so innocent as may seem, it is specially complicated when the scaling of the system cannot be described by the FV ansatz (see chapter 3).

Another important aspect to be studied in all random systems is the correlation, the spatial correlation in the case of surface growth. This function is defined as

$$C(t, l) = \{ \langle \Delta h(x+l, t) \Delta h(x, t) \rangle_x \} . \quad (2.7)$$

Typically, for a fixed time, the correlation function takes a (large) positive value at  $l = 0$ . Actually, the function  $C(t, l = 0)$  is equal to the square of the global width. Further, when  $l$  is increased the correlations decay, and they become zero above a certain distance  $\xi$ . This basic scheme is maintained for every moment, but the distance at which the correlations vanish increases with time,  $\xi \sim t^{1/z}$ . The exponent  $z$  is known as the dynamic exponent and gives information about how fast the correlations expand through out the system. That exponent is related to  $\alpha$  and  $\beta$  by a simple scaling relation;  $z = \alpha/\beta$ . This expression is motivated by the fact that correlations can not expand for ever in a system of finite size,  $L$ . Hence, the expansion must stop at a certain time,  $t_\times \sim L^z$ , for which  $\xi(t_\times) = L$ . After that time, the dynamics of the system reaches a stationary state, where the width or correlations change no more.

There exists another function that is second order in  $\Delta h$ , and that must be mentioned. It is the height-height correlation function at equal time,

$$G(t, l) = \{ \langle (h(x+l, t) - h(x, t))^2 \rangle_x \} = \{ \langle (\Delta h(x+l, t) - \Delta h(x, t))^2 \rangle_x \} . \quad (2.8)$$

The function  $G$  is a bridge between the global width and the correlation function,  $G(t, l) = 2W^2(t, L) - 2C(t, l)$ . Its scaling behaviour is quite similar to that of the local width. Indeed, in some occasions, as for values of  $\alpha$  close to one [Buceta 2000], it may be a better estimator for the exponents.

The functions presented so far are all in the direct space. There are, however, many mathematical tools that employ other *reciprocal* spaces. The most famous of those techniques is the Fourier transform. The Fourier transformation of  $\Delta h$  ( $\hat{h}(t, k) = (2\pi)^{-d/2} \int dk \Delta h(t, x) \exp(-ikx)$ ) is in general a complex function and, as a consequence, it is not very useful directly. However, this is not the case for the transformation of the correlation function;

the power spectrum  $S(k, t)$ . The function  $S()$  is real due to the symmetry  $l \rightarrow -l$  that is satisfied by the correlations,  $C(t, l) = C(t, -l)$ . Finally, as the correlation function is the convolution of  $\Delta h$  with itself, its Fourier transform, the function  $S()$ , is related to  $\hat{h}$  by the equation:  $S(k, t) = \{\hat{h}(t, k) \hat{h}(t, -k)\}$ . The latter expression is often used as a definition for  $S()$ .

The scaling of the power spectrum is the transformed version of the preceding Family-Vicsek ansatz for direct space magnitudes. The main functional form remains still as power laws, but the correlation length  $\xi$  transforms now in a characteristic wave-length  $k_\times \sim 1/\xi$ . This wave-length decrease in time as  $k_\times \sim t^{-1/z}$ . The compact expression for the power spectrum FV scaling is

$$S(k, t) = \frac{1}{k^{2\alpha+d}} S_{FV}(k t^{1/z}). \quad (2.9)$$

The scaling function  $S_{FV}()$  presents the following asymptotic behaviour

$$S_{FV} \sim \begin{cases} u^{2\alpha+d} & \text{if } u \ll 1 \\ \text{const} & \text{otherwise.} \end{cases} \quad (2.10)$$

The power spectrum is also related to other second order functions of  $\Delta h$ : To the global width, as a result of the Parseval identity,  $W^2(t, L) = \int dk S(k, t)$ , and to the height-height correlation function  $G()$  by the equation  $G(t, l) \propto \int dk [1 - \cos(kl)] S(k, t)$ . It has been shown that the direct space methods, except for the global width, are not able to measure roughness exponents bigger than one [Leschhorn 1993]. This circumstance makes  $S()$  one of the most reliable estimators for  $\alpha$  and  $z$  exponents [Roux 1994, Schmittbuhl 1995].

The basic functions (basis) of Fourier transform are plane waves,  $e^{ikx}$ . Those waves are very well determined in frequency ( $k$ ), but completely unlocalized in space ( $x$ ). The wide spatial spread of its basis leads Fourier's method to take an average over space during the transformation. Hence, some important information about the local behaviour of the transformed function may be lost. To avoid this effect, the so called wavelet transform was developed in the field of signal analysis during the last two decades. The basis used by this transform is composed by functions with a compact localization (finite domain) both in space and in frequency. There is not a unique functional form for that basis. Any function,  $\Psi(x)$ , holding the conditions  $\int_{-\infty}^{\infty} \Psi(x) dx = 0$  and  $\int_{-\infty}^{\infty} \Psi^*(x) \Psi(x) dx < \infty$  may be a good candidate to mother wavelet. From that mother wavelet, the basis for the transform is

defined as

$$\Psi_{a,b} = \Psi\left(\frac{x-b}{a}\right),$$

and the wavelet transformation as

$$W[\Delta H](a,b) = \frac{1}{\sqrt{a}} \int_{-\infty}^{\infty} \Delta h(x,t) \Psi_{a,b}(x) dx. \quad (2.11)$$

If the function to be transformed is a random self-affine fractal, as happens with  $\Delta h$  for  $t > t_{sat} \sim L^z$ , after taking averages over the disorder the dependence of the wavelet transform on the scale  $a$  goes as  $AW[\Delta](a,b) = \{W[\Delta h](a,b)\} \sim a^{\alpha+(1/2)}$ , allowing thus the determination of the roughness exponent [Simonsen 1998, Ahr 2000].

The preceding methods are all based on integrations or integral transformations of the function  $\Delta h$ . There is other family of procedures that use a different approximation to measure the exponent  $\alpha$ . If a fractal set of dimension  $D$  is intersected by a hyper-plane of dimension  $d < D$ , the resulting set is other fractal with a Hausdorff dimension  $D' = D - d$ . The same happens with a self-affine fractal, but in that case the Hausdorff dimension of the intersection is  $D' = d_s + 1 - \alpha - d$ , where  $d_s + 1$  is the dimension of the embedding space. Hence, measuring directly or indirectly the dimension of that set,  $D'$ , it is possible to estimate the roughness exponent. For instance, in (1+1) dimension an interface is a random self-affine curve. The intersection of that curve with a line is a group of points with Hausdorff dimension  $1 - \alpha$ . As happens in all self-similar fractals, the distribution of holes (the distance between consecutive points of intersection) presents a probability density function that goes as  $p(d) \sim d^{-1-D'} \sim d^{-2+\alpha}$ . This method is known as the first return probability [Schmittbuhl 1995], and may also be generalized to determine any return probability. This latter probability, which is called the multi-return probability, shows a different functional dependence on the distance  $p_{mr}(d) \sim d^{-\alpha}$ .

## 2.2 Models and equations with annealed disorder

Theoretical models are simplified versions of real phenomena. This simplification is expected not to miss the crucial elements of the real counter-part.

Models constitute, thus, an easy to handle system that still conserves part of the original behaviour. Classically, those models were expressed by equations that describe the evolution of the whole system or of elements that form it, as the Langevin's equation for Brownian motion. Later, with the arrival of computers, it has become possible to simulate processes directly, starting from a few suppositions about the basic components of the problem and the interactions among them. Those interactions may be local, as in the Ising model, or non local when a field, e.g. electric field in a group of charge particles, or the conservation of a global quantity, as mass in the fluids, requires it. In the next subsections, some of the most important models in surface growth are introduced.

### 2.2.1 The Edwards-Wilkinson equation

Let us imagine a pool filled with a quiet fluid; e.g. water. Some granular material is poured onto the fluid. That material is composed by small grains that, due to friction, reach quickly a regime with a constant and low velocity. The grains are deposited onto the substrate and attach to the interface in the most stable of all local configurations; i.e. the local minimum of the surface.

This system may be easily implemented in a computer program. The resulting algorithm is known as the random deposition with surface relaxation

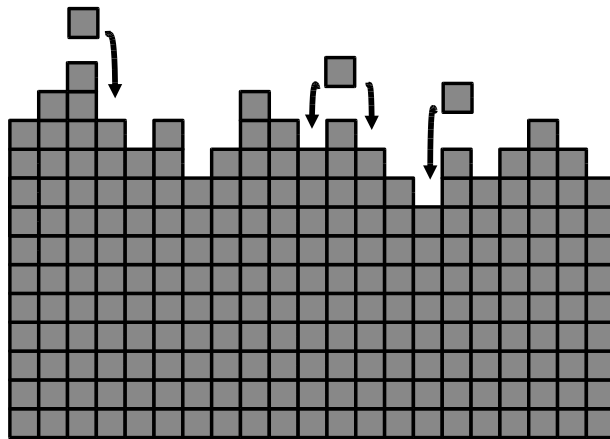


Figure 2.2: Rules of the algorithm for a model of random deposition with surface relaxation.

model [Barabási 1995]. In this algorithm, the substrate is represented by a square lattice configuration with  $L^d$  sites. In each time step, a site,  $i$ , is randomly chosen. If the height at this site,  $h_i$ , is lower than that of its neighbours, it is updated,  $h_i \rightarrow h_i + 1$ . Otherwise, the lowest of the nearest neighbours is updated. The exponents measured in the computer simulation of this model in (1+1) dimension are  $\alpha = 0.48 \pm 0.02$  and  $\beta = 0.24 \pm 0.01$  [Barabási 1995] from [Family 1986].

In order to write down an equation for the coarse-grained interface of this system, we can split the problem into two independent processes. The first element to be taken into account during the growth is the flux of incoming particles. The flux is constant in time except for the shot noise. This behaviour may be included with a term of the kind  $F + \eta(x, t)$ . Where  $F$  is a constant and  $\eta$  is a white noise with zero average. Then, there is the relaxation of deposited particles. The main characteristic of this process is the conservation of mass. The mass in each site is proportional to the height,  $m_i = \rho_i h_i$ . Therefore, the relaxation may be described by a current pointing to the minima of the interface and proportional to the local gradient,  $\vec{j}(x, t) \propto -\nabla h(x, t)$ . Putting together these two independent ingredients, we get the continuous equation

$$\frac{\partial h}{\partial t} = \nu \nabla^2 h + F + \eta(x, t) , \quad (2.12)$$

where the correlations of noise term  $\eta$  satisfy  $\{\eta(x, t)\eta(x', t')\} = A^2 \delta(x - x')\delta(t - t')$ . This linear coarse-grained Langevin equation is known as the Edwards-Wilkinson (EW) equation [Edwards 1982]. The exponents  $\alpha$  and  $\beta$  may be easily obtained for this system with a simple scaling argument. If in a substrate of (d+1) dimension, space and time variables are rescaled as  $\vec{x} \rightarrow b\vec{x}$  and  $t \rightarrow b^z t$ , the height function as  $h \rightarrow b^\alpha h$ , and we introduce those changes in the EW equation we have

$$\frac{\partial h}{\partial t} = \nu b^{z-2} \nabla^2 h + b^{-\frac{(z+d)}{2}-\alpha+z} \eta(x, t) . \quad (2.13)$$

The constant force  $F$  does not appear because the only effect this term produces in the surface growth is a constant velocity that may be eliminated by a Galilean transformation  $h \rightarrow h + Ft$ , and, consequently, has no influence on the interface roughness. If we now impose scale-invariance, the exponents of  $b$  should vanish:  $z = 2$  and  $\alpha = \frac{z-d}{2}$ . In (1+1) dimension, the exponents are  $z = 2$ ,  $\alpha = \frac{1}{2}$  and  $\beta = \alpha/z = \frac{1}{4}$ . Note that  $\alpha \leq 0$  for dimensions

$d \geq 2$ , what implies that the interfaces of this model are flat for substrates of dimension higher than one.

These results may also be obtained solving directly the EW equation [Nattermann 1992]. By Fourier transforming equation (2.10) we obtain

$$-i\omega\tilde{h}(k, \omega) = -\nu k^2 \tilde{h}(k, \omega) + \tilde{\eta}(k, \omega) , \quad (2.14)$$

where the term  $\tilde{\eta}(k, \omega) = \int dk \eta(x, t) e^{-ikx+i\omega t}$ . The function  $\tilde{\eta}$  has zero average and its correlations are  $\{\tilde{\eta}(k, \omega)\tilde{\eta}(k', \omega')\} = A^2\delta(k+k')\int_0^\infty d\tau e^{i(\omega+\omega')\tau}$ . To calculate the latter correlations is necessary to have into account the initial condition of the interface;  $h(x, t=0) = 0$ , this can be included with the restriction  $\eta(x, t) = 0$  for  $t \leq 0$ . The equation 2.12. implies that

$$\tilde{h}(k, \omega) = \tilde{\eta}(k, \omega)/(\nu k^2 - i\omega) . \quad (2.15)$$

Performing an inverse Fourier transformation of this expression, it is possible to calculate the amplitude of modes  $\hat{h}(k, t)$ , and

$$\{\hat{h}(k, t)\hat{h}(k', t)\} = (A^2/2\nu k^2)(1 - e^{-2\nu k^2 t})(2\pi)^d \delta^d(k+k') . \quad (2.16)$$

Finally, the power spectrum,  $S(k, t)$ , may be obtained from the latter equation by making  $k' = -k$  and by integrating over all the possible directions of  $\vec{k}$ .

$$S(k, t) = \frac{S_d A^2}{2\nu k^{2-d+1}}(1 - e^{-2\nu k^2 t})(2\pi)^d \quad (2.17)$$

The constant  $S_d$  comes from the integration of the solid-angle element to all directions in a space of dimension  $d$ . The exponents then are  $\alpha = (2-d)/2$ ,  $z = 2$  and  $\beta = (2-d)/4$ . For  $d = 2$ , the power spectrum goes as  $1/k$  for  $k > k_\times \sim t^{1/2}$ , this means that the width presents a logarithmic dependence on the system size. For dimensions higher than  $d_c = 2$ , the surface is flat,  $\alpha < 0$ .

### 2.2.2 The Kardar-Parisi-Zhang equation

In the argument that led us to the EW equation was explicitly supposed that the particles were deposited in a ballistic way. The particles arrived from a direction perpendicular to the substrate. There are many cases of surface

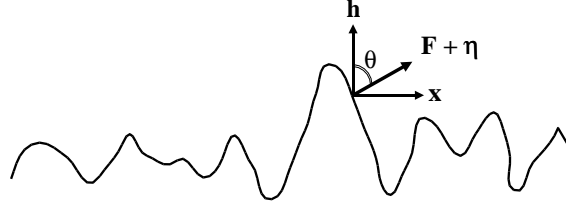


Figure 2.3: The growth of an interface usually occurs in the local normal direction to the surface. This lateral growth is what produces the nonlinear term in KPZ equation.

growth in which this condition is not satisfied. For instance, if the deposited grains were very small and were immersed in hot water, those grains should suffer diffusion (they would move following Brownian trajectories) before arriving the surface. In addition, if those grains could easily be adhered to the interface, they would attached to the surface in the first point of contact, or in a near place. The interface then would tend to grow in the direction that is locally normal (as it is shown in the figure 2.3). That lateral growth introduces an important correction to the original EW model.

In the EW equation, the term  $\partial h/\partial t$  takes into account the growth in the perpendicular direction to the substrate. So, if the force,  $F$ , and the shot noise,  $\eta$ , lay in the local normal direction to the interface (see figure 2.3), only their projection onto the vertical axis will contribute to the growth equation. This implies the substitution of the latter force-noise term by other of the kind  $[F + \eta(x, t)] \cos \theta = [F + \eta(x, t)]/\sqrt{1 + (\nabla h)^2}$ . In the limit  $|\nabla h| \ll 1$ , that expression takes the form  $[F + \eta(x, t)] \cos \theta = [F + \eta(x, t)](1 - \frac{1}{2}(\nabla h)^2 + \frac{3}{4}(\nabla h)^4 + \dots)$ . Introducing the term at the lowest order in  $\nabla h$  in a EW-like equation, we obtain

$$\frac{\partial h}{\partial t} = \nu \nabla^2 h + \frac{\lambda}{2} (\nabla h)^2 + F + \eta(x, t) . \quad (2.18)$$

Where  $\nu$ ,  $\lambda$  and  $F$  are constants, and the noise term  $\eta$  has the same properties as the EW equation counterpart  $\{\eta(x, t)\} = 0$  and  $\{\eta(x, t)\eta(x', t')\} = A^2\delta(x - x')\delta(t - t')$ .

The expression (2.18) is the KPZ equation, firstly proposed by M. Kardar, G. Parisi and Y.-C. Zhang [Kardar 1986]. This equation can be mapped onto two other important physical problems. By the change of variable  $\vec{v} = -\nabla h$  and in the case  $\lambda = 1$ , the KPZ equation transforms into the noisy Burgers equation [Burgers 1974], a classic system in the field of fluid dynamics and turbulence. While the nonlinear change of variable  $\omega(x, t) = \exp \lambda h/2\nu$  maps the KPZ model onto the evolution equation of the Boltzmann weight of directed polymers in random media [Kardar 1987].

Due to the great physical significance of this model, it is important to obtain its exponents for all substrate dimensions. As a first approach, we can apply a scaling argument performing the scale transformation:  $x \rightarrow bx$ ,  $t \rightarrow b^z t$  and  $h \rightarrow b^\alpha h$ , getting to

$$\frac{\partial h}{\partial t} = \nu b^{z-2} \nabla^2 h + \frac{\lambda}{2} b^{\alpha+z-2} (\nabla h)^2 + b^{\frac{z-d}{2}-\alpha} \eta(x, t). \quad (2.19)$$

To hold the condition of scale invariance, the exponents of  $b$  must be zero. However, this implies that  $\alpha$  and  $\beta$  should satisfy simultaneously three incompatible relations:  $z = 2$ ,  $\alpha + z = 2$  and  $\alpha = \frac{z-d}{2}$ . In order to avoid this problem, the most relevant contributions to scaling must be chosen. The expression  $\alpha + z = 2$ , coming from the nonlinear term, has been found to result from the Galilean invariance of Burgers equation [Krug 1987], and consequently it is always fulfilled. If we consider as the second relation that coming from the diffusion, the final exponents would be  $z = 2$  and  $\alpha = 0$ . The same exponents as in the case of the EW equation for  $d > 2$ . On the contrary, if the expression coming from the noise is considered, the result would be  $z = (4 + d)/3$  and  $\alpha = (2 - d)/3$ .

As well as numerical integrations of the equation [Amar 1990, Moser 1994, Newman 1996, Lam 1998], there exist many discrete models that are thought to belong to KPZ universality class. Therefore, it is possible to obtain the exponents of the KPZ equation by the simulation of those models. Some examples are the Eden model [Plischke 1984, Zabolitzky 1986, Wolf 1987] or the ballistic deposition [Meakin 1986]. The simplest of those automata is the Kim-Kosterlitz model [Kim 1989]. The components of this model are the sites of a hyper-cubic lattice. The growing site,  $i$ , is randomly chosen among the  $L^d$  possible positions, and it is updated,  $h_i \rightarrow h_i + 1$ , only if the RSOS

condition,  $|h_i + 1 - h_{i\pm 1}| \leq 1$ , is satisfied. The exponents measured in this model for dimensions  $(1+d)$  are [Kim 1989, Ala-Nissila 1993]:

$d$	1	2	3	4	5	6	7
$\alpha$	1/2	0.40(1)	0.308(2)	0.139(2)	–	–	–
$\beta$	1/3	0.250(5)	0.180(2)	0.245(1)	0.107(2)	0.10(2)	0.08(2)

The exponents of that table do not agree with those predicted by the scaling argument. To obtain a more reliable result, a Flory-type approach may be used [Hentschel 1991]. Essentially, this method is equal to the previous argument but a different scaling is supposed the noise term,  $\eta(bx, b^z t) \sim b^{-z/2 - \alpha d/2} \eta(x, t)$ . This allows to have an idea of what is happening on intermediate scales, which are important in the strong-coupling regime of KPZ equation. The exponents evaluated with this method are  $\alpha = 2/(d+3)$ ,  $z = 2(d+2)/(d+3)$  and  $\beta = 1/(d+3)$ . Those values were also proposed, based on their numerical results, by Kim and Kosterlitz [Kim 1989]. They are actually an upper cutoff for the real exponents.

More elaborated theoretical techniques have also been applied to find the values of those exponents. Techniques such as perturbation of the linear equation followed by dynamic renormalization group analysis [Kardar 1986, Medina 1989, Frey 1994], functional renormalization group [Nattermann 1991], mode-coupling theory [Doherty 1994, Moore 1995, Stepanow 1997, Colaioni 2001], mapping onto directed polymers [Doty 1992, Lässig 1997], quantized scaling [Lässig 1998], real-space renormalization [Castellano 1998, Castellano 1999] and width distributions [Marinari 2001].

In order to gain a further insight into the problem, it may be a good idea to review the perturbation method. The starting point of this technique is the Fourier transformation of the KPZ equation

$$-i\omega \tilde{h}(k, \omega) = -\nu k^2 \tilde{h}(k, \omega) + \tilde{\eta}(k, \omega) + \frac{\lambda}{2} \int dq d\Omega q(q-k) \tilde{h}(q, \Omega) \tilde{h}(q-k, \Omega-\omega).$$

With a small reorganization on this expression, the integral equation

$$\tilde{h}(k, \omega) = \tilde{\eta}(k, \omega) G_o(k, \omega) + \frac{\lambda}{2} G_o(k, \omega) \int dq d\Omega q(q-k) \tilde{h}(q, \Omega) \tilde{h}(q-k, \Omega-\omega)$$

is obtained, where  $G_o(k, \omega) = 1/(\nu k^2 - i\omega)$ . The terms  $\tilde{h}$  within the integral may be substituted by the whole right part of the latter expression. When

this process is repeated, we obtain a series with terms of increasing power of  $\lambda$ . If  $\lambda \ll 1$ , it is possible to neglect the high order terms of the expansion. Finally, if an average over disorder realization is taken, we obtain an expression for  $\tilde{h}$ . At first order in  $\lambda$ , the integrals that appear are divergent. Hence, it is necessary to apply a renormalization group technique to extract some information of how that divergence behaves. The flow equations for this one-loop renormalization method can be obtained. One has

$$\begin{aligned}\frac{d\lambda}{dl} &= \lambda [\alpha + z - 2] \\ \frac{d\nu}{dl} &= \nu [z - 2 + S_d g^2 (2 - d)/(4d)] \\ \frac{dA}{dl} &= A [\frac{1}{2}(z - d) - \frac{1}{8}\alpha + \frac{1}{8} S_d g^2],\end{aligned}\tag{2.20}$$

where  $g$  ( $g^2 = (\lambda A)^2/(2\nu^3)$ ) is a dimensionless parameter, called coupling constant.  $S_d$  is the area of a  $d$ -dimensional hyper-sphere of unit radius. The equations for  $\nu$  and  $A$  are not independent, since both contain a term with  $g^2$ , and  $g$  is a combination of  $\nu$ ,  $A$  and  $\lambda$ . These two equations may be reduced to only one on  $g$ ,

$$\frac{dg}{dl} = \frac{2-d}{2}g + S_d \frac{2d-3}{4d}g^3.\tag{2.21}$$

Looking for the fixed points of the flow equations for  $\lambda$ , the expression of the Galilean invariance  $\alpha + z = 2$  is recovered. The fixed points in the equation for  $g$  present a richer behaviour, the number of fixed points and their attractive or repulsive character depend on the dimension  $d$ . In  $d = 1$ , there are three fixed points  $g_1^* = 0$  and  $g_{2,3}^* = \pm\sqrt{2/S_d}$ , among which only the latest two are attractive. Those fixed points imply that  $\alpha^{(1+1)} = 1/2$  and  $z^{(1+1)} = 3/2$ . These values are also obtained from a master equation approximation and are exact for  $d = 1$ . However, for  $d = 2$  the situation changes. There exists only one fixed point at  $g = 0$ , and it is repulsive. Finally, for  $d > 2$  there are again three fixed points, but only  $g^* = 0$  is attractive (see the figure 2.4). The region of values of  $g$  where the flow is divergent is known as the strong-coupling regime for KPZ. This region is not accessible by perturbation procedures. This has motivated the application of a wide range of different analytical methods, without the consecution (by now) of conclusive results. The small zone close to the attractive fixed point

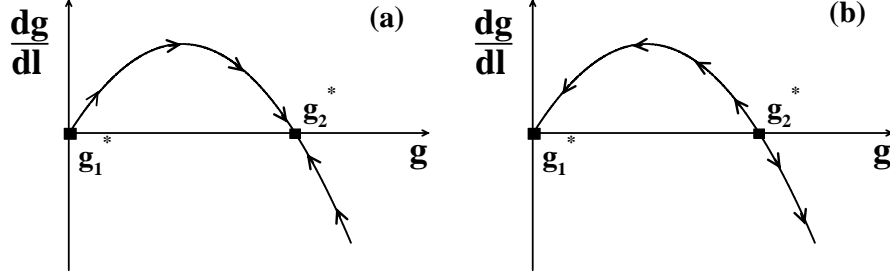


Figure 2.4: The flow of the coupling constant  $g$  for (a)  $d = 1$  and (b)  $d \geq 3$ .

$g_1^* = 0$  for  $d \geq 3$  belongs to EW universality class. The surfaces are smooth because the dimension is higher than the critical  $d_c$  for EW. On the other hand, interfaces are rough in the strong coupling regime (at least below  $d = 4$ ; dimension that some authors believe to be the critical dimension of KPZ). Hence at the two repulsive fixed points  $g_{2,3}^* = \pm \sqrt{2d(d-2)/S_d(2d-3)}$  there is a roughening transition.

### 2.2.3 The MBE growth equations

The situation in crystal growth by MBE is similar to the model of deposition that motivated the introduction of EW equation. However, there exists a crucial difference in the behaviour of the deposited particles, atoms in the case of MBE. Once an atom arrives to the surface, it diffuses with a probability that follows an Arrhenius law,  $R \sim \exp(-E_d/kT)$ . The activation energy  $E_d$  depends on the number of bonds that the atom has with its neighbours,  $E_d = E_o + nE_n$ , where  $n$  is the number of neighbours and  $E_o$  and  $E_n$  are activation energies. Hence, the higher is the number of neighbours, the more stable that configuration results. The atoms also have some probability of leaving the interface. But in general the desorption is more unlikely than the diffusion and atoms are able to find a stable position.

The implementation of this process in a computer program is made via a kinetic Montecarlo (KMC) method [Tamborenea 1993]. In this model, diffusion and desorption rates are calculated from the external parameters;

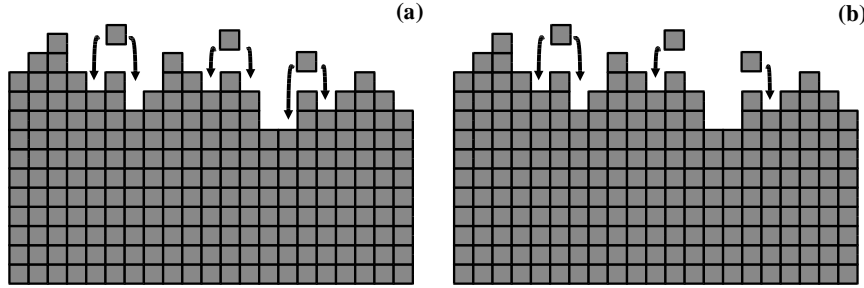


Figure 2.5: Rules for the algorithms of (a) DT model and (b) WV model.

the temperature,  $T$ , and the activation energies. Every atom that reaches the surface moves or is detached with those probability rates till it is covered by other atoms or is desorbed. The exponents measured from this model vary with temperature. If  $T$  is very low, the atoms are not able to diffuse or detach. So, this model behaves as a random deposition, while, in the high temperature regime, the atoms may diffuse along great distances, and they only stop when find a very stable configuration, producing thus smooth interfaces.

Wolf and Villain [Wolf 1990] and Das Sarma and Tamborenea [Das Sarma 1991] proposed independently two simple deposition models that were supposed to mimic the main characteristics of KMC model in the intermediate temperature regime. The substrate in both models is represented by a square lattice. The simulation begins when an atom reaches the surface at a randomly chosen position ( $i$ ). The next step is slightly different for each model (see figure 2.5). In the Wolf-Villain (WV) algorithm, the particle moves to the site with the highest coordination number among  $i$  and its nearest neighbours. In the case of Das Sarma-Tamborenea model (DT), a site that increases the coordination number is randomly selected in the neighborhood of  $i$ . Though the exponent values and the universality classes of these models have been widely discussed [Kotrla 1992, Das Sarma 1992, Krug 1993, Tamborenea 1993], early simulations of both models gave as result the exponent value  $\alpha \sim 1.5$  and  $\beta \sim 0.365$  in 1+1 dimension [Das Sarma 1991, Wolf 1990].

The growth equations that describe the MBE phenomenon must take into account the major characteristics of the problem. The mass is conserved

during the diffusion and the atoms tend to establish in the places with a high coordination number. The mass conservation symmetry implies that the equation must be of the type  $\partial h/\partial t = -\nabla \vec{j}$ , where  $\vec{j}$  is the particle current that depends on the local topology ( $\nabla h$ ,  $\nabla(\nabla^2 h)$ ,  $\nabla(\nabla h)^2$ , etc) of the surface. Thus, this symmetry prevents the existence of a KPZ nonlinear term. On the other hand, the tendency of atoms to move to the sites with a higher number of neighbours, i.e. positions of high curvature of the interface  $\mu = \nabla^2 h$ , may be included in a equation by means of a current  $\vec{j} \propto -\nabla \mu = -\nabla(\nabla^2 h)$ . The final expression one gets to is then

$$\frac{\partial h}{\partial t} = -K \nabla^4 h + F + \eta(x, t), \quad (2.22)$$

where  $K$  is a constant and  $\eta$  is a white noise with zero average and with a variance  $A^2$ . This equation is known as Mullins-Herring equation [Lai 1991]. It may be exactly solved as the EW equation, but a simple scaling argument is enough to obtain the exponents. If, in the latter expression, the space and time variable are re-scaled as  $x \rightarrow bx$ ,  $t \rightarrow b^z t$  and  $h \rightarrow b^\alpha h$ , we obtain

$$\frac{\partial h}{\partial t} = -K b^{z-4} \nabla^4 h + b^{\frac{z-d}{2}-\alpha} \eta. \quad (2.23)$$

When the exponents over  $b$  are zero, the following relations must be fulfilled:  $z = 4$  and  $\alpha = (4 - d)/2$ . The high value of  $z$  implies a very slow dynamics of the model. The value of  $\alpha = 1.5 > 1$  (for  $d = 1$ ) is an example of super-roughness, a very special case of scaling that will be discussed further in the next chapter. The values of  $\alpha$  and  $\beta = \alpha/z = 0.375$  coincide with the exponents found in the initial simulations of WV and DT models. In  $2 + 1$  dimension, the exponents become  $\alpha = 1$  and  $\beta = 0.25$ . The critical dimension for this equation is  $d_c = 4$ .

Some authors have suggested that a nonlinear term of the kind  $\nabla^2(\nabla h)^2$  should be included in the growth equation [Sun 1989, Lai 1991, Villain 1991]. The origin of this term would be a preference of the particles to be attached to the flattest areas (close to the extremes of  $h$ ). The resulting equation is

$$\frac{\partial h}{\partial t} = -K \nabla^4 h + \lambda_2 \nabla^2(\nabla h)^2 + F + \eta(x, t). \quad (2.24)$$

This model is referred to as the Lai-Das Sarma-Villain (LDV) equation. As happens with the KPZ model, a scaling-type argument is not valid for this

nonlinear equation. The exponents, however, may be obtained using the dynamic renormalization group. The flow equations for the parameters of the LDV model in the one-loop approximation are

$$\begin{aligned} \frac{dK}{dl} &= K [z - 4 + S_d (\lambda_2 A^2 / 2K^3) (6 - d) / (4d)] \\ \frac{d\lambda_1}{dl} &= \lambda_1 [z + \alpha - 4] \\ \frac{dA}{dl} &= \frac{A}{2} [z - 2\alpha - d] . \end{aligned} \tag{2.25}$$

The existence of a nontrivial fixed point in those equations implies the following relations between the exponents:  $z + \alpha = 4$  and  $z - 2\alpha = d$ . From them, the following exponent values may be extracted:  $\alpha = (4 - d)/3$ ,  $z = (8 + d)/3$  and  $\beta = (4 - d)/(8 + d)$ . These formulae give  $\alpha^{(1+1)} = 1$ ,  $\beta^{(1+1)} = 1/3$  and  $\alpha^{(2+1)} = 2/3$ ,  $\beta^{(2+1)} = 1/5$ .

The exponents of the linear and nonlinear equations in  $2 + 1$  dimensions may be compared with those obtained in the experiments described in the first table of chapter one. As already mentioned, the exponent values depend crucially on the temperature. However, there is a clear tendency for the exponents to be close to the values predicted by the Mullins-Herring and the LDV equations. This general trend is only broken, within the group presented in that table, by the experiments [Ojeda 2000], [Desjardins 1999] and [You 1993]. These deviations from MBE universality may be explained if the coarse-grained equations that describe those experiments include other higher order nonlinear terms.

A similar situation raised with more detailed studies on the discrete models [Šmilauer 1994, Das Sarma 1996, Das Sarma 1997, Punyindu 1998]. Actually, in the stochastic equation that describes the WV model a term of the kind  $\nabla(\nabla h)^3$ , which renormalizes into a EW diffusion term, must be included. Analogously, the DT model belongs to the LDV universality class instead of to the linear Mullins-Herring class. Indeed, some discrete MBE models, where the rules of diffusion take into account the possibility of diffusion along the vertical direction, are clearly in the KPZ universality class [Yan 1992, Kessler 1992].

## 2.3 Models with quenched disorder

The models presented in the previous section are not able to explain the exponents measured in the experiments of fluid flow through porous medium or paper burning. The roughness exponents of those experiments, as may be seen in the previous chapter, are higher than those expected from KPZ or EW universality. This means that a key ingredient of the dynamics of those experiments is missing by KPZ or EW equations. One possible solution was proposed by [Bruinsma 1984], [Koplik 1985] and [Parisi 1992]. It is based on the use of a different kind of disorder.

The noise of the equations KPZ or EW is a function of both space and time. The disorder modeled in such a way must vary in time in every point of the interface. However, the disorder in the fluid experiments is of a quite different nature. The heterogeneous media through which the fluid, or the fire front, moves is prefixed for each experimental realization. This type of disorder is better represented by a noise that depends on the surface position inside the medium,  $\eta(x, h)$ , and not on time.

The introduction of *quenched* disorder in the preceding models leads to a very rich and novel behaviour. In those models, as KPZ for instance, the roughness or dynamic exponents of the surfaces were the same if the term of the pushing force,  $F$ , was present or not. The average velocity of the front was the only characteristic controlled by  $F$ . Hence, a simple change

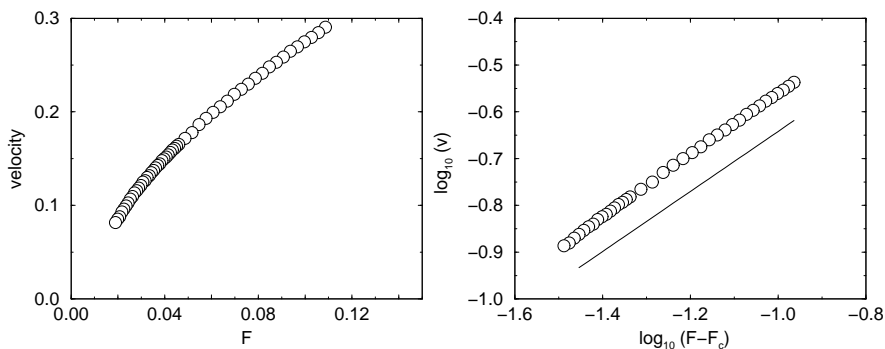


Figure 2.6: Velocity versus distance to critical driving force for a DPD model with system size  $L = 800$ . The figure on the right is the log-log plot of the same data. The slope of the straight line is  $\theta \approx 0.64$ .

of variable, as a Galilean transformation, maintained invariant the fractal properties of the interface. If the disorder is quenched, this is no longer true. When the driving force is too low, the interfaces are pinned by the disorder, and consequently they are smooth. On the other hand, when the surfaces are moving very fast,  $\{\langle \partial_t h \rangle_x\} = v \gg 0$ , the quenched noise term reduces to an annealed one,  $\eta(x, h) \approx \eta(x, vt)$  if  $h \sim vt$ , and the KPZ or EW universality are recovered.

Between those two regimes, at a determined value of the force,  $F_c$ , there is a phase transition called depinning transition, which often has continuous character [Middleton 1992]. In that case, the correlation length,  $\zeta$ , corresponds to the average size of the pinned (depinned) sites when we approach the transition from above (below). This correlation length diverges when the critical force is approached as  $\zeta \sim |F - F_c|^{-\nu}$ . The mean velocity of the front plays the role of the order parameter, and  $F$  (though this is not the only possibility as will be shown in the chapter 4) is the control parameter. For values of the pushing force close above the transition, the velocity shows a power law dependence,  $v \sim f^\theta$ , on the relative distance to the critical point  $f = (F - F_c)/F_c$  (see figure 2.6). In this regime, the motion of the front is quite jerky, most of time driven by avalanches that present a critical size distribution,  $p(s) \sim s^{-\tau}$ , at the transition point. The roughness and dynamic exponents at the transition and above are manifestly higher than those of KPZ or EW equations.

The discrete models and equations in the literature on this topic may be separated essentially into two universality classes [Amaral 1994]. Following this idea, I have divided this section in two subsections.

### 2.3.1 The quenched EW equation

If in the EW equation the noise term is replaced by a quenched noise, we obtain

$$\frac{\partial h}{\partial t} = \nu \nabla^2 h + F + \eta(x, h). \quad (2.26)$$

As in the original equation  $\nu$  is the diffusion coefficient,  $F$  the driving force and  $\eta$  is a noise with zero average and white correlations:  $\{\eta(x, h)\eta(x', h')\} = A_q^2 \delta^d(x - x') \Delta(|h - h'|)$ . Where  $\Delta(z)$  is a short-range fast decaying function of  $z$ . This is the quenched Edwards-Wilkinson (QEW) equation. It was firstly proposed by [Bruinsma 1984] as a suitable model for the borders of magnetic domains in random field Ising model, and by [Koplik 1985, Kessler 1991] as

a model for fluid moving in heterogeneous media. This equation can also be obtained minimizing a Hamiltonian, which corresponds to an elastic string inside a heterogeneous medium. That medium is represented by a quenched random potential with the Hamiltonian

$$H[h, F] = \frac{\nu}{2} \int (\nabla h)^2 dx + \int dx \int_0^h [\eta(x, h') - F] dh'. \quad (2.27)$$

The QEW equation is recovered by the Hamilton equation:  $\partial_t h = -\delta H / \delta h$ . The mapping of this problem onto a elastic string moving in a disordered medium allows the straightforward construction of discrete models. Those models are composed by discrete elements with an elastic interaction among them, and impulsed by a constant force,  $F$ , inside a medium with randomly distributed wells of the potential [Dong 1993, Jensen 1995]. The values of the exponents of this universality class have been obtained from those models. However, the most accurate estimation of the exponents are due to a cellular automata proposed by [Leschhorn 1993b], which is based on a simplification of the continuous equation. The height of the interface over each substrate position is represented by an integer variable  $h_i$ . The surface advances ( $h_i \rightarrow h_i + 1$ ) whenever the following condition  $v_i = \Delta^2 h_i + G\eta_{i,h} > 0$  is hold.  $\Delta^2$  is the lattice Laplacian,  $G$  is the amplitude of the dichotomous quenched noise  $\eta$ .

This model presents a depinning transition for a value of  $G$ ,  $G_c$ . The exponents measured by Leschhorn close and above to the critical point were  $\alpha^{(1+1)} \approx 1.25$ ,  $\beta^{(1+1)} \approx 0.88$ ,  $\theta^{(1+1)} \approx 0.25$  and  $\nu^{(1+1)} \approx 1.33$  for dimensions 1+1, and  $\alpha^{(2+1)} \approx 0.74$ ,  $\beta^{(2+1)} \approx 0.47$ ,  $\theta^{(2+1)} \approx 0.65$  and  $\nu^{(2+1)} \approx 0.8$  in 2+1 dimensions. In a more recent work, M. Jost and K.D. Usadel [Jost 1998] reported the existence of a cross-over from  $\alpha^{(1+1)} \sim 1.25$  to  $\alpha^{(1+1)} = 1$  on very big scales. They also measured  $\alpha^{(3+1)} \approx 0.33$  and  $\beta^{(3+1)} \approx 0.21$ . The avalanches of this discrete model have also been studied in low substrate dimensions [Pang 1997]. The value of the exponent found in that work for the avalanche size distribution in 1+1 was:  $\tau \approx 2.0$ .

The explicit dependence of the noise on the surface height,  $h$ , makes more complex the use of the standard theoretical tools to obtain the exponents of this model. One simple argument, proposed initially by [Larkin 1970], allows to gain some insight in the depinning transition of QEW equation. It is based on a rough estimation of the influence that each term of the equation has on the roughness of the interface. Let us consider a portion of the surface with longitudinal size  $\ell$ , and whose width is less than one lattice

space  $a$ . The diffusion term, whose value is approximately  $\nu a \ell^{-2}$ , tries to make the interface flat. While the quenched noise,  $\Delta(0)^{1/2} \ell^{-d/2}$ , tries to make it rough. We can evaluate the dominant term by dividing the contribution of the diffusion by that of the quenched noise,  $(\nu a / \Delta(0)^{1/2}) \ell^{(d-4)/2}$ . This ratio tends to  $\infty$  when  $\ell \rightarrow \infty$  for  $d > 4$ , and it tends to zero for  $d < 4$ . If it tends to  $\infty$ , the interfaces generated by the model are flat because the diffusion term is dominant. Hence, there exists a critical dimension for the QEW equation of  $d_c = 4$ .

The contributions of both terms are equal for a distance  $\ell_c \sim (\nu a / \Delta(0)^{1/2})^{2/(4-d)}$ . For  $d < d_c = 4$ , the interface is rough on scales  $\ell > \ell_c$  and flat below  $\ell_c$ . This argument also allows us to have a first estimation of the critical force of this model. All the interfaces are moving if the force compensates the quenching effect of the noise  $F_c \sim \Delta(0)^{1/2} \ell_c^{-d/2} = \Delta(0)^{1/2} (\Delta(0)^{1/2} / \nu a)^{d/(d-4)}$  for  $d < 4$  and  $F_c = 0$  for  $d > 4$ .

A first approach to the exponents of this equation may be obtained by the simple power counting method as the one used in previous sections. If the variables of the QEW equation are rescaled as  $x \rightarrow bx$ ,  $t \rightarrow b^z t$  and  $h \rightarrow b^\alpha h$ , and the noise term is supposed to scale as  $\eta(bx, b^\alpha h) \rightarrow b^{-d/2-\alpha/2} \eta(x, h)$ . The exponents for this model would be  $z = 2$  and  $\alpha = (4-d)/3$ . A more developed theoretical tool, the functional renormalization group, was applied to this equation by [Nattermann 1992b, Narayan 1993, Leschhorn 1997]. This method is similar to the dynamic renormalization used with KPZ equation, but instead of considering only one coefficient for the noise, all the terms of a power expansion of  $\Delta(z)$  are renormalized. The results, the first elements of a  $\epsilon = 4 - d$  expansion, are  $\alpha \approx \epsilon/3$  and  $z \approx 2 - (2\epsilon/9)$ ,  $\theta \approx 1 - (2\epsilon/3(6-\epsilon))$  and  $\nu \approx 3/(6-\epsilon)$ . The exponents predicted by these formulae are closer to those obtained numerically for the small values of  $\epsilon$ . Hence, it is still necessary further work to understand the exponents in low dimensions.

### 2.3.2 The quenched KPZ equation

The importance of lateral growth leads to the inclusion of the KPZ nonlinear term in the EW model. We can also add a nonlinear term in the QEW equation to obtain the Quenched KPZ equation (QKPZ) [Parisi 1992]:

$$\frac{\partial h}{\partial t} = \nu \nabla^2 h + \lambda (\nabla h)^2 + F + \eta(x, h). \quad (2.28)$$

[Tang 1992] and [Buldyrev 1992] demonstrated that a couple of models proposed by them showed a depinning transition very different from QEW universality. Those algorithms are known as directed percolation depinning models (DPD). In Tang's version, the height of the interface over the substrate is an array of integer values  $h_i$ . The quenched disorder is represented by a random number between 0 and 1 assigned to every lattice position  $\eta_i(h_i)$ . In each time step, a site ( $i$ ) is randomly chosen. If any of its neighbours is lower than  $h_i$  by two or more lattice spaces,  $h_i - h_{j\text{nn}i} \geq 2$ , this neighbour site grows,  $h_j \rightarrow h_j + 1$ . In case that more than one neighbour fulfills the previous relation, one is selected at random to grow. Otherwise, the quenched noise in  $i$  is compared with the external pushing force  $F$ . If  $F > \eta_i(h_i)$ , the interface advances:  $h_i \rightarrow h_i + 1$ .

This model shows a pinning-depinning transition at a fixed value of the force,  $F_c$ . At  $F_c$ , the blocked sites (those for which  $\eta_i(h_i) > F$ ) are enough to form a continuous cluster that spans through the whole system. In these circumstances, the interface is stopped by the lowest hyper-surface of those pinning clusters. Hence, by knowing the characteristics of those hyper-surfaces (or of the clusters), it is possible to infer the exponents of the DPD model at  $F_c$ . Typically, the mean size of the pinning clusters diverges as  $\zeta_{\parallel} \sim |F - F_c|^{-\nu_{\parallel}}$  and  $\zeta_{\perp} \sim |F - F_c|^{-\nu_{\perp}}$  when the critical force is approached. This behaviour implies that, for instance, the width of the interface of the correspondent DPD model goes as  $w \sim \zeta_{\perp} \sim |F - F_c|^{-\nu_{\perp}} \sim \zeta_{\parallel}^{\nu_{\perp}/\nu_{\parallel}}$ . Hence,  $\alpha = \nu_{\perp}/\nu_{\parallel}$  at  $F = F_c$ . Similarly, the time needed by a surface to overcome a cluster of blocked sites depends on the cluster lateral size. Actually,  $t \sim \zeta_{\parallel}$  because the lateral growth is the only permitted motion. So, the velocity close to the critical force behaves as  $v \sim \zeta_{\perp}/\zeta_{\parallel} \sim |F - F_c|^{\nu_{\parallel} - \nu_{\perp}}$ , so  $\theta = \nu_{\parallel} - \nu_{\perp}$ .

In (1+1) dimension, the cluster of blocked sites at  $F_c$  forms a directed percolation (DP) path. DP is a very well known problem [Hinrichsen 2000], for a more general introduction to percolation theory see [Stauffer 1994]. The exponents measured for DP are  $\nu_{\parallel} = 1.733$  and  $\nu_{\perp} = 1.097$ , with a critical density  $\rho_c = 0.5387 = 1 - F_c^{(1+1)}$ . Hence,  $\alpha^{(1+1)} = \nu_{\perp}/\nu_{\parallel} = 0.633$  and  $\theta^{(1+1)} = \nu_{\parallel} - \nu_{\perp} = 0.636$ . It has been also measured  $z^{(1+1)} = 1$  [Tang 1992]. In (2+1) dimension, the latter mapping onto DP is no longer valid. Instead of directed percolation paths, now it is necessary to consider directed surfaces (DS). DS and the DPD model in dimensions  $d > 1$  were analyzed by [Amaral 1995b]. The results are shown in the next table. The dynamic exponent in those

dimensions may also be obtained from a mapping onto *isotropic* percolation [Havlin 1995]. From this mapping, it was found that the exponent  $z$  increases with  $d$  (see the following table) till it reaches the mean field value  $z = 2$  for  $d = 7$ . This is the critical dimension (at least for the dynamics) of this model.

It is also important to note that the exponents measured from this model close to and above the critical transition are not equal to those of the preceding table. Generally, they are a bit higher ( $\alpha_m = 0.75$  and  $\beta_m = 0.74$  for 1+1) [Makse 1995] and suffer a cross-over to those of KPZ universality for large scales [Amaral 1995]. The size where the cross-over takes place is the usual lateral correlation length,  $\zeta_{\parallel}$  (the mean size of the pinning clusters). The scaling of the avalanches of DPD model was estimated using a cellular automaton by [Barabási 1996], the values measured in this work were  $\tau^{(1+1)} \approx 1.7$  and  $\tau^{(2+1)} \approx 2.2$ . Those exponents were also determined directly from the DPD model [Amaral 1995b]:  $\tau^{(1+1)} \approx 1.26$  and  $\tau^{(2+1)} \approx 1.51$ .

<i>dimension</i>	$\alpha$	$z$	$\nu_{\parallel}$	$\theta$
1+1	0.633	1	1.733	0.636
2+1	0.48	1.15	1.16	0.8
3+1	0.38	1.36	0.95	1.0
4+1	0.27	1.58	0.66	1.0
5+1	0.25	1.7	0.6	–
6+1	0.2	1.8	0.5	–

This has been a rough description of DPD, a discrete model that presents a depinning transition different from the QEW universality. But, can the QKPZ equation be included in the same universality class?. The answer is affirmative, as was shown by [Amaral 1994, Amaral 1995]. Apart from direct integration of QKPZ equation [Csahók 1993, Csahók 1993b, Leschhorn 1996], the way to know if a KPZ nonlinear term is present in the effective equation describing a discrete model is by the addition of an overall tilt to the interface;  $h' \rightarrow h + mx$ . If that effective equation is as QKPZ, the mean velocity of the front must show a parabolic dependence on the tilt  $\{\langle \partial_t h \rangle_x\} = v_o + \lambda m^2$ . When this method is applied to DPD model, a clear parabola is observed. The curvature of that parabola diverges when the critical force is approached,  $\lambda \sim |F - F_c|^{-\phi}$ . Hence, discrete models may be classified in two different classes close to the depinning transition, depending on how they behave when an overall tilt is added to the interface. If the velocity does not change with the tilt or the curvature of the parabola vanishes when  $F \rightarrow F_c$ , they belong

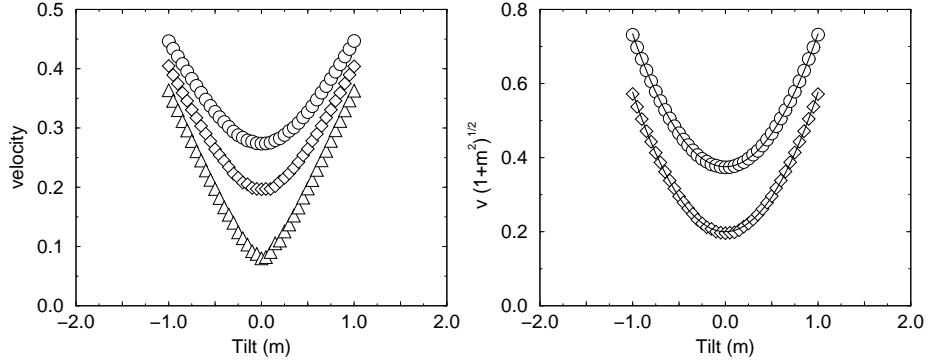


Figure 2.7: Velocity versus tilt for a Tang's DPD model of lateral size  $L = 800$ . The curves are for different driving forces; ( $\circ$ )  $F = 0.56$ , ( $\diamond$ )  $F = 0.52$  and ( $\triangle$ )  $F = 0.48$ . On the right, two of the precedent curves are analyzed following Neshkov's formula. The fits correspond to a couple of parabolas of curvatures  $\lambda_1 \sim 0.36$  and  $\lambda_2 \sim 0.38$ .

to QEW universality. On the other hand, if the curvature of that parabola diverges, the model is in the QKPZ class.

Actually, that divergence is due to an incorrect interpretation of the effect of the tilt on the velocity of surfaces [Neshkov 2000]. In fact, the velocity goes as  $v \sim (v_o + \lambda m^2) / \sqrt{1 + m^2}$  (see the figure 2.7), and not as a simple parabola. When this new formula is employed, discrete models have again two possible behaviours close and above to the transition. Either the curvature of the parabola tends to zero when  $F \rightarrow F_c$ , they belong to QEW universality, or remains constant and greater than zero at the transition, the models are in the DPD or QKPZ universality class.

The nonlinearity of KPZ equation is due to the lateral growth of the surface. So, it was expected to be proportional to the velocity. But, as it has been explained in the previous paragraph, some models are described by an effective QKPZ equation with a non vanishing nonlinearity even at the depinning threshold where  $v = 0$ . The question is: Which is the origin of this non-vanishing KPZ term?. Some authors [Tang 1995] proposed that it is generated by the anisotropy of the quenched disorder. A bit more clear is the effect that the presence of the KPZ nonlinearity has on the interface, the local slope is constrained to low values as happens in restricted solid on solid discrete models [Makse 1995b].

Finally, it is important to note that the QKPZ equation may exhibit a very different behaviour at the depinning transition when the product  $\lambda F$  is positive or negative. In the "classic" case  $\lambda F > 0$ , all mentioned above is valid, and this model may be included in the DPD universality class [Leschhorn 1996]. On the contrary, if  $\lambda F < 0$  the QKPZ equation presents a discontinuous phase transition at  $F_c$  [Jeong 1996, Jeong 1999, Szabó 2001]. The interface, at the critical point of this case, is formed by facets of constant slope.

### 2.3.3 Self-Organized Depinning models

There are a great number of physical systems whose fluctuations follow a power law distribution. Initially, they presented a big challenge for physics because the prediction of the central limit theorem is a Gaussian functional form for that distribution. Only in the very special case of a critical point was expected a scale-free distribution. However, the probability that a real system is in a critical point starting from a random configuration is almost zero; it is just a point in a parameter space with dimension  $D \geq 1$ . Hence, a new ingredient was necessary to explain the profusion of power-law distributions in experiments. Self-organized criticality (SOC) is one of the possible theoretical solutions for this problem [Bak 1987, Bak 1988]. The idea is that the dynamics of a system may be trapped, with no need of any external intervention, by an attractor including a critical point and its neighbourhood. In that case, the distribution of fluctuations is critical.

As was explained in the previous subsections, fronts moving inside a heterogeneous medium suffer a depinning transition at a critical value of the driving force. Hence, it is possible to look for a SOC model whose attractor lies close to  $F_c$ . The first couple of self-organized depinning (SOD) models were proposed by [Sneppen 1992]. In both, the height of the interface over the substrate takes the form of an integer array,  $h_i$ . The disorder is simulated by a random real number,  $\eta_i(h_i)$ , between zero and one assigned at every site of the lattice, as in the DPD model. The difference respect to that model comes from the dynamics. In the first algorithm, model A, there are some special sites where the interface may advance without breaking the RSOS condition ( $|h_i + 1 - h_{j \text{nn} i}| \leq 1$ ). The site with the lowest value of the disorder  $\eta$  is chosen to grow among those privileged sites. In the second model (B) the site with the lowest value of  $\eta$ ,  $i$ , is directly selected, the surface advances there,  $h_i \rightarrow h_i + 1$ , and an avalanche starts till the RSOS condition

( $\Delta h \leq 1$ ) is reestablished.

The first version, model A, exhibits faceted interfaces quite similar to those reported by [Jeong 1996] for the depinning transition of QKPZ with  $\lambda F < 0$ . The early measurement of the exponents of this model gave as result  $\alpha = 1$  and  $\beta \approx 0.95$  in 1+1. Though a more complete study about its scaling and exponents will be included in chapter three.

The second version, algorithm B, corresponds to a SOC model close to the DPD critical point. The roughness exponents of this model are  $\alpha^{(1+1)} \approx 0.63$  and  $\alpha^{(2+1)} \approx 0.50$  [Falk 1994]. Those values, as in DPD, are caused by the identification of interfaces with a directed percolation cluster (directed surfaces for  $d > 1$ ) composed by the biggest values of  $\eta$  [Tang 1993]. Although the geometry of the front admits a simple explanation, the same cannot be applied to the dynamics [Sneppen 1993, Sneppen 1993b]. As may be seen in the figure 2.8, the motion of interfaces tends to concentrate the activity. In general, the next site to grow will be close to one that has been recently actualized, producing thus a motion by avalanches. The size distribution of those avalanches, or *associated processes* as they are referred to in the literature, follows a power-law,  $P(s) = s^{-\tau} f(s/\Delta f^\gamma)$ . Where  $\Delta f$  gives an idea of the distance of the model to the criticality; if  $\eta_m$  is the biggest noise among those of the sites already chosen to grow,  $\Delta f = \eta_{critic} - \eta_m$ .

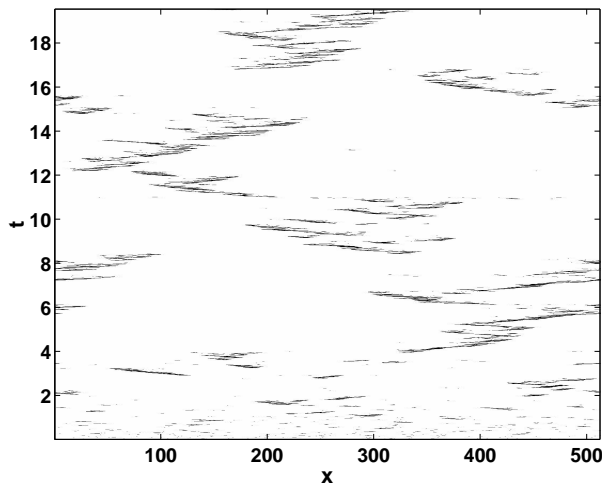


Figure 2.8: Associated processes (avalanches) for Sneppen's B model. The lateral size of the system is  $L = 512$ .

The exponents measured numerically for the associated process of model B are  $\tau^{(1+1)} \approx 1.25$  [Leschhorn 1994, Olami 1994] and  $\tau^{(2+1)} \approx 1.45$  [Falk 1994]. These exponents may be obtained analytically from the interface geometry. The steady state motion of this model is characterized by a sequence of surfaces corresponding to the advance of the interface. Two consecutive surfaces may overlap in many sites, and they are different in the places affected by an associated process. The geometry, roughness exponent, of those interfaces is known, hence it is possible to relate it to the distribution of the hyper-volumes enclosed between the surfaces. Initially, there were two proposals for that relation:  $\tau = 2/(1 + \alpha)$ ,  $\gamma = (1 + \alpha)/\alpha$  by [Olami 1994, Olami 1995] and  $\tau = 1 + (d - (1/\nu))/(d + \alpha)$  and  $\gamma = (d + \alpha)/\nu$  by [Maslov 1994, Maslov 1994b, Paczuski 1996]. In the latter formulae  $\nu = \nu_{\parallel}$  is the exponent measuring the divergence of the lateral cluster (directed surface) in the DP model when the critical density is approached from below.

The punctuated motion that the interfaces of B model suffer due to the associated processes generates temporal multiscaling in the width and correlations. If a new correlation function is defined as  $G_q(t, l) = \{\langle (h(x + l, t) - h(x, t))^q \rangle_x\}$ , the early time scaling  $G_q(t, l) \sim t^{q\beta_q}$  is observed, where  $\beta_q \neq (q/2)\beta_2$ . In fact, following the same ideas as for the distribution of sizes of associated processes, it is possible to establish the relation  $\beta_q = (q\alpha + d)/(q\alpha + qd)$  for  $q > 0$ .

As for the DPD, there also exists a SOC model whose dynamics takes place close to QEW depinning transition. Instead of choosing the site with the lowest noise value to grow, the selected site is that where  $\nabla^2 h + \eta_i(h_i)$  is minimum [Roux 1994]. The exponents measured from this model are equal to those of QEW at the critical pushing force.

## 2.4 Non-local models

There exist many physical systems where non-local laws must be taken into account to obtain a realistic model. Examples of those type of systems are DLA [Witten 1981], competitive needle growth models as the grass model [Krug 1997], bacteria or fungus colonies [López 1998], etc. The physical origin of non-locality may have several sources. It may be due to a shadowing effect in the growth process. In such systems, the competition for the growing material, as happens in a forest for the sunlight, produces that the peaks evolve faster than the valleys (they are shadowed by peaks). That effect has

a very long range influence, so local models are not useful to characterize this problem. It may also be due to a global conservation law. Some examples of this are fluid fronts, where the total mass is conserved, or fracture of brittle materials, where the energy travels through the whole system till it is dissipated in the crack front.

I will come back later to fracture experiments, in last chapter of this thesis. By now, let us focus on fluid motion in porous media to have an applied example of a non-local model. As it was explained in chapter one, experiments with fluids are carried out in two different working modes. Either with constant injection rate, or with constant pressure. As a consequence of mass conservation, in the first case fronts move with a fixed velocity. While in the second one, interfaces decelerate,  $v \sim t^\gamma$  with  $\gamma < 1$ , till they finally stop. The geometry of those pinned fronts was initially thought to correspond to a Directed Percolation (DP) cluster [Buldyrev 1992]. However, this identification has recently been questioned [Lam 2000, Dubé 2001, Lam 2001]. The problem is the *locality* of DP theory, which does not take into consideration the global mass conservation rule.

To surpass local models a phase-field model was recently proposed [Dubé 1999, Hernández-M 2001]. The main ingredient of this model is a field  $\phi(\vec{x}, t)$ , which takes a different value for each of the two fluids;  $\phi = \pm 1$ . The potential for  $\phi$  is  $V(\phi) = -(\phi^2/2) + (\phi^4/4) - \alpha(\vec{x})\phi$ , what ensures that there are only two stable values for  $\phi$  (those of the two fluids), and that  $\phi$  is not going to diverge anywhere. The dynamics is governed by a continuity equation to satisfy the mass conservation law,

$$\partial_t \phi = \nabla^2 [-\nabla^2 \phi - \phi + \phi^3 - \alpha(\vec{x})] - \vec{v} \nabla \phi. \quad (2.29)$$

$\alpha$  represents the disorder of the medium where the fluids are moving, and  $v$  is the injection rate. The exponents that are obtained from a numerical integration of this model are  $\alpha^{(1+1)} \approx 1.25$  and  $\beta^{(1+1)} \approx 0.32$  [Dubé 2000]. From the previous equation is possible to get an expression for the evolution of the interface,

$$\int_{-\infty}^{\infty} dx' \delta h' g(x, h|x', h') \partial_t h'(x', t) \propto \nabla^2 h + \eta(x, h), \quad (2.30)$$

and also to recover some of the well known fluid dynamics equation as Darcy law or Poisson equation for pressure [Hernández-M 2001].

## **2.5 Conclusions**

This has been a sketch of the theoretical development in this field during the last two decades. Though those models are able to explain some of the features observed in the experiments, they are still far from being a complete description of the experimental behaviour. I hope what is coming in next chapters to be a step further in that direction.



# Chapter 3

## Anomalous scaling

Interfaces of many growth models or experiments follow the scaling behaviour proposed by Family and Vicsek (FV) [Family 1985] for the evolution of the width. However, this is not a general rule. There are many other cases where this scaling is not able to represent the dynamics of the system.

### 3.1 Why is a new scaling needed?

In the Family-Vicsek scaling ansatz, growth universalities are characterized by three exponents. The roughness exponent  $\alpha$ , the growth exponent  $\beta$ , and the dynamic exponent  $z$ . Only two of those exponents are independent because of the self-consistency condition  $z = \alpha/\beta$ . The exponents  $\alpha$  and  $\beta$  may be measured, as was explained in the previous chapter, using both global or local width estimators.

In a self-affine fractal, the system size,  $L$ , acts as an upper cutoff for the scale invariance symmetry. Hence, when a magnitude is estimated close to that scale the power-law functional form is lost. This effect may be taken into account in a theory by means of a simple artifact known as finite-size scaling. For instance, for an interface after saturation, the local width goes as  $w(l) \sim l^\alpha$  up to system size scale  $L$ . The upper cutoff may be included in that formula as  $w(l, L) \sim l^\alpha f(l/L)$ . Where the function  $f(u)$  is constant for small values of  $u$  ( $u \ll 1$ ), and it is equal to  $u^{-\alpha}$  for  $u \approx 1$ . One of the consequences of the previous argument is that it gives a way to deal with global scales. If it is valid, the global width must increase with growing system size as  $W(L) \sim L^\alpha$ . The same power law dependence, and the same

exponent, as for the local width. This means that the comparison of widths of two systems of different sizes follows the same law as local widths of two scales inside only one system. Indeed, if the ratio  $(L_2/L_1) = (l_2/l_1)$  is hold, it can be extrapolated to the widths;  $(W(L_2)/W(L_1)) = (w(l_2)/w(l_1))$ . The FV scaling is based on a finite-size scaling argument. Hence, global and local estimators are expected to give the same values for the exponents.

There are, however, some theoretical growth models in which the symmetry between global and local magnitudes has been found to be broken. This phenomenon was initially discovered in super-rough interfaces [Leschhorn 1993]. Examples of this kind of surfaces appear in models as common as the QEW equation at the critical point [Leschhorn 1993b, Roux 1994, López 1997], or the linear MBE equation [Wolf 1990, Lai 1991]. Let us focus on the linear MBE model described by the Mullins-Herring equation

$$\frac{\partial h}{\partial t} = -K \nabla^4 h + F + \eta(x, t), \quad (3.1)$$

where  $K$  is a constant, and  $\eta$  is a white noise of zero average and a variance  $A^2$ . As may be seen in figure 1, the local and global width behave in a very different way. The roughness exponent measured from the local width is  $\alpha_{loc} \approx 1$ , while the global width gives  $\alpha \approx 1.5$ , closer to the value calculated analytically in the previous chapter. In this particular case, the problem is, as was shown in [Leschhorn 1993], that a local estimator cannot grow faster

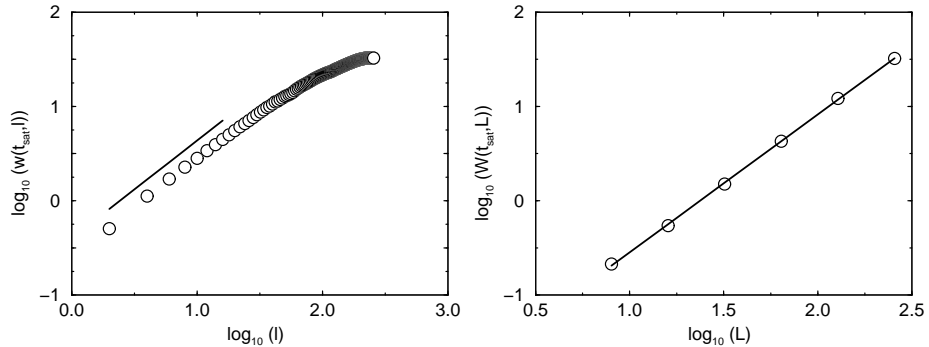


Figure 3.1: The local (left) and global (right) width of linear MBE equation in saturation. The circles ( $\circ$ ) represent data from simulation, the slope of the straight lines are  $\alpha_{loc} = 1$  on the left, and  $\alpha \approx 1.46$  on the right.

than the scale  $l$ . Hence,  $\alpha_{loc} = 1$  is an upper cutoff for local magnitudes. This is not the only possibility for anomalous roughening. As was demonstrated in [López 1997c], there can be anomalous scaling without super-roughening.

A second property that characterizes the anomalous scaling is the time evolution of the mean square slope. This function is defined as  $s(t) = \{ \langle (\nabla h)^2 \rangle_x \}$ . Its discrete version is the height-height correlation function at equal time evaluated for nearest neighbours:  $G(t, l = 1) = \{ \langle (h(x + 1, t) - h(x, t))^2 \rangle_x \}$ . In the Family-Vicsek scaling, the function  $G(t, l)$  reaches a steady state situation for a time  $t_\times(l) \sim l^z$ . Thus, the smaller  $l$  is, the faster the function  $G(t, l)$  saturates. Due to that,  $s(t)$  should remain constant for all value of time  $t > 0$ . However, in systems with anomalous scaling  $s(t)$  increases in time as a power law,  $s(t) \sim G(t, l = 1) \sim t^{2\kappa}$ , till the whole system saturates at  $t_\times \sim L^z$ . This behaviour, as will be established in following sections, is a consequence of the different scaling dependence of the global and local scales. It was firstly observed in MBE models [Amar 1993, Krug 1994, Das Sarma 1994, Das Sarma 1996, Dasgupta 1996, López 1996, Dasgupta 1997, Punyindu 1998], both linear and LDV equations but it is also present in QEW [López 1997].

In experiments, anomalous scaling has been observed in a wide range of fields: MBE growth [Yang 1994, Jeffries 1996, Zhao 2000], electro-deposition [Huo 2001], fracture [López 1998b, Morel 1998, Morel 2000] or fluid displacement inside heterogeneous media [Soriano 2002].

### 3.2 The anomalous scaling ansatz

The FV scaling was firstly proposed as a finite-size scaling argument for the evolution of the width of growing interfaces. The anomalous scaling ansatz may be also defined for the width, but the final result is more compact in the reciprocal space (that of power spectrum). Both scaling schemes, FV and anomalous, are based on the same assumption about the dynamics of the system. That postulate is the existence of only one characteristic scale  $\xi$ ,  $k_\times$  in reciprocal space. The scale  $\xi$  is the mean lateral size of the clusters of correlated growing sites. It increases in time as a power law  $\xi \sim t^{1/z}$ ,  $k_\times \sim t^{-1/z}$ , till it becomes equal to the system size  $\xi = L$ , and then the evolution reaches a steady state. If we put together this idea with the expected long-range correlations in the stationary regime, we obtain the

following scaling ansatz for the power spectrum

$$S(k, t) = \frac{1}{k^{2\alpha+d}} s(k/k_\times) = \frac{1}{k^{2\alpha+d}} s(kt^{1/z}) . \quad (3.2)$$

Where  $\alpha$  is the roughness exponent and the space where the interface is moving is  $(1+d)$ -dimensional. This functional form is common for FV and anomalous scaling. The difference comes in the asymptotic behaviour of the function  $s()$ . In the case of Family-Vicsek ansatz, it is

$$s_{FV}(u) \sim \begin{cases} u^{2\alpha+d} & \text{if } u \ll 1 \\ \text{const} & \text{otherwise} . \end{cases} \quad (3.3)$$

The value of  $s()$  in the region with  $u \gg 1$  ( $k \gg k_\times$ ) ensures that, on small scales  $l \sim 1/k < \xi$  the power-spectrum is independent of time. In this regime,  $S(k)$  decays as a power-law with  $k$ ,  $S(k) \sim 1/k^{2\alpha+d}$ . In direct space, this means that the correlations become constant in time on scales below  $\xi$ , including the mean square slope. This is not the case when anomalous scaling is present, as was explained in the previous section. Hence, the way to introduce the anomalous scaling in that ansatz is to add a new asymptotic power law dependence in the function  $s()$  for  $k \gg k_\times$  [López 1997b].

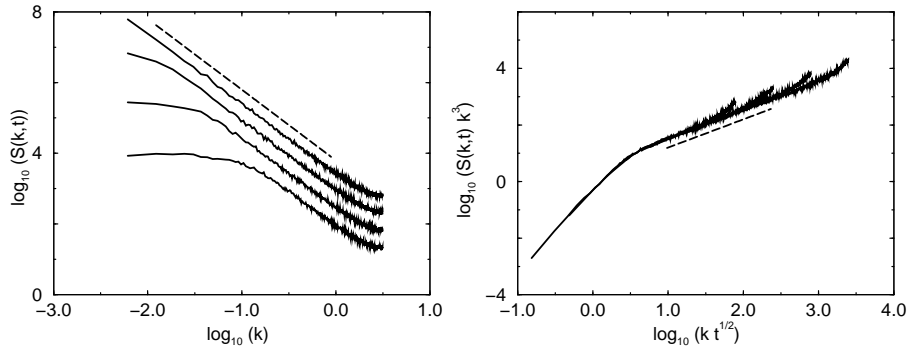


Figure 3.2: Power spectra for different times and their collapse using (3.4). Those power spectra are obtained from the discrete model proposed by [Bianconi 1999] with parameters ( $p = 0.75$ ,  $a = 1$ ). The slopes of the dashed lines are  $-(2\alpha_s + 1) = -2$  (on the left) and  $2\theta = 1$  (on the right).

$$s_A(u) \sim \begin{cases} u^{2\alpha+d} & \text{if } u \ll 1 \\ u^{2\theta} & \text{otherwise,} \end{cases} \quad (3.4)$$

the new exponent  $\theta$  may be written as the difference between other two exponents  $\theta = \alpha - \alpha_s$ . In such a way that the asymptotic functional form of the power spectrum for  $k \gg k_\times$  decays also as a power law with  $k$ , but now with a new exponent  $\alpha_s$ ;  $S(k, t) \sim t^{2\theta/z} / k^{(2\alpha_s+d)}$ . After saturation, this expression for the power spectrum becomes  $S(k, t > t_{sat}) \sim L^{2(\alpha-\alpha_s)} / k^{2\alpha_s+d}$ . The new exponent  $\alpha_s$  is called spectral roughness exponent. As it is shown in the appendix A, the spectral exponent is not always observable with direct space methods. However, it plays a very important role in how the scaling of direct magnitudes are.

### 3.3 Scaling in direct space

The scaling ansatz has been introduced in the reciprocal space. To extract further information, and also to compare clearly with the FV scaling, it is necessary to find how the second order momenta of  $\Delta h$  behave in the direct space. As may be seen in the previous chapter, the power spectrum is related to (local) global width and correlation functions by integral transformations. For instance, the global width of the interface may be obtained from  $S(k, t)$  with the following Parseval identity

$$W^2(t, L) = \frac{1}{aL} \sum_k S(k, t) \approx \int_{2\pi/L}^{\pi/a} d\mathbf{k} S(k, t) . \quad (3.5)$$

The lower cutoff in  $k$ -space,  $2\pi/L$ , is due to the finite lateral size of the interface  $L$ . While, the upper cutoff, Nyquist's frequency  $\pi/a$ , must be introduced because of the discrete character of the system. The constant  $a$  corresponds to the lattice spacing.

Similarly, we can find an expression relating the power spectrum to the local width. However, mathematically it is easier to use the height-height correlation function instead. This change has not a special significance because both quantities show a similar scaling;  $G(t, l) \sim w(t, l)$ . The function  $G(l, t)$  may be obtained by an integral transformation of  $S(k, t)$ ,

$$G(t, l) = \frac{2}{aL} \sum_k [1 - \cos(kl)] S(k, t) \approx \int_{2\pi/L}^{\pi/a} d\mathbf{k} [1 - \cos(kl)] S(k, t) . \quad (3.6)$$

Hence, in order to find the scaling of direct space magnitudes, we must carry out those integrals with the scaling ansatz (3.4) of the latter section. This process presents different characteristics, difficulties and results depending on the values of the exponents  $\alpha$  and  $\alpha_s$ . As a consequence, we may classify the scaling behaviour in four different groups:

$$\left\{ \begin{array}{l} \text{if } \alpha_s < 1 \Rightarrow \alpha_{loc} = \alpha_s \\ \text{if } \alpha_s > 1 \Rightarrow \alpha_{loc} = 1 \end{array} \right\} \left\{ \begin{array}{l} \alpha_s = \alpha \Rightarrow \text{Family-Vicsek scaling} \\ \alpha_s \neq \alpha \Rightarrow \text{Intrinsic anomalous} \\ \alpha_s = \alpha \Rightarrow \text{Super-roughening} \\ \alpha_s \neq \alpha \Rightarrow \text{Faceted interfaces} \end{array} \right.$$

The value of  $\alpha_{loc}$  is deduced from the scaling ansatz for  $G(l, t)$  in direct space; taking into account that this function goes as  $G(l, t > t_{sat}) \sim l^{2\alpha_{loc}}$  in the saturated regime. The step by step calculation of FV direct space scaling is carried out in the appendix A. For the sake of simplicity, the more complex mathematical formalism has been separated from the physical conclusions. Let us analyze the results for each particular case.

### 3.3.1 Family-Vicsek scaling

This is the scaling version proposed by Family and Vicsek [Family 1985]. As was explained in a previous section, it is based on a finite size scaling

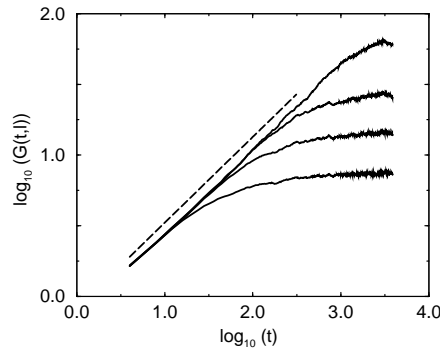


Figure 3.3: Temporal evolution of the height-height correlation function for KPZ model. The different curves correspond, from bottom to top, to scales  $l = 16, 32, 64, 256$ . The system size is  $L = 512$  and the slope of the straight line is  $2\beta \approx 0.61$ .

argument applied to the width estimator. This scaling may be recovered as a particular case from the general anomalous scaling ansatz. It corresponds to  $\alpha = \alpha_s < 1$ . In the appendix A, it is shown (expressions A.4 and A.5) that, with those restrictions for roughness exponent and starting from the power spectrum ansatz (3.4), the global width must behave as

$$W^2(t, L) \sim \begin{cases} t^{2\alpha/z} & \text{if } t \ll t_\times \\ L^{2\alpha} & \text{otherwise .} \end{cases} \quad (3.7)$$

Similarly, it is found (equations A.8, A.10 and A.17) that the height-height correlation function scaling is (see fig. 3.3) given by

$$G(t, l) \sim \begin{cases} t^{2\alpha/z} & \text{if } t \ll t_\times(l) \\ l^{2\alpha} & \text{otherwise .} \end{cases} \quad (3.8)$$

As an example of this scaling, the temporal evolution of the height-height correlation for KPZ equation is shown in figure 3.3. As well, the power spectrum for different times for the same model may be seen in figure 3.4. In this figure, it is also plotted a collapse of those data following the ansatz (3.4). The KPZ and EW universalities show, as many other systems, a Family-Vicsek scaling behaviour. The interfaces of those systems at saturation may be geometrically described by just one roughness exponent lower than unity. This fact implies that those interfaces are actual self-affine fractal objects. It

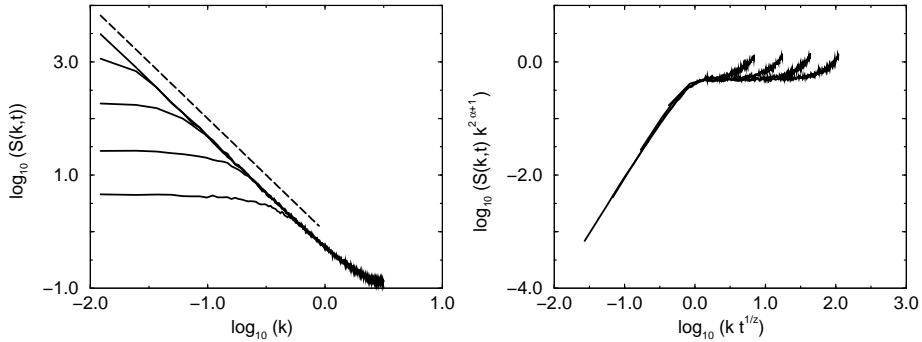


Figure 3.4: Power spectrum for different times for KPZ equation. The slope of that straight line is  $-(2\alpha + 1) \approx 2$ . The second figure is the collapse of four of those spectra following the ansatz (3.4) with  $\alpha = 0.5$  and  $z \approx 1.7$ .

also means that their only characteristic length, the system size  $L$ , enters in a simple finite-size scaling manner. There is thus no real distinction between local and global magnitudes. As a consequence, the estimators saturate for the smallest scales faster than for the global ones; on scale  $l$ , the saturation time is  $t_{\times}(l) \sim l^z$ . This leads to the fact that the dispersion of local slope profile,  $s(t)$ , does not grow in time.

### 3.3.2 Intrinsic Anomalous roughening

This scaling happens when  $\alpha \neq \alpha_s < 1$ . This is a more general (and complex) situation than the previous Family-Vicsek case. From the equations (A.4) and (A.5), we find that the global magnitudes still behave in a similar way as before

$$W^2(t, L) \sim \begin{cases} t^{2\beta} & \text{if } t \ll t_{\times} \\ L^{2\alpha} & \text{otherwise .} \end{cases} \quad (3.9)$$

However, the same can not be applied for the local estimators (equations A.8, A.11 and A.18), which are found to scale as

$$G(t, l, L) \sim \begin{cases} t^{2\alpha/z} & \text{if } t \ll t_{\times}(l) \\ t^{2(\alpha-\alpha_s)/z} l^{2\alpha_s} & \text{if } t_{\times}(l) < t < t_{\times} \\ l^{2\alpha_s} L^{2(\alpha-\alpha_s)} & \text{otherwise .} \end{cases} \quad (3.10)$$

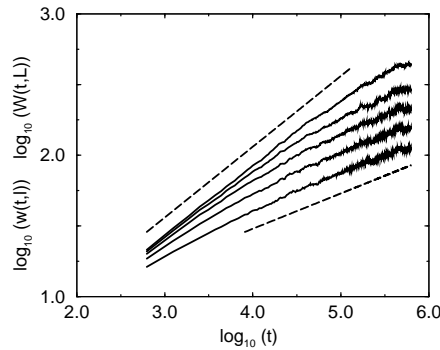


Figure 3.5: The global and local width for Bianconi's model. The curves are simulation data corresponding to the next scales from top to bottom: system size  $L = 1024, l = 256, 64, 32$  and  $2$ . The slopes of the two lines are  $\beta \approx 0.5$  and  $\kappa \approx 0.25$ .

From the previous expression, we can identify  $\alpha_{loc} = \alpha_s$  and  $\kappa = (\alpha - \alpha_s)/z$ . For a practical example see figures 3.1 and 3.5. Surfaces that show intrinsic anomalous behaviour might still be confused with self-affine fractals (their roughness exponent  $\alpha_{loc}$  is lower than one), though they have other novel properties. The global scales do not enter in this problem by means of a simple finite size scaling. On the contrary, local functions of saturated interfaces depend on the system size  $L$ . Indeed, the roughness exponents measured from global and local estimators are different ( $\alpha_{loc} = \alpha_s \neq \alpha$ ). This difference implies that the saturation of local quantities takes no longer place at  $t_\times(l)$  but at  $t_\times(L)$ , at the same time as for the whole system. That behaviour also affects  $s(t)$ ; the dispersion of the slope profile increases at early times ( $t < t_\times$ ) as  $t^{2\kappa}$ . In saturation, this function also depends on the system size,  $s(t > t_\times) \sim L^{2(\alpha - \alpha_s)}$ .

### 3.3.3 Super-roughness

The global roughness exponent is now higher than one,  $\alpha = \alpha_s > 1$ . Even so, the global quantities scaling is the same (eq. A.4 and A.5)

$$W^2(t, L) \sim \begin{cases} t^{2\alpha/z} & \text{if } t \ll t_\times \\ L^{2\alpha} & \text{otherwise .} \end{cases} \quad (3.11)$$

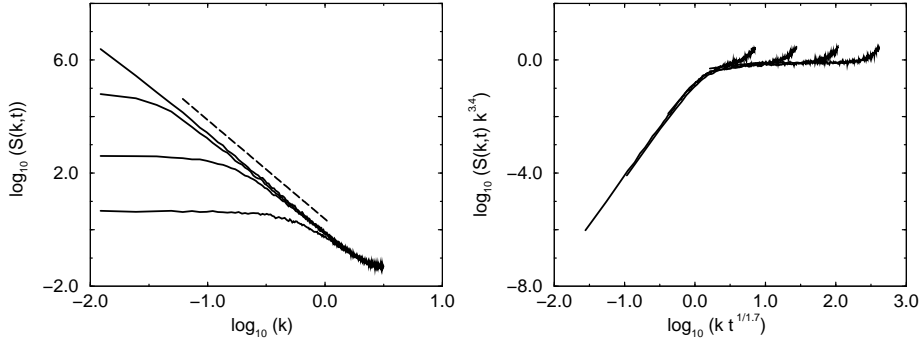


Figure 3.6: Power spectrum of the QEW model at the critical point. The slope of the straight line corresponds to  $\alpha \approx 1.25$ . The figure on the right is a collapse using ansatz (3.4).

Local magnitudes, on the other hand, show some special features (see eq. A.8, A.13, A.19, and figure 3.7)

$$G(t, l, L) \sim \begin{cases} t^{2\beta} & \text{if } t \ll t_{\times}(l) \\ t^{2(\alpha-1)/z} l^2 & \text{if } t_{\times}(l) < t < t_{\times} \\ l^2 L^{2(\alpha-1)} & \text{otherwise .} \end{cases} \quad (3.12)$$

The local roughness exponent is clearly  $\alpha_{loc} = 1 \neq \alpha_s$ . Although this asymptotic behaviour looks too much like the scaling for the intrinsic anomalous case (apart from the fact that  $\alpha_{loc} \neq \alpha_s$ ), the origin is very different. Super-rough interfaces cannot longer be considered as self-affine objects. For instance in a (1+1) dimensional space, the fractal dimension of those surfaces would be  $D = 2 - \alpha < 1$ , which corresponds to a group of points instead of to a curve. Despite of this fact, the local and global functions have the same characteristics as in the previous case. The local exponent has always as upper cutoff the value 1 [Leschhorn 1993], which is its actual value under these circumstances. It is that difference between  $\alpha$  and  $\alpha_{loc}$  what produces the anomalous behaviour of  $s(t)$ , see fig. 3.7.

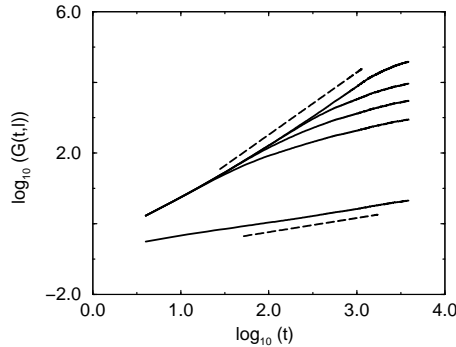


Figure 3.7: The height-height correlation function for QEW equation at the critical depinning transition. The scales of the different curves are from top to bottom  $l = 256, 64, 32, 16$  and  $2$ . The system size is  $L = 512$ . The slopes of the dashed lines are  $2\beta \approx 1.76$  and  $2\kappa \approx 0.4$  respectively.

### 3.3.4 Faceted surfaces

This is the latest scaling behaviour that has been found [Ramasco 2000]. It appears when  $\alpha_s > 1$  and  $\alpha_s \neq \alpha$ . This happens, for instance, at the critical transition of the QKPZ with  $(\lambda F) < 0$ . The global magnitudes go as (see eq. A.4 and A.5)

$$W^2(t, L) \sim \begin{cases} t^{2\alpha/z} & \text{if } t \ll t_\times \\ L^{2\alpha} & \text{otherwise .} \end{cases} \quad (3.13)$$

In the same way as in previous cases. The local magnitudes, however, show a singular behaviour (eq. A.8, A.15, A.20 and fig. 3.8)

$$G(t, l, L) \sim \begin{cases} t^{2\alpha/z} & \text{if } t \ll t_\times(l) \\ t^{2(\alpha-1)/z} l^2 & \text{if } t_\times(l) < t < t_\times \\ l^2 L^{2(\alpha-1)} & \text{otherwise .} \end{cases} \quad (3.14)$$

Again, the local roughness exponent is equal to one,  $\alpha_{loc} = 1$ . But, this is no the only information that we can extract from the latter expression. The value of  $\alpha_s$  is higher than one by definition, and it could be thought that this fact does not affect  $\alpha$ . However, the asymptotic behaviour of the height-height correlation leads to the condition  $\alpha \geq 1$ . On the contrary, the function  $G()$  would decrease in time in the intermediate regime. If  $\alpha > 1$ ,

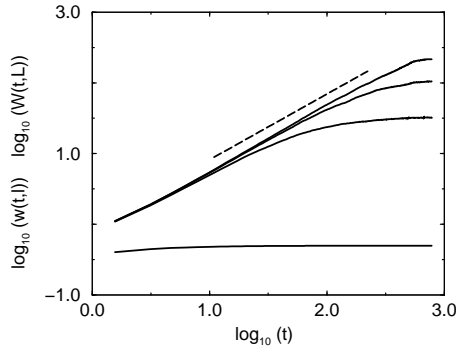


Figure 3.8: Time evolution of local and global width for Sneppen A model. The scales of observation are from bottom to top  $l = 2, 128, 512$  and  $L = 2048$ . The slope of the dashed line is  $\beta \approx 0.93$ .

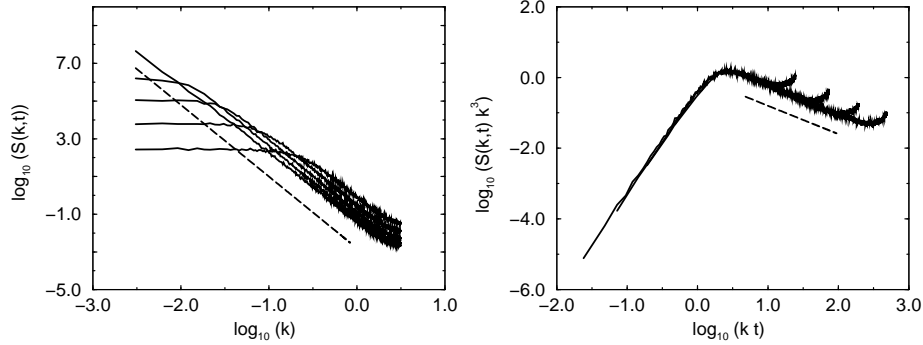


Figure 3.9: Power spectrum for different times obtained from S neppen A model. The slope of the dashed line on the left is  $2\alpha_s + 1 \approx 3.7$ . The second plot is a collapse of those spectra employing the ansatz (3.4). The value of the exponents used in the collapse are  $\alpha = 1$  and  $z = 1$ .

the scaling of direct space local magnitudes cannot be distinguished from the super-rough case. On the other hand, if  $\alpha = 1$ , the height-height correlation behaves in a similar way as in FV scaling. The main difference between those scaling forms and this one is in the power spectrum displacement in time. This may be seen in figure 3.9.

As was mentioned at the beginning of this section, the QKPZ with  $(\lambda F) < 0$  equation shows this scaling behaviour at the depinning critical point. At that point, a first-order phase transition takes place. The geometry of the interfaces at the transition is like a train of consecutive facets. One example of those interfaces, obtained from the SOD model proposed by [S neppen 1992], is plotted in figure 3.10. Let us consider only one of those facets, simplifying it as a triangle with base  $L$  and an angle  $\phi$  between the base and its sides ( $a = \tan \phi$ ). This object may be analyzed using the same techniques that are applied to interfaces. The mean height is then  $\langle h \rangle = (1/L) \int_0^L dx h(x) = aL/4$ , the global width  $W^2(L) = \langle h^2 \rangle - \langle h \rangle^2 = a^2 L^2/48$ , and the height-height correlation function goes as  $G(l, L) = \langle [h(x+l) - h(x)]^2 \rangle \sim a^2 l^2 - a^2 l^3/(3L)$ . The latter expression has been calculated with periodic boundary conditions. From those identities, the roughness exponents are  $\alpha = 1$ , and  $\alpha_{loc} = 1$ . On the other hand, the power-spectrum of that figure may be also calculated. The leading term of the spectrum is  $S(k, L) \sim L^{-1}/k^4$ . Comparing this expression

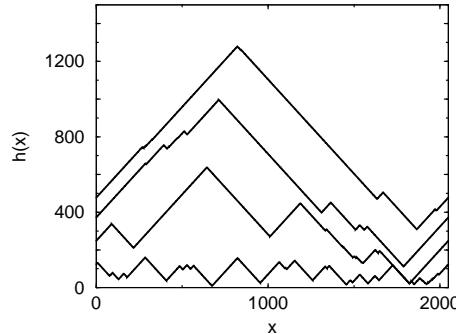


Figure 3.10: Interfaces of Sneppen A model for different times,  $L = 2048$ .

with the asymptotic behaviour of the power spectrum in anomalous scaling  $S(k) \sim k^{-2(\alpha_s+1)} L^{2(\alpha-\alpha_s)}$ , we find that  $\alpha_s = 3/2$ . Hence, the scaling of that simple object belongs to this group. The roughness exponent  $\alpha_s$  for the SOD model is a bit lower  $\alpha_s \approx 1.35$ ; an interface of this model is not composed only of one facet but of a random number of them of different sizes. It follows the same kind of scaling, though.

In general, this type of scaling may be expected when structures of a definite shape are involved in the problem. They do not have to be only triangles, but any kind of mound formation. Similar objects appear for instance in MBE growth for a determined region of experimental parameters [Ballestad 2001]. However, it is important to note that those structures must reach a stationary state in dispersion; their width cannot grow forever.

### 3.4 How to predict the presence of anomalous scaling

In the second chapter, it was mentioned that many growth universalities may be represented by continuous equations. This was the case, for example, for the Kim-Kosterlitz model [Kim 1989] and KPZ equation [Kardar 1986]. We may then formulate the following question: Are we able to know with a simple technique how the scaling behaviour of a given growth equation is?. The answer is affirmative in some cases, as was shown by [López 1999]. Let

us suppose that we have a growth equation

$$\frac{\partial h}{\partial t} = \Phi(\nabla h) + \eta(\mathbf{x}, t), \quad (3.15)$$

where  $h$  is, as usual, the height of the interface over the substrate,  $\Phi()$  is a functional that defines the growth model, and  $\eta$  is a zero average white noise with a variance  $A^2$ . In the previous sections, it has been demonstrated that the presence of super-rough, intrinsic anomalous or faceted scaling, implies that the variance of the slope profile must grow in time in the intermediate regime. This happens even in the marginal cases where  $s(t)$  grows logarithmically. To find how the slope behaves, we can apply the gradient operator to the previous equation, obtaining

$$\frac{\partial \Upsilon}{\partial t} = \frac{\delta \Phi}{\delta \Upsilon} \nabla \Upsilon + \nabla \eta. \quad (3.16)$$

The function  $\Upsilon(\mathbf{x}, t)$  is the gradient of  $h$ ,  $\Upsilon = \nabla h$ . Without losing generality, we can assume that  $\langle \Upsilon \rangle_x = 0$  in each direction of the substrate  $x$ . For instance, this condition is exact for an interface with periodic boundary conditions. The following step is to calculate the dispersion of  $\Upsilon$ ;  $W_{\Upsilon}(t, L) = \{\langle \Upsilon^2(\mathbf{x}, t) \rangle_{\mathbf{x}}\}^{1/2} = s(t)^{1/2}$ . Whenever a scaling behaviour different from Family-Vicsek is present, that function has a temporal regime where it grows as  $W_{\Upsilon} \sim G(t, l=1)^{1/2} \sim t^{\kappa}$  with  $\kappa > 0$ . The  $\kappa$  exponent is connected to the roughness exponents  $\alpha$  and  $\alpha_{loc}$  by the scaling relation  $\kappa = (\alpha - \alpha_{loc})/z$ . Hence, if we were able to find how  $W_{\Upsilon}$  behaves in time (as well as which is the value of  $\alpha$  or  $\alpha_{loc}$ ), the scaling of the model would be completely determined.

In order to have some practical examples, this method may be applied to several of the growth equations with annealed disorder mentioned in the previous chapter. The reason to do so is twofold: their exponents may be obtained analytically using a simple Flory-type scaling argument, and on the other hand they represent universality classes. The first model to be taken into consideration is KPZ equation,

$$\frac{\partial h}{\partial t} = \nu \nabla^2 h + \lambda (\nabla h)^2 + \eta(x, t). \quad (3.17)$$

As usual, the term  $\eta$  is a zero mean white noise with a dispersion  $A$ . In the second chapter, a Flory argument was already used with this equation. The exponents found with this method are exact only in  $(1+1)$  dimensions,

for higher dimensions they are only an upper cutoff for the actual exponents. The estimation for the exponents were  $\alpha = 2/(3+d)$  and  $z = (4+2d)/(3+d)$ . Note that the value predicted for  $\alpha$  is less than one in any dimension.

If a gradient operator is applied to the latter growth equation, it becomes

$$\frac{\partial \Upsilon}{\partial t} = \nu \nabla^2 \Upsilon + \lambda \nabla \Upsilon^2 + \nabla \eta(x, t), \quad (3.18)$$

where  $\Upsilon = \nabla h$ . This is a conservative equation; it may be written as  $\partial_t \Upsilon = -\nabla J$  with  $J = -\nu \nabla \Upsilon - \lambda \Upsilon^2 - \eta$ . If the function  $\Upsilon$  is treated as a rough interface, a Flory argument may be employed to obtain the exponents; both  $\alpha_\Upsilon$  (roughness) and  $\kappa$  (growth). Let us then consider a fluctuation of  $\Upsilon$ ,  $\Upsilon_l$ , which takes place on a scale  $l$ , and lives for a time  $t_l$ . Each term in the equation (3.18) may be approached as:  $\langle |\partial \Upsilon / \partial t| \rangle_l \sim \Upsilon_l / t_l$ ,  $\langle |\nabla^2 \Upsilon| \rangle_l \sim \Upsilon_l / l^2$ , and  $\langle |\nabla \Upsilon^2| \rangle_l \sim \Upsilon_l^2 / l$ . The noise term is a special case, it may be estimated as  $\langle \eta \rangle_l \sim l^{-(1+d/2)} t_l^{-1/2}$  or as  $\langle \eta \rangle_l \sim l^{-1} (t_l \Upsilon_l^d)^{-1/2}$  depending on the relative importance of  $l$  and  $\Upsilon_l$ . For the KPZ equation in the strong coupling-regime,  $\Upsilon_l$  is more significant and  $\eta$  must be approached by the second expression [Hentschel 1991].

The nonlinear term dominates on large scales over the diffusion. Thus by equating it to  $\langle |\partial \Upsilon / \partial t| \rangle_l$ , we get a characteristic fluctuation scale  $\Upsilon_l \sim l / t_l$ . On the other hand, by equating the noise and  $\langle |\partial \Upsilon / \partial t| \rangle_l$ , we find that:  $\Upsilon_l^{1+d/2} \sim t_l^{1/2} / l$ . Joining those expressions for  $\Upsilon_l$ , the result is  $\Upsilon_l \sim t_l^{-1/(4+d)}$ . The *growth* exponent for the field  $\Upsilon$  is then  $\kappa = -1/(4+d)$ . It is always negative, what implies that for KPZ the scaling is Family-Vicsek. The same asseveration is valid for the EW universality. The EW equation is obtained when  $\lambda = 0$  in KPZ equation. The value of  $\kappa$  is then  $\kappa = -d/4$ .

The next models to be analyzed concern MBE growth. The simplest equation of this group is the Mullins-Herring's

$$\frac{\partial h}{\partial t} = -K \nabla^4 h + \eta(\mathbf{x}, t). \quad (3.19)$$

This equation may be solved analytically, as was mentioned in the previous chapter, and the exponent values are  $\alpha = (4-d)/2$  and  $z = 4$ . In  $d = 1$  dimension, the roughness exponent is higher than unity. Hence, a super-rough (or faceted) scaling may be expected. The application of a gradient operator on that equation transforms it into

$$\frac{\partial \Upsilon}{\partial t} = -K \nabla^4 \Upsilon + \nabla \eta. \quad (3.20)$$

Using an argument similar to that of KPZ equation, we can estimate the terms of the latter equation:  $\langle |\nabla^4 \Upsilon| \rangle_l \sim \Upsilon_l/l^4$  and  $\langle |\nabla \eta| \rangle_l \sim (l^{d+2} t_l)^{-1/2}$ . If they are equated to the left hand side term, it is found that  $\Upsilon_l \sim t_l^{(2-d)/8}$ . This model shows thus a super-rough scaling for  $d = 1$ . With  $\alpha = 3/2$  and  $\kappa = (\alpha - \alpha_{loc})/z = 1/8$ . There is a critical dimension at  $d = 2$ , and finally Family-Vicsek scaling for  $d > 2$ .

Other local model proposed to describe MBE phenomenon is LDV equation (see chapter two),

$$\frac{\partial h}{\partial t} = -K \nabla^4 h + \lambda_2 \nabla^2 (\nabla h)^2 + \eta(\mathbf{x}, t). \quad (3.21)$$

The exponents of LDV equation may be obtained by a dynamic renormalization group technique,  $\alpha = (4 - d)/3$  and  $z = (8 + d)/3$ . The roughness exponent  $\alpha \leq 1$  for all space dimension. Consequently, there is no reason a priori to expect a scaling behaviour different from FV (except for  $d = 1$ , which could be marginally super-rough). If the gradient operator is applied to that equation, we obtain

$$\frac{\partial \Upsilon}{\partial t} = -K \nabla^4 \Upsilon + \lambda_2 \nabla (\nabla^2 \Upsilon^2) + \nabla \eta. \quad (3.22)$$

As before, a Flory-type argument may be employed to find the exponents of this new equation. As was done for KPZ, each term can be estimated as  $\langle |\nabla^4 \Upsilon| \rangle_l \sim \Upsilon_l/l^4$  and  $\langle |\nabla \nabla^2 \Upsilon^2| \rangle_l \sim \Upsilon_l^2/l^3$ . For this equation, as happened for KPZ, the intermediate scales are important due to the nonlinearity. Thus, the noise term must be approximated by  $\langle |\nabla \eta| \rangle_l \sim (l^2 \Upsilon_l^d t_l)^{-1/2}$ . From those expressions, the temporal evolution of a fluctuation is  $\Upsilon_l \sim t_l^{1/(8+3d)}$ . This model presents, as far as this approximation to find the exponents is valid, intrinsic anomalous roughening with  $\alpha = (4 - d)/3$  and  $\alpha_{loc} = \alpha - z\kappa = (8 + d - d^2)/(8 + 3d)$ .

Unfortunately, the only equation that may belong to faceted scaling, QKPZ with  $\lambda F < 0$ , can not be solved by a Flory-like approach of the kind above described. Neither it is possible to treat the general QKPZ equation by simple analytical means.

### 3.5 Conclusions

Anomalous scaling is the behaviour that arises from the interplay between the geometrical difference between global and local scales, and the existence of a

unique correlation length that grows in time as a power law. The difference between local and global scales is a feature that probably appears in many other situations where fractals are involved, no matter if time is present or not. However, it is not evident that these scale-invariant structures may go on receiving the name of *fractals*, at least with its classical meaning. A better understanding of the geometry of these sets remains still as an open question.

On the other hand, when the system under consideration evolves in time, we have proved that the different global and local scaling properties affect the dynamics of the system. In the case in which the unique correlation length increases in time as  $\xi \sim t^{1/z}$ , the Family-Vicsek scaling is no longer the only possible behaviour, actually other three different cases may appear. The main characteristic of these new scaling cases is the peculiar behaviour of the quantity  $\langle |\nabla h| \rangle_x$ . This function grows in time as  $\langle |\nabla h| \rangle_x \sim t^\kappa$ , where  $\kappa = (\alpha - \alpha_{loc})/z > 0$ . The local and global roughness exponents are independent quantities and, in contrast to FV scaling, three exponents are now required to describe the scaling of the system. This is a very important point, because in many cases only the local exponents have been measured. This is the case, for instance, of many fracture front experiments, for a review see [Bouchaud E. 1997]. The proposal of a unique universality class for mode II fracture [Bouchaud E. 1990] had to be reconsidered when the global roughness exponents were measured [López 1998b, Morel 1998]. The use of only local magnitudes may thus lead to the loss of a great deal of information about the surface scaling properties.



# Chapter 4

## Inside heterogeneous media

This chapter deals with a different but related problem to that of the previous chapter. The scaling is an ubiquitous question in surface growth, but in this case, we will focus on a more particular aspect; local growth in quenched disorder. As was explained in chapter two, when quenched disorder is present at the critical transition there are essentially two universality classes. The question is: Is there any relation between them?.

### 4.1 Other way to get depinned

The object of study in this chapter is the QKPZ equation. It is similar to the usual Kardar-Parisi-Zhang growth equation, but with the annealed noise term substituted by a quenched noise. This kind of disorder depends only on the spatial position and not on time. In this way, this sort of models are expected to be able to mimic more closely the conditions of fronts moving through heterogeneous media. The QKPZ equation is then

$$\frac{\partial h}{\partial t} = \nu \nabla^2 h + \lambda (\nabla h)^2 + F + \eta(\mathbf{x}, h) , \quad (4.1)$$

where, as usual,  $h(\mathbf{x}, t)$  represents the height of the surface over the substrate position  $\mathbf{x}$  at time  $t$ .  $\nu$ ,  $\lambda$  and  $F$  are constants, and  $\eta$  is a zero average white noise with variance  $A^2$ .

As was already mentioned, this model suffers a depinning transition for a determined value of  $F$ ,  $F_c$ . For values of the driving force below  $F_c$ , the interface remains pinned. On the other side, above the critical point, it

moves with a constant velocity and belongs to the KPZ universality class (on very large scales). The question here is to check if that transition may be realized using other quantity as control parameter. In order to find a candidate for that role, we can start by taking an spatial average over the previous equation.

$$v = \langle \partial_t h \rangle_{\mathbf{x}} = \lambda \langle (\nabla h)^2 \rangle_{\mathbf{x}} + F + \langle \eta(\mathbf{x}, h) \rangle_{\mathbf{x}} . \quad (4.2)$$

When  $\lambda$  is zero, the only two terms that remain on the left hand side are the driving force and the noise. If the force is positive, below the transition the interface is pinned in the sites  $(\mathbf{x}, h)$  where the quenched noise is such that the global condition  $F + \langle \eta \rangle_{\mathbf{x}} \leq 0$  is satisfied. This means that the surface essentially matches with the sites with the lowest value (the most negative) of the quenched disorder. On the other hand, the term  $\langle (\nabla h)^2 \rangle_{\mathbf{x}}$  is always positive. Thus, it can also contribute to free the interface. That contribution is a dynamic effect. It starts being zero due to the original flatness of the surface, and increases later because of the roughness induced by the noise. Hence, the only possible candidate to free pinned interfaces, apart from the pushing force, is the nonlinear lateral growth term  $\lambda (\nabla h)^2$ .

At first sight, this conclusion seems to be in contradiction with several papers published in the 90's [Amaral 1994, Amaral 1995, Makse 1995b]. In those works, an overall tilt,  $h \rightarrow h + m x$ , is added to interfaces of discrete models close to the depinning transition. If the model may be described with an effective growth equation similar to QKPZ, it is expected that the velocity shows a parabolic dependence on the tilt,  $v \sim v_0 + \lambda m^2$ . With this method, it was found that the known local growth models lay in two categories. The effective nonlinearity either vanishes or diverges as a power law when the critical point is approached from above;  $\lambda \sim (F - F_c)^{-\phi}$  with  $\phi$  either positive or negative. Those models, as the Random Field Ising model, whose effective  $\lambda$  vanishes belong to the QEW universality class. While the others, those with diverging  $\lambda$ , are in the DPD universality class. The origin of the nonlinearity is different for each class. In the QEW universality, it appears due to a dynamic effect. In the DPD universality, it may be originated by the anisotropy of the quenched disorder [Tang 1995]. These results suggest that an infinite  $\lambda$  is necessary to depin surfaces.

The interpretation of the tilt method was revised by [Neshkov 2000]. He claimed that the velocity actually goes as  $v \sim (v_0 + \lambda m^2) / \sqrt{1 + m^2}$  with the tilt,  $m$ . With this functional form, the effective  $\lambda$  does not change significantly close to and above the transition. Apart from this, a simple Larkin

[Larkin 1970] argument may be used to evaluate the effect of the nonlinearity at the depinning transition. This argument is based on a rough estimation of each term of the growth equation close to the depinning transition. Let us  $\ell$  be a lateral scale on which, in average, the roughness of the interface is lower than a lattice spacing  $a$ . The diffusion term, which on this scale is approximately  $\nu \nabla^2 h \sim \nu a \ell^{-2}$ , tends to make the surface flat. On the contrary, the quenched disorder, which may be estimated as  $\eta \sim A \ell^{-d/2} a^{-1/2}$ , tries to make it rougher. The interplay between these two terms produces a characteristic length scale  $\ell_c \sim (\nu a^{3/2}/A)^{2/(4-d)}$ . Above this scale the interface is rough and below is flat. To get a rough estimation of the critical force, we can equate the maximum contribution of the disorder (that on scale  $\ell_c$ ) with the pushing force to get:  $F_c \sim (A^{4/d}/\nu a^{(2+d)/d})^{d/(4-d)}$  for  $d < 4$ . The same can be applied, when the pushing force is zero, to the nonlinear term;  $\lambda_c \sim \nu a$ . Or, if the two terms are present, to a combination of both:  $F_c + \lambda_c \ell_c^{-2} a^2 \sim A a^{-1/2} \ell_c^{-d/2}$ , which leads to the expression  $\lambda_c(F_c) \sim \nu/a - (\nu a^{(d-1)/2}/A)^{4/(4-d)} F_c$ . Hence, this argument predicts that there exists a finite value of  $\lambda_c(F = 0)$  to depin the interface, and that the relation between  $F_c$  and  $\lambda_c$  is linear. The higher  $\lambda$ , the lower driving force is needed to free the surface.

## 4.2 The model

In order to check which of the preceding arguments is correct, it is necessary to integrate QKPZ equation in (1+1) dimensions. The discretization scheme that we have used is an Euler algorithm, which gives

$$h_i(t + \Delta) = h_i(t) + \Delta [\nu (h_{i+1}(t) + h_{i-1}(t) - 2h_i(t)) + \lambda \left( \frac{(h_{i+1}(t) - h_{i-1}(t))}{2} \right)^2 + F + A \xi(i, \hat{h}_i(t))], \quad (4.3)$$

where  $\Delta$  is the time step,  $\hat{h}$  represents the integer part of  $h$  and  $\xi$  is a Gaussian zero average noise that is delta-correlated in space,  $\{\xi(i, \hat{h}) \xi(j, \hat{h}')\} = \delta_{ij} \delta_{\hat{h}\hat{h}'}$ . The simulation always starts with a flat interface  $h_i(t = 0) = 0$  for all  $i$ , and periodic boundary conditions are used.

Our intention here is to use this discretization scheme to explore the region of high values of  $\lambda$ . There are however several works warning of instabilities in that region [Amar 1990, Newman 1996, Lam 1998]. We have

also observed those instabilities in our simulations. The instability is due to the way in which the nonlinearity is discretized. For instance, let us suppose that there is no noise and that the initial condition is a flat interface except for one site that has a height  $h_o$ . With this method, the nearest neighbours of that site suffer an advance  $\Delta h_{nn\ i} = \Delta[\nu h_o + \lambda h_o^2/4]$  during the first time step. The advance rate decreases when their heights become closer to that of the site  $i$ , but they may grow further whenever the condition  $\Delta h_{nn\ i} = \Delta[-\nu h_o + \lambda h_o^2/4] > 0$  holds. This relation imposes a maximum value for  $h_o$ ,  $h_o = 4\nu/\lambda$ . All perturbations above that value spread laterally and increase till some infinities are generated in the algorithm. The results about QKPZ reported hereafter lay in a stable region of parameters. In most of our simulations, we have used natural units with  $\nu = 1$  and  $A = 1$ .

### 4.3 What we found

The first question to be taken into account is the existence or not of a depinning transition caused by the nonlinear term. To check this, we have decided to consider the QKPZ equation without pushing force. Hence, most of our

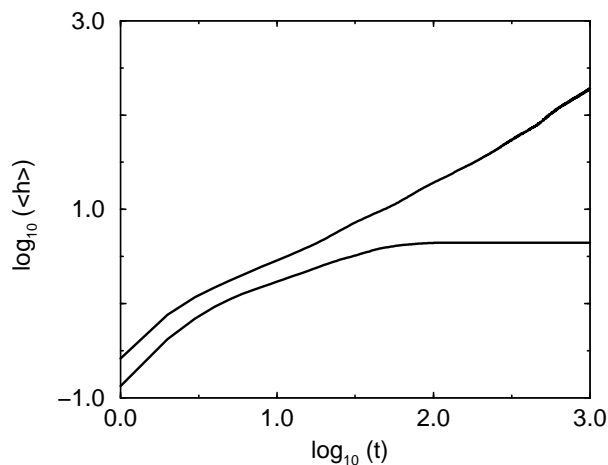


Figure 4.1: Mean height versus time of the QKPZ equation for a system of size  $L = 4096$  with only one disorder realization. The driving force is  $F = 0$ . The bottom curve corresponds to  $\lambda = 2.6$  and the top to  $\lambda = 4.6$ .

results correspond to  $F = 0$ . As may be seen in figure 4.1, a few realizations are enough to check that actually the transition may be obtained by tuning the parameter  $\lambda$ . The next step is to characterize that transition in detail.

### 4.3.1 The depinning transition

Apart from what has been mentioned about how the models with quenched disorder may be classified by its behaviour when an overall tilt is introduced, other elements are needed to define a universality class. Those elements are the critical exponents. In a continuous phase transition, it is expected to find an order parameter that vanishes (as a power law in the neighborhood of the critical point) when the system changes from one phase to another. In this case the order parameter is the velocity. As was explained in chapter 2, it goes as  $v \sim (F - F_c)^\theta$  when the critical driving force is approached from above. The force does not play any role now, its place is taken by the nonlinear constant  $\lambda$ . We can tune up the relative importance of the nonlinearity upon the other terms of the equation. In the figure 4.2, it is plotted how the velocity changes when  $\lambda$  is varied within the stable region.

The form of  $v$  may be fit by a function of the kind  $v \sim (\lambda - \lambda_c)^\theta$  as is shown in the next figure. The critical value of the nonlinear parameter that best fits that dependence is  $\lambda_c = 3.60 \pm 0.01$ , while the value of the critical exponent is found to be  $\theta = 0.635 \pm 0.007$ .

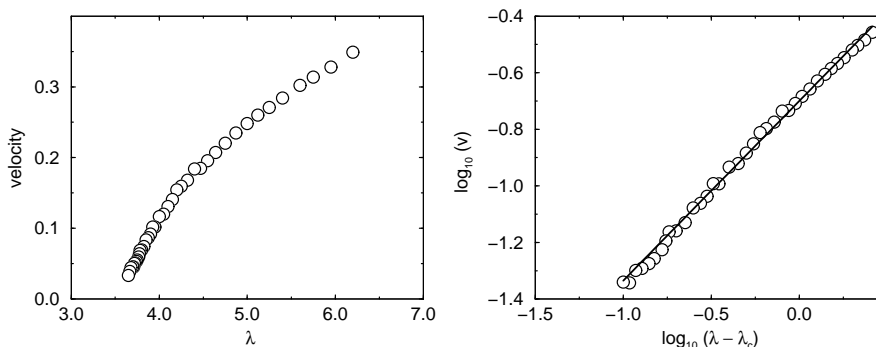


Figure 4.2: The variation of the velocity with the nonlinearity constant  $\lambda$  for a system size  $L = 8192$ . On the right, it is the same figure but with a log-log scale. The slope of the straight line is  $\theta = 0.635$  and  $\lambda_c = 3.60$ .

### 4.3.2 Which universality does this transition belong to?

Once the first critical exponent has been estimated, we can face the question of which is the universality class this transition settles in. The corresponding exponent for the velocity in the QEW class is  $\theta_{QEW} \approx 0.25$ , and that of the DPD model  $\theta_{DPD} \approx 0.636$ . The value of  $\theta$  obtained from the simulations point clearly towards the DPD universality, but it is necessary some further results to conclude safely in which universality class this model lies.

That something else might be the exponent  $\nu$  associated to the correlation length. The correlation length,  $\zeta$ , is the mean size of the clusters of sites that are in the minority phase. For instance, if  $\lambda > \lambda_c$ , the length  $\zeta$  represents the average size of the clusters of pinned sites. The correlation length is function of the distance to the critical point  $\epsilon = (\lambda - \lambda_c)$ ; actually it shows a power law divergence as that point is approached,  $\zeta \sim \epsilon^{-\nu}$ . Unfortunately, this is a quantity very difficult to estimate numerically. However, above the transition, its presence is clearly reflected in well known magnitudes such as the global or local width [Kertész 1989, Amaral 1995]. This is a well-known

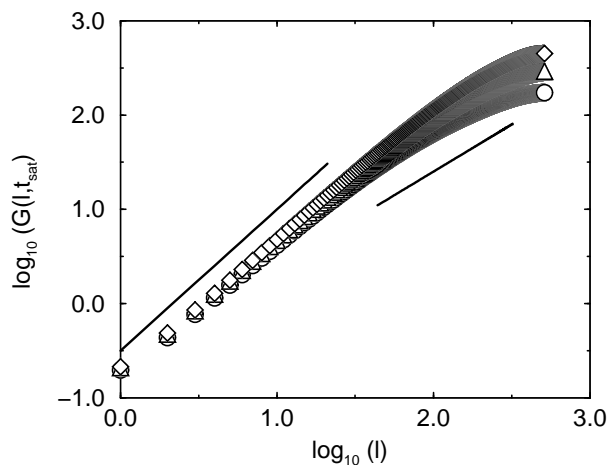


Figure 4.3: The height-height correlation function for QKPZ in saturation. The data are for different values of  $\epsilon$ ; ( $\circ$ )  $\epsilon = 2.16$ , ( $\triangle$ )  $\epsilon = 1.152$  and ( $\diamond$ )  $\epsilon = 0.648$ . The slopes of the two solid lines are  $2\alpha_e \approx 1.5$  and  $2\alpha = 1$ .

effect in all the roughening transitions. The scaling of those magnitudes is affected by the correlation length on scales below  $\zeta$ . For example, the local width scales at saturation as

$$w(l, t_{sat}) \sim l^{\alpha_e} \zeta^{-\varphi'} g(l/\zeta) \sim l^{\alpha_e} \epsilon^\varphi g(l \epsilon^\nu), \quad (4.4)$$

where  $\alpha_e$  is an effective roughness exponent (which may be different from that measured at the critical point  $\alpha_c$ ), and  $\varphi$  is a new exponent. The function  $g()$  goes as  $g(u) \sim u^{\alpha-\alpha_e}$  for  $u \gg 1$  and is constant otherwise. This behaviour ensures that the common exponent for  $l$  is recovered far above the transition (KPZ in this case), but with a shift in the curves for different values of  $\epsilon$ ;  $w(l, t_{sat}) \sim l^\alpha \epsilon^{\varphi_{KPZ}}$ . All these different exponents are related by the self-consistency condition  $\varphi_{KPZ} = \varphi + \nu(\alpha - \alpha_e)$ . In the figure 4.3, the height-height correlation function is displayed for a range of values of  $\epsilon$ . From those data, we find that  $\varphi \approx 0.13$  and  $\alpha_e \approx 0.75$ .

The same applies to the temporal scaling below a certain characteristic time  $t_c \sim \zeta^z$ . The global width before saturation behaves as

$$W(t, L) \sim t^{\beta_e} t_c^{-\kappa'} f(t/t_c) \sim t^{\beta_e} \epsilon^\kappa f(t \epsilon^{z\nu}), \quad (4.5)$$

where, again,  $\beta_e$  is an effective growth exponent found in the proximities of the critical point, and  $\kappa$  is a new exponent to take into account the shift of the curves with  $\epsilon$ . Asymptotically, the function  $f()$  goes as  $f(u) \sim u^{\beta-\beta_e}$  for  $u \gg 1$ , and is constant for small arguments. A shift with  $\epsilon$  is also observed for  $t \gg t_c$ , what defines a new exponent  $\kappa_{KPZ} = \kappa + z\nu(\beta - \beta_e)$ . All these exponents, either the effective  $\alpha_e$  or  $\beta_e$  or  $\kappa$  and  $\varphi$ , are characteristic for each universality class.

In the figure 4.4, the global width early time evolution of QKPZ equation is displayed for a range of values of  $\epsilon$ . There the cross-over generated by the existence of  $\zeta$  may be clearly observed. We can measure directly from those data the effective growth exponent  $\beta_e = 0.73 \pm 0.07$  and the growth exponent in the final regime  $\beta \approx 0.3$ . The error being of approximately 10%. Within this error bar,  $\beta$  matches with the growth exponent expected for KPZ universality. The shift of those curves in the late time regime allow us to estimate  $\kappa_{KPZ} = -0.57 \pm 0.06$ . With those values of the exponents the width curves may be collapsed in a single curve. The collapse is plotted on the right side of the same figure.

The effective exponents expected for the QEW universality are  $\alpha_e \approx 0.92$ ,  $\beta_e \approx 0.86$ ,  $\varphi \approx -0.44$  and  $\kappa \approx 0.0$ , while the values obtained from the DPD

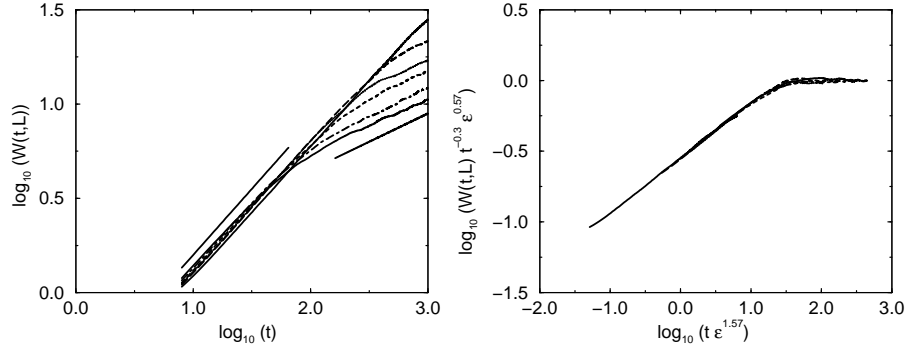


Figure 4.4: The global width versus time for different values of  $\epsilon$ ; from top to bottom (on the right)  $\epsilon = 0.144, 0.648, 0.864, 1.152, 1.656$  and  $2.16$ . The slopes of the straight lines are  $\beta_e \approx 0.7$  and  $\beta \approx 0.3$ . On the right, the collapse of those data using the expression 4.5.

model are  $\alpha_e \approx 0.75$ ,  $\beta_e \approx 0.74$ ,  $\varphi \approx 0.12$ ,  $\kappa \approx 0.11$  and  $\kappa_{KPZ} \approx -0.65$  [Amaral 1995]. The depinning transition obtained by tuning the nonlinearity seems to lie then in the same universality class as the DPD model. As was already mentioned, in DPD the nonlinearity does not vanish at the transition, instead it remains constant [Neshkov 2000]. The depinning takes place changing the pushing force. This means that both ways of freeing interfaces are equivalent, because the same exponents are found independently of which control parameter is employed.

### 4.3.3 Searching for a phase diagram

If two parameters may produce a transition, it is not longer possible to specify the phase of the system by giving only one of them. Thus, the parameter space is not a line but a plane, and transition does no longer takes place at a critical point but at a critical curve. In order to check this idea, we have carried out a set of simulations of the QKPZ equation. The operation mode was the following: the parameter  $\lambda$  was fixed, and the critical force  $F_c(\lambda)$  was looked for. For each of these critical points, the value of the exponent  $\varphi$  was also measured. As we said before, this is the fairest indication of which universality does the transition belong to, because the sign of that exponent is different for each universality; negative for QEW and positive for QKPZ.

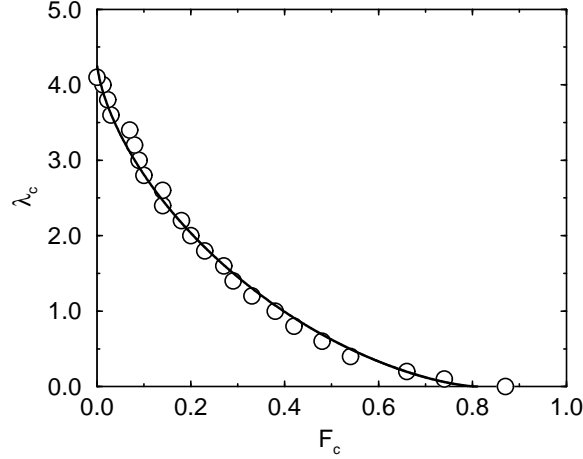


Figure 4.5: The critical force estimated for several values of  $\lambda$ . The system size is  $L = 1024$ .

The QEW class only appears in a small neighborhood of  $F_c(\lambda = 0)$ . The size of that region decreases for larger system sizes. Thus, in the thermodynamic limit it becomes, very likely, only the critical point for  $\lambda = 0$ . All these results are shown together in figure 4.5.

The figure 4.6 has been completed with the case  $\lambda F < 0$  studied by [Jeong 1996, Jeong 1999]. According to that work, for that region of parameters a discontinuous phase transition is expected. The QEW universality is then reduced to a tricritical point, where first-order and DPD transition curves join. Despite of that, this is the only point of the whole critical region where some analytic results are available [Nattermann 1992b, Narayan 1993, Leschhorn 1997]. In the quadrants with  $\lambda F > 0$ , we have searched for a simple expression that matches the shape of the DPD critical curve. We found that

$$\left(\frac{\lambda_c}{b_1}\right)^{2/3} + \left(\frac{F_c}{b_2}\right)^{2/3} = 1 \quad (4.6)$$

gives a nice fit to the critical line, where the constants  $b_1 = 4.31 \pm 0.04$  and  $b_2 = 0.81 \pm 0.03$ . This fitting curve, apart from having some practical interest to estimate the critical force ( $\lambda_c$ ), is a matter that requires theoretical explanation. It is indeed a result to be reproduced in any theory for the

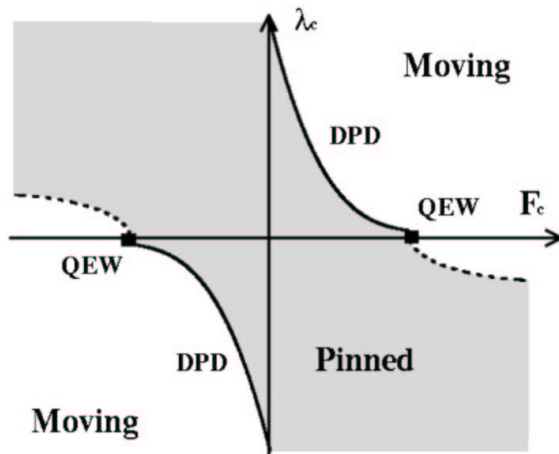


Figure 4.6: A representation of how the phase diagram of QKPZ must look like having into account the most recent results. The dashed curves correspond to discontinuous phase transitions, while the continuous represent second order phase transitions, DPD or QEW.

QKPZ problem.

## 4.4 Finite size scaling and phase transitions

One of the most difficult questions when we are treating with a phase transition is to establish the position of the critical point,  $\lambda_c$ . This is an important task because the values of the exponents are very sensitive to small changes in  $\lambda_c$ . Not in vain the relation between the exponents and the position of the critical point is not linear. Let us suppose  $\mathcal{B}$  to be a magnitude that we want to estimate close to the transition. If  $\mathcal{B}$  has a power law behaviour in the neighborhood of  $\lambda_c$ ;  $\mathcal{B} \sim (\lambda - \lambda_c)^\sigma$ , a slight variation of the position of  $\lambda_c$  produces a relative alteration of  $\delta\sigma/\sigma \approx \delta\lambda_c/[(\lambda - \lambda_c) \log(\lambda - \lambda_c)]$  in the evaluation of the critical exponent  $\sigma$ . This change becomes catastrophic when  $\lambda$  approaches  $\lambda_c$ .

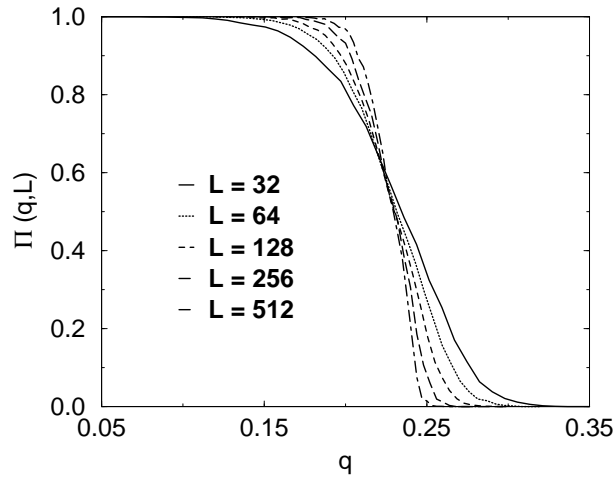


Figure 4.7: The probability of being in the smooth phase versus the control parameter for different system sizes;  $L = 32, 64, 128, 256, 512$ . This model, that was studied in [Alon 1996], has no absorbing phase. The transition takes place at  $q_c = 0.233$ .

The main source of uncertainty of the position of the critical point comes from the finite size of the system. If the size was infinite, the phase transition would be sharp at a certain value  $\lambda_c(L = \infty)$  of the control parameter. On the contrary, when the size is finite the transition is softer, and there is a small region of control parameter values close to  $\lambda_c(L = \infty)$  where both phases may be found. This effect disturbed also the simulation presented before, hence we tried to characterize it. This is the reason why I have considered important to include this section here.

A way to understand why the critical point transforms into a critical region is to see how the correlation length behaves. As was already mentioned, it grows close to the critical point as  $\zeta \sim \epsilon^{-\nu}$  where  $\epsilon = \lambda - \lambda_c$ . But  $\zeta$  can not increase indefinitely in a finite size system. Actually when the relation  $\zeta(\lambda) = L$  is satisfied, the system behaves in the same way as if it is actually at the critical point. This means that it may be in both phases with a certain probability. The size of the region of  $\lambda$  where that takes place grows as the system size decreases. A practical example of this behaviour may be seen in figure 4.7. There, the probability  $\Pi(\lambda, L)$  of finding the system in a certain phase is displayed versus  $\lambda$  for systems of different sizes.

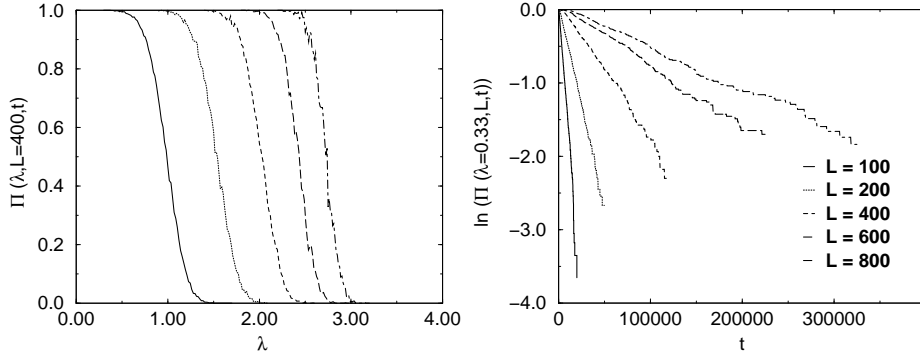


Figure 4.8: On the left plot, the probability of being in the phase of zero density for contact process model [Dickman 2000] in a range of creation rate. The time of evolution of the system is different for each curve; from left to right  $t = 25, 50, 100, 200$  and  $400$ . In the second figure, it is displayed the time evolution of  $\Pi$  for fixed  $\lambda = 3.3$  and system size. In this case the critical point is  $\lambda_c = 3.29785$ .

This discussion is valid both for equilibrium and non equilibrium systems. However in the out of equilibrium case, it is also necessary to consider the temporal evolution of the system. Essentially, there are two types of behaviour. The system may be switching from one phase to another without any restriction, or there may be some absorbing states. When this happens, the system may be trapped by one of those states and remains forever in the corresponding phase. One example of that behaviour is the depinning transition. The pinned phase is constituted by a set of absorbing states. Once an interface is pinned, no further evolution takes place. This fact affects the probability distribution function  $\Pi$ . In order to understand how, let us consider  $\mathcal{N}$  copies of the same system with different disorder realizations. The evolution starts, if the system reaches an internal stationary regime (as happens for instance to interfaces when they saturate), the probability of falling in one of the absorbing states is time-independent. The variation in time of the number of copies in the non-absorbing phase goes then as  $d\mathcal{N} \sim -\mathcal{N}dt/\tau$ , where  $\tau$  is the mean time at which a copy gets trapped. This implies that the function  $\Pi$  behaves as

$$\Pi(\lambda, L, t) = e^{-t/\tau} . \quad (4.7)$$

In figure 4.8, the function  $\Pi$  is shown for the DPD model with  $L = 400$  at different times. The shift with time of those curves may be clearly observed there. The temporal evolution of  $\Pi$  may also be seen in that figure, where  $\tau$  is measured. The magnitude  $\tau$  is not a constant, actually it depends on how far we are from the critical point. We could make the assumption that it is related to the correlation length as  $\tau(\lambda) \sim \zeta^{z_t}$ . This idea is based on the similar behaviour of both quantities close to the transition; the mean survival time must grow when the critical point is approached till it diverges at  $\lambda_c$ , as  $\zeta$  does. On the other hand, it is also justified by the collapse of figure 4.9. To get this collapse, the expression 4.7 has been slightly altered. We have assumed that  $\tau = -c\zeta^{z_t} = cL^{z_t}/\ln(f((\lambda - \lambda_c)L^{1/\nu}))$ , where  $f()$  is a scaling function that is constant for large argument values and goes as  $f(u) \sim \exp(u^{-\nu/z_t})$  otherwise. If this behaviour is included in 4.7, the result is  $\Pi(\lambda, L, t) = f((\lambda - \lambda_c)L^{1/\nu})^{t/aL^{z_t}} = [1 - g((\lambda - \lambda_c)L^{1/\nu})]^{t/aL^{z_t}}$ .

The relation between  $\tau$  and  $\zeta$  give us also, apart from a new exponent  $z_t$ , a new way to look for the critical point. In the general case, we can use the order parameter  $\mathcal{M}$ . As was explained, it goes as  $\mathcal{M} \sim \epsilon^\theta \sim \zeta^{-\nu\theta}$  when the critical point is approached. Only at the critical point, the relation  $\zeta = L$  is always valid. Hence, it is possible to look for  $\lambda_c$  by plotting  $\mathcal{M}$  versus  $L$  for different values of  $\lambda$  in a log-log figure. The only straight line corresponds to  $\mathcal{M}$  at the critical point. This is, however, an almost impossible task in the

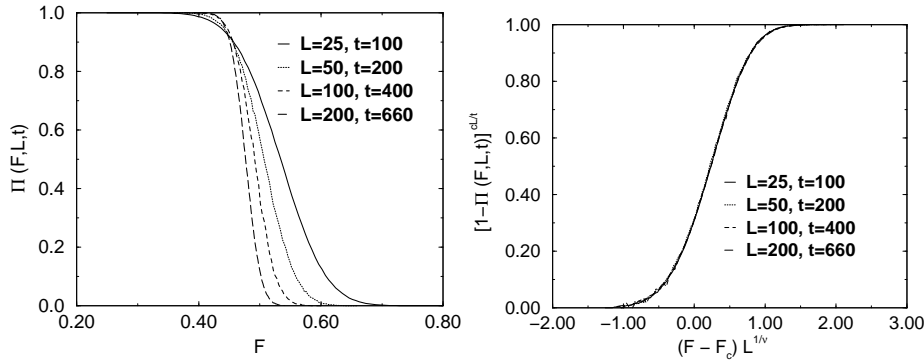


Figure 4.9: Probability of being in the pinned phase for the DPD model versus the pushing force. Those curves correspond to diverse sizes and times. All of them are collapsed in the figure on the right. The constant  $c$  is equal to 2, and the exponents are  $z_t = 1$  and  $\nu = 1.777$ .

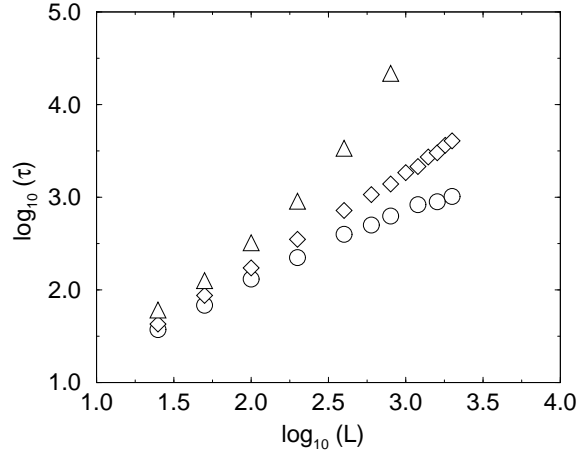


Figure 4.10: Characteristic time  $\tau$  for different system sizes of the DPD model with three values of the driving force: ( $\diamond$ )  $F_c = 0.4615$ , ( $\circ$ )  $F = 0.45$  and ( $\triangle$ )  $F = 0.48$ .

case of the depinning transition. The velocity, which is the order parameter now, results in practice unmeasurable close to  $\lambda_c$  (or  $F_c$ ). The mean height increases in time as a power law for a long time before taking a definite velocity. To avoid this problem, we can use  $\tau$  instead of the order parameter. This quantity also goes as  $\tau \sim \zeta^{z_t} \sim L^{-\nu z_t}$  at the critical point. Hence, it works as well as  $\mathcal{M}$  to estimate  $\lambda_c$ , and in our case it is much easier to measure. This may be seen in the figure 4.10.

## 4.5 Conclusions

The depinning transition may be thus obtained by tuning the nonlinearity of the equation. This opens a great number of possibilities for future work. On the theoretical side, the phase diagram for QKPZ equation must be explained. That is not an easy task, because perturbation methods (as that employed with QEW) can not be used. On the other hand, as far as QKPZ equation is an approximation to real interfaces, our results imply that an interface may be depinned just by changing the nonlinear contribution, or the properties of the disorder in which it is embedded. The discovery (or the measurement) of this effect is also a great experimental challenge.

## Part II

# Some experimental examples



# Chapter 5

## Fracture fronts

Along the time of realization of this PhD thesis, I have been involved in two experimental works. The first work took place in Oslo, during a several months stay at the Physics Department of Oslo University. These experiments were carried out in collaboration with K.J. Måløy and J. Schmittbuhl, and deal with fracture fronts. This chapter is roughly composed by the report that I wrote about them.

### 5.1 Introduction

The fracture of solids may present essentially two dynamic behaviours. If the crack front advances faster than a certain velocity, very likely, new secondary fracture fronts will be generated. The final structure that this process produces is like a percolation cluster; there is a percolating backbone, the main crack, and a group of secondary paths that spread in all directions [Bouchaud J.P. 1993, Bouchaud E. 1993]. On the other hand, when the velocity is low, there is only one fracture front displacing inside the solid. This experiment was designed essentially to study crack fronts in the latter advance mode.

The front of a fracture crack may be considered as a curve inside a three dimensional space. Following [Ertas 1992], there exist two different roughening directions. The roughness exponent may be estimated in the axis parallel to the mean velocity of the front to obtain  $\alpha_{\parallel}$ . Or similarly, the exponent may be measured along the axis  $z$  that is perpendicular to  $v$  to find  $\alpha_{\perp}$ . These two exponents are not expected to be equal, though they are related each



Guilloteau 1996], for some reviews see [Bouchaud E. 1997], [Fineberg 1999], [Fisher 1998] or [Sahimi 1998]. The result of those experiments was an almost ubiquitous value for  $\alpha_{\perp}$  of approximately 0.8 on the range of scales going from  $\mu m$  to  $mm$ . Below them, the critical value  $\alpha_{\perp c} \approx 0.5$  was found [Daguier 1996, Daguier 1997]. This fact has led to the conjecture of a unique universality class for fracture [Bouchaud E. 1990]. A very counter-intuitive idea, if one considers fracture in materials as different as glass or wood. Those results were recently re-interpreted using anomalous scaling (see chapter 3) to analyze the crack fronts [López 1998b, Morel 1998]. The universal value of  $\alpha_{\perp}$  actually corresponds to the local roughness exponent. The perpendicular global roughness exponent is material dependent, and usually higher than one.

The measurement of parallel exponents is much more difficult. The first experimental studies were carried out in the pinned phase of crack fronts. To mark the position of those fronts, ink was injected in the fracture. After a while the ink got dry, then the fracture of the block was completed. The position of the front at the moment of the injection was thus clearly identified. From those data a critical exponent  $\alpha_{\parallel c} \approx 0.54$  was estimated [Daguier 1996]. In order to observe the parallel projection of crack fronts at the moving phase, it is necessary that the fracture is produced inside a transparent material. A camera placed over the solid block is then able to record the development of the front. This kind of experiments was performed in Oslo by A. Delaplace, J. Schmittbuhl and K.J. Måløy [Schmittbuhl 1997, Delaplace 1999]. The value of the exponent that they reported was  $\alpha_{\parallel} \approx 0.63$ . The experiments described hereafter were carried out in collaboration with this same group. The experimental setup is therefore almost the same. A detailed description may be found in the following section.

Recently, it has been shown [Morel 2000] that the presence of anomalous scaling in fracture has important macroscopic consequences. The rate of energy dissipation,  $G$ , at the crack front is thought to follow the Griffith criterion.  $G$  starts from a very low value, and then increases in time until a stationary state is reached. This kind of behaviour has been directly observed in our experiments, as may be seen in the section devoted to the strain gage. In the steady state, the value of  $G$  was not expected to be system size dependent. However, in some recent experiments such a dependence has been detected [Morel 2000]. This phenomenology is satisfactorily explained only if fracture front dynamics show intrinsic anomalous scaling.

## 5.2 Experimental setup

A simplified scheme of the setup may be seen in figure 5.2. It consists of a sample, a press to produce the fracture, a strain gage and a microphone to measure the force and its fluctuations, and a CCD camera to record the front. Each sample is composed by two plates of polymethyl-methacrylate GS that is a transparent material. The upper plate is 32 cm long, 14 cm wide and 1 cm thick. While the bottom one is 34 cm long, 0.4 cm thick and of variable width. To prepare the sample, the contact faces of the plates are sandblasted; introducing thus a certain quenched disorder in the spatial distribution of toughness. After that, they are glued together by inserting them in a press that produces an uniform pressure. The whole structure is placed in a ceramic oven. There, the melting temperature is reached by means of a carefully controlled linear heating. That temperature (205 °C) is maintained for half an hour, and later a very slow cooling process starts until room temperature is reached. The transparency of the sample is affected by all these changes. Initially, the plates are transparent. They become almost white after the sandblasting; the light is diffused by the affected face, and

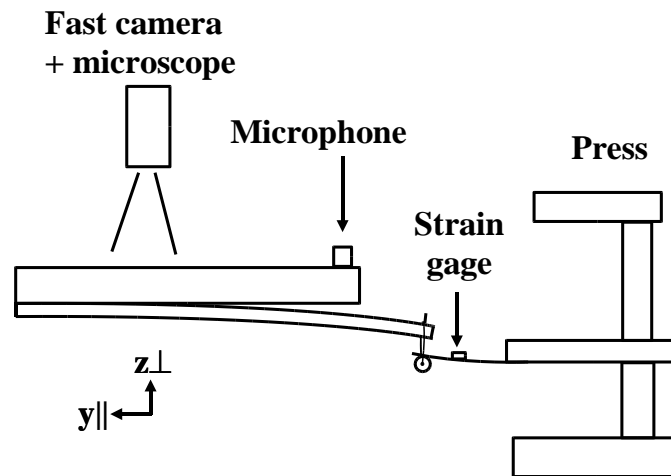


Figure 5.2: Scheme of the experimental setup.

finally they are transparent again when the heating treatment has finished.

The fracture was generated when the press pushed down the bottom plate of the sample. The crack advance was constrained in the plane between the two plates. The press was moved by a continuous motor that produced a velocity of approximately  $2 \mu\text{m/s}$ . Instead of a direct contact between the press and the sample, a metallic plate was included in the middle to allow the measurement of the force applied over the bottom plate of the sample (and perhaps also of its fluctuations). Actually, what was measured is the way in which that metallic plate bent when some force acted upon its tip. The way to do so is to place a strain gage onto the plate. A strain gage is a resistance whose electric properties vary when its length changes. The gage was included in a Whitestone bridge that determines at each moment the electric resistance. After calibration the whole system was able to clearly detect forces as low as 4 gr. Finally, the metallic plate was attached to the lowest plate of the sample by means of a rope.

Also with the idea of estimating the fluctuation of the energy dissipation at the crack front, we included a microphone onto the thickest plate of the sample. This was a semiconductor microphone that was supposed to be able to measure in a wide range of sound frequencies. The setup was completed with a fast CCD camera with a maximum resolution of  $1536 \times 1024$  pixels. It was connected to a microscope, and the whole set was mounted onto a moving platform that allows displacements in the  $x$  and  $y$  directions. To get a better light contrast, lamps were situated close to the sample as well as a black background below.

### 5.3 Results

The aim of this experimental work is twofold. On one side, we want to take a first step towards the measurement of the energy dissipation in the crack front. In order to get it, the strain gage and the microphone were installed. The gage is able to estimate the force that the press is applying to the lower plate of the sample. The microphone should be able to detect the sound produced by the energy dissipation while the front moves.

On the other hand, we also want to check the scaling properties of the fracture cracks produced. It is important to know if anomalous scaling is present in the in-plane projection, as it seems to be the case for the out of plane one [López 1998b, Morel 1998]. The fronts of fracture reach very

rapidly a stationary state, i.e. saturation of spatial height-height correlations. Fracture cracks do not start from a flat initial configuration, and thus a power law growth of the type  $\sim t^\beta$  may no longer be expected for the width. The only way to detect anomalous roughening in this case is to change the system size and to measure stationary properties. This is the reason why the width of the bottom plate of the sample is variable. In the next tables, the width of these plates for each experiment, as well as other experimental parameters, are displayed.

	<i>Experiment number</i>			
	1	2	3	4
<i>Date (dd/mm/2000)</i>	3/11	4/11	5/11	6/11
<i>Image size (pixels)</i>	480×512	480×512	480×512	512×240
<i>Width of image (mm)</i>	8.95	8.95	8.95	9.55
<i>Speed of press (<math>\mu\text{m/s}</math>)</i>	by hands	1.86	1.9	1.22
<i>Distance press-front (cm)</i>	23	16	12	12
<i>Frames/second</i>	250	250	125	125
<i>Shutter time (s)</i>	1/500	1/500	1/500	1/500
<i>Width of bottom plate (cm)</i>	12	6	5	4
<i>Mean speed of front (mm/s)</i>	0.2	0.047	0.085	0.038
<i>Resolution microscope</i>	1.0	1.0	1.0	1.0

	<i>Experiment number</i>			
	5	6	7	8
<i>Date (dd/mm/2000)</i>	8/11	8/11	9/11	10/11
<i>Image size (pixels)</i>	512×240	512×240	512×240	512×240
<i>Width of image (mm)</i>	9.55	4.77	9.55	9.55
<i>Speed of press (<math>\mu\text{m/s}</math>)</i>	1.9	1.9	1.98	1.94
<i>Distance press-front (cm)</i>	12	17	10	9.5
<i>Frames/second</i>	125	250	125	125
<i>Shutter time (s)</i>	1/500	1/500	1/500	1/500
<i>Width of bottom plate (cm)</i>	3	3	2	1.5
<i>Mean speed of front (mm/s)</i>	0.031	0.015	0.036	0.063
<i>Resolution microscope</i>	1.0	2.0	1.0	1.0

There were other group of experiments running from number 9 till 14. The aim of this second series was different. The front was not recorded with

the fast CCD camera but with a video tape recorder. In this way, a longer record was possible, which allows a more detailed study of the front mean position. These data were compared with the force measurements from the strain gage. The widths of the lower plate of the sample were 2, 1, 1, 2, 3 and 4 cm respectively. In the following subsections, results for each measuring device are separately described.

### 5.3.1 The microphone

The measurement on the noise produced in the crack advance is a matter of great interest because, in this way, statistics of both avalanches sizes and energy dissipation may be obtained. However, this was a novel part of the experiment, and thus our initial aim was to know how the signal noise relation is. In a complete experiment, while the crack front is advancing, there are many other instruments working; lamps, camera, computers, press, etc. All of them produce a great deal of background noise.

In the early trials with the microphone, it was found that the sound coming from those devices had a very characteristic Fourier spectrum. As the electricity network, it showed a fair peak at 50 Hz, and even at some other harmonics; 100 Hz or 150 Hz. On the other hand, the noise coming from the crack had a very high frequency. In order to reduce as much as possible the background, we used a high-pass filter with a threshold frequency fixed

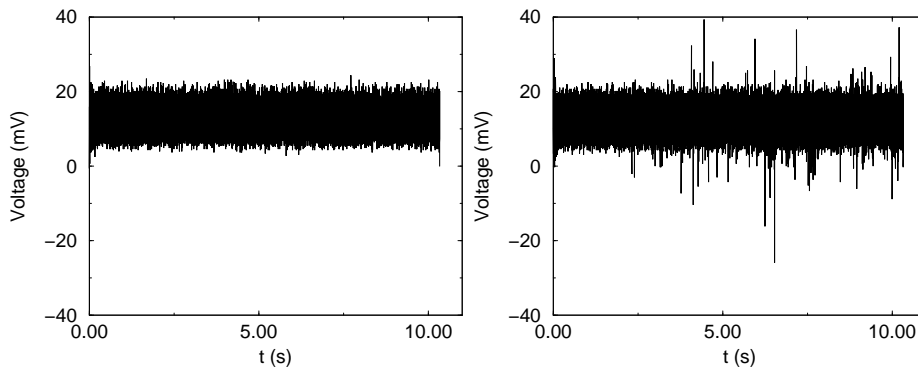


Figure 5.3: On the left, the background noise as was measured from the ADC card after filtering it, and on the right the noise from the crack measured with the same setup.

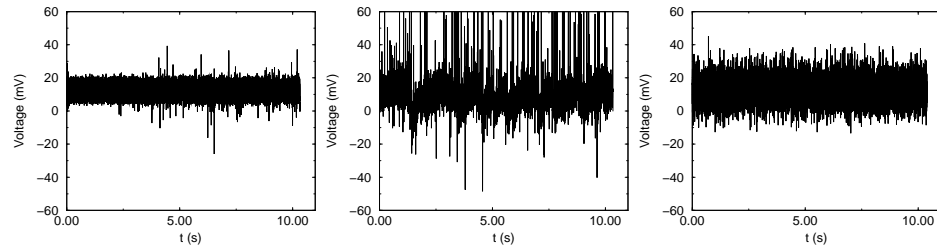


Figure 5.4: The first figure corresponds to the measurement of the noise coming from the crack advance. The second and the third plots correspond to the noise produced by the motor of the press and by the lamps, respectively.

just above 100 Hz. The output of this system was connected to a fast data acquisition card (ADC). In the following attempts, the noise from the crack was recorded while either the press or the lamps were turned off. The lower plate of the sample was pushed manually. The result may be seen in the figure 5.3. In the same figure, a background measurement is also represented.

From that figure, it becomes clear that the sound coming from the crack may be detected with this setup. However, it would be necessary a faster ADC card to be able to distinguish a certain structure inside those pulses. As was already mentioned, the main problem with the noise produced by fracture advance is its very high frequency; probably closer to MHz than to kHz (the upper cutoff of the frequencies that could be detected with our microphone was of the order of hundreds of kHz).

The next step was to turn on the remaining devices, in order to check if all could work together. This was an interesting point because, in that way, it would be possible to correlate the avalanches observed with the camera and the peaks of activity measured with the microphone. The result is in the figure 5.4. As may be seen there, a better isolation of the microphone is needed in order to separate signal from noise. At the same time, it would be also convenient the use of other kind of microphone to detect ultra-sound noise. Nevertheless, this was a first attempt in a very promising direction.

### 5.3.2 The strain gage

The output of the strain gage was connected to a multimeter, and from there to a computer. In that way, we were able to take very long time measurements

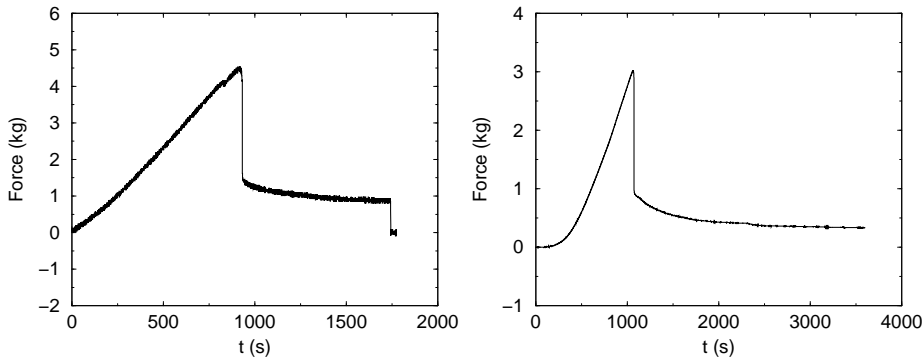


Figure 5.5: Evolution in time of the force applied by the press onto the lower plate of the sample. On the left, for experiment number 3 with a width of 5 cm, and, on the right, for experiment 13 with a width of 3 cm.

of the force. Each fracture experiment took approximatively one hour. In this time, and at a rate of 5 data per second, 18000 force measurements were stored in memory. The figure 5.5 shows some of the curves, force versus time, obtained for the experiments of the above detailed table.

These curves have a very peculiar form. At the beginning, there is a linear increment of the applied force; most of the energy is stored in the elasticity of both the sample and the metallic plate (regime I of figure 5.6). Then, at a certain time, that energy over-pass a local threshold related to the toughness of the sample at each point, and the crack front starts to move (regime II). After that, a big avalanche takes place. This sudden burst could make the interface to advance several centimeters in a few seconds (regime III). After that avalanche, there is a slower relaxation, while the crack front decelerates. Finally, a steady state is reached, and an almost constant force is maintained between the press and the sample; regime IV of figure 5.6. This last regime corresponds to a constant velocity of the front.

The height of the first peak depends on the distance between the crack front and the press. The further fracture surface is, the higher the momentum with the same force in the press-sample junction. As a consequence, less energy is elastically stored and the burst results smoother. On the other hand, the force level at the stationary state is function of the bottom plate width of the sample. As may be seen in figure 5.7, the wider the plate is, the larger the force that is needed to get the front moving.

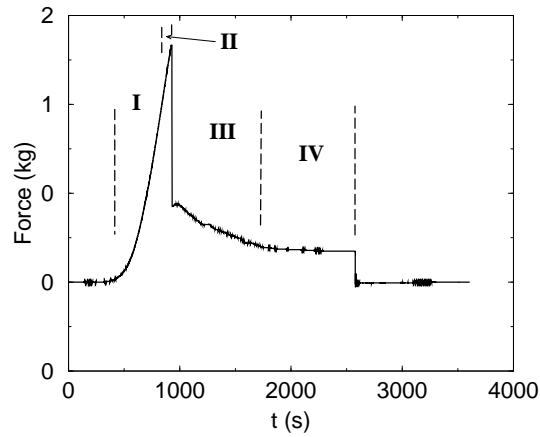


Figure 5.6: The different time regimes in the force/energy dissipation evolution. Those data correspond to experiment number 10 with a sample of a low plate width of 1 cm.

We also tried to connect the output of the strain gage to the ADC card. The aim was to measure the force fluctuations in the steady state regime (IV). Unfortunately, the gage was not sensible enough to detect those fluctuations.

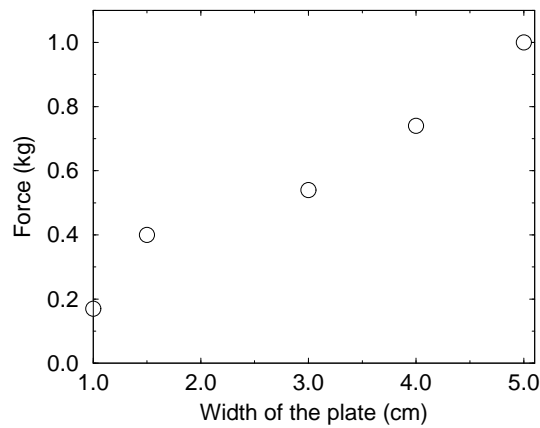


Figure 5.7: The force in the stationary state versus the width of the lower plate of the sample.

### 5.3.3 The camera

A typical example of a crack recorded with the CCD camera may be seen in figure 5.8. With a gray levels analysis, the cracked region (the white one) is separated from the region ahead the fracture. In this way, the front profile was obtained. Several tools are then employed to remove the overhangs and the non percolating paths.

The overhangs appear when the function  $h(\mathbf{x})$  is multivaluated in many points. To eliminate them, we can consider the maximum (minimum) of  $h$  as its value at  $\mathbf{x}$ . This method is justified theoretically whenever the result is invariant to which of the two possibilities (either the maximum or the minimum of  $h$  over all  $\mathbf{x}$ ) is chosen. In that case, the overhangs have a characteristic size, which implies that their influence in the scaling behaviour of the interface is negligible. This question has been checked in the fracture

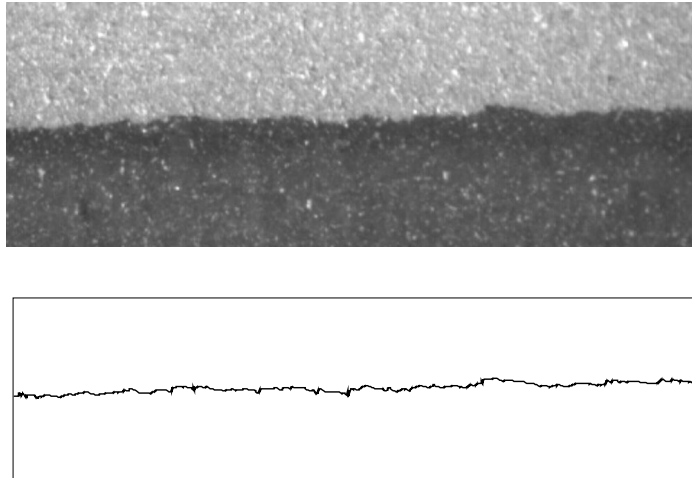


Figure 5.8: An picture of one of the fronts of experiment 1 taken with the CCD camera. Below it, the interface profile extracted from that image.

fronts of the present work, the method works well and we have concluded that overhangs are irrelevant.

### The mean height

The velocities of the fronts given in the above summary table were obtained by a linear fit of the mean height temporal evolution. An example is shown in the figure 5.9. In that figure, apart from the growth of  $\langle h \rangle$ , other effect is also exposed. This effect has its origin in the lamps that are needed by the camera to work properly. The light emitted by them fluctuates with the AC electric current obtained from the general network; i.e. with a 50 Hz frequency. Those fluctuations affect the definition of the crack front, and, as a consequence, also to the mean height. In figure 5.9, a zoom of a small region of the  $\langle h \rangle (t)$  curve is also represented. There, the oscillations can be clearly observed.

### The width

Due to the characteristics of the experiment, the global width can not be obtained. The quantities that are studied here correspond thus to the local width; the width over a small window of the front. Nevertheless, this estimator is a very important quantity in order to check if anomalous scaling occurs. If intrinsic anomalous scaling is present, the local width after saturation must

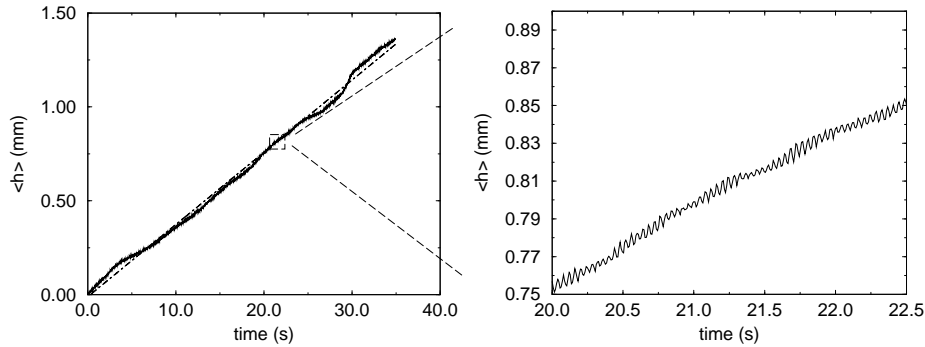


Figure 5.9: The mean height temporal evolution of the experiment number 4. The slope of the dot-dashed line correspond to a velocity of 0.038 mm/s. On the right, a zoom of a small region of the previous curve.

go as  $w(l, t > t_{sat}) \sim l^{\alpha_{loc}} L^{\alpha - \alpha_{loc}}$ . All the fronts from these experiments are in saturation; fracture interfaces had evolved for a while before we started to record images. Hence, if there exists a dependence of the local width for a fixed  $l$  on the system size  $L$ , that is a clear fingerprint of the presence of anomalous scaling in this system.

While we were trying to analyze the fronts to get their local width, we found other curious effect. Fronts can not be treated directly, it is firstly necessary to subtract the average tilt. This tilt comes from the fact that the camera has usually an orientation slightly deviated from the mean horizontal line of the front (axis  $x$  in figure 5.1). However, as can be seen in figure 5.10, that method is not enough to describe the interface. In the low width samples, there are very strong boundary effects on the fronts. This gives the whole surface a general parabolic form. It must be parabolic, because this is the geometry that any elastic string acquires when pulled at the extremes.

In figure 5.11, the local width for a length  $l = 8.95$  mm is displayed both with and without using the parabolic correction. The local width does not seem to be system size dependent. At least, it does not grow with the increasing width of the lower plate of the sample. This means that the scaling in the parallel direction should be Family-Vicsek with  $\alpha = \alpha_{loc}$ .

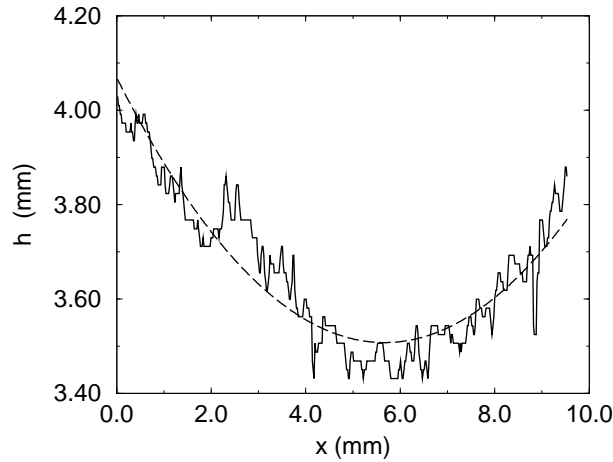


Figure 5.10: The height profile for a front of experiment number 8. The width of the lower plate of the sample is 1.5 cm. The dashed curve is a parabolic fitting to the interface.

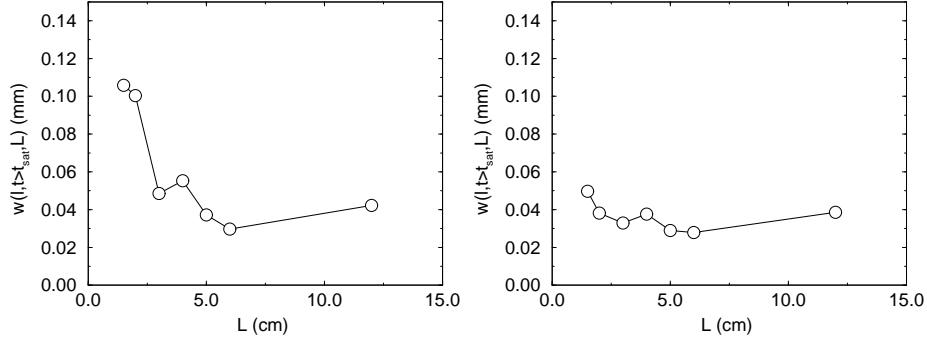


Figure 5.11: The local width on a fixed local scale  $l = 8.95$  mm and different system sizes. The wide of the lower plate of the sample goes from  $L = 12$  cm to  $L = 1.5$  cm. On the left, the width of the fronts when only the average tilt is subtracted. On the right, the same but when the full second order approximation is taken.

### The height-height correlations

In order to be able to estimate the growth exponent  $\beta$ , we have used a generalized version of the height-height correlations. Instead of the simple form for  $G(l, t)$  introduced in chapter two, the following function is employed

$$\Gamma_q(l, \tau) = \{ \langle |\Delta h(x + l, t + \tau) - \Delta h(x, t)|^q \rangle_{xt} \}^{1/q}. \quad (5.1)$$

Where  $\Delta h(x, t) = h(x, t) - \langle h \rangle_x(t)$ . For  $\tau = 0$  and  $q = 2$ , this function becomes the square root of the height-height correlation function at equal time,  $G(l, t)$ , defined before. The scaling of that quantity after saturation is thus  $\Gamma_2(l, \tau = 0) = G(l, t > t_{sat})^{1/2} \sim l^{\alpha_{loc}} L^{(\alpha - \alpha_{loc})}$ . If, as in this case, the scaling is FV, both roughness exponents coincide,  $\alpha = \alpha_{loc}$ . This means that  $\Gamma_2(l, \tau = 0)$  is a function only of  $l$ , which has been used to obtain  $\alpha$  (see figure 5.12). On the other hand, when  $l = 0$ , it must behave as  $\Gamma_q(l = 0, \tau) \sim \tau^\beta$ . This last point is not so clear when the system follows any kind of anomalous scaling (intrinsic, super-rough or faceted). However, we have checked the validity of that asseveration in models such as KPZ or EW growth equations with Family-Vicsek scaling. The behaviour of  $\Gamma$  for a range of values of  $\tau$  is displayed in figure 5.12. The results for the exponents  $\beta$  and  $\alpha$  from the different experiments are listed in the following table.

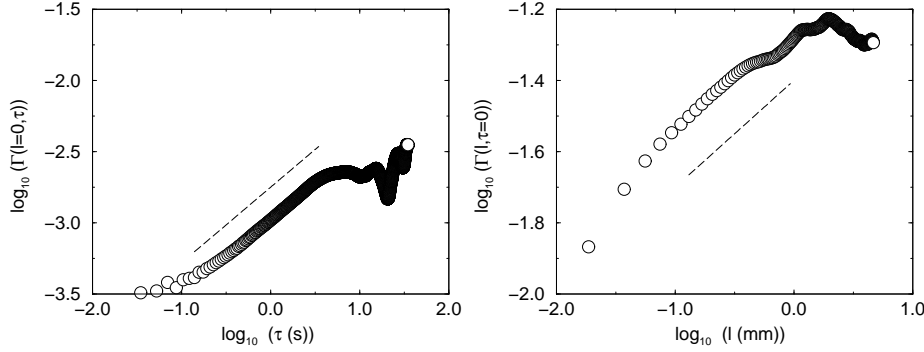


Figure 5.12: The function  $\Gamma$  for both  $l = 0$  (on the left) and  $\tau = 0$  (on the right). These data come from the experiments number 4 and 5. The slopes of the dashed lines are 0.53 and 0.3 respectively.

Experiment number	$\alpha_{loc}$	$\beta$
1	0.26	0.46
3	0.27	0.55
4	0.32	0.53
5	0.30	0.63
7	0.25	0.48
8	0.29	0.61

We could not obtain any values from the data of experiments 2 and 6. Those results imply a value for the exponents  $\beta_{\parallel} = 0.54 \pm 0.06$  and  $\alpha_{\parallel} = 0.28 \pm 0.02$ . With this method, we have also checked the presence of spatial multi-scaling. This kind of scaling appears if different roughness exponents are found for diverse values of  $q$  in the  $\Gamma$  function. The result is negative, in these experiments there is no multi-scaling.

### The power spectrum

As another way to verify the previous result, the power spectrum of the fronts has also been considered, as shown in figure 5.13. The values of the roughness exponent estimated with this method are in the following table.

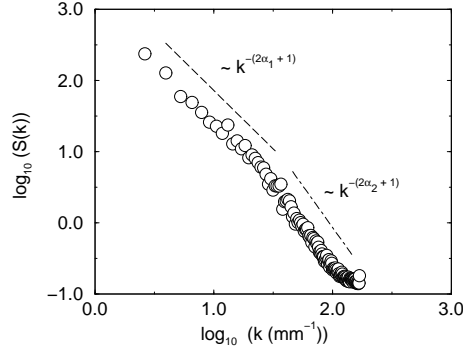


Figure 5.13: The power spectrum for the experiment number 8. The slopes of the dashed lines are  $-(2\alpha_1 + 1) \approx -1.64$  and  $-(2\alpha_2 + 1) \approx -2.33$ .

Experiment num.	1	2	3	4	5	6	7	8
$\alpha_1$	0.20	0.25	0.22	0.30	0.33	0.49	0.41	0.32
$\alpha_2$	0.51	0.32	0.45	0.56	0.52	0.49	0.63	0.64

This data give an average exponent of  $\alpha_{\parallel} = 0.31 \pm 0.06$ . Close to the value found in the latter section, though in clear disagreement with the exponent obtained in previous works [Schmittbuhl 1997, Delaplace 1999]. However, as may be seen in the power spectrum, figure 5.13, there exists a cross-over at a scale  $l \approx 0.3$  mm below which the value of the roughness exponent becomes  $\alpha_{\parallel,2} = 0.54 \pm 0.07$ , in closer concordance with early results. This fact may also explain the large value of the roughness exponent measured in experiment 6, in which the resolution of the microscope was double.

### The avalanches

The motion of fracture interfaces is not continuous but in bursts of activity or avalanches. The life time of avalanches, as well as their lateral sizes, are related to the elastic characteristics of the medium in which the crack is advancing. Avalanches are usually very fast processes with a lateral size that can be considerable. However, their vertical size does not seem to be important, in average. Some recent theoretical works have predicted a power-law distribution for the lateral size of these bursts [Ramanathan 1998].

In order to check how the avalanches are in our experiments, we have studied the velocity of the fronts. The instantaneous local velocity is obtained

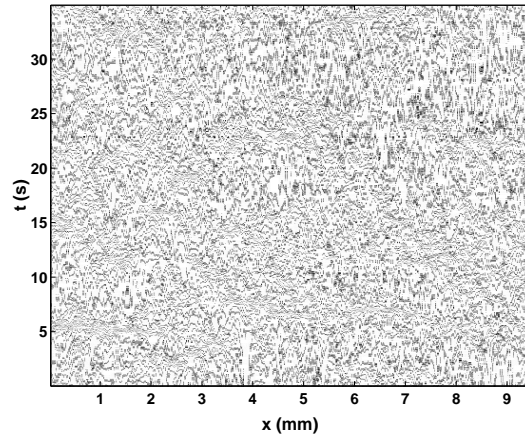


Figure 5.14: The velocity distribution in experiment number 4. The black spots correspond to sites where the local velocity is non-zero.

by comparison of two consecutive images acquired by the camera. At each time  $t$ , we have a height profile  $h(x, t)$ . The local velocity is defined as the ratio between the distance from  $h(x, t)$  to  $h(x, t + \Delta)$ , in the direction of the local normal to  $h(x, t)$ , and the time step  $\Delta$ . A two dimensional representation of the distribution of this local velocity may be seen in Figure 5.14, where black spots correspond to moving sites.

The statistics about the sizes of spots does not give a lot of information. The individual activity clusters do not have a very large size, not bigger than  $l \sim 0.2$  mm both in vertical and horizontal directions. Despite that, the localization where those bursts take place might be correlated with other neighbouring avalanches. In the same way, the presence of one burst in a particular  $x$ -coordinate value might be related with the previous avalanches that have happened there. To find an answer to these questions, the correlations (and power spectrum) of the local velocity have been analyzed both in space at the same time, and in time for a fixed  $x$ -coordinate.

The temporal evolution of the activity of the whole fracture front for experiment 2 is displayed in Figure 5.15. This activity is the fraction of sites of the front that are advancing. In the same figure, it is also shown the power spectrum of that signal. From this plot, it is obvious that there exist some characteristic frequencies at which those bursts take place. These frequencies are at 50 Hz and 100 Hz, i.e. the electric network characteristic

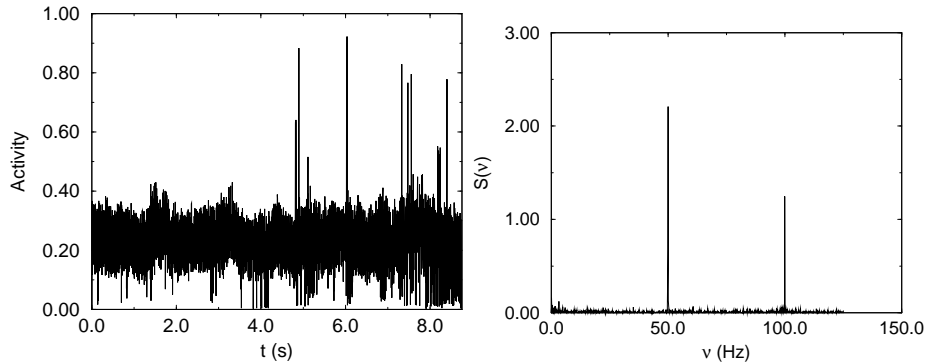


Figure 5.15: The normalized activity of the whole fracture interface for experiment number 2. On the right, the corresponding power spectrum of the time signal.

frequency and its first harmonic. This fact indicates that there may be some influence of the press motor in the rate of creation of new avalanches. A second consequence is that there exists a characteristic time for the duration of avalanches.

The result for the lateral size of avalanches is a bit different. The power-spectrum of the local velocity at a fixed time shows a clear structure. This

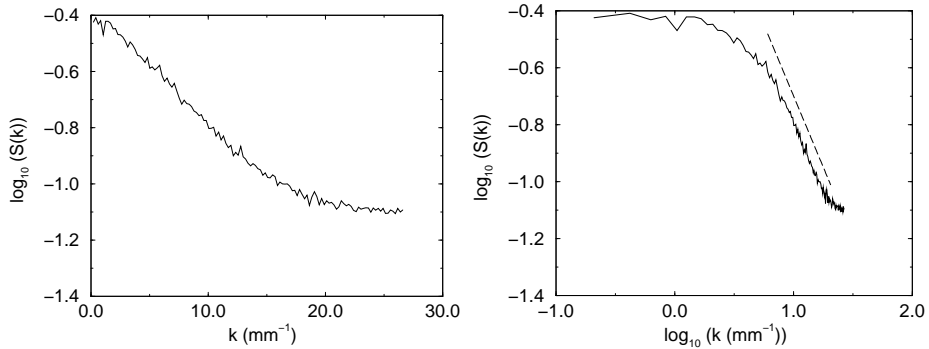


Figure 5.16: Log-normal and log-log plot of the correlation of the local velocity for a fixed time. These data correspond to experiment 8. The slope of the dashed line is  $-1$ .

may be in Figure 5.16, where this function is represented for experiment 8. This figure may be fitted by an exponential decay on the range of scales above 0.1 mm. Though, below that scale, a power-law of the type  $\sim 1/k$  fits satisfactorily.

## 5.4 Conclusions

This work has been an attempt to obtain a greater insight in the study of fracture fronts. We have carried out a set of fracture experiments with samples of different widths. In this way, the scaling of crack fronts has been determined. The in-plane projection of fracture interfaces show a Family-Vicsek scaling. This fact might seem surprising, since the scaling of the out of plane projection is intrinsic anomalous. It agrees, however, with the results reported in [Morel 2000, Morel 2002] for the Griffith criterion applied to fracture of blocks of different materials and sizes. The Griffith criterion establishes how the rate of energy dissipation at the crack front,  $G$ , behaves. This quantity may be expressed as  $G = \gamma \delta A_r / \delta A_p$ , where  $\gamma$  is a constant,  $A_r$  is the crack surface and  $A_p$  is its in-plane projection.  $G$  initially suffers a transitory regime in which it grows, until a stationary state is reached. The value of  $G$  in this final state is related to the scaling of the fracture fronts by means of  $A_r$  and  $A_p$  [Morel 2000]. If anomalous scaling is present  $G$  in saturation must depend on the block size  $L$ ,  $G_{sat} \sim L^\theta$  with  $\theta = (\alpha_\perp - \alpha_{\perp loc}) - (\alpha_\parallel - \alpha_{\parallel loc})$ . But  $\theta$  has been experimentally found to be  $\theta \approx \alpha_\perp - \alpha_{\perp loc}$ . This result may be easily explained if the scaling of the in-plane fracture is FV, and thus  $\alpha_\parallel = \alpha_{\parallel loc}$  as we have directly confirmed.

Apart from the scaling type, we have also measured the exponents. In the case of the roughness exponent a cross-over has been found. On large scales, above  $\ell_c \sim 0.3$  mm, we have found that the roughness exponent  $\alpha_{\parallel 1} = 0.31 \pm 0.06$ . This value has been previously measured in [Delaplace 1999], it seems to arise from a resolution problem. Below this scale, the roughness exponent becomes  $\alpha_{\parallel 2} = 0.54 \pm 0.07$ . This exponent value is closer to the one reported in previous experimental studies of in-plane fracture [Schmittbuhl 1997, Delaplace 1999]. In addition, the growth exponent has also been estimated to be  $\beta_\parallel = 0.54 \pm 0.06$  in our experiments.

Finally, other aim of our experiments was to measure directly the bursts of activity in which the fracture fronts move. Unfortunately, the devices used (the microphone and the strain gage) were not sensible enough to succeed.

However, the correlations of these avalanches were estimated studying the difference between consecutive fronts. The spatial correlations seem to be long ranged, the power spectrum of these correlations decays as  $\sim k^{-1}$ . On the other hand, no temporal self-correlation has been detected for the bursts, indeed they seem to have a very short characteristic time scale.

# Chapter 6

## Fluid flow in porous media

The second experimental work in which I was involved was on the topic of fluid flow through heterogeneous media. It was carried out in a laboratory belonging to the *Departament d'Estructura i Constituents de la Matèria* of the University of Barcelona. The members of the group that have carried out this work are J. Soriano, A. Henández-Machado, J. Ortín, M.A. Rodríguez and myself. The results of the experiment have been published in [Soriano 2002]. In this chapter, a brief description of these experiments and the obtained results is included.

### 6.1 Introduction

The kinetic roughening of stable fluid-fluid interfaces has already been briefly introduced in the section 1.4 of chapter one. This kind of experiments are performed by driving a very viscous fluid, such as glycerin, against other fluid with less viscosity (air) in a heterogeneous medium. The heterogeneity of the medium is obtained by including a random distribution of impurities (e.g. glass beads) between two parallel plates of a transparent material. In this way, a rough front is achieved in the surface of separation of the two fluids.

The exponents of this type of fluid-fluid fronts (either roughness, or growth or both) have been measured in many previous experimental works [Rubio 1989], [Horváth 1990], [Horváth 1995], [Zik 1997], [Balakin 2000], [Hernández-M 2001], for a review see [Meakin 1998]. However, no final theoretical understanding has been achieved yet. There exist partial theories

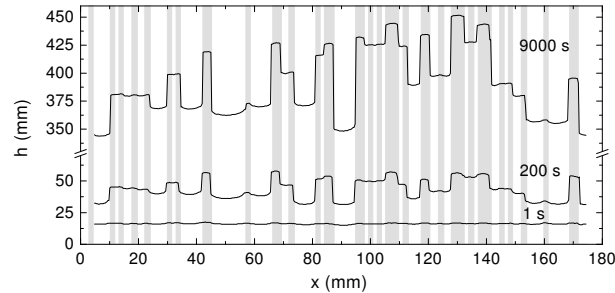


Figure 6.1: Sequence of typical oil–air interfaces. The silicone oil moves upwards in the picture, and the disorder pattern is represented in grey. The experimental parameters are  $b = 0.36$  mm and  $v = 0.04$  mm/s.

for some important cases, as the directed percolation and the front depinning in paper wetting experiments [Buldyrev 1992, Buldyrev 1992b]. But, even those cases are still matter of a strong debate [Lam 2000, Dubé 2001, Lam 2001]. Other promising theoretical framework was proposed independently by [Dubé 1999] and [Hernández-M 2001]. It is based on a phase-field model where each fluid takes the role of a phase.

Most of the roughness exponents measured so far are local exponents. Indeed, some of them lay close to one [Horváth 1990, He-S. 1992, Balakin 2000], which implies that the global exponents might be greater than one. In this case, the scaling would correspond to super-roughness instead to FV and, as happens with intrinsic anomalous scaling, other independent exponent (global roughness) must be estimated in order to characterize properly the interface scaling.

Several operational modes are possible in fluid flow experiments. The fronts may be impulsed either by a constant rate of mass injection, or by a constant pressure. In the first case, the velocity of the front is constant, while in the second it decreases as a power law in time  $v \sim t^\gamma$ . This effect is mainly due to the viscosity of the fluid. The other effect that dominates the evolution of fluid-fluid fronts is the capillarity. The fluid moves faster where the conduct to go through is narrower. The classic experiments to quantify this effect were performed with a capilar (a very narrow pipe) that was inserted in a fluid by one of its extremes. The fluid rises then along the capilar until a certain height, which is function of the pipe width, the viscosity of the fluid and its density. We study a set of associated capilars.

The experimental setup consists of continuous copper tracks on a fiber-glass substrate in the front advancing direction and randomly distributed in the perpendicular direction, as can be seen in Figure 6.1. In this situation, the correlation of the disorder in the advancing direction is infinite and the local motion relative to the average interface position is driven by capillarity. This effect is caused by the different curvatures of the advancing front in the third dimension, depending on whether the oil is on a copper track or in the fiber-glass substrate, and is responsible for the resulting rough interface.

## 6.2 Experimental setup

The experiments have been performed in a horizontal Hele-Shaw cell,  $190 \times 550$  ( $L \times H$ )  $\text{mm}^2$ , made of two glass plates 20 mm thick. The copper tracks on the substrate are randomly distributed along  $x$ , with a filling factor  $f = 35\%$ . The tracks are  $d = 0.06 \pm 0.01$  mm high and have a lateral size of  $1.50 \pm 0.04$  mm. The distance between the top plate and the substrate defines the gap spacing  $b$ , which has been varied in the range  $0.16 \leq b \leq 0.75$  mm. We have used 4 different disorder configurations and carried out 2

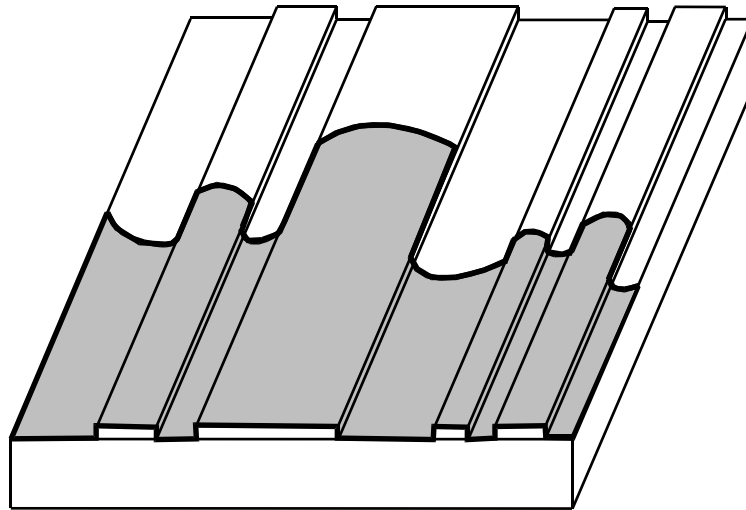


Figure 6.2: A rough representation of our experimental setup, the grey area corresponds to the volume already invaded by oil.

identical runs per configuration. A silicone oil (kinematic viscosity  $\nu = 50 \text{ mm}^2/\text{s}$ , density  $\rho = 998 \text{ kg/m}^3$ , and surface tension oil–air  $\sigma = 20.7 \text{ mN/m}$  at room temperature) was injected at one side of the cell at constant volumetric injection rate. The oil completely wets the glass plates, the substrate, and the copper tracks. The evolution of the interface at average velocity  $v$  was monitored using two CCD cameras with a resolution of  $0.38 \text{ mm/pixel}$ . Further details may be found in [Hernández-M 2001]. In Figure 6.2, a rough sketch of an experiment realization is represented.

## 6.3 Analysis of the results

The first task to be completed with the results of our experiments is to check the kind of interface scaling. In order to do so, several quantities, both in the direct and Fourier space, have been considered. The first section is devoted to the velocity of the front. Because of the different operational modes in which the experiments with fluid fronts may be performed, this is not an irrelevant matter. Later, the roughness (global and local) and growth exponents are estimated by means of local width and correlations. Finally, the scaling type and the exponents found are checked by performing a data collapse of the power spectra at different times.

### 6.3.1 The velocity of the fronts

In our experiments, the fluid mass is injected at a constant rate. Hence, the mean velocity of the fronts is constant too. However, the local behaviour of the velocity is very rich. As was explained above, the fluid moves faster in the narrower parts of the disorder. Initially, a group of *fingers* are observed upon the copper tracks. These fingers grow independently for a while, what produces a fair height difference with the front in the sites without tracks, valleys. The independence of the fingers does not last for very long, because the tension of the oil surface decelerate them. In this way, lateral correlations spread through out the system. When the characteristic length of those correlations,  $\xi$ , has become equal to the system size,  $\xi = L$ , evolution is no longer observed in the system. In physical terms, this final state (saturation) implies that the velocities of the fingers and valleys are equated by the surface tension. As a consequence, the width of the interface cannot grow anymore.

In Figure 6.3, the velocity of fingers,  $v_+$ , and valleys,  $v_-$ , is represented

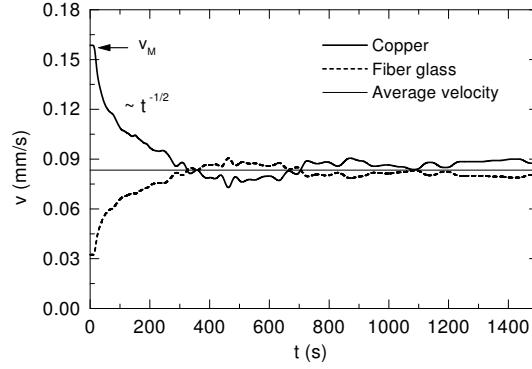


Figure 6.3: Local interface velocity on copper tracks ( $v_+$ ) and on fiber-glass tracks ( $v_-$ ), for  $b = 0.36$  mm and  $v_{sat} = 0.08$  mm/s.

for one experimental realization. We find that the local velocity decreases (increases) in the fingers (valleys) as a power law in time,  $v_+ \sim v_{sat} - a t^{-1/2}$  ( $v_- \sim v_{sat} + a t^{-1/2}$ ) where  $a$  is a constant. This velocity difference plays a very important role in the scaling behaviour of the fronts, as will be explained in detail later.

### 6.3.2 Width and correlations

In contrast to what happened with fracture fronts, the evolution of fluid-fluid interfaces is slow enough to allow an exhaustive dynamical study. In addition, the initial shape of the fronts is almost flat because a horizontal track has been included at the bottom of the Hele-Shaw cell. In this way, the early dynamic of the system may be examined. It also makes possible, by scanning the temporal evolution of the width, to measure directly the growth exponent.

As it is explained in chapter two, the most general scaling form for the scaling of the local width,  $w(t, l) = \{ \langle [h(x, t) - \langle h \rangle_l]^2 \rangle_l \}^{1/2}$ , is

$$w(t, l, L) \sim \begin{cases} t^{\alpha/z} & \text{if } t \ll t_{\times}(l) \\ t^{(\alpha-\alpha_{loc})/z} l^{\alpha_{loc}} & \text{if } t_{\times}(l) < t < t_{\times} \\ l^{\alpha_{loc}} L^{(\alpha-\alpha_{loc})} & \text{otherwise,} \end{cases} \quad (6.1)$$

where  $L$  is the system size, and  $t_{\times}(l) \sim l^z$  and  $t_{\times} \sim L^z$  are the saturation times for the scale  $l$  and for the whole system, respectively. Unfortunately,

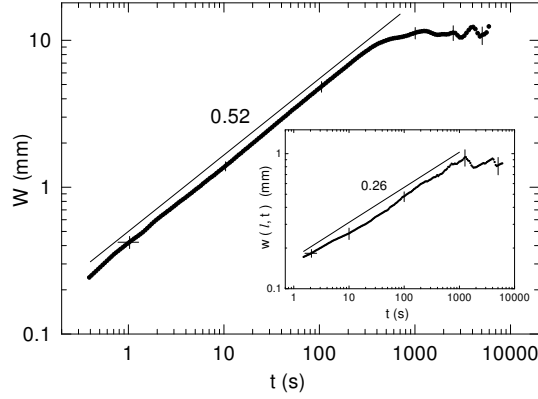


Figure 6.4: Experimental determination of  $\beta$  (main plot) and  $\kappa$  (inset). The scale of the main plot is  $l_2 = 18$  cm, while that of the inset is  $l_1 = l_2/128$ . We plot  $w(t, l) = [w^2(l, t) - w^2(l, t = 0)]^{1/2}$  to minimize the influence of the intrinsic width. The experimental parameters are  $b = 0.36$  mm,  $v = 0.08$  mm/s.

the size of the system cannot be varied in this experiment, it would imply the change of the Hele–Shaw cell. Hence, the presence of the anomalous scaling cannot be checked comparing the width in saturation for different system sizes, as we did in the preceding chapter with fracture fronts. As an alternative, the early dynamics of the local width may be measured for one of the smallest scales  $l_1$  that we can reach. If the local width at scale  $l_1$  goes on increasing with time until the global saturation, we can be certain that the scaling is anomalous. Indeed, the exponent  $\kappa = (\alpha - \alpha_{loc})/z$  might be estimated. This procedure has been followed in Figure 6.4. There, it is clearly established the existence of anomalous scaling, and the values of the exponents  $\beta = 0.52 \pm 0.02$  and  $\kappa = 0.26 \pm 0.03$  are found.

Apart from the local width, we have also employed the correlation function  $\Gamma_q(l, \tau) = \{ \langle |\Delta h(x+l, t+\tau) - \Delta h(x, t)|^q \rangle_{x,t} \}^{1/q}$ , with  $\Delta h(x, t) = h(x, t) - \langle h \rangle_x(t)$ . In Figure 6.5,  $\Gamma_q(l, \tau = 0)$  and  $\Gamma_q(l = 0, \tau)$  are represented for several values of  $q$ . From these plots, we can conclude that this system shows multi-scaling (the local roughness exponent depends on  $q$ ,  $\alpha_{loc}(q)$ ). The value of local roughness  $\alpha_{loc} = \alpha_{loc}(q = 2) = 0.61 \pm 0.04$  has been determined.

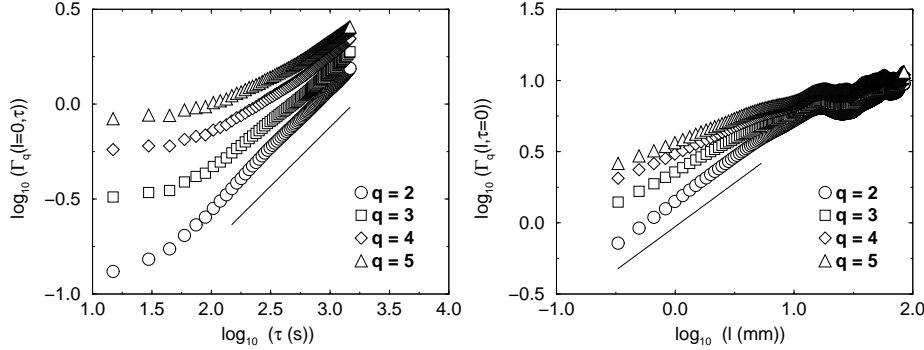


Figure 6.5: The correlation function  $\Gamma(l, \tau)$ . On the left side,  $\Gamma(l = 0, \tau)$  versus time for different value of  $q$ , the slope of the straight line is  $\beta \approx 0.6$ . On the right hand,  $\Gamma(l, \tau = 0)$  is represented. The linear fit corresponds to a slope  $\alpha_{loc} = 0.61 \pm 0.04$ . The experimental parameters are  $b = 0.36$  and  $v = 0.08$  mm/s

### 6.3.3 Power spectrum

In addition to the direct space magnitudes, correlations and local width, we have also calculated the power spectrum of the fluid fronts. This a useful method to check the scaling and exponents already measured. The presence of anomalous scaling can be directly observed in the power spectra displayed in Figure 6.6. The region of long wave-lengths shows a shift with time that must correspond to a power law of the type  $\sim t^{2\kappa}$ . Also, the slope of this region in the log-log plot must be  $-(2\alpha_{loc}+1)$ . This fact allows us to estimate  $\alpha_{loc} \approx 0.6$ , in good agreement with the value found before by means of the correlation function. The best way to check both, the scaling and the exponents, is to try to collapse the power spectra obtained for different times. This is what is plotted on the right side of Figure 6.6. A nice collapse is obtained for the exponents  $\alpha = 1.0 \pm 0.1$ ,  $z = 2.0 \pm 0.2$ , which implies that  $\beta = 0.50 \pm 0.04$  and  $\kappa = 0.25 \pm 0.03$ , in excellent agreement with our previous estimation (see sec. 6.3.2)

### 6.3.4 A phase diagram

In the Section 6.3.1, the local characteristic of the velocity of the fronts has already been mentioned. In the sites where a copper track is placed, the fluid

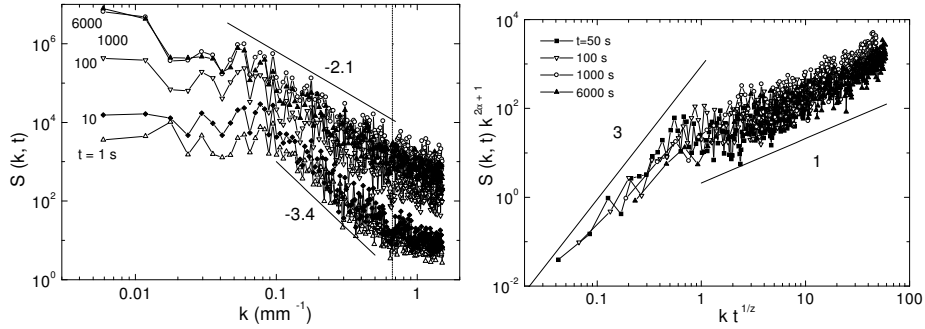


Figure 6.6: Temporal evolution of the power spectrum. The vertical line gives the value of  $k$  associated with the spatial scale of the disorder. On the right side, the collapse of the experimental power spectra for  $t > 10$  s.

moves faster because there the space between the plates of the Hele–Shaw cell,  $b$ , is narrower. This velocity is reduced later due to the surface tension. Let us then define  $v_M$  as the initial (and maximum) velocity of the front in the sites with a copper track. Apart from  $v_M$ , there exists other velocity that must be taken into account, the velocity at saturation  $v_{sat} = v$ . This latter magnitude depends on the injection rate, which is an external control parameter.

These two velocities  $v$  and  $v_M$  actually control the scaling of the fluid–fluid interfaces. The anomalous scaling appears whenever  $v_M > v$ . This fact implies that the average slopes of the interface grow in time, while the velocity difference between valleys and finger persists. This difference, though decreases in time, lasts till global saturation occurs. As it was explained in chapter 3, one important feature of intrinsic anomalous scaling is the increment in time of the mean slope of the system ( $\sigma(t) = \{ \langle |\nabla h| \rangle_x \}$ ).  $\sigma$  grows in time as a power law [López 1999],  $\sigma(t) \sim t^\kappa$ , until the whole system saturates. The origin of the anomalous scaling thus lies in the higher velocity of the fluid over the copper tracks. On the other hand, when the fluid is injected at a very high rate, the velocity at saturation increases till finally  $v > v_M$ . In that case, anomalous scaling is not expected anymore. In Figure 6.7, a phase diagram summarizing our experimental results is shown.

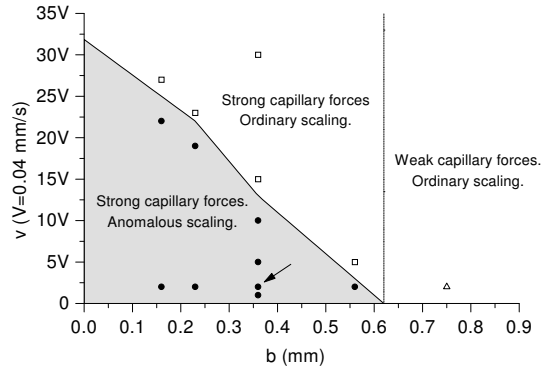


Figure 6.7: Phase diagram  $v(b)$  indicating the regions where the anomalous scaling is seen. The symbols represent the different regions explored experimentally, and the arrow indicates the parameters used in the paper.

## 6.4 A first step towards a theoretical framework

The simple geometry of our experiment has led us to formulate a theoretical model to try to reproduce the experimental results. In this first stage, a local model approach has been employed. Although, we know that this is essentially a non-local problem due to the global mass conservation requirement [Hernández-M 2001, Dubé 1999, Lam 1998, Dubé 2001, Lam 2000]. Non-local models are in the scope of future works.

The phenomenological model that we have developed is based on a set of independent columns, representing the tracks, within which the driving force takes a value  $v + A(t)\eta(x)$ . The disorder term  $\eta(x)$  is taken to be a dichotomous noise with only possible values  $+1$  and  $-1$ , i.e. not correlated between neighbouring columns. The width of these columns is randomly chosen from an exponential distribution with mean size  $\lambda$ . In this way, we try to reproduce the conditions in the Hele-Shaw cell of the experiment. We have also included an amplitude  $A(t)$ , which diminishes in time as  $(v_M - v)t^{-1/2}$ , to mimic the behaviour of the local velocity of the front described in the Figure 6.3. This is a purely phenomenological term. Finally, the interaction between neighbouring columns is introduced by means of a diffusive term.

The model is then given by

$$\frac{\partial h}{\partial t} = \nabla D(x) \nabla h(x, t) + v + (v_M - v) t^{-1/2} \eta(x). \quad (6.2)$$

The diffusive coupling ensures the value  $z = 2$  for the dynamic exponent, a close value to the one observed experimentally. The rest of exponents may be obtained by either numerical simulation, or by scaling arguments as those presented in the section 3.4 of Chapter 3 and in [López 1999]. If the diffusion is uniform ( $D$  is a constant), the global exponents found for this model are  $\alpha = 1$ ,  $\beta = 1/2$  and, thus,  $z = 2$ . These values are in good agreement with the exponents obtained from experimental data. However, the scaling of this model is not intrinsic anomalous but Family-Vicsek. This implies that the local roughness exponent is  $\alpha_{loc} = 1$  unlike the one found in the experiments.

In order to recover the different local scaling, the fact that the interface is almost flat inside each track, and fluctuations occur only between tracks (see Fig. 6.1), must be taken into account. Analytically, this behaviour is included in Equation 6.2 by means of an inhomogeneous diffusion coefficient  $D(x)$ . In a practical way, this effect has been introduced by spatially averaging the interface along each column once at every time step. We thus recover interfaces that are morphologically analogous to the experimental surfaces. The exponents derived from the scaling of the power spectra shown in Fig. 6.8, and the multi-scaling exponents, reproduce the values determined experimentally. It is remarkable that the spectra obtained in our model, averaged

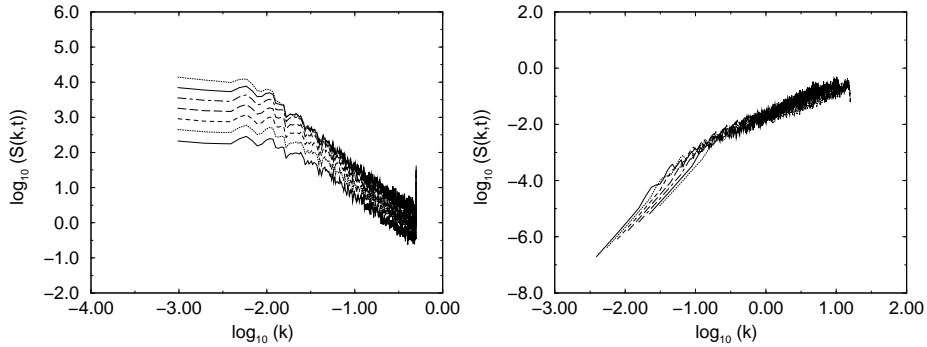


Figure 6.8: The power spectrum for different times of our model. On the right side, it is shown a collapse of these spectra obtained with the set of exponents  $\alpha = 1$ ,  $z = 2$  and  $\alpha_{loc} = 1/2$ .

over 50 runs, and the experimentally measured spectra, averaged over only 4 experimental runs, have comparable dispersions. This is due to the lack of self-averaging in this problem with persistent disorder. In summary, our phenomenological model enables the relevant effects in the experiment to be both identified and calibrated.

## 6.5 Conclusions

We have carried out a series of experiments of fluid-fluid fronts in a very simple geometry. This geometrical distribution with columnar disorder should allow the construction of easier-to-handle theoretical models. The non-local models proposed so far for experiments with a more elaborated disorder distribution have not yet obtained a satisfactory description of this phenomenon.

The type of scaling of our experimental fronts has been found to be mass rate injection dependent. Anomalous scaling is present whenever the capillarity effects are stronger than the injection. This happens for a large region of experimental parameters. Capillarity makes that in the sites with copper track, the velocity of the interface is higher,  $v_M$  at  $t = 0$ . The velocity difference of the fluid on regions with and without copper is the origin of the observed anomalous scaling. We have also measured the scaling exponents,  $\alpha = 1 \pm 0.1$ ,  $z = 2.0 \pm 0.2$  and  $\kappa = 0.25 \pm 0.03$ . This means that  $\alpha_{loc} = \alpha - \kappa z = 0.50 \pm 0.08$ . These experimental values have been found to be consistent with direct space measures (correlation function, local width) and spectra.

We have also proposed a phenomenological theoretical model that reproduces the exponent values mentioned above. It is based on the assumption that diffusion between neighbouring tracks is the main interaction. Though, to recover anomalous scaling as seen in our experiment a very strong diffusion inside each track has to be introduced. We think that this fact may be avoided if a more complex model (a non-local one) is considered.



# Appendix A

## Detailed calculation of direct space functions

This appendix includes the step by step deduction of the global width and of height-height correlation functions asymptotic behaviour taking as starting point the anomalous scaling ansatz proposed for the power spectrum. The reason to separate this part of chapter 3, which is devoted to scaling of interfaces, is that in this way the more technical questions settle apart from the physical conclusions.

### A.1 Global magnitudes

The global width may be obtained from the power spectrum as

$$W^2(t, L) \approx \int_{2\pi/L}^{\pi/a} d\mathbf{k} S(k, t) = \int_{2\pi/L}^{\pi/a} d\mathbf{k} \frac{s(k \xi)}{k^{2\alpha+d}}. \quad (\text{A.1})$$

We may perform the variable change  $\mathbf{u} = \xi \mathbf{k}$  to obtain

$$W^2(t, L) \approx \xi^{2\alpha} \int_{2\pi\xi/L}^{\pi\xi/a} d\mathbf{u} \frac{s(u)}{u^{2\alpha+d}}. \quad (\text{A.2})$$

For global quantities, we must consider two different time regimes. The early time behavior  $t < t_\times$ , when correlations are still expanding through the system;  $L > \xi \sim t^{1/z}$ , and the saturated regime  $t > t_\times$ , when correlations grow no more;  $\xi = L$ . We can find the asymptotic behavior of the latter

integral for the first regime by taking the thermodynamic limit ( $L \rightarrow \infty$  and  $a \rightarrow 0$ ) in the cutoffs,

$$W^2(t < t_\times, L) \approx \xi^{2\alpha} \int_0^\infty d\mathbf{u} \frac{s(u)}{u^{2\alpha+d}}. \quad (\text{A.3})$$

This integral is convergent for all scaling cases. Its argument is constant for the lower cutoff, and it tends to zero as a power law,  $s(u)/u^{2\alpha+d} \sim u^{-\alpha_s-d}$  for  $u \gg 1$ , in the upper limit. In addition, in this regime we may substitute  $\xi$  by  $t^{1/z}$ . Hence, the latter expression increases in time as

$$W^2(t < t_\times, L) \sim t^{2\alpha/z} \sim t^{2\beta}. \quad (\text{A.4})$$

In the opposite regime, we must remember that  $\xi = L$ . As a consequence, when we substitute  $\xi$  by  $L$ , the lower cutoff of the integral becomes  $2\pi$ . If, after that, we take the thermodynamic limit and replace  $s(u)$  by its asymptotic value for arguments  $u \geq 2\pi > 1$ , we obtain

$$W^2(t > t_\times, L) \approx L^{2\alpha} \int_{2\pi}^\infty \frac{d\mathbf{u}}{u^{2\alpha_s+d}} \sim L^{2\alpha}. \quad (\text{A.5})$$

The global magnitudes in the asymptotic limit thus behave in the same way as for the Family-Vicsek scaling. FV scaling for the global width is recovered no matter whether  $\alpha$  is equal to  $\alpha_s$  or not, or even if some of them is greater than one. However, as will be shown below, this is not the case for local estimators.

## A.2 Local estimators

As a paradigm of the local functions, we may study the height-height correlation function at equal time. It was established in section 3.3 of chapter three that this function may be obtained from the power spectrum by the integral

$$G(t, l) \approx \int_{2\pi/L}^{\pi/a} d\mathbf{k} [1 - \cos(kl)] S(k, t) = \int_{2\pi/L}^{\pi/a} d\mathbf{k} \frac{[1 - \cos(kl)]}{k^{2\alpha+d}} s(k\xi).$$

If the variable change  $\mathbf{u} = l\mathbf{k}$  is applied, this expression becomes

$$G(t, l) \approx l^{2\alpha} \int_{2\pi l/L}^{\pi l/a} d\mathbf{u} \frac{[1 - \cos(u)]}{u^{2\alpha+d}} s(u\xi/l). \quad (\text{A.6})$$

This integral may be split into two terms; one with the small arguments of the function  $s()$ , and other for the big values of  $u \xi/l$ ,

$$G(t, l) \approx l^{2\alpha} \left\{ (\xi/l)^{2\alpha+d} \int_{2\pi l/L}^{l/\xi} d\mathbf{u} [1 - \cos(u)] \right. \\ \left. + (\xi/l)^{2(\alpha-\alpha_s)} \int_{l/\xi}^{\pi l/a} d\mathbf{u} \frac{[1 - \cos(u)]}{u^{2\alpha_s+d}} \right\}. \quad (\text{A.7})$$

For local magnitudes, we must deal with three important characteristic length scales. The system size and the correlation length  $\xi$ , as happened for the global width, but also the observation scale  $l$ . As a consequence, three different time regimes must be considered: early time regime  $t < t_\times(l) \sim l^z$ , intermediate regime  $t_\times(l) < t < t_\times \sim L^z$ , and saturation  $t > t_\times$ . In these regimes, we may obtain the behaviour of  $G(l, t)$  from the equations (A.6) or (A.7).

### A.2.1 Early time regime, $t \ll l^z$

In the early time regime, the correlation length satisfies the condition  $\xi \ll l$ . We thus can take the limit of big values of  $l/\xi$ . What means that we can neglect the second integral in (A.7); the contribution of that term is of the order of  $(l/\xi)^{-2\alpha}$ . Taking only the first integral, in the thermodynamic limit, we find that

$$G(l, t < t_\times(l)) \approx l^{-d} \xi^{2\alpha+d} \int_0^{l/\xi} d\mathbf{u} [1 - \cos(u)] \sim \xi^{2\alpha} \sim t^{2\alpha/z} \sim t^{2\beta}. \quad (\text{A.8})$$

This conclusion is valid whatever the values of  $\alpha$  and  $\alpha_s$  are.

### A.2.2 Intermediate regime, $l^z \ll t \ll L^z$

The following time regime, the intermediate one, is characterized by a value of the correlation length between the observation scale and the system size,  $l \ll \xi \ll L$ . In such conditions, the contribution of the first term of (A.7) is of the order of  $(\xi/l)^{-2(1-\alpha)}$ . Hence, it may be neglected whenever  $\alpha < 1$ . The outcome of the remaining integral, as well as the asymptotic behaviour when  $\alpha > 1$  depends on the particular value of the exponents. So, it is better to analyze each case separately.

### a) Family-Vicsek

This scaling is characterized by the relation  $\alpha_s = \alpha < 1$  between the roughness exponents. In this situation, the expression (A.7) reduces to

$$G(l, t_\times(l) < t < t_\times) \approx l^{2\alpha} \int_{2\pi l/L}^{\pi l/a} d\mathbf{u} \frac{[1 - \cos(u)]}{u^{2\alpha+d}}. \quad (\text{A.9})$$

If we take the thermodynamic limit, it becomes:

$$G(l, t_\times(l) < t < t_\times) \approx l^{2\alpha} \int_0^\infty d\mathbf{u} \frac{[1 - \cos(u)]}{u^{2\alpha+d}} \sim l^{2\alpha}. \quad (\text{A.10})$$

The latter integral is convergent whether  $\alpha < 1$ .

### b) Intrinsic anomalous scaling

Now,  $\alpha$  is different from  $\alpha_s$ , but the latter is still lower than one. Hence, in the thermodynamic limit we obtain a similar integral as before but the asymptotic behaviour of  $G(t, l)$  is different

$$G(l, t_\times(l) < t < t_\times) \approx l^{2\alpha_s} \xi^{2(\alpha-\alpha_s)} \int_0^\infty d\mathbf{u} \frac{[1 - \cos(u)]}{u^{2\alpha_s+d}} \sim l^{2\alpha_s} t^{2(\alpha-\alpha_s)/z}. \quad (\text{A.11})$$

### c) Super-roughness

This scaling case takes place when  $\alpha = \alpha_s > 1$ . With that  $\alpha$  exponent, none of the terms of the equation (A.7) is convergent in the limit  $l/\xi \rightarrow 0$ . To avoid this problem, we can consider the diverging contribution of each term, and select the most important as a part of the scaling of  $G(t, l)$ . The first integral may be carried out exactly, the main contribution of that term is proportional to  $(l/\xi)^{2(1-\alpha)}$ . The second integral is divergent in the limit in which its lower cutoff tends to zero. To estimate the integral in that cutoff, we can substitute the function  $(1 - \cos(u))$  by its approximation for low arguments  $u^2/2$ ,

$$(l/\xi)^{2(\alpha_s-\alpha)} \int_{l/\xi}^\infty d\mathbf{u} \frac{[1 - \cos(u)]}{u^{2\alpha_s+d}} \sim (l/\xi)^{2(\alpha_s-\alpha)} (l/\xi)^{2-2\alpha_s} \sim (l/\xi)^{2-2\alpha}. \quad (\text{A.12})$$

Hence, the two terms in equation (A.7) behave in the same way. This means that the scaling of  $G(t, l)$  becomes

$$G(l, t_{\times}(l) < t < t_{\times}) \sim l^{2\alpha} (l/\xi)^{2(1-\alpha)} \sim l^2 t^{2(\alpha-1)/z} . \quad (\text{A.13})$$

In the marginal situation  $\alpha = 1$ , the height-height correlations go as

$$G(l, t_{\times}(l) < t < t_{\times}) \sim l^2 \log(t) . \quad (\text{A.14})$$

#### d) Faceted roughening

This is the last possible case of scaling. Here,  $\alpha_s$  is bigger than one, and different from  $\alpha$ . This implies that the second integral of the expression (A.7) is divergent. As in the previous case, the main diverging contribution of that term is  $(l/\xi)^{2(1-\alpha)}$ . Hence, the asymptotic behaviour of the function  $G(t, l)$  is given by

$$G(l, t_{\times}(l) < t < t_{\times}) \sim l^2 t^{2(\alpha-1)/z} . \quad (\text{A.15})$$

### A.2.3 Saturation regime, $t \gg L^z$

The last time regime is saturation. For  $t > t_{\times} \sim L^z$ , the correlation length has already grown up to system size ( $\xi = L$ ), and the whole system has reached a stationary state. The local scaling in this regime can be easily obtained if we substitute  $\xi$  by its value in the equation (A.6). The integral becomes

$$G(l, t \gg t_{\times}) \approx l^{2\alpha} \int_{2\pi l/L}^{\pi l/a} d\mathbf{u} \frac{[1 - \cos(u)]}{u^{2\alpha+d}} s(uL/l) . \quad (\text{A.16})$$

Here, the argument of the function  $s()$  is always bigger than  $2\pi$ . Hence, we can substitute the asymptotic behaviour of  $s(u)$  for  $u \gg 1$ . But, as that behaviour depends on the value of the exponents  $\alpha$  and  $\alpha_s$ , the result is much more involved and therefore, each possible combination of those exponents will be treated separately.

#### a) Family-Vicsek scaling

In this case, the function  $s(u)$  is constant for this range of values of its argument. We can take the thermodynamic limit to find

$$G(l, t \gg t_{\times}) \approx l^{2\alpha} \int_0^{\infty} du \frac{[1 - \cos(u)]}{u^{2\alpha+d}} \sim l^{2\alpha} , \quad (\text{A.17})$$

where it has been taken into account that the latter integral is convergent if  $\alpha < 1$ .

### b) Intrinsic anomalous roughening

If anomalous scaling is present, the function  $s(\cdot)$  goes as  $s(u) \sim u^{2(\alpha-\alpha_s)}$  for large values of  $u$ . If we use this asymptotic behaviour in the equation (A.16), we obtain

$$G(l, t \gg t_\times) \approx l^{2\alpha_s} L^{2(\alpha-\alpha_s)} \int_0^\infty d\mathbf{u} \frac{[1 - \cos(u)]}{u^{2\alpha_s+d}} \sim l^{2\alpha_s} L^{2(\alpha-\alpha_s)}. \quad (\text{A.18})$$

### c) Super-roughness

In this case, the function  $s(\cdot)$  is again constant for high arguments. But, now the integral of equation (A.16) is divergent, due to its lower cutoff, when the thermodynamic limit is taken. As we made for the intermediate regime, we can estimate which is the main diverging contribution of the integral, and include it in the scaling. By doing so, we find

$$G(l, t \gg t_\times) \approx l^{2\alpha} \int_{2\pi l/L}^\infty d\mathbf{u} \frac{[1 - \cos(u)]}{u^{2\alpha+d}} \sim l^{2\alpha} (l/L)^{2(1-\alpha)} \sim l^2 L^{2(\alpha-1)}. \quad (\text{A.19})$$

### d) Faceted interfaces

Now, the function  $s(\cdot)$  behaves asymptotically in the same way as in the anomalous scaling case,  $s(u) \sim u^{2(\alpha-\alpha_s)}$ . But in addition, the remaining integral is divergent in the thermodynamic limit. Applying the same method as in the previous case, we obtain

$$G(l, t \gg t_\times) \approx l^{2\alpha_s} L^{2(\alpha-\alpha_s)} \int_{2\pi l/L}^\infty d\mathbf{u} \frac{[1 - \cos(u)]}{u^{2\alpha_s+d}} \sim l^2 L^{2(\alpha-1)}. \quad (\text{A.20})$$

# Appendix B

## Resumen en castellano

Este apéndice es un resumen en castellano del resto de la tesis doctoral. En él, se pretende que queden suficientemente claros tanto los objetivos que guiaron los trabajos de investigación aquí presentados, como los principales resultados obtenidos en cada uno de ellos. La estructura de este resumen se corresponde, por tanto, con el de los capítulos de la tesis, aunque, con el fin de facilitar su lectura, no siempre de forma literal.

### B.1 Introducción

El objeto de estudio en esta tesis son las interfases. Una interfase es la separación entre dos sustancias diferentes, o entre distintas fases de una misma sustancia. La experiencia diaria nos muestra que dichas superficies pueden presentar una gran diversidad de morfologías, pueden ser planas como sucede, por ejemplo, con los vidrios de las ventanas, o rugosas como la superficie de los fragmentos de dichos vidrios cuando se rompen. Además, las escalas en las que este fenómeno sucede son, también, muy diversas. Van desde los Åmstrongs ( $10^{-10}$  m) en el caso del crecimiento de estructuras cristalinas, hasta las centenas de kilómetros de las grandes cadenas montañosas. En la sección que sigue se detalla con mayor detenimiento la manera de realizar experimentos para intentar caracterizar las interfases.

### B.1.1 Experimentos con interfases

En un experimento de cualquier disciplina científica, lo más importante es la reproductibilidad de los resultados. Para lograr ese objetivo, las condiciones en las que los experimentos transcurren han de ser cuidadosamente controladas. En los experimentos con interfases, los resultados (los frentes específicos) no son exactamente reproducibles. Al igual que sucede con los sistemas caóticos, no se pueden preparar dos sistemas exactamente en las mismas condiciones (el mismo desorden). Sin embargo, como en la teoría del caos, siempre existen una serie de observables, que suelen ser promedios sobre realizaciones del desorden, y que permiten establecer unos criterios universales para caracterizar cuantitativamente el crecimiento de interfases. Uno de dichas características es la anchura de la interfase  $w$ , que es la dispersión del frente con respecto a su altura promedio.

Como ya se ha mencionado, los experimentos con interfases pueden tratar fenómenos físicos en una gran variedad de escalas. A continuación se describen brevemente algunos de esos trabajos experimentales. Estos experimentos en particular son especialmente importantes para esta tesis. Los estudios sobre el crecimiento cristalino, en la forma de crecimiento epitaxial, fueron los que dieron lugar a la aparición de la teoría del escalado anómalo, que es sobre lo que trata el capítulo tres. En los capítulos quinto y sexto, por otro lado, se describen sendos trabajos experimentales, unos sobre la fractura de sólidos y otro sobre frentes de fluidos.

#### Crecimiento epitaxial

Recibe este nombre el crecimiento de estructuras cristalinas llevada a cabo en el interior de una cámara de muy baja presión y con un flujo de partículas pequeño. De esta forma se consiguen crear cristales mediante un crecimiento capa a capa de átomos.

El resultado de este tipo de experimentos depende de la temperatura  $T$ . Si la temperatura es muy baja, los átomos al llegar a la superficie se quedan en el primer lugar de contacto. La interfase se convierte rápidamente en una estructura rugosa pero sin interconexión entre lugares vecinos. Si por el contrario  $T$  es muy alta, los átomos tienen la energía suficiente para liberarse de los enlaces que los ligan al primer lugar de contacto. Lo que hacen entonces es buscar los lugares con un mayor número de vecinos (donde el número de enlaces es mayor) porque son energéticamente más favorables. En el límite

de muy alta temperatura los cristales crecen con interfases planas. En medio de estos dos extremos, existe un amplio rango de temperaturas donde los átomos, al llegar, buscan una situación favorable energéticamente, pero en un entorno local a su punto de llegada. La interfase en ese régimen es rugosa, pero no con anchura infinita como en  $T = 0$ .

### Frentes de fluidos

Este tipo de experimentos está más cerca de nuestra experiencia diaria que el crecimiento cristalino, ya que tienen lugar a la escala humana. La cámara donde se realizan este tipo de experimentos está formada por dos placas transparentes, para permitir el seguimiento de la evolución de los frentes. Entre las placas se colocan una serie de *impurezas*. Dichas impurezas (el desorden) pueden estar formadas por pequeñas bolas de cristal de distintos tamaños, como en el caso de los experimentos más antiguos, o incluso por pistas de cobre de circuitos electrónicos, como es el caso del experimento descrito en el capítulo 6. En el espacio entre las dos placas se inyecta un fluido de una alta viscosidad, como glicerina o aceite. La evolución de la geometría del frente puede entonces ser estudiada en detalle.

### Fractura

Cuando se aplica una fuerza externa  $F$  sobre un sólido, se produce una deformación. Para un cierto rango de valores de  $F$ , dicha deformación es proporcional a la fuerza aplicada. Además, si  $F$  disminuye, el sólido tiende a recuperar su forma original. Este tipo de comportamiento es conocido como elasticidad. Sin embargo, cuando la fuerza externa supera un cierto límite, se produce una deformación permanente o, incluso, una fractura. Las características morfológicas de la fractura depende de la velocidad con la que avance. Para velocidades altas, no existe un único frente de fractura, sino que hay uno principal y una serie de ramificaciones secundarias, algo similar a lo que sucede con las lunas de los coches tras un choque. Por el contrario si el frente avanza de forma cuasiestática, existe en cada momento una interfase de fractura bien definida.

Los frentes de fractura, en el régimen cuasiestático, toman la forma de una curva rugosa en tres dimensiones. La rugosidad les viene del hecho de que los materiales no son perfectamente homogéneos, y por tanto la fractura en algunos lugares requiere un mayor gasto energético que en otros. La forma

de la superficie del material fracturado en cada lugar está relacionada con la geometría del frente de fractura cuando se encontraba sobre dicho lugar. En esta idea es en la que se basan la mayoría de los experimentos clásicos en este campo. Se toma uno de los dos fragmentos del material fracturado y se estudia para cada corte perpendicular a esa superficie la forma que ésta tiene.

### **B.1.2 Modelos teóricos**

Los modelos teóricos para las interfases explotan su principal propiedad, la ausencia de una escala característica. Estos modelos, por tanto, no llevan asociadas ninguna unidad, no hay en ellos constantes expresadas en metros, milímetros o micrómetros, puesto que el mismo modelo es válido para todas esas escalas. Este tipo de fenómenos, independientes de la escala, son conocidos como fenómenos críticos, porque fueron inicialmente observados en los puntos críticos de las transiciones de fase continuas. La física de los procesos críticos está únicamente dominada por las simetrías del sistema. Así que, distintos sistemas críticos, compuestos por distintas sustancias y a distintas escalas pueden ser descritos por un único modelo. Esta idea fue la que dio origen a las clases de universalidad, que es como son clasificados los distintos sistemas críticos. Cada una de dichas clases aparece como resultado de unas simetrías diferentes propias de un grupo de fenómenos críticos.

Las matemáticas desarrolladas para estudiar los fenómenos invariantes de escala se incluyen dentro de las denominadas teorías fractales.

#### **Fractales e invariancia de escala**

Los fractales son conjuntos que permanecen invariantes a los cambios de escala. La invariancia puede ser literal, al hacer un zoom de una parte se observa exactamente la misma estructura, o puede ser estadística: no se ve exactamente lo mismo, pero el resultado del zoom es indistinguible del conjunto original. Cualquier estimador estadístico que se aplique a dicho conjunto da lugar a los mismo resultados que si se aplica al conjunto completo. Los conjuntos con esta propiedad de invariancia son conocidos como fractales auto-similares.

Existen otro tipo de fractales, conocidos como auto-afines que son los conjuntos que permanecen invariantes (estadística o literalmente) a transformaciones de escala no isótropas. Si uno de los ejes de coordenadas se

transforma al hacer el zoom como  $x \rightarrow bx$ , el resto de ejes coordenados han de variar como  $y \rightarrow b^{\alpha_y} y$ ,  $z \rightarrow b^{\alpha_z} z$ , etc. Los exponentes sobre la constante  $b$ , y que nos indican cual es el grado de anisotropía del conjunto, se denominan exponentes de Hurst. Las interfases son consideradas como fractales auto-afines aleatorios al efecto de construir un marco teórico donde estudiarlas de forma cuantitativa. En este caso, todas las direcciones del substrato son equivalentes, luego sus exponentes de Hurst son iguales a uno. Sin embargo, hay dos *direcciones* que no se pueden incluir en esa afirmación: la dirección de crecimiento y el tiempo. La dirección de crecimiento suele ser perpendicular al substrato, y su exponente de Hurst recibe el nombre de exponente de rugosidad  $\alpha$ . En referencia al tiempo, las interfases no son estructuras estáticas, los modelos de crecimiento, así como los experimentos, comienzan por una condición inicial particular, habitualmente  $h(x, t = 0) = 0$  para todos los puntos sobre el substrato  $x$ , y luego se van desarrollando hasta llegar a un estado estacionario (aunque normalmente no de equilibrio). El exponente de Hurst para el tiempo es conocido como exponente dinámico  $z$ .

### Escalado dinámico

La invariancia de escala se hace patente en la forma funcional que tiene los estimadores aplicados a cualquier fractal (auto-afín o auto-similar), su dependencia con la distancia o el tiempo se suele expresar mediante leyes de potencias. Éste es el caso, por ejemplo, de la anchura  $w(t, l)$ . Como acaba de ser explicado, las interfases suelen comenzar desde una condición inicial plana,  $w(t = 0, l) = 0$ . Más tarde, el frente comienza a desarrollarse y la interfase se hace rugosa, su anchura crece en el tiempo de la siguiente manera  $w(t, l) \sim t^\beta$ . Mientras la anchura crece, la posición de los sitios se va correlacionando con la de sus vecinos. Esas correlaciones terminan para una cierta distancia de correlación  $\xi$ , que es la única escala característica del sistema, y que crece en el tiempo como  $\xi \sim t^{1/z}$ . Finalmente, debido a que la escala  $l$  a la que estamos observando el sistema no es infinita, cuando la distancia de correlación llega a igualarla,  $\xi(t_\times(l)) = l$ , la evolución del sistema llega a un estado estacionario (saturación), en el que la anchura no crece más. El tiempo de saturación depende de la escala y se comporta como  $t_\times(l) \sim l^z$ . En la saturación, el sistema es un fractal auto-afín hasta la escala  $l$ , la anchura va con la escala como  $w(l, t > t_{sat}) \sim l^\alpha$ . Estos dos regímenes para la anchura pueden ser unidos en una sólo expresión conocida

como escalado dinámico,

$$w(t, l) = t^\beta f(l/\xi) = t^\beta f(l/t^z). \quad (\text{B.1})$$

La función  $f(u)$  es una función de escalado, que es constante para los valores pequeños de su argumento,  $u \ll 1$ , y que va como  $f(u) \sim u^\alpha$  cuando  $u$  es grande. De la expresión anterior también se puede deducir la relación de escalado (entre exponentes)  $z = \alpha/\beta$ , que ha de cumplirse por auto-consistencia.

Igual que sucede con la anchura, se pueden definir un escalado dinámico para otra serie de funciones. Si la interfase se puede escribir como una función  $h(x, t)$ , que representa la altura del frente sobre cada posición en el substrato  $x$  en un tiempo  $t$ , la correlación altura-altura se define como:  $G(t, l) = (1/L) \sum_x [h(x+l, t) - h(x, t)]^2$ . El escalado de esta función es similar al del cuadrado de la anchura  $G(t, l) \sim w^2(t, l) \sim t^{2\beta} f^2(t/l^z)$ . Por último, otra de las funciones importantes de la interfase es el espectro de potencias,  $S(k, t)$ . Dicha función se define como la transformada de Fourier de la función de correlación  $C(t, l) = w^2(t, l) - (1/2) G(t, l)$ ,  $S(k, t) = (2\pi)^{-d/2} \int dl C(l, t) \exp(ikl)$ . Realizando esa transformación de Fourier, se encuentra que el escalado de  $S(k, t)$  es

$$S(k, t) = \frac{1}{k^{(2\alpha+d)}} s(k t^{1/z}), \quad (\text{B.2})$$

donde  $d$  es la dimensión del substrato, y la función  $s(u)$  se comporta como una constante para  $u \gg 1$ , y va como  $s(u) \sim u^{2\alpha+d}$  en el límite  $u \ll 1$ .

El escalado dinámico mencionado en este apartado se corresponde al tipo de escalado más sencillo, al que se le conoce con el nombre de sus descubridores *Family-Vicsek* (o FV). Existen otros tipos de escalado dinámico, aunque su descripción quedará para la sección siguiente, ya que una parte importante del trabajo de esta tesis se realizó sobre este tema. El capítulo tercero, por ejemplo, está al completo dedicado a esta cuestión.

### Modelos discretos de crecimiento

Los modelos discretos de crecimiento son algoritmos para ordenador basados en el método de Montecarlo. Sus reglas de crecimiento son adaptaciones al computador de los fenómenos físicos más importantes que se sabe tienen lugar en el crecimiento experimental. Por ejemplo, la descripción del crecimiento epitaxial permite implementar fácilmente el comportamiento de las partículas en el caso  $T = 0$ . Bastaría con depositar al azar cada partícula,

y considerar que se establecen en el primer punto de llegada. Este modelo se denomina crecimiento aleatorio, y no ofrece mucho información porque la anchura de la interfase crece sin cesar con un ritmo  $w(t, l) \sim t^{1/2}$ . Además, no hay saturación porque las correlaciones no se extienden lateralmente.

Otro sencillo modelo, que puede ser considerado como una complicación del anterior, se consigue si la partícula escoge para establecerse la posición más baja entre el sitio  $i$  donde cayó y sus dos vecinos más próximos,  $i + 1$  e  $i - 1$ . Este modelo es conocido como crecimiento aleatorio con relajación superficial, los exponentes que se encuentran para él en dimensión (1+1) (una para el sustrato y otra para la dirección de crecimiento) son:  $\alpha = 1/2$ ,  $\beta = 1/4$  y  $z = 2$ .

Existen otros muchos modelos similares. Sin embargo, los resultados que se obtienen de ellos no siempre difieren entre sí. Como ya se mencionó previamente, el crecimiento de interfases es un fenómeno crítico, y por ello no es extraño que modelos diferentes tengan los mismos exponentes. El grupo de modelos con los mismos exponentes recibe el nombre de clase de universalidad. Para representar a cada una de esas clases se elige un modelo como paradigma. Siempre que es posible, se escoge para ese puesto a un modelo continuo, una ecuación de crecimiento.

### Modelos continuos

Las ecuaciones de crecimiento son ecuaciones de tipo Langevin (estocásticas) con las que se intenta representar una clase de universalidad. Su deducción se basa en las simetrías que se sabe tiene el modelo al que representan. El ejemplo más sencillo es la ecuación EW (*Edwards-Wilkinson*):

$$\frac{\partial h}{\partial t} = \nu \nabla^2 h + F + \eta(x, t). \quad (\text{B.3})$$

$\nu$  y  $F$  son constantes, la difusividad y la fuerza impulsora (o el flujo de partículas) respectivamente, mientras que  $\eta(x, t)$  es un ruido blanco de media cero y dispersión  $A$ , que habitualmente es Gaussiano. La ecuación de EW se basa sólo en la difusión entre sitios vecinos, éste es el modelo continuo correspondiente al crecimiento aleatorio con relajación superficial. Por lo tanto, sus exponentes son los mismo en dimensión (1+1),  $\alpha = 1/2$ ,  $\beta = 1/4$  y  $z = 2$ .

El siguiente modelo en complicación es la ecuación KPZ (*Kardar-Parisi-Zhang*). Esta ecuación tiene en cuenta el efecto que produce el que las

interfases crezcan en la dirección localmente normal al frente. Este efecto, en el orden más bajo de un desarrollo en  $|\nabla h|$ , introduce un término no lineal en la ecuación EW,

$$\frac{\partial h}{\partial t} = \nu \nabla^2 h + \lambda (\nabla h)^2 + F + \eta(x, t). \quad (\text{B.4})$$

Los exponentes de esta nueva universalidad son  $\alpha = 1/2$ ,  $\beta = 1/3$  y  $z = 3/2$  en dimensión (1+1).

Para los fenómenos de crecimiento epitaxial se propusieron otras dos ecuaciones, la MH (*Mullins-Herring*) y la LDV (*Lai-Das Sarma-Villain*). Estas ecuaciones tratan de incorporar el comportamiento de los átomos mencionado en el apartado anterior para este tipo de crecimiento, es decir el hecho de que tiendan a establecerse en los lugares con un mayor número de vecinos (con una mayor curvatura). La ecuación LDV es

$$\frac{\partial h}{\partial t} = -K \nabla^4 h + \lambda_2 \nabla^2 (\nabla h)^2 + F + \eta(x, t). \quad (\text{B.5})$$

Los exponentes para ella en una sólo dimensión (en (1+1)) son  $\alpha = 1$ ,  $\beta = 1/3$  y  $z = 3$ . La ecuación de Mullins-Herring se recupera de la LDV para el caso en que  $\lambda_2 = 0$ , sus exponentes en una dimensión son  $\alpha = 3/2$ ,  $\beta = 3/8$  y  $z = 4$ . El exponente de rugosidad para este último modelo es mayor que la unidad, esta situación dará lugar a que el escalado de este modelo no se ajuste al caso clásico de FV.

### Desorden congelado

Las ecuaciones mencionadas hasta ahora tiene un desorden de tipo térmico, que varía en el tiempo para cada posición. Sin embargo, al describir los experimentos con frentes de fluidos, se explico como el desorden estaba formado por un conjunto de impurezas colocadas entre las dos placas transparentes. Dichas impurezas, que podían ser por ejemplo pequeñas bolas de diversos tamaños, no cambian de posición durante la inyección del fluido en el espacio entre placas. La diferencia entre los exponentes encontrados en los experimentos y los obtenidos por los modelos con desorden térmico, llevó a proponer que el desorden congelado (en el tiempo) podía tener una importante influencia en la clase de universalidad del modelo.

Cuando el término  $\eta(x, t)$  de las ecuaciones con ruido térmico se sustituye por otro del tipo  $\eta_q(x, h)$ , donde  $\eta_q$  tiene las mismas propiedades que

$\eta$  (blanco de media cero y dispersión  $A_q$ ) pero depende sólo de la posición espacial de la interfase, se encuentra que la universalidad no es lo único que cambia. La fuerza impulsora  $F$ , que no ha tenido hasta el momento la menor importancia (ya que una simple transformación de Galileo la hace desaparecer de las ecuaciones), se convierte en un elemento esencial para determinar el comportamiento de las interfases. Por debajo de un cierto valor de  $F$ ,  $F_c$ , los frentes se acaban parando, por encima de ese valor,  $F > F_c$ , se mueven a una velocidad constante. En  $F = F_c$  hay una transición de fase de no equilibrio, que en la mayoría de los casos es continua. El parámetro de orden de la transición es la velocidad promedio de los frentes,  $v$  es cero a un lado de la transición y toma valores mayores que cero al otro. Si la transición es continua, la velocidad tiende a cero en las proximidades del punto crítico (por arriba) como  $v \sim |F - F_c|^\theta$ .

La transición de fase introduce también una nueva escala característica,  $\zeta$ , que es función de la distancia a la que se esté de  $F_c$ ,  $\zeta \sim |F - F_c|^{-\nu}$ . La escala  $\zeta$  representa el tamaño medio de los grupos de sitios que se encuentran en la fase contraria a la general, parados si la interfase se está moviendo. Por debajo de dicha escala los exponentes de los modelos son diferentes al de las universalidades con ruido térmico (EW, KPZ, MH o LDV). Se ha encontrado, además, que existen sólo dos clases de universalidad en el punto crítico, la QEW (EW con ruido congelado) con exponentes  $\alpha \approx 1.25$ ,  $\beta \approx 0.88$ ,  $\theta \approx 0.25$  y  $\nu \approx 1.33$  en dimensión (1+1), y la DPD con exponentes  $\alpha \approx 0.633$ ,  $\beta \approx 0.633$ ,  $\nu \approx 1.733$  y  $\theta \approx 0.636$ . El DPD es un modelo discreto de crecimiento propuesto inicialmente para dar cuenta de los resultados experimentales encontrados en algunos experimentos con fluidos (experimentos de mojado de papel). Sus reglas tiene dos versiones, la más sencilla consiste en colocar un ruido congelado, un número elegido al azar en el intervalo (0, 1), en cada una de las posiciones de una red cuadrada. La interfase es inicialmente plana. Se escoge al azar entre todos los sitios de la superficie un candidato para crecer,  $i$ . Si alguno de sus vecinos,  $h_{i\pm 1}$ , tiene una diferencia de altura de dos o más sitios con él,  $|h_i - h_{i\pm 1}| > 2$ , se hace avanzar a la interfase en ese sitio vecino, y se va de nuevo al principio del algoritmo (se busca otro sitio para crecer). En caso contrario, se compara el desorden sobre el sitio elegido,  $\eta_q(i, h_i)$ , con una fuerza impulsora  $F$  que se introduce como un parámetro externo de control. Si  $F > \eta_q(i, h_i)$ , entonces la interfase crece en  $i$ . Este modelo establece una clase de universalidad que esta relacionada con la percolación dirigida. Dicha clase tiene también relación con la ecuación QKPZ (KPZ con ruido congelado), este tema es tratado más profundamente

en el capítulo 4 de la tesis.

## B.2 Escalado anómalo

Esta sección es un resumen del capítulo tres, dicho capítulo está dedicado al estudio de los distintos tipos de escalado que pueden presentar las interfaces. Mi contribución a este tema fue la exploración de la que es la cuarta y última forma posible de escalado dinámico. El nombre que le dimos a esta última forma es escalado en facetas (facetado), ya que se da en interfaces con una forma geométrica muy peculiar, similar a las facetas de los cristales. Comencemos, sin embargo, contando como se originó el escalado anómalo, donde encaja esta nueva forma, y por qué pensamos que es la última posible.

### Introducción

Previamente (en la sección dedicada al escalado dinámico, en B.1.2) se ha mencionado como en el proceso de crecimiento de una interfase, la distancia de correlación crece en el tiempo como una ley de potencias,  $\xi \sim t^{1/z}$ . Esta característica es el único requisito indispensable en la teoría que presentamos. Es decir, podrían existir otras formas de escalado aparte de las cuatro que mencionaremos a continuación pero incumplen esa condición: tener una sola distancia de correlación, que crece en el tiempo como una ley de potencias.

Aclarado este punto, también se comentó en el mismo apartado como se puede proponer una forma sencilla para el escalado de la anchura de las interfaces  $w(t, l) = t^\beta f(t/l^z)$ , donde  $l$  es la escala de observación y  $f(u)$  es una función de escalado que es constante para valores pequeños de su argumento, y que va como  $f(u) \sim u^\alpha$  para  $u \gg 1$ . Al proponer este escalado dinámico para la anchura, se dijo que las interfaces no presentan ninguna escala característica. Esta afirmación es válida dentro de un cierto rango de escalas, porque, por supuesto, la invariancia de escala no se mantiene por encima del tamaño del sistema  $L$ . Sin embargo, en el caso del escalado FV, el tamaño del sistema se comporta como una escala más. El comportamiento de la anchura global (la de toda la interfase) es el mismo que el de la local cambiando  $l$  por  $L$ ,  $W(t, L) = t^\beta f(t/L^z)$ , la saturación de todo el sistema tiene lugar para  $t_\times(L) \sim L^z$  (cuando  $\xi = L$ ), y si se comparan sistemas con distintos tamaños en saturación, su anchura global va como  $W(t > t_{sat}, L) \sim L^\alpha$ .

Durante la década de los noventa, se descubrió que hay algunos sistemas que no se comportan de esa forma tan sencilla. Dos de ellos son, por ejemplo, las universalidades representadas por las ecuaciones MH y LDV. En estos sistemas, las anchuras global y local, tras la saturación de todo el sistema, continúan dependiendo de la escala con una forma funcional en ley de potencias, pero lo hacen con exponentes distintos,  $w(t > t_{sat}) \sim l^{\alpha_{loc}}$  y  $W(t > t_{sat}, L) \sim L^\alpha$ . Este hecho origina una diferenciación entre escalas globales y locales que hasta entonces no existía.

Otra de las características que presenta el nuevo escalado, está relacionada con el tiempo de saturación. El sistema completo sigue saturando para un tiempo  $t_\times(L) \sim L^z$ , sin embargo las escalas pequeñas ya no saturan para  $t_\times(l)$ . En su lugar, lo que sucede es que la anchura local (o las correlaciones altura-altura, o las pendientes  $\langle |\nabla h| \rangle$ ) continúan creciendo en el tiempo tras ese momento, pero con un exponente,  $\kappa$ , diferente de  $\beta$  y que está relacionado con  $\alpha$  y  $\alpha_{loc}$ ,  $\kappa = (\alpha - \alpha_{loc})/z$ .

### Escalado dinámico

La forma más general para el escalado dinámico habitualmente se propone en el espacio de Fourier, para el espectro de potencias. Ésto es así, porque con dicha función se puede incluir todos los casos en una única forma de escalado dinámico

$$S(k, t) = \frac{1}{k^{2\alpha+d}} s_A(k t^{1/z}). \quad (\text{B.6})$$

Esta expresión es la misma que para el escalado FV, la diferencia está en el comportamiento de la función de escalado  $s_A(u)$ :

$$s_A(u) \sim \begin{cases} u^{2\alpha+d} & \text{si } u \ll 1 \\ u^{2\theta} & \text{si } u \gg 1. \end{cases} \quad (\text{B.7})$$

El nuevo exponente  $\theta$  (no confundir con el exponente del mismo nombre usado en el caso del desorden congelado) puede ser escrito como  $\theta = \alpha - \alpha_s$ , donde  $\alpha$  es el exponente de rugosidad habitual y a  $\alpha_s$  se le conoce como exponente de rugosidad del espectro. La introducción de  $\alpha_s$  nos permite expresar el espectro de potencias como  $S(k, t) \sim t^{2\theta/z} / k^{(2\alpha_s+d)}$ , lo que significa que en la zona con argumentos de  $s_A(u)$  grandes el espectro todavía decae como una ley de potencias, aunque ahora con un exponente distinto,  $-(2\alpha_s + d)$ . Después de la saturación, esa última expresión se transforma en  $S(k, t > t_{sat}) \sim L^{2(\alpha-\alpha_s)} / k^{2\alpha_s+d}$ .

El escalado de las funciones del espacio directo se puede recuperar desde las expresiones anteriores para  $S(k, t)$ . La anchura global, por ejemplo, se obtiene mediante la integral

$$W^2(t, L) = \frac{1}{aL} \sum_k S(k, t) \approx \int_{2\pi/L}^{\pi/a} d\mathbf{k} S(k, t), \quad (\text{B.8})$$

que es simplemente una relación de Persival. Así mismo, la correlación altura-altura  $G(t, l)$ , que escala de la misma manera que el cuadrado de la anchura local, se obtiene mediante la expresión siguiente:

$$G(t, l) = \frac{2}{aL} \sum_k [1 - \cos(kl)] S(k, t) \approx \int_{2\pi/L}^{\pi/a} d\mathbf{k} [1 - \cos(kl)] S(k, t). \quad (\text{B.9})$$

El calcular estas integrales no siempre es una tarea fácil, los detalles del cálculo está en el apéndice A. El problema principal es que cuando se toma el límite termodinámico,  $L \rightarrow \infty$  y  $t \rightarrow \infty$ , algunas de ellas, dependiendo de cual sea el valor de  $\alpha_s$ , divergen. Los dos límites, el de tamaños y el de tiempos infinitos, no conmutan. Si se toma primero  $L \rightarrow \infty$  se llega al comportamiento del sistema en el tiempo previo a la saturación, mientras que si, al contrario, se considera primero  $t \rightarrow \infty$  lo que se obtiene es el escalado en saturación. Dependiendo de los valores de  $\alpha_s$  y  $\alpha$  hemos encontrado cuatro casos diferentes de escalado dinámico en el espacio directo:

$$\left\{ \begin{array}{l} \text{si } \alpha_s < 1 \Rightarrow \alpha_{loc} = \alpha_s \\ \text{si } \alpha_s > 1 \Rightarrow \alpha_{loc} = 1 \end{array} \right\} \left\{ \begin{array}{l} \alpha_s = \alpha \Rightarrow \text{Family-Vicsek} \\ \alpha_s \neq \alpha \Rightarrow \text{Anómalo intrínseco} \\ \alpha_s = \alpha \Rightarrow \text{Super-rugosidad} \\ \alpha_s \neq \alpha \Rightarrow \text{Facetado} \end{array} \right.$$

El exponente  $\alpha_{loc}$  se extrae del comportamiento de  $G(t, l)$  con la escala de observación  $l$  en saturación. El escalado de las funciones globales y locales en el espacio directo para cada uno de los casos mencionados en esta tabla se encuentran en las secciones 3.3.1, 3.3.2, 3.3.3 y 3.3.4 del capítulo 3. Dado que ésto pretende ser un resumen, no voy a comentar todos los casos uno a uno, aunque debido a que se debe explicitar las principales novedades que esta tesis introduce en sus capítulos, sí que se incluyen a continuación algunos comentarios sobre el escalado facetado.

### Facetas

Este tipo de escalado lo encontramos en un modelo discreto que se supone representa el punto crítico de la ecuación QKPZ en la región de parámetros  $\lambda F < 0$ . Dicho modelo fue inicialmente propuesto por Kim Sneppen en 1992. Consta de una red cuadrada donde, en cada sitio, se define un ruido en el intervalo  $(0, 1)$ . El algoritmo escoge para crecer el sitio  $i$ , con el menor valor del ruido posible que cumpla la siguiente condición  $|h_i + 1 - h_{i\pm 1}| < 2$ . Es decir, que una vez que la interfase haya crecido, se sigan manteniendo las pendientes en el rango de valores  $(0, \pm 1)$ . La interfase originalmente es plana, y como es usual las condiciones de contorno son periódicas. El aspecto de las interfases generadas por este modelos se puede ver en la Figura 3.10. Cada interfase esta formada por un conjunto de *triángulos* (facetas) de distintos tamaños distribuidas al azar.

Si dichas facetas se correspondiesen con un solo triángulo (o con una serie de triángulos con el mismo tamaño) de base  $L$ , se puede obtener analíticamente como se comportan las distintas funciones de la interfase. Por ejemplo, el espectro de potencia debe ir como  $S(k) \sim L^{-1}/k^4$ , que cuando se compara con el espectro de potencias propuesto para el escalado anómalo en saturación,  $S(k, t > t_{sat}) \sim L^{2(\alpha-\alpha_s)}/k^{2(\alpha_s+1)}$ , implica que, para este caso,  $\alpha_s = 3/2$  y  $\alpha = 1$ , mientras que de la forma de la correlación altura-altura se llega a que  $\alpha_{loc} = 1$ . Por tanto, incluso este sencillo esquema teórico muestra escalado de tipo facetado. En el caso del modelo de Sneppen el escalado es dinámico, a parte de  $\alpha_s > \alpha = 1$ , existe también un exponente dinámico  $z$ . Además, los tamaños de esas facetas no son regulares, lo que hace que sus exponentes de rugosidad sean ligeramente diferentes de los encontrados con un solo triángulo:  $\alpha_s \approx 1.35$ ,  $\alpha = 1$  y  $z \approx 1$ .

Las funciones en el espacio real para las interfases con escalado de tipo facetado se comportan en general como

$$W(t, L) \sim \begin{cases} t^{\alpha/z} & \text{si } t \ll t_{\times} \\ L^{\alpha} & \text{si } t \gg t_{\times} \end{cases} \quad (\text{B.10})$$

para la anchura global, y

$$G(t, l, L) \sim \begin{cases} t^{2\alpha/z} & \text{si } t \ll t_{\times}(l) \\ t^{2(\alpha-1)/z} l^2 & \text{si } t_{\times}(l) < t < t_{\times}(L) \\ l^2 L^{2(\alpha-1)} & \text{si } t \gg t_{\times}(L) \end{cases} \quad (\text{B.11})$$

para la correlación altura-altura. De esta última expresión se deduce que  $\alpha_{loc} = 1$ .

## Conclusiones

En este trabajo se ha estudiado intensivamente los posibles escalado que las interfases pueden presentar. El único requisito para entrar dentro de estas consideraciones, es que las correlaciones se expandan por el sistema al ritmo dado por una única distancia de correlación, que crece como  $\xi = t^{1/z}$ . Hemos encontrado que, bajo ese supuesto, el escalado debe ir regido por una forma determinada del espectro (la del escalado anómalo). De dicha forma funcional general se pueden deducir, además del caso *clásico* del escalado FV, otros tres casos: super-rugosidad, anómalo intrínseco y facetado. En todos ellos, para determinar de forma clara la universalidad de una interfase es necesario conocer tres exponentes independientes (al contrario que en el FV que sólo eran dos): la rugosidad global  $\alpha$ , la rugosidad del espectro  $\alpha_s$  y el exponente dinámico  $z$ .

## B.3 Crecimiento debido a no-linealidades

El capítulo tres de la tesis, que es sobre lo que versa esta sección, esta dedicado a la transición de fase que aparece en los modelos con desorden congelado. La idea es intentar entender que es lo que esta sucediendo con la ecuación QKPZ, que como ya ha sido explicado (sección B.1.2, desorden congelado) no proporciona un modelo claro para una clase de universalidad en el punto crítico, al contrario que la QEW.

### Introducción

La ecuación QKPZ fue propuesta como un modelo para el crecimiento de interfases en medios desordenados. Es similar a la ecuación KPZ, pero el desorden térmico es sustituido por un término de desorden congelado.

$$\frac{\partial h}{\partial t} = \nu \nabla^2 h + \lambda (\nabla h)^2 + F + \eta(x, h). \quad (\text{B.12})$$

$\nu$ ,  $\lambda$  y  $F$  son parámetros externos, y  $\eta(x, h)$  es un ruido blanco, de media cero, habitualmente Gaussiano y con una dispersión  $A_q$ .

En el caso térmico, la no-linealidad de la ecuación KPZ se incluyó para tener en cuenta el crecimiento lateral de las interfases. Este término surge de la proyección de un crecimiento normal a la interfase en cada punto sobre el eje paralelo a la velocidad promedio. La constante  $\lambda$  debe ser, en tal caso,

proporcional a la velocidad. Se ha especulado bastante sobre cual puede ser el origen de ese término en el caso de que la velocidad de la interfase sea muy pequeña debido al desorden congelado, o incluso nula en el caso de la transición en  $F_c$ . Se sabe que existe ese término porque a los modelos discretos con ruido congelado, como en DPD, se les ha aplicado la prueba de la pendiente. Dicha prueba consiste en introducir una pendiente promedio en el modelo,  $h \rightarrow h + mx$ , si la ecuación efectiva que representa a ese modelo es del tipo QKPZ, la velocidad promedio del frente ha de crecer con la pendiente como  $v \sim v_o + \lambda_{ef} m^2$ . Se ha encontrado que los modelos con ruido congelado pueden ser clasificados en dos grupos según sus resultados en esta prueba: por un lado están aquellos para los que el  $\lambda_{ef}$  tiende a cero según la transición se acerca, a éstos se les considera en la universalidad de la ecuación QEW. Por otro lado, hay otros, incluido el DPD, para los cuales  $\lambda_{ef}$  diverge en la transición. No obstante, más tarde se demostró que la interpretación de ese método estaba equivocada, y que sólo existen dos posibilidades: o  $\lambda_{ef} \rightarrow 0$  cuando se acerca la transición o permanece con un valor finito y constante.

La liberación de las interfases atrapadas por el desorden, se suele llevar a cabo, como ya se comentó, mediante el ajuste de la fuerza impulsora externa  $F$ . La primera cuestión que pretendemos responder en este capítulo es: ¿Se puede realizar la transición variando algún otro parámetro de la ecuación QKPZ?. Si toma un promedio espacial sobre esa ecuación, sólo hay tres términos que sobreviven  $\langle \partial_t h \rangle \approx \lambda \langle (\nabla h)^2 \rangle + F + \langle \eta \rangle$ , por tanto, cuando  $F = 0$ , el único término que se opone al ruido, que es quien deja a la interfase parada, es la no linealidad. Para estudiar que sucede cuando se varía, hemos empleado un esquema de Euler para discretizar la ecuación QKPZ, los resultados que encontramos se describen en la siguiente sección.

### Resultados de la simulación

El primer resultado es el que puede verse en la Figura 4.1, la transición puede lograrse cambiando la constante del término no lineal aunque  $F = 0$ . Una vez adquirida esta certeza, el siguiente paso es caracterizar la transición, investigar a cual de las dos clases de universalidad que se dan en ese punto crítico pertenece, o incluso si es una nueva. Esto se hace en la Figura 4.2, donde se representa  $v$  frente al parámetro de control  $\lambda$ . Allí, se ve que la transición es continua, y se estima el valor del exponente de la velocidad,  $v \sim |\lambda - \lambda_c|^\theta$ , que vale  $\theta = 0.635 \pm 0.007$ . Desafortunadamente, el exponente  $\nu$ , que nos permitiría clasificar con seguridad la transición, no puede

ser medido directamente. Aunque existe otro medio; como se comentó en la sección dedicada al desorden congelado, cerca de la transición hay una nueva distancia de correlación  $\zeta$ . El exponente  $\nu$  se podría haber medido si hubiésemos podido estimar  $\zeta$  directamente, cosa que no es sencilla. Lo que si lo es, es estudiar sus efectos sobre otras funciones, por ejemplo sobre la anchura global y la correlación. Para escalas menores que  $\zeta$ , o tiempos anteriores a  $\zeta^z$ , esas cantidades muestran unos ciertos exponentes, y para escalas mayores, o  $t > \zeta^z$ , pasan a los clásicos de KPZ o EW. Mediante esos exponentes en las escalas pequeñas, que están relacionados con  $\nu$ , se puede saber en que universalidad está la transición. El resultado de este análisis, que se muestra en las Figuras 4.3 y 4.4, se corresponde con que esta transición pertenezca a la universalidad del modelo discreto DPD. Ésto mismo se encuentra también para toda la región con  $\lambda F > 0$  cuando la transición se realiza variando  $F$ . Lo que implica que la transiciones obtenidas variando  $F$  y  $\lambda$  son equivalentes.

Si la fase dentro de una transición ha de ser especificada por dos parámetros, en lugar de uno, lo que se tiene es un diagrama de fases en dos dimensiones. Para intentar explorarlo, realizamos una serie de simulaciones estableciendo para cada una de ellas un determinado valor de  $\lambda < \lambda_c$ , y buscando para cada caso el valor de  $F_c$ . El resultado es el diagrama de la Figura 4.5. De una forma completamente fenomenológica encontramos que un buen ajuste para esa curva se podía obtener con una expresión del tipo

$$\left(\frac{\lambda_c}{b_1}\right)^{2/3} + \left(\frac{F_c}{b_2}\right)^{2/3} = 1, \quad (\text{B.13})$$

donde  $b_1 = 4.31 \pm 0.04$  y  $b_2 = 0.81 \pm 0.03$  son constantes. Por supuesto, ésta sólo es una aproximación para los cuadrantes donde  $\lambda F > 0$ , aunque la curva continua mas allá de esas regiones. Con estos resultados, y los ya conocidos de la literatura, se puede construir el diagrama de fases de la Figura 4.6 para la ecuación QKPZ.

## Conclusiones

Hemos estudiado la ecuación QKPZ y su diagrama de fases. Hemos encontrado que la transición para liberar las interfases del ruido congelado puede obtenerse variando la importancia relativa del término no lineal, además de cambiando la fuerza impulsora  $F$ . Dicha transición ha sido caracterizada, y hemos encontrado que pertenece a la universalidad del DPD. También,

hemos establecido la equivalencia de la variación de  $F$  y  $\lambda$  a la hora de realizar la transición, y, finalmente, hemos propuesto un posible escenario para un diagrama de fases para esta ecuación.

Estos resultados son importantes, tanto desde el punto de vista teórico como desde el experimental. Desde el lado de la teoría, es necesario encontrar una explicación para todo el diagrama de fases, que incluya al único resultado analítico hasta la fecha, para la ecuación QEW, como un caso particular. Desde el punto de vista experimental, se puede considerar como un desafío el encontrar frentes que se muevan variando las propiedades del desorden o de sus superficies en lugar de mediante fuerzas impulsoras externas.

## B.4 Experimentos de fractura

Esta sección da cuenta de los experimentos descritos en el capítulo quinto de la tesis sobre frentes de fractura. Estos experimentos tuvieron lugar en el otoño pasado durante una estancia de varios meses en la universidad de Oslo, y son el resultado de la colaboración con Jean Schmittbuhl (École Normale Supérieure de París) y con Knut Jørgen Måløy (Universidad de Oslo).

### Introducción

Como se describió en la sección B.1.1, la fractura en los sólidos puede mostrar dos comportamientos distintos dependiendo de la velocidad de los frentes. En la modalidad rápida, se generan nuevos frentes partiendo de uno principal, la estructura global tienen una forma intrincada y muy ramificada. Por el contrario, cuando la velocidad es baja, sólo aparece un único frente de fractura. Es a esta segunda modalidad a la que pertenecen los experimentos descritos a continuación. En aquella sección, se comentó también como los frentes de fractura son curvas que se encuentran en el interior de un espacio tridimensional, y que, por tanto, se pueden estudiar la distintas proyecciones de dichos frentes. La proyección más sencilla de estudiar es la que es perpendicular a la velocidad media del frente, este ha sido hasta ahora el caso más estudiado. Para él se encontró que el exponente de rugosidad en la dirección perpendicular (a la velocidad media) valía para una gran variedad de materiales 0.8. Este hecho llevo a postular la existencia de una clase de universalidad para los frentes de fractura. Sin embargo, un tiempo más tarde se demostró que, en realidad, ese exponente es local, y que el exponente global

depende del material en el que tenga lugar la fractura. Siendo el escalado de la dirección perpendicular, por tanto, de tipo anómalo intrínseco.

Este tipo de escalado en la fractura tiene importantes consecuencias. Por ejemplo, el ritmo de gasto de energía en el frente de fractura cuando éste avanza, sigue una ley conocida desde hace tiempo como criterio de Griffith. Dicho criterio establece que cuando el frente comienza a moverse, el gasto energético representado por la función de Griffith  $G$  crece, finalmente el frente adquiere una cierta velocidad y el gasto de energía llega a un estado estacionario. Si el escalado de la interfase de fractura fuese de tipo FV, la función  $G$  en el estado estacionario no debería depender del tamaño total del sólido donde se produce la fractura. Sin embargo, se ha encontrado de forma experimental que la función de Griffith en el estacionario sí depende del tamaño del bloque que se está rompiendo. Esta dependencia sólo puede ser explicada si el escalado de la interfase es anómalo, como por otro lado ha sido directamente comprobado.

### Descripción del experimento

Se puede encontrar un esquema del experimento en la Figura 5.2. La muestra a fracturar se compone de dos placas de metacrilato, inicialmente transparente. La placa más gruesa tiene unas dimensiones de  $32 \times 14 \times 1$  cm, mientras que la otra tiene 34 cm de largo, 0.4 de grosor y una anchura variable. A continuación, se somete a una cara de cada placa a desgaste mediante un chorro de arena, con este proceso se consiguen dos cosas que las caras que eran planas adquieran cierta rugosidad y que adquieran un cierto color blanco. La transparencia se pierde porque la luz se difunde debido a la rugosidad de esa cara. Una vez que se les ha aplicado el desgaste, se las introduce juntas (con las dos caras desgastadas en contacto) en una prensa que mantiene una presión constante entre las dos placas, que a su vez se coloca en el interior de un horno de cerámica. En el siguiente paso, se inicia entonces un proceso de calentamiento cuidadosamente controlado hasta la temperatura de fusión del metacrilato, 205 °C. Esa temperatura se mantiene durante 30 min., luego se inicia un lento enfriamiento hasta la temperatura ambiente. La muestra recupera la transparencia tras el proceso de calentamiento.

Para el experimento, la muestra así preparada se coloca sobre una plataforma a la que está firmemente sujeta. Sobre la muestra se coloca una cámara CCD y un micrófono. La placa más larga (y menos gruesa) está conectada a una placa metálica sobre la que hay una resistencia eléctrica que es capaz de

medir la curvatura de dicha placa. Esa resistencia se coloca con la idea de determinar cual es la fuerza que se hace sobre la placa inferior de la muestra. Finalmente, la placa metálica está atornillada a una prensa que tiene un motor continuo que la hace moverse en la dirección vertical. Cuando la prensa comienza a moverse hacia abajo, la placa más delgada comienza a despegarse de la gruesa. La zona por la que ha pasado la fractura vuelve a perder la transparencia, facilitando así el contraste entre ambas. Los frentes de fractura son grabados por la cámara, mientras que el ruido que hacen al avanzar queda registrado por un micrófono y la fuerza que se hace sobre la muestra (y sus fluctuaciones) es detectada por la resistencia.

## Resultados

El micrófono era la primera vez que se empleaba, luego lo que pretendíamos con él era determinar la relación señal-ruido que se puede lograr con ese tipo de instrumentos. Como vemos en la Figura 5.3, es posible detectar el ruido de la fractura, aunque el micrófono no tiene resolución suficiente para distinguir estructura en la señal. Desafortunadamente, cuando se pretende que el resto de instrumentos funcionen al mismo tiempo, el ruido que originan acaba produciendo una muy mala relación señal-ruido. En futuros trabajos, será necesario utilizar otro tipo de micrófonos para frecuencias mayores (ultrasonidos) y mejor aislados.

Con la resistencia variable, por otra parte, obtuvimos unas series de evolución temporal muy buenas. Puede verse alguna de ellas en la Figura 5.5. Con este instrumento se pudo incluso distinguir entre distintos regímenes dentro de esa evolución temporal, Figura 5.6, aunque no pudimos medir las fluctuaciones en la fuerza debido a una falta de sensibilidad en la resistencia.

Por otro lado, con la cámara pudimos grabar una buena cantidad de frentes sobre los que aplicamos diversos métodos de análisis. Se determinó la altura media y velocidad de los frentes, su anchura local, la dependencia de sus correlaciones altura-altura con la escala espacial y temporal, y también su espectro de potencias. Los principales resultados de este análisis fueron dos: el primero se obtuvo comparando la anchura local para placas de distinta anchura global (como ya se comentó, la anchura de las placas menos gruesas es variable). Con ello se encontró que la anchura local para una escala fija no depende del tamaño del sistema, o lo que es lo mismo que el escalado para la dirección paralela (a la velocidad media) es de tipo FV para los frentes de fractura. Por otro lado, además del tipo de escalado, medimos también los

valores de los exponentes:  $\alpha_{\parallel} = 0.54 \pm 0.07$  y  $\beta_{\parallel} = 0.54 \pm 0.06$ .

Finalmente, también estudiamos las avalanchas con las que se mueve la fractura. Los frentes de fractura no se mueven de forma continua, sino que cuando la fuerza sobre la placa menos gruesa supera cierto umbral, que depende del lugar, el frente avanza en esa zona. Para definir las avalanchas lo que hicimos fue comparar imágenes consecutivas obtenidas con la cámara CCD. El tiempo entre dos de esas imágenes es de unos 8 ms. Tomamos como velocidad instantánea y local  $v(x, t)$  a la diferencia entre los dos frentes en la normal al más antiguo de los dos. Luego, estudiamos tanto las correlaciones temporales como las espaciales de dicha velocidad instantánea. El resultado fue que las avalanchas no parecen tener una estructura en la dirección temporal, tienen un tiempo de duración característico muy pequeño. Sobre la correlación espacial podemos decir algo más, como se puede ver en la Figura 5.15, el espectro de potencias (espacial) para la velocidad presenta una cola larga. Incluso se encuentra un decaimiento en ley de potencias  $S \sim 1/k$  para las escalas pequeñas.

## Conclusiones

Hemos realizado un experimento de fractura en el cual hemos estudiado los frentes en la dirección paralela a su velocidad media. Hemos determinado los exponentes de dichos frentes,  $\alpha_{\parallel} = 0.54 \pm 0.07$  y  $\beta_{\parallel} = 0.54 \pm 0.06$ , lo cual no es una gran novedad porque ya se han observado en un par de trabajos previos. Sin embargo, el tipo de escalado no había sido considerado previamente. Se pensaba que podía ser anómalo, ya que el de la dirección perpendicular lo es. Contradiendo esta última idea, hemos encontrado un escalado de tipo Family-Vicsek. Este hallazgo confirma también los resultados obtenidos para la medida de la función de Griffith en el estacionario, ya que la dependencia de  $G$  con el tamaño del bloque a romper debería ser  $G \sim L^{(\alpha_{\perp} - \alpha_{\perp loc}) - (\alpha_{\parallel} - \alpha_{\parallel loc})}$  en caso de que el escalado en la dirección paralela fuese también anómalo, sin embargo los resultados obtenidos experimentalmente para esa función se ajustan más bien a  $G \sim L^{\alpha_{\perp} - \alpha_{\perp loc}}$ , lo que implica que  $\alpha_{\parallel} = \alpha_{\parallel loc}$ .

## B.5 Frentes de fluidos

Este último apartado se corresponde al capítulo seis. En ese capítulo se describen unos experimentos con frentes de fluidos que se llevaron a cabo

en los laboratorios de la Universidad de Barcelona. Las personas que hemos colaborado en este trabajo son Jordi Soriano, Aurora Hernández Machado y Jordi Ortín, de la Universidad de Barcelona, y Miguel Ángel Rodríguez y yo mismo, de la UC-CSIC.

## Introducción

Los experimentos con interfases de fluidos suelen realizarse en el interior de cámaras con paredes transparentes y que han sido previamente rellenas con materiales de diversos tipos. Estas impurezas, que pueden estar compuestas por bolas de diversos tamaños, arenas o arcillas, pistas de cobre, ... etc, tienen como fin el crear un medio desordenado a través del cual el fluido pueda moverse. Cuando el líquido se encuentra con una zona estrecha (un poro) de ese medio, su velocidad se ve incrementada por las fuerzas capilares, hecho que lleva a la creación de un frente rugoso.

En la literatura, hay una buena cantidad de experimentos que se ocupan del estudio de los frentes de fluidos. Se puede ver un resumen en la tabla de la página 15. Sus resultados, en lo referente a los exponentes medidos, son dispares. Esta diversidad puede ser entendida por las diferentes modalidades de operación que estos experimentos poseen. El fluido puede ser impulsado a presión constante, en cuyo caso su velocidad media va a decrecer con el tiempo, debido a la viscosidad, hasta pararse; o puede ser inyectado a volumen constante, con lo que su velocidad media se mantiene, aunque la presión en el frente oscile. Los exponentes para ambos tipos de frentes no tiene por qué ser los mismos, como tampoco lo son en los modelos con desorden congelado en las proximidades del punto crítico. Algunas de las propuestas teóricas para explicar estos experimentos apuntan precisamente en dirección a esos modelos. El DPD fue propuesto inicialmente para explicar experimentos de mojado de papel, en los que el fluido ascendía a presión constante por una hoja de papel hasta que se detenía a una cierta altura. Aunque, este tipo de modelos locales están siendo ahora muy cuestionados debido a que la conservación de la masa impone una condición global que no se puede incluir en ellos.

Nuestros experimentos tratan con una configuración mucho más sencilla. No pretendemos estudiar los frentes en un medio completamente heterogéneo, sino en uno con desorden columnar. La situación es similar a la que se da cuando el fluido asciende por un solo tubo capilar, sólo que ahora existe un conjunto de capilares en contacto unos con otros. Con esa configuración

esperamos simplificar el problema, y hacerlo más sencillamente abordable desde el punto de vista teórico.

### Descripción del experimento

La cámara del experimento se compone de dos placas de cristal paralelas de  $19 \times 55 \text{ cm}^2$ , que están separadas por una distancia que puede variar para distintos experimentos, y que es utilizada como un parámetro de control externo. Entre ellas se coloca una base para circuitos electrónicos. La distancia entre la base y la placa superior es el parámetro de control  $b$ . Sobre la placa para circuitos se distribuyen al azar pistas de cobre, cada una de las cuales tienen un grosor de 0.06 mm, una anchura de 1.5 mm y que recorren, a lo largo, toda la cámara. El nivel de ocupación de la cámara por las pistas se fija en el 35 %. Seguidamente, se inyecta a flujo constante un aceite de silicona con una densidad de  $\rho = 998 \text{ kg/m}^3$ , una viscosidad  $\nu = 50 \text{ mm}^2/\text{s}$  y una tensión superficial para aceite-aire de  $\sigma = 20.7 \text{ mN/m}$  en condiciones estándar. La celda de Hele-Shaw se encuentra sobre una mesa. En la vertical al experimento se sitúa cámara CCD, con la que se graban los frentes.

### Análisis de los resultados experimentales

Los frentes grabados por la cámara CCD son luego cuidadosamente analizados. La primera magnitud considerada fue la velocidad. La velocidad media de los frentes es constante, como corresponde a un experimento realizado a un ritmo constante de inyección de fluido, sin embargo presenta importantes particularidades locales. Las fuerzas capilares aumentan la velocidad del aceite sobre las pistas de cobre, empiezan a desarrollarse así una serie de columnas (*dedos*) que inicialmente crecen de forma independiente. Pasado un tiempo, la tensión superficial del fluido retarda el crecimiento de esas columnas (que coinciden con las pistas de cobre) y acelera el crecimiento en el resto de zonas. El estado final es una velocidad constante para todo el frente  $v$ , que se corresponde con la velocidad producida por la inyección del fluido. Un seguimiento detallado de la evolución de la velocidad del fluido sobre las pistas  $v_+$ , y sobre el resto de zonas  $v_-$ , puede encontrarse en la Figura 6.3. De estos datos se deduce que la velocidad local va como  $v_{\pm} = v \pm a t^{1/2}$ .

En este experimento los frentes empiezan desde una configuración casi plana (en la parte inferior de la cámara hay una pista perpendicular al resto, y que hace planas las interfases), lo que permite estudiar la evolución de

la anchura en el tiempo. En la Figura 6.4 se representa la evolución de la anchura local promediada sobre diversas realizaciones del desorden. Si el escalado de las interfases fuese FV, la anchura debería saturar antes para las escalas más pequeñas. Para saber cual es el tipo de escalado, hemos representado en esa figura dos escalas diferentes, una de  $l_2 = 18$  cm casi tan grande como todo el sistema (19 cm), y otra tan pequeña como nos permitía la resolución,  $l_1 = 1.4$  mm. La escala pequeña no satura, al menos no hasta que lo hace la grande, sino que muestra un crecimiento en ley de potencias con el tiempo con un exponente  $\kappa = 0.26 \pm 0.03$ . La escala más grande crece a su vez como  $\sim t^\beta$ , con  $\beta = 0.52 \pm 0.02$ . El que exista un exponente  $\kappa \neq 0$ , implica que el escalado es de tipo anómalo, y además  $\kappa = (\alpha - \alpha_{loc})/z$ .

Para poder encontrar el valor de uno de esos exponentes de rugosidad utilizamos las correlaciones altura-altura. La evolución temporal de esa magnitud, además de su comportamiento para diferentes escalas en saturación, se puede ver en la Figura 6.5. En esa gráfica, encontramos que este sistema tiene multi-escalado, sus exponentes son diferentes dependiendo del momento estadístico de sus interfases que se considere. Este es un hecho importante porque puede estar relacionado con el escalado anómalo. El exponente de rugosidad local que medimos (para el momento de segundo orden) es  $\alpha_{loc} \approx 0.6$ .

Como última comprobación del escalado, y de los exponentes medidos, estudiamos la evolución del espectro de potencias de los frentes. Se puede encontrar una serie de estos espectros en la Figura 6.6. Utilizando los exponentes  $\alpha = 1$  y  $z = 2$  conseguimos un buen colapso de los datos experimentales para el espectro.

Una vez caracterizados los frentes para un determinado valor de la separación entre placas, podemos estudiar que sucede cuando se varia  $b$ . El origen del escalado anómalo reside en la diferencia de velocidades iniciales que el fluido tiene sobre las zonas con pistas de cobre y en las que no las tienen. Dicha diferencia provoca, además de que crezca la anchura del frente, que se incremente también la pendiente promedio de la interfase,  $\langle |\nabla h| \rangle \sim t^\kappa$ . Este comportamiento continua hasta que la velocidad de todo el frente alcanza la velocidad nominal  $v$ , que es fijada por el ritmo de inyección, y al mismo tiempo llega a la saturación. Como ya se comentó en la sección B.2, el que la anchura de las escalas pequeñas ( $\langle |\nabla h| \rangle$  es en realidad la dispersión para una escala  $l \rightarrow 0$ ) sature al mismo tiempo que las grandes (la global) es una de las propiedades fundamentales del escalado anómalo. Con el parámetro  $b$  lo que se controla es la velocidad inicial que tiene el fluido sobre las zonas con y sin pistas  $v_{o,\pm}$  ( $v_M = v_{o,+}$ ). El escalado anómalo aparece entonces cuando

$v_{o,+} > v$ , por tanto variando  $b$  se puede conseguir que  $v_{o,+} = v$  lo que lleva a la desaparición de ese tipo de escalado. Con los datos obtenidos en varios experimentos donde hemos estudiado el escalado de los frentes para varios valores de  $b$  y  $v$ , hemos realizado el diagrama de fases de la Figura 6.7.

### Un modelo teórico

Con los resultados mencionados en la sección previa hemos tratado de desarrollar un primer marco teórico. Hemos buscado la máxima sencillez posible, por tanto, el modelo es local. La interacción entre columnas consecutivas, aquellas con pistas de cobre y sin ellas, se introduce mediante difusión. El término de ruido se toma de tal forma que reproduzca lo más posible el desorden del experimento: es un ruido dicotómico, toma sólo dos posibles valores  $+1$  y  $-1$ , y es columnar, sólo depende de la coordenada  $x$ . Para simular la distribución de las pistas, el ruido es constante dentro de columnas cuya anchura sigue una distribución de tipo  $P(l) \sim e^{-l/l_c}$ . Esta es la distribución que se observa también en los experimentos. El ruido no está correlacionado entre columnas diferentes. Por otro lado, con el fin de incluir la forma en que la diferencia de  $v_+$  y  $v_-$  evoluciona, la amplitud del ruido varía en el tiempo como  $(v_M - v)t^{1/2}$ . Juntando todos estos ingredientes, el modelo que proponemos es

$$\frac{\partial h}{\partial t} = \nabla D(x) \nabla h(x, t) + v + (v_M - v)t^{-1/2} \eta(x). \quad (\text{B.14})$$

El que la interacción entre columnas sea difusiva origina un valor de  $z = 2$ , muy cercano al encontrado para el experimento,  $z = 2.0 \pm 0.2$ . Cuando la difusividad  $D(x)$  es constante, el resto de exponentes para este modelo son  $\alpha = 1$  y  $\beta = 1/2$ , además de  $z = 2$ , que se corresponden con los exponentes globales medidos en el experimento. Sin embargo, el tipo de escalado no es anómalo, sino FV, lo que implica que  $\alpha_{loc} = 1$ . Para reproducir también el escalado local, es necesario tener en cuenta que los frentes experimentales son casi planos dentro de cada columna, tenga pista o no (esto se puede ver en la Figura 6.1). Esta característica se puede incluir en el modelo mediante una  $D(x)$  que no sea constante. La forma más simple para hacerlo, es que tras cada paso de tiempo se tome como altura del frente en cada columna el promedio de las alturas dentro de dicha columna. Tras implementar eso en el programa, se encuentra que el escalado se convierte en anómalo, que los frentes presentan ahora multi-escalado, que los exponentes globales se mantienen y, finalmente, que  $\alpha_{loc} = 1/2$ .

**Conclusiones**

En el sexto capítulo de la tesis se describen una serie de experimentos con frentes de fluidos. Hemos realizado el primer estudio experimental de las interfaces de un fluido inmerso en un desorden columnar. Hemos encontrado que su escalado es de tipo anómalo con unos exponentes  $\alpha \approx 1$ ,  $z \approx 2$  y  $\alpha_{loc} \approx 0.55$ . Además, proponemos una explicación para la presencia de ese tipo de escalado y hemos explorado como el cambio de los parámetros experimentales le afectan. Finalmente, proponemos un modelo teórico que consigue reproducir los resultados experimentales.



# Appendix C

## Publication list

The results of this thesis have been partially published in

- Juan M. López, José J. Ramasco, and Miguel A. Rodríguez, *Comment on "Macroscopic equation for the roughness of growing interfaces in quenched disorder"*, Physical Review Letters **82** 1337 (1999).
- José J. Ramasco, Juan M. López, and Miguel A. Rodríguez, *Generic dynamic scaling in kinetic roughening*, Physical Review Letters **84** 2199 (2000).
- José J. Ramasco, Juan M. López, and Miguel A. Rodríguez, *Interface depinning in the absence of an external driving force*, Physical Review E **64** 066109 (2001).
- J. Soriano, J.J. Ramasco, M.A. Rodríguez, A. Hernández-Machado, and J. Ortín  
*Anomalous roughening of Hele-Shaw flows with quenched disorder*, Submitted to Physical Review Letters.



# Appendix D

## Reprints

In this appendix, the reprints of the papers mentioned in the list of Appendix C are included.

### Comment on "Macroscopic Equation for the Roughness of Growing Interfaces in Quenched Disordered Media"

In a recent Letter [1] Braunstein and Buceta introduced a "macroscopic" equation for the time evolution of the width of interfaces belonging to the directed percolation depinning (DPD) universality class [2]. From numerical simulations of the DPD model, they inferred an ansatz [Eq. (1) in Ref. [1]] for the time derivative of the interface width (called DSIW in Ref. [1]) at the depinning transition. Braunstein and Buceta found that their formula fitted the numerical data at the depinning transition, for  $q_c = 0.539$  and  $\beta = 0.63$ , with the appropriate election of some arbitrary constants.

Here we argue that, contrary to what is claimed in Ref. [1], Braunstein and Buceta's formula does not describe the macroscopic behavior of the interface. The formula proposed in Ref. [1] for the DSIW is an approximation to the very short times regime (when less than one layer has been completed), which is not significant for the description of the surface dynamics at large scales. We obtain analytically the short time behavior of the DPD model, which is valid for any  $q$  and explains the appearance of an exponential term in the formula of Ref. [1] for the DSIW.

Let us consider the DPD model in a system of size  $L$  and a density  $q$  of blocked cells ( $p = 1 - q$  density of free cells). We are interested in the very short times regime when the first monolayer still has not been completed, i.e., the number of growth attempts  $N$  is  $N \ll L$  (this corresponds to times  $t = N/L \ll 1$ ). In this regime, the probability of having a column  $i$  with height  $h_i > \min(h_{i-1}, h_{i+1}) + 2$  is negligible and the columns are growing almost independently. The growth at this early stage can be seen as a random deposition (RD) process [3] in which every column grows in one unit with probability  $p/L$ . The short time regime of the DPD model is then like RD, which is solvable exactly, but with the additional ingredient of a density  $q$  of blocked sites.

One can see that, within this approximation, the probability of having a column with height  $h$  after  $N$  growth attempts is given by

$$P(N, h) = \frac{(Ns p)^h}{h!} e^{-Ns} + q p^h \sum_{r=h+1}^N \frac{(Ns)^r}{r!} e^{-Ns}, \quad (1)$$

where  $s = 1/L$  is the probability of attempting to grow a column and the usual approximation  $s^r (1-s)^{N-r} N! / [(N-r)! r!] \approx (Ns)^r \exp(-Ns) / r!$  has been made.

From the probability (1), one can calculate the interface width  $W^2 = \langle h^2 \rangle - \langle h \rangle^2$  and then the time derivative, whose leading terms are

$$\frac{dW^2}{dt} = p e^{-qt} + 2p^2 e^{-qt} \left( \frac{e^{-qt} - 1}{q} + t \right), \quad (2)$$

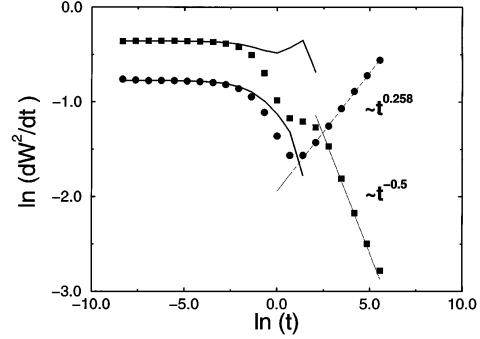


FIG. 1. Numerical results for the DPD model in a system of size  $L = 2^{13}$  for  $q_c = 0.539$  (circles) and  $q = 0.3$  (squares). Continuous lines correspond to Eq. (2) and fit the data for  $t \ll 1$ . For larger times our approximation is not valid any longer and the power law  $t^{2\beta-1}$  takes over with  $\beta = 0.623$  and  $\beta = 0.3$  for  $q_c = 0.539$  and  $q = 0.3$ , respectively (dashed lines).

where  $t = Ns = N/L$  is the time in the units used in Ref. [1]. This formula gives the exact time evolution of  $\frac{dW^2}{dt}$  for any  $q$  (not only at  $q_c = 0.539$ ) and is valid for times  $t \ll 1$ . For times  $t > 1$  differences between neighboring columns are likely to be larger than 2 resulting in horizontal correlations and the breakdown of (2). A comparison of Eq. (2) with numerical simulations of the DPD model is presented in Fig. 1.

Our calculation suggests that the exponential term in the ansatz of Ref. [1] is actually produced by the usual random depositionlike dynamics, which occurs in any growth model [3] for short times.

Juan M. López

Department of Mathematics, Imperial College  
180 Queen's Gate, London SW7 2BZ, United Kingdom

José J. Ramasco<sup>1,2</sup> and Miguel A. Rodríguez<sup>2</sup>

<sup>1</sup>Departamento de Física Moderna, Universidad de Cantabria  
Avenida Los Castros s/n, Santander E-39005, Spain

<sup>2</sup>Instituto de Física de Cantabria  
Consejo Superior de Investigaciones Científicas  
Universidad de Cantabria, Santander E-39005, Spain

Received 8 October 1998

[S0031-9007(98)08359-8]

PACS numbers: 64.60.Ht, 05.40.-a, 05.70.Ln

- [1] L. A. Braunstein and R. C. Buceta, Phys. Rev. Lett. **81**, 630 (1998).
- [2] L.-H. Tang and H. Leshorn, Phys. Rev. A **45**, R8309 (1992); S. V. Buldyrev *et al.*, Phys. Rev. A **45**, R8313 (1992).
- [3] A.-L. Barabási and H.E. Stanley, *Fractal Concepts in Surface Growth* (Cambridge University Press, Cambridge, England, 1995).

### Generic Dynamic Scaling in Kinetic Roughening

José J. Ramasco,<sup>1,2,\*</sup> Juan M. López,<sup>3,†</sup> and Miguel A. Rodríguez<sup>1</sup>

<sup>1</sup>*Instituto de Física de Cantabria, CSIC-UC, E-39005 Santander, Spain*

<sup>2</sup>*Departamento de Física Moderna, Universidad de Cantabria, E-39005 Santander, Spain*

<sup>3</sup>*Dipartimento di Fisica and Unità INFN, Università di Roma "La Sapienza", I-00185 Roma, Italy*

(Received 12 July 1999)

We study the dynamic scaling hypothesis in invariant surface growth. We show that the existence of power-law scaling of the correlation functions (scale invariance) does not determine a unique dynamic scaling form of the correlation functions, which leads to the different anomalous forms of scaling recently observed in growth models. We derive all the existing forms of anomalous dynamic scaling from a new generic scaling ansatz. The different scaling forms are subclasses of this generic scaling ansatz associated with bounds on the roughness exponent values. The existence of a new class of anomalous dynamic scaling is predicted and compared with simulations.

PACS numbers: 68.35.Fx, 05.40.-a, 05.70.Ln

The theory of kinetic roughening deals with the fate of surfaces growing in nonequilibrium conditions [1,2]. In a typical situation an initially flat surface grows and roughens continuously as it is driven by some external noise. The noise term can be of thermal origin (such as, for instance, fluctuations in the flux of particles in a deposition process) or a quenched disorder (such as in the motion of driven interfaces through porous media). A rough surface may be characterized by the fluctuations of the height around its mean value. So, a basic quantity to look at is the *global* interface width,  $W(L, t) = \langle [h(x, t) - \bar{h}]^2 \rangle^{1/2}$ , where the overbar denotes average over all  $x$  in a system of size  $L$  and the brackets denote average over different realizations. Rough surfaces then correspond to situations in which the stationary width  $W(L, t \rightarrow \infty)$  grows with the system size. Alternatively, one may calculate other quantities related to correlations over a distance  $l$  as the *height-height* correlation function,  $G(l, t) = \langle [h(x+l, t) - h(x, t)]^2 \rangle$ , or the *local* width,  $w(l, t) = \langle \langle [h(x, t) - \langle h \rangle_l]^2 \rangle \rangle^{1/2}$ , where  $\langle \cdot \rangle_l$  denotes an average over  $x$  in windows of size  $l$ .

In the absence of any characteristic length in the problem growth processes are expected to show power-law behavior of the correlation functions in space and time, and the Family-Vicsek dynamic scaling ansatz [1–3],

$$W(L, t) = t^{\alpha/z} f(L/\xi(t)), \quad (1)$$

ought to hold. The scaling function  $f(u)$  behaves as

$$f(u) \sim \begin{cases} u^\alpha & \text{if } u \ll 1 \\ \text{const} & \text{if } u \gg 1, \end{cases} \quad (2)$$

where  $\alpha$  is the roughness exponent and characterizes the stationary regime, in which the horizontal correlation length  $\xi(t) \sim t^{1/z}$  ( $z$  is the so called dynamic exponent) has reached a value larger than the system size  $L$ . The ratio  $\beta = \alpha/z$  is called growth exponent and characterizes the short time behavior of the surface. As occurs in equilibrium critical phenomena, the corresponding critical exponents do not depend on microscopic details of the system under investigation. This has made it possible to

divide growth processes into universality classes according to the values of these characteristic exponents [1,2].

A most intriguing feature of some growth models is that the above standard scaling of the global width differs substantially from the scaling behavior of the local interface fluctuations (measured either by the local width or the height-height correlation). More precisely, in some growth models the local width (and the height-height correlation) scales as in Eq. (1), i.e.,  $w(l, t) = t^\beta f_A(l/\xi(t))$ , but with the anomalous scaling function

$$f_A(u) \sim \begin{cases} u^{\alpha_{\text{loc}}} & \text{if } u \ll 1 \\ \text{const} & \text{if } u \gg 1, \end{cases} \quad (3)$$

where the new independent exponent  $\alpha_{\text{loc}}$  is called the local roughness exponent. This is what has been called *anomalous* roughening in the literature, and has been found to occur in many growth models [4–10] as well as experiments [11–15]. Moreover, it has recently been shown [16,17] that anomalous roughening can take two different forms. On the one hand, there are *super-rough* processes, i.e.,  $\alpha > 1$ , for which always  $\alpha_{\text{loc}} = 1$ . On the other hand, there are *intrinsically* anomalous roughened surfaces, for which  $\alpha_{\text{loc}} < 1$  and  $\alpha$  can actually be any  $\alpha > \alpha_{\text{loc}}$ .

Anomalous scaling implies that one more independent exponent,  $\alpha_{\text{loc}}$ , may be needed in order to assess the universality class of the particular system under study. In other words, some growth models may have exactly the same  $\alpha$  and  $z$  values seemingly indicating that they belong to the same universality class. However, they may have different values of  $\alpha_{\text{loc}}$  showing that they actually belong to distinct classes of growth. As for the experiments, only the local roughness exponent is measurable by direct methods, since the system size remains normally fixed. Fracture experiments [14] in systems of varying sizes have succeeded in measuring both the local and global roughness exponents, in good agreement with the scaling picture described above.

In this Letter we introduce a new anomalous dynamics in kinetic roughening. We show that, by adopting more

general forms of the scaling functions involved, a generic theory of dynamic scaling can be constructed. Our theory incorporates all the different forms that dynamic scaling can take, namely, Family-Vicsek, super-rough, and intrinsic, as subclasses and predicts the existence of a new class of growth models with novel anomalous scaling properties. Simulations of the Snieppen model (rule A) [18] of self-organized depinning (and other related models) are presented as examples of the new dynamics.

First, let us consider the Fourier transform of the height of the surface in a system of size  $L$ , which is given by  $\hat{h}(k, t) = L^{-1/2} \sum_x [h(x, t) - \bar{h}(t)] \exp(ikx)$ , where the spatial average of the height has been subtracted. The scaling behavior of the surface can now be investigated by calculating the structure factor or power spectrum,

$$S(k, t) = \langle \hat{h}(k, t) \hat{h}(-k, t) \rangle, \quad (4)$$

which is related to the height-height correlation function  $G(l, t)$  defined above by

$$\begin{aligned} G(l, t) &= \frac{4}{L} \sum_{2\pi/L \leq k \leq \pi/a} [1 - \cos(kl)] S(k, t) \\ &\propto \int_{2\pi/L}^{\pi/a} \frac{dk}{2\pi} [1 - \cos(kl)] S(k, t), \end{aligned} \quad (5)$$

where  $a$  is the lattice spacing and  $L$  is the system size.

In order to explore the most general form that kinetic roughening can take, we study the scaling behavior of surfaces satisfying what we will call a *generic* dynamic scaling form of the correlation functions. We will consider that a growing surface satisfies a generic dynamic scaling when there exists a correlation length  $\xi(t)$ , i.e., the distance over which correlations have propagated up to time  $t$ , and  $\xi(t) \sim t^{1/z}$ ,  $z$  being the dynamic exponent. If no characteristic scale exists but  $\xi$  and the system size  $L$ , then power-law behavior in space and time is expected and the growth saturates when  $\xi \sim L$  and the correlations [and from Eq. (5) also the structure factor] become time-independent. The global roughness exponent  $\alpha$  can now be calculated in this regime from  $G(l = L, t \gg L^z) \sim L^{2\alpha}$  [or  $W(L, t \gg L^z) \sim L^\alpha$ ]. In general, as we will see below, the scaling function that enters the dynamic scaling of the local width (or the height-height correlation) takes different forms depending on further restrictions and/or bounds for the roughness exponent values. These kinds of restrictions are very often assumed and not valid for every growth model. For instance, only if the surface were *self-affine*, saturation of the correlation function  $G(l, t)$  would also occur for intermediate scales  $l$  at times  $t \sim l^z$  and with the very same roughness exponent. However, the latter does not hold when anomalous roughening takes place, as can be seen from the scaling of the local width in Eq. (3).

Our aim here is to investigate *all* possible forms that the scaling functions can exhibit when solely the existence of

generic scaling is assumed. So, if the roughening process under consideration shows generic dynamic scaling (in the sense explained above), and no further assumptions (such as, for instance, surface self-affinity or implicit bounds for the exponent values) are imposed, then we propose that the structure factor is given by

$$S(k, t) = k^{-(2\alpha+1)} s(kt^{1/z}), \quad (6)$$

where the scaling function has the general form

$$s(u) \sim \begin{cases} u^{2(\alpha-\alpha_s)} & \text{if } u \gg 1 \\ u^{2\alpha+1} & \text{if } u \ll 1, \end{cases} \quad (7)$$

and the exponent  $\alpha_s$  is what we will call the *spectral* roughness exponent. This scaling ansatz is a natural generalization of the scaling proposed for the structure factor in Refs. [16,17] for anomalous scaling.

In the case of the global width, one can make use of

$$W^2(L, t) = \frac{1}{L} \sum_k S(k, t) = \int \frac{dk}{2\pi} S(k, t), \quad (8)$$

to prove easily that the global width scales as in Eqs. (1) and (2), independently of the value of the exponents  $\alpha$  and  $\alpha_s$ .

However, the scaling of the local width is much more involved. The existence of a generic scaling behavior such as (7) for the structure factor always leads to a dynamic scaling behavior,

$$w(l, t) \sim \sqrt{G(l, t)} = t^\beta g(l/\xi), \quad (9)$$

of the height-height correlation (and local width), but the corresponding scaling function  $g(u)$  is not unique. When substituting Eqs. (7) and (6) into (5), one can see that the various limits involved [ $a \rightarrow 0$ ,  $\xi(t)/L \rightarrow \infty$ , and  $L \rightarrow \infty$ ] do not commute [16,17]. This results in a different scaling behavior of  $g(u)$  depending on the value of the exponent  $\alpha_s$ .

Let us now summarize how all scaling behaviors reported in the literature are obtained from the generic dynamic scaling ansatz (7). We shall also show how a new roughening dynamics naturally appears in this scaling theory. Two major cases can be distinguished, namely,  $\alpha_s < 1$  and  $\alpha_s > 1$ . On the one hand, for  $\alpha_s < 1$  the integral in Eq. (5) has already been computed [16,17] and one gets

$$g_{\alpha_s < 1}(u) \sim \begin{cases} u^{\alpha_s} & \text{if } u \ll 1 \\ \text{const} & \text{if } u \gg 1. \end{cases} \quad (10)$$

So, the corresponding scaling function is  $g_{\alpha_s < 1} \sim f_A$  and  $\alpha_s = \alpha_{\text{loc}}$ , i.e., the intrinsic anomalous scaling function in Eq. (3). Moreover, in this case the interface would satisfy a Family-Vicsek scaling (for the local as well as the global width) only if  $\alpha = \alpha_s$  were satisfied for the particular growth model under study. Thus, the standard Family-Vicsek scaling turns out to be one of the possible scaling forms compatible with generic scaling invariant growth, but not the only one.

On the other hand, a new anomalous dynamics shows up for growth models in which  $\alpha_s > 1$ . In this case, one

finds that, in the thermodynamic limit  $L \rightarrow \infty$ , the integral Eq. (5) has a divergence coming from the lower integration limit. To avoid the divergence one has to compute the integral keeping  $L$  fixed. We then obtain the scaling function

$$g_{\alpha_s > 1}(u) \sim \begin{cases} u & \text{if } u \ll 1 \\ \text{const} & \text{if } u \gg 1. \end{cases} \quad (11)$$

So in this case one always gets  $\alpha_{\text{loc}} = 1$  for any  $\alpha_s > 1$ . Thus, for growth models in which  $\alpha = \alpha_s$ , one recovers the super-rough scaling behavior [16,17].

However, it is worth noting that neither the spectral exponent  $\alpha_s$  nor the global exponent  $\alpha$  are fixed by the scaling in Eqs. (7) and (11) and, in principle, they could be different. Therefore, growth models in which  $\alpha_s > 1$  but  $\alpha \neq \alpha_s$  could also be possible and represent a new type of dynamics with anomalous scaling. The main feature of this new type of anomalous roughening is that it can be detected only by determining the scaling of the structure factor. Whenever such a scaling takes place in the problem under investigation the new exponent  $\alpha_s$  will show up only when analyzing the scaling behavior of  $S(k, t)$  and will not be detectable in either  $W(L, t)$ ,  $w(l, t)$ , or  $G(l, t)$ . In fact, as we have shown, the stationary regime of a surface exhibiting this kind of anomalous scaling will be characterized by  $W(L) \sim L^\alpha$  and  $w(l, L) \sim \sqrt{G(l, L)} \sim lL^{\alpha-1}$ ; however, the structure factor scales as  $S(k, L) \sim k^{-(2\alpha_s+1)}L^{2(\alpha-\alpha_s)}$ , where the spectral roughness exponent  $\alpha_s$  is a new and independent exponent. We can summarize our analytical results as follows:

$$\left\{ \begin{array}{l} \text{if } \alpha_s < 1 \Rightarrow \alpha_{\text{loc}} = \alpha_s \\ \text{if } \alpha_s > 1 \Rightarrow \alpha_{\text{loc}} = 1 \end{array} \right. \left\{ \begin{array}{l} \alpha_s = \alpha \Rightarrow \text{Family-Vicsek} \\ \alpha_s \neq \alpha \Rightarrow \text{intrinsic} \\ \alpha_s = \alpha \Rightarrow \text{super-rough} \\ \alpha_s \neq \alpha \Rightarrow \text{new class.} \end{array} \right. \quad (12)$$

In the following we present simulations of a one-dimensional growth model that is a nice example of the new dynamics. We have performed numerical simulations of the Sneppen model of self-organized depinning (model A) [18]. We have found that this model exhibits anomalous roughening of the type described by Eq. (7) for  $\alpha_s > 1$  and  $\alpha_s \neq \alpha$ . In this model the height of the interface  $h(i, t)$  is taken to be an integer defined on a one-dimensional discrete substrate  $i = 1, \dots, L$ . A random pinning force  $\eta(i, h)$  is associated with each lattice site  $[i, h(i)]$ . The quenched disorder  $\eta(i, h)$  is uniformly distributed in  $[0, 1]$  and uncorrelated. The growth algorithm is then as follows. At every time step  $t$ , the site  $i_0$  with the smallest pinning force is chosen and its height  $h(i_0, t)$  is updated  $h(i_0, t+1) = h(i_0, t) + 1$  provided that the conditions  $|h(i_0, t) - h(i_0 \pm 1, t)| < 2$  are satisfied. Periodic boundary conditions are assumed. We have studied the behavior of the model in systems of different sizes from  $L = 2^6$  up to  $L = 2^{13}$ . From calculations of the saturated global width  $W(L)$  for various system sizes, we find a global roughness exponent  $\alpha = 1.000 \pm 0.005$

in agreement with previous simulations [18]. We have checked that the scaling of the global width is given by Eq. (1) with a scaling function such as (2). Also in agreement with previous work [18], we find that the time exponent  $\alpha/z = 0.95 \pm 0.05$ . The local width  $w(l, t)$  scales as  $w(l, t) = t^{\alpha/z} g(l/\xi)$  where the scaling function is given by Eq. (11), and also  $\alpha_{\text{loc}} = 1$ .

From these simulation results, one could conclude that the behavior of the Sneppen growth model is rather trivial and that the exponents  $\alpha = \alpha_{\text{loc}} = z = 1$  describe its scaling properties. Quite the opposite, this model exhibits no trivial features that can be noticed when the structure factor is calculated. In Fig. 1 we show our numerical results for the structure factor  $S(k, t)$  in a system of size  $L = 2048$ . Note that in Fig. 1 the curves  $S(k, t)$  for different times are shifted downwards reflecting that  $\alpha < \alpha_s$ . This contrasts with the case of intrinsic anomalous roughening [16,17] where  $\alpha_s = \alpha_{\text{loc}}$  and  $\alpha_{\text{loc}} \leq 1$ . The slope of the continuous line is  $-3.7$  and indicates that a new exponent  $\alpha_s = 1.35$  enters the scaling. This can be better appreciated by the data collapse shown in Fig. 2, where one can observe that, instead of being constant, the scaling function  $s(u)$  has a negative exponent  $u^{-0.7}$  for  $u \gg 1$ . The exponents used for the data collapse are  $\alpha = 1$ ,  $z = 1$  and the scaling function obtained is in excellent agreement with Eq. (7) and a spectral exponent  $\alpha_s = 1.35 \pm 0.03$ .

The interface in the Sneppen model A is formed by facets with constant slope  $\pm 1$  [18]. The value of the exponents  $\alpha = \alpha_{\text{loc}} = 1$  and  $\alpha_s = 1.35$  is related to the faceted form of the interface at saturation. It is easy to understand how the anomalous spectral roughness exponent appears due to the faceted form of the interface. For the simpler (and trivial) case of a faceted interface formed by a finite number of identical segments,  $N$ , of constant slope,  $\pm m$ , one can show analytically that the

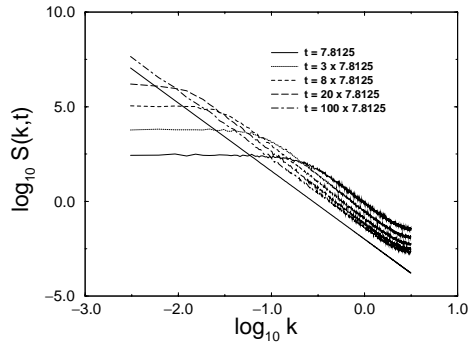


FIG. 1. Structure factor of the Sneppen model for interface depinning at different times. The continuous straight line is a guide to the eye and has a slope  $-3.7$ . Note the anomalous downwards shift of the curves for increasing times.

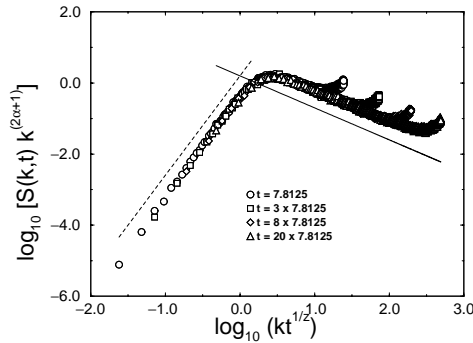


FIG. 2. Data collapse of the graphs in Fig. 1. The exponents used for the collapse are  $\alpha = 1.0$  and  $z = 1.0$ . The straight lines have slopes  $-0.7$  (solid) and  $3.0$  (dashed) and are a guide to the eye. The scaling function is given by Eq. (7) with a spectral roughness exponent  $\alpha_s = 1.35 \pm 0.03$ . The deviations from the scaling for large values of the argument  $kt^{1/z}$  are due to the finite lattice spacing.

global width  $W(L) \sim m^2 L^2 / N^2$ , and the height-height correlation function  $G(l) \sim l^2 m^2 - Nm^2 l^3 / L$ , which leads to  $\alpha = \alpha_{loc} = 1$ , while the spectrum  $S(k, L) \sim k^{-4} L^{-1}$  as  $k \rightarrow 0$ . A simple comparison with the anomalous scaling form for the stationary spectrum  $S(k, L) \sim k^{-(2\alpha_s+1)} L^{2(\alpha-\alpha_s)}$  leads to  $\alpha_s = 1.5$ . Actually, the facets occurring in the Sneppen model are not formed by identical segments, but rather follow a random distribution [19], which leads to a spectral exponent different from the trivial case.

In summary, we have presented a generic theory of scaling for invariant surface growth. We have shown that the existence of power-law scaling of the correlation functions (scale invariance) does not determine a unique form of the scaling functions involved. This leads to the different dynamic scaling forms recently observed in growth models [4–10] and experiments [11–15] exhibiting anomalous roughening. In particular, interface scale invariance does not necessarily imply Family-Vicsek dynamic scaling. We have derived all the types of scaling (Family-Vicsek, super-rough, and intrinsic anomalous) from a unique scaling ansatz, which is formulated in the Fourier space. The different types of scaling are subclasses of our generic scaling ansatz associated with bounds on the values that the new spectral roughness exponent  $\alpha_s$  may take. This generalization has allowed

us to predict the existence of a new kind of anomalous scaling with interesting features. Simulations of a model for self-organized interface depinning have been shown to be in excellent agreement with the new anomalous dynamics. It has recently been shown [20] that anomalous roughening stems from a nontrivial dynamics of the mean local slopes  $\langle(\nabla h)^2\rangle$ . In contrast, the new anomalous dynamics can be pinned down to growth models in which the stationary state consists of faceted interfaces.

The authors would like to thank R. Cuerno for an earlier collaboration that led to Refs. [16,17]. This work has been supported by the DGES of the Spanish Government (Project No. PB96-0378-C02-02). J.J.R. is supported by the Ministerio de Educación y Cultura (Spain). J.M.L. is supported by a TMR Network of the European Commission (Contract No. FMRXCT980183).

\*Electronic address: ramasco@ifca.unican.es

†Electronic address: jmlopez@pil.phys.uniroma1.it

- [1] A.-L. Barabási and H.E. Stanley, *Fractal Concepts in Surface Growth* (Cambridge University Press, Cambridge, England, 1995).
- [2] J. Krug, *Adv. Phys.* **46**, 139 (1997).
- [3] F. Family and T. Vicsek, *J. Phys. A* **18**, L75 (1985).
- [4] J. Krug, *Phys. Rev. Lett.* **72**, 2907 (1994).
- [5] M. Schroeder *et al.*, *Europhys. Lett.* **24**, 563 (1993).
- [6] J.M. López and M.A. Rodríguez, *Phys. Rev. E* **54**, R2189 (1996).
- [7] S. Das Sarma *et al.*, *Phys. Rev. E* **53**, 359 (1996).
- [8] C. Dasgupta, S. Das Sarma, and J.M. Kim, *Phys. Rev. E* **54**, R4552 (1996).
- [9] J.M. López and M.A. Rodríguez, *J. Phys. I (France)* **7**, 1191 (1997).
- [10] M. Castro *et al.*, *Phys. Rev. E* **57**, R2491 (1998).
- [11] H.-N. Yang, G.-C. Wang, and T.-M. Lu, *Phys. Rev. Lett.* **73**, 2348 (1994).
- [12] J.H. Jeffries, J.-K. Zuo, and M.M. Craig, *Phys. Rev. Lett.* **76**, 4931 (1996).
- [13] J.M. López and J. Schmittbuhl, *Phys. Rev. E* **57**, 6405 (1998).
- [14] S. Morel *et al.*, *Phys. Rev. E* **58**, 6999 (1998).
- [15] A. Bru *et al.*, *Phys. Rev. Lett.* **81**, 4008 (1998).
- [16] J.M. López, M.A. Rodríguez, and R. Cuerno, *Phys. Rev. E* **56**, 3993 (1997).
- [17] J.M. López, M.A. Rodríguez, and R. Cuerno, *Physica (Amsterdam)* **246A**, 329 (1997).
- [18] K. Sneppen, *Phys. Rev. Lett.* **69**, 3539 (1992).
- [19] J.J. Ramasco, J.M. López, and M.A. Rodríguez (unpublished).
- [20] J.M. López, *Phys. Rev. Lett.* **83**, 4594 (1999).

## Interface depinning in the absence of an external driving force

José J. Ramasco,<sup>1,2,\*</sup> Juan M. López,<sup>1,3,†</sup> and Miguel A. Rodríguez<sup>1</sup><sup>1</sup>Instituto de Física de Cantabria, CSIC-UC, E-39005 Santander, Spain<sup>2</sup>Departamento de Física Moderna, Universidad de Cantabria, E-39005 Santander, Spain<sup>3</sup>INFM, Sezione di Roma 1, Università di Roma "La Sapienza," Piazzale Aldo Moro 2, I-00185 Roma, Italy

(Received 15 May 2001; published 19 November 2001)

We study the pinning-depinning phase transition of interfaces in the quenched Kardar-Parisi-Zhang model as the external driving force  $F$  goes towards zero. For a fixed value of the driving force, we induce depinning by increasing the nonlinear term coefficient  $\lambda$ , which is related to lateral growth, up to a critical threshold. We focus on the case in which there is no external force applied ( $F=0$ ) and find that, contrary to a simple scaling prediction, there is a finite value of  $\lambda$  that makes the interface to become depinned. The critical exponents at the transition are consistent with directed percolation depinning.

DOI: 10.1103/PhysRevE.64.066109

PACS number(s): 05.70.Ln, 47.55.Mh, 68.35.Fx, 05.40.-a

## I. INTRODUCTION

The dynamics of random interfaces in the presence of noise is an interesting example of critical phenomena and generic scale-free behavior in systems far from equilibrium. In the case of surface growth dominated by thermal fluctuations, the Kardar-Parisi-Zhang (KPZ) equation [1] has been very much studied for it represents a whole universality class of growth, which includes many well-known discrete computer models [2]. In many experimental situations, however, interface motion is affected by the existence of random pinning forces (see [2] and references therein). In this case, the simplest way to model interface roughening is to replace the noise term  $\eta(\mathbf{x},t)$  in KPZ by a quenched disorder  $\eta(\mathbf{x},h)$ ,

$$\frac{\partial h}{\partial t} = \nu \nabla^2 h + \lambda (\nabla h)^2 + F + \eta(\mathbf{x},h), \quad (1)$$

which is often referred to as the quenched Kardar-Parisi-Zhang (QKPZ) equation. The first term on the right-hand side describes the smoothing effect of surface tension,  $F$  is the driving force that pushes the interface through the disorder, and the term  $\lambda(\nabla h)^2$  comes from lateral growth and represents the nonlinear most relevant correction. The quenched disorder has short-range correlations  $\langle \eta(\mathbf{x},h) \eta(\mathbf{x}',h') \rangle = \delta(\mathbf{x} - \mathbf{x}') \Delta(h - h')$ , where the correlator  $\Delta(u)$  is a very rapidly decreasing function of  $|u|$  and is the term actually responsible for the pinning of the interface. This equation is expected to describe interface roughening in many disordered systems, including the nonequilibrium dynamics of magnetic domain walls in disordered materials [3–6], an elastic chain in a quenched disorder [7], fracture cracks propagation [8], etc. Its applicability to describing fluid-fluid displacement in porous media might be less justified though [9].

The QKPZ model described by Eq. (1) exhibits a continuous phase transition at a certain critical value  $F_c$  of the external driving force  $F$ . For  $F$  larger than  $F_c$ , the interface

moves with a finite velocity. However, the interface remains pinned by the disorder for  $F < F_c$ . The critical point  $F = F_c$  is known as depinning transition. The interface velocity scales as  $v \sim (F - F_c)^\theta$  near and above the transition and plays the role of an order parameter.

The value of the critical force depends on the parameters of the model, in particular, it depends on the value of the coefficient  $\lambda$  of the nonlinear term. Therefore, by keeping constant the rest of the equation parameters, one may find a critical line  $F_c = f(\lambda)$  separating the pinned from the depinned phase. Alternatively, we can see this critical line the other way around and let  $\lambda_c = f^{-1}(F)$  be the critical value of the KPZ nonlinearity above which the interface gets depinned. The driving force  $F$  favors the advance of the interface and thus, the lower the driving force is, the larger the critical value  $\lambda_c$  of the nonlinearity that is needed in order to get the interface depinned. Indeed, one would expect that as  $F \rightarrow 0$  depinning becomes more and more difficult until eventually, at  $F=0$ , the threshold  $\lambda_c \rightarrow \infty$  and depinning becomes impossible. This intuitive picture can be justified by means of a simple scaling argument as follows. Consider a typical region of size  $l$  pinned by the disorder. Equation (1) applied to that region reads

$$\nu h l^{-2} + \lambda h^2 l^{-2} + F - \Delta(0)^{1/2} l^{-d/2} = 0. \quad (2)$$

If one supposes that the nonlinear term dominates over the diffusion, the interface remains pinned whenever  $\lambda a^2 l^{-2} \ll \Delta(0)^{1/2} l^{-d/2}$ , where  $a$  is the lattice spacing in the growth direction. This defines a characteristic length,  $l_c = [\lambda^2 a^4 / \Delta(0)]^{1/(4-d)}$ , such that for  $l \ll l_c$  the interface gets pinned. Now to estimate the critical force that is necessary to depin a region of typical size  $l_c$ , one equates the force term with the disorder in Eq. (2) to get an expression for the critical line,  $F_c \sim \Delta(0)^{2/(4-d)} (\lambda a^2)^{-d/(4-d)}$ . Inverting the latter, one finds

$$\lambda_c \sim \frac{\Delta(0)^{2/d}}{a^2} F^{-(4-d)/d} \quad (3)$$

\*Electronic address: ramasco@ifca.unican.es

†Electronic address: lopez@ifca.unican.es

RAMASCO, LÓPEZ, AND RODRÍGUEZ

PHYSICAL REVIEW E 64 066109

for the critical line of the depinning transition [10]. In  $1+1$  dimensions for instance, Eq. (3) predicts a diverging  $\lambda_c \sim F^{-3}$  as  $F \rightarrow 0$  [11].

In this paper, we show that, contrary to this scaling picture, there is always a finite critical value  $\lambda_c$  of the KPZ nonlinearity such that the interface gets depinned even for  $F=0$ . Our conclusions are based upon numerical integration of Eq. (1) in  $d=1$ . We numerically calculate the critical line and find that  $\lambda_c(F=0) = 3.60 \pm 0.01$  (in natural units) for the QKPZ equation. Our results support the somehow counterintuitive conclusion that an interface may get depinned in the absence of the external driving force by the sole effect of nonlinearities.

## II. NUMERICAL RESULTS

In order to numerically integrate Eq. (1), the equation parameters can easily be rescaled to have only two independent tuning parameters—namely, the nonlinear KPZ coefficient  $\lambda$  and the driving force  $F$ . We have used a standard finite-difference scheme for integrating the QKPZ equation given (in natural units) by

$$\begin{aligned} h(i,t+\Delta t) = & h(i,t) + \Delta t F + \Delta t \eta[i, \tilde{h}(i,t)] + \Delta t [h(i+1,t) \\ & + h(i-1,t) - 2h(i,t)] \\ & + \Delta t \lambda \left[ \frac{h(i+1,t) - h(i-1,t)}{2} \right]^2, \end{aligned} \quad (4)$$

where the lattice spacing has been set to unity. We start our simulation from a flat initial condition  $h(x,0)=0$  and periodic boundary conditions, i.e.,  $h(0,t)=h(L,t)$  and  $h(L+1,t)=h(1,t)$ , are imposed on the interface.  $\tilde{h}(i,t)$  stands for the integer part of  $h(i,t)$ , and the quenched disorder is Gaussian distributed and has correlations  $\langle \eta(i, \tilde{h}) \eta(j, \tilde{h}') \rangle = \delta_{i,j} \delta_{\tilde{h}, \tilde{h}'}$ . Simulations with different time steps were carried out, and the scheme proved to be stable and well behaved for a time step  $\Delta=0.01$  (or smaller) for the range of tuning parameters simulated. Following Newman and Bray [12], who found some numerical instabilities when numerically integrating KPZ, we took special care in checking that no numerical instabilities appear (i.e., surface cusps are effectively smoothed by the Laplacian term) even for the large values of  $\lambda$  used here.

We carried out simulations in systems of size  $L=128, 256, \dots, 8192$ . For each value of the of the nonlinear coefficient  $\lambda$ , we computed the critical value of force needed to get the interface depinned. Our results are summarized in Fig. 1. As expected, we find that as the driving force is smaller, the critical value  $\lambda_c$  of the nonlinear coefficient required in order to depin the interface becomes larger. However, as anticipated above, the critical point  $\lambda_c$  always remains finite, even for  $F=0$ . At a purely phenomenological level, we find that the critical line can be fitted very nicely by

$$\left( \frac{\lambda}{b_1} \right)^{2/3} + \left( \frac{F}{b_2} \right)^{2/3} = 1, \quad (5)$$

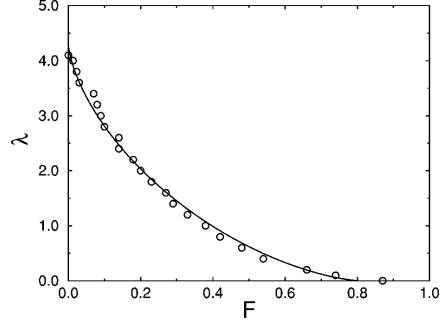


FIG. 1. Critical line  $\lambda_c = f(F)$  for the QKPZ equation. Symbols are points obtained from numerical simulations in a system of size  $L=1024$ . The line is a fit according to Eq. (5). Note that  $\lambda_c$  remains finite, even at  $F=0$ .

where the constants  $b_1 = 4.31 \pm 0.04$  and  $b_2 = 0.81 \pm 0.03$  (see Fig. 1). To our knowledge, this is the first formula for the critical line and demands theoretical explanation.

In the following, we focus on the case in which no external driving  $F=0$  pushes the interface and depinning is due solely to nonlinear lateral growth. We have studied the critical behavior in the vicinity of  $\lambda_c(F=0) = 3.60 \pm 0.01$  in order to address the problem of the nature of the critical point. First, we have computed the scaling behavior of the stationary interface velocity at  $F=0$  as the transition is approached. In Fig. 2 (inset) we plot  $v$  vs  $\lambda$  for  $F=0$  and a system of size  $L=8192$  showing that the transition is continuous. The critical behavior of the order parameter  $v$  is shown in Fig. 2. We find that close to the depinning threshold, the interface velocity scales as  $v \sim (\lambda - \lambda_c)^\nu$  with a critical exponent  $\theta = 0.635 \pm 0.007$ .

The depinning mechanism for  $F=0$  is the following. Starting from a flat initial condition  $h(x,t=0)=0$ , all the

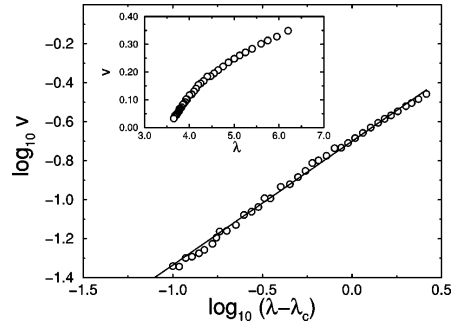


FIG. 2. Interface velocity vs coefficient  $\lambda$  for the QKPZ equation at  $F=0$  (inset) close to the threshold  $\lambda_c(F=0)$ . The critical behavior of the velocity  $v \sim (\lambda - \lambda_c)^\nu$  is shown in the main panel. A straight line is found for  $\lambda_c = 3.60 \pm 0.01$  and the slope corresponds to the velocity critical exponent  $\nu = 0.635 \pm 0.007$ .

INTERFACE DEPINNING IN THE ABSENCE OF . . .

PHYSICAL REVIEW E 64 066109

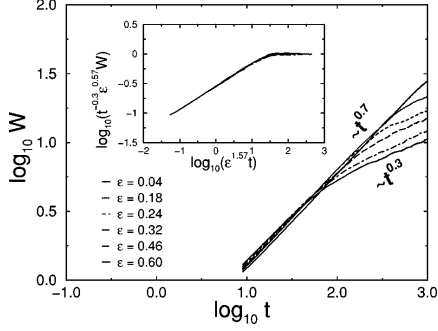


FIG. 3. In the main panel, we plot the global width for different distances (as shown)  $\epsilon = (\lambda - \lambda_c)/\lambda_c$  to the threshold for  $F=0$  in a system of size  $L=8192$ . The crossover from  $t^{0.7}$  to  $t^{0.3}$  occurs at times that scale as  $t_c \sim \epsilon^{-\gamma}$  with the distance to the threshold. Inset shows a data collapse according to Eq. (8) of the sets shown in the main panel. A good collapse is found for the exponents  $\beta_{kpz} = 0.3$ ,  $\kappa = 0.57$ , and  $\gamma = 1.57$ .

terms in Eq. (1) are zero except for the disorder. At time  $t=0$ , the quenched random term  $\eta(x, h)$  generates inhomogeneities in the front, which in turn produce a finite value of  $(\nabla h)^2$ . For small values of  $\lambda$ , these inhomogeneities smear out and the interface gets pinned by the disorder at one of the infinite pinning paths. However, for  $\lambda > \lambda_c$  these initial inhomogeneities are effectively amplified by the nonlinearity and the interface gets moving with a finite velocity.

As occurs in the standard case of depinning driven by an external force, we find that the depinned phase  $\lambda \gg \lambda_c$  is rough and belongs to the universality class of KPZ. This can be seen by studying the scaling behavior of the the global width  $W(L, t) = [\langle h(x, t)^2 \rangle - \langle h(x, t) \rangle^2]^{1/2}$ , where the average is over all  $x$  and different realizations of disorder [13]. We obtain that the global width scales as [14]

$$W(L, t) \sim \begin{cases} t^\beta & \text{if } t \ll t_\times \\ L^\alpha & \text{if } t \gg t_\times, \end{cases} \quad (6)$$

with a time exponent  $\beta = 0.33 \pm 0.01$  and a roughness exponent  $\alpha = 0.50 \pm 0.01$  in agreement with the KPZ class of growth.

However, when approaching the depinning transition from above,  $\epsilon = (\lambda - \lambda_c)/\lambda_c \rightarrow 0^+$ , the scaling of the global width is affected by the existence of a diverging correlation length  $\xi \sim \epsilon^{-\nu}$ . This is the typical size of the fluctuations of the majority phase, i.e., the characteristic size of connected regions formed by pinned sites. As we show in Fig. 3, the global width (and similarly, the local width) displays a crossover from  $\sim t^{0.7}$  to KPZ-like behavior  $\sim t^{0.33}$ . More precisely, one can see in Fig. 3 that the width approximately behaves as

$$W(t, \epsilon) \sim \begin{cases} t^{\beta_c} \epsilon^{\kappa_c} & \text{if } t \ll t_c \\ t^{\beta_{kpz}} \epsilon^{-\kappa} & \text{if } t \gg t_c, \end{cases} \quad (7)$$

where  $\kappa_c$ , in view of the dependence of the curves on  $\epsilon$ , must be very small. These two regimes are separated by a crossover time  $t_c$  that depends on  $\epsilon$ . Indeed, following Kertesz and Wolf [15], near a roughening phase transition, one expects the crossover time to scale with the distance to the threshold as  $t_c \sim \xi^z \sim \epsilon^{-\gamma}$ , where  $\gamma = z\nu$ . Direct examination of Fig. 3 immediately suggests the scaling ansatz

$$W(t, \epsilon) \sim t^{\beta_{kpz}} \epsilon^{-\kappa} g(t/t_c), \quad (8)$$

which is characteristic of systems close to a roughening transition [15–17]. The scaling function is given by

$$g(u) \sim \begin{cases} u^{\beta_c - \beta_{kpz}} & \text{if } u \ll 1 \\ \text{const.} & \text{if } u \gg 1, \end{cases} \quad (9)$$

and the scaling relation

$$\kappa_c + \kappa = (\beta_c - \beta_{kpz}) \gamma \quad (10)$$

among critical exponents must be fulfilled so that both regimes match.

In Fig. 3 (inset) we show a data collapse of  $t^{-\beta_{kpz}} \epsilon^\kappa W(t, \epsilon)$  vs  $\epsilon^\gamma t$ . A good data collapse is obtained for the exponents  $\beta_{kpz} = 0.3$ ,  $\kappa = 0.57$ , and  $\gamma = 1.57$ , the error in estimating these exponents being of about 10%. From the scaling relation (10), one also gets  $\beta_c = 0.73$  in good agreement with our previous estimate.

The value of the critical exponents is consistent with those of the DPD model [18,19] just above the transition [16,2]. We thus conclude that the lateral growth-driven depinning point at  $F=0$  and  $\lambda = \lambda_c$  also belongs to the universality class of DPD.

### III. DISCUSSION

Our results indicate that in the absence of any external driving field, an interface may get depinned by increasing the nonlinear term  $\lambda$  in Eq. (1) up to its critical value. From the experimental point of view, this implies that, assuming the parameter  $\lambda$  is tunable in the laboratory, an interface could become depinned even when no external driving force is applied. In the following, we discuss the role of anisotropy of the background random medium in generating the KPZ term  $\lambda(\nabla h)^2$ , and how this mechanism may be used to raise the value of  $\lambda$  in experiments by increasing the degree of disorder anisotropy.

The QKPZ equation for  $\lambda=0$  is known as the quenched Edwards-Wilkinson (QEW) equation and has been much studied in recent years. The critical exponents at the depinning transition have been well determined by several authors [20–23,7]. In  $(1+1)$ -dimensions one finds  $\alpha \sim 1.25$  and  $\beta \sim 0.85$  at the threshold  $F = F_c$  and  $\alpha = 1/2$  and  $\beta = 1/4$  in the moving phase for  $F \gg F_c$ , where the disorder  $\eta(x, h)$  may be replaced by  $\eta(x, \nu t)$  and the exponents of the EW universality class [2] are recovered. The QEW equation arises naturally as the Langevin equation for the Hamiltonian  $H = \int dx [\sqrt{1 + (\nabla h)^2} + V(\mathbf{x}, h)]$  describing the elastic energy of an interface in a disordered potential  $V(\mathbf{x}, y)$  [3–5]. The term  $\lambda(\nabla h)^2$  cannot be deduced as a variation of any Hamil-

tonian and is added as the most relevant nonlinear correction [2]. Geometrically, it accounts for growth in a direction locally normal to the interface and is referred to as nonlinear lateral growth term.

In the past, the physical origin of the KPZ nonlinearity in interface depinning has been found to be related to two distinct mechanisms for different models [24]. On the one hand, in the spirit of the original work of KPZ [1], the  $\lambda$  term may have a purely kinematic origin, so that  $\lambda \propto v$  [20,24]. In this case, the term  $\lambda(\nabla h)^2$  goes to zero at the depinning transition,  $F = F_c$ , and the system thus belongs to the QEW universality class. On the other hand, there are models [24] for which  $\lambda$  remains finite at the transition [25]. These models have exponents that correspond to the DPD universality class [20,26]. Tang, Kardar, and Dhar [27] have shown that this finite  $\lambda$  term may arise in some models because of an underlying anisotropy in the random medium, i.e., models that have a growth direction determined by the random medium. A further numerical step on this direction has recently been achieved by Park, Kim, and Kim [28] by studying a model with an anisotropic disorder correlator. The effect of anisotropy on real experiments has also been successfully tested by Albert *et al.* [29]. Experiments on fluid flow in a random medium formed by packed glass beads [30] are now known to belong to the isotropic QEW universality class [29]. However, the scaling exponents obtained for paper wetting [19,31,32] are close to the prediction of the anisotropic DPD universality class. A definite identification of paper wetting with DPD is still an open question though [9,33]. In paper-wetting experiments, a sheet of paper is vertically suspended over a reservoir of liquid (usually black ink). The fluid then wets the paper and the interface between wet and dry phases rises until it eventually stops. The interface grows upwards because of capillary forces in the paper pores. Notice that there is no external driving force. The anisotropic paper fiber distribution determines the quenched disorder term. Disorder

in these systems is thus highly anisotropic. Pressure difference between the reservoir and the paper pores leads to a coarse-grained effective nonlinear term, which depends on viscosity of the invading fluid and microstructure of the medium. Whenever the effectively generated  $\lambda$  term is large enough to be above  $\lambda_c$ , depinning of the wetting front occurs.

In summary, we have studied the QKPZ equation focusing on the case in which there is no external driving force ( $F = 0$ ). We have shown that there exists a depinning transition for a finite value of the KPZ coefficient  $\lambda = \lambda_c (F = 0)$  and that transition belongs to the DPD universality class. Moreover, we find that the interface velocity scales as  $v \sim (\lambda - \lambda_c)^\theta$  with a critical exponent  $\theta = 0.635 \pm 0.007$ , which is identical to the scaling in the case of depinning driven by an external force. This seems to indicate that the  $\lambda$  term upon renormalization gives rise to a constant term in a linear fashion that makes the role of a finite driving force. A finite value of the nonlinear coefficient  $\lambda$  appears in systems with anisotropic disorder, such as for instance in paper wetting experiments. In this system, there is no external driving force and depinning occurs due to local capillary forces, which drive the interface through the anisotropic lateral growth term  $\lambda(\nabla h)^2$ . We conclude that by varying the anisotropy degree of the corresponding random medium in other experimental systems, depinning is possible even with no external driving.

#### ACKNOWLEDGMENTS

We thank S. Zapperi and S. Stepanow for discussions. Financial support from DGES of the Spanish Government (Project No. PB96-0378-C02-02) is acknowledged. J.M.L. was supported by a TMR Network of the European Commission (Contract No. FMRXCT980183) at INFN (Roma). J.J.R. was supported by the Ministerio de Educación, Cultura y Deportes.

- 
- [1] M. Kardar, G. Parisi, and Y.-C. Zhang, *Phys. Rev. Lett.* **56**, 889 (1986).
- [2] A.-L. Barabási and H. E. Stanley, *Fractal Concepts in Surface Growth* (Cambridge University Press, Cambridge, 1995).
- [3] R. Bruinsma and G. Aeppli, *Phys. Rev. Lett.* **52**, 1547 (1984).
- [4] D.S. Fisher, *Phys. Rev. Lett.* **56**, 1964 (1986).
- [5] O. Narayan and D.S. Fisher, *Phys. Rev. B* **48**, 7030 (1993).
- [6] M. Jost and K.D. Usadel, *Phys. Rev. B* **54**, 9314 (1996).
- [7] H.J. Jensen, *J. Phys. A* **28**, 1861 (1995).
- [8] D. Ertas and M. Kardar, *Phys. Rev. E* **49**, R2532 (1994).
- [9] M. Dubé *et al.*, *Phys. Rev. Lett.* **83**, 1628 (1999); *Eur. Phys. J. B* **15**, 701 (2000).
- [10] In the case of depinning for  $\lambda = 0$ , the diffusion term must equilibrate the disorder and one gets to a driving force  $F_c = [\Delta(0)^{4d}/(va)]^{d/(2(4-d))}$  instead of Eq. (3).
- [11] Here, we assume implicitly that the intrinsic roughness does not depend on  $\lambda$ . If this was the case, the scaling argument might fail leading to a finite  $\lambda_c$ .
- [12] T.J. Newman and A.J. Bray, *J. Phys. A* **29**, 7917 (1996).
- [13] Following [14], we also checked that there is no anomalous scaling phenomena by computing the local width and power spectrum.
- [14] J.M. López, M.A. Rodríguez, and R. Cuerno, *Phys. Rev. E* **56**, 3993 (1997); J.M. López, *Phys. Rev. Lett.* **83**, 4594 (1999); J.J. Ramasco, J.M. López, and M.A. Rodríguez, *Phys. Rev. Lett.* **84**, 2199 (2000).
- [15] J. Kertész and D.E. Wolf, *Phys. Rev. Lett.* **62**, 2571 (1989).
- [16] H.A. Makse and L.A.N. Amaral, *Europhys. Lett.* **31**, 379 (1995).
- [17] J.M. López and H.J. Jensen, *Phys. Rev. Lett.* **81**, 1734 (1998).
- [18] L.-H. Tang and H. Leschhorn, *Phys. Rev. A* **45**, R8309 (1992).
- [19] S.V. Buldyrev *et al.*, *Phys. Rev. A* **45**, R8313 (1992); L.A.N. Amaral *et al.*, *Phys. Rev. E* **51**, 4655 (1995).
- [20] L.A.N. Amaral, A.-L. Barabási, and H.E. Stanley, *Phys. Rev. Lett.* **73**, 62 (1994); L.A.N. Amaral, A.-L. Barabási, H.A. Makse, and H.E. Stanley, *Phys. Rev. E* **52**, 4087 (1995).
- [21] H. Leschhorn, *Physica A* **195**, 324 (1993).
- [22] S. Roux and A. Hansen, *J. Phys. I* **4**, 515 (1994).

INTERFACE DEPINNING IN THE ABSENCE OF . . .

PHYSICAL REVIEW E **64** 066109

- [23] J.M. López and M.A. Rodríguez, *J. Phys. I* **7**, 1191 (1997).
- [24] S. Stepanow, *J. Phys. II* **5**, 11 (1995).
- [25] Notice that, although it was first thought that in DPD models  $\lambda \rightarrow \infty$  as the depinning transition is approached, it has recently been shown [26] that this inconsistency was due to the incorrect definition of the tilt-velocity dependence used in [20]. In fact,  $\lambda$  remains finite at the transition [26].
- [26] N. Neshkov, *Phys. Rev. E* **61**, 6023 (2000).
- [27] L-H. Tang, M. Kardar, and D. Dhar, *Phys. Rev. Lett.* **74**, 920 (1995).
- [28] K. Park, H.-J. Kim, and I.-M. Kim, *Phys. Rev. E* **62**, 7679 (2000).
- [29] R. Albert *et al.*, *Phys. Rev. Lett.* **81**, 2926 (1998).
- [30] M.A. Rubio, C.A. Edwards, A. Dougherty, and J.P. Gollub, *Phys. Rev. Lett.* **63**, 1685 (1989).
- [31] V.K. Horváth and H.E. Stanley, *Phys. Rev. E* **52**, 5166 (1995).
- [32] A.S. Balankin, A. Bravo-Ortega, and D.M. Matamoros, *Philos. Mag. Lett.* **80**, 503 (2000).
- [33] C.-H. Lam and V.K. Horváth, *Phys. Rev. Lett.* **85**, 1238 (2000); see also the comment by M. Dubé *et al.*, *ibid.* **86**, 6046 (2001), and the reply by C.-H. Lam and V.K. Horváth, *ibid.* **86**, 6047 (2001).

### Anomalous roughening of Hele-Shaw flows with quenched disorder

J. Soriano<sup>1</sup>, J.J. Ramasco<sup>2,3</sup>, M.A. Rodríguez<sup>2</sup>, A. Hernández-Machado<sup>1,4</sup>, and J. Ortín<sup>1</sup>

<sup>1</sup> *Departament ECM, Facultat de Física, Universitat de Barcelona  
Diagonal 647, E-08028 Barcelona, Spain*

<sup>2</sup> *Instituto de Física de Cantabria, CSIC  
Avenida Los Castros, E-39005 Santander, Spain.*

<sup>3</sup> *Departamento de Física Moderna, Universidad de Cantabria, E-39005 Santander, Spain.*

<sup>4</sup> *Groupe de Physique des Solides, Université Pierre-et-Marie-Curie  
Tour 23, 2 place Jussieu, 75251 Paris Cedex 05, France.*

(November 29, 2001)

The kinetic roughening of a stable oil-air interface, moving in a Hele-Shaw cell which contains a quenched columnar disorder (tracks) has been studied. Capillarity is responsible for the dynamic evolution of the resulting rough interface, which exhibits anomalous scaling. The three independent exponents needed to characterize the anomalous scaling are determined experimentally. The scaling anomalies are explained in terms of the initial acceleration and subsequent deceleration of the interface tips in the tracks coupled by mass conservation. A phenomenological model that reproduces the measured global and local exponents has been introduced.

PACS: 47.55.Mh, 68.35.Ct, 05.40.-a

Viscous fluid fronts in porous media can be good prototypes of rough growing interfaces in disordered media [1]. The motion of oil or water through soils has interesting practical applications in oil recovery, aquifer contamination or isolation of nuclear waste. The characterization of the statistical properties of a roughening front has been usually done in terms of the *rms* interfacial width. Recently, a generic ansatz [2] has been proposed to derive all the existing forms of dynamic scaling, e.g. the standard Family-Vicsek (FV) dynamic scaling and several forms of anomalous dynamic scaling in which the scaling of the global width differs substantially from the scaling of the local interface fluctuations. In this latter case, three independent exponents, instead of two as in the FV case, are necessary to characterize the anomalous behaviour. This fact makes the analysis of experiments difficult and questions the validity of other approaches performed in the past. Recently, some experiments on molecular beam epitaxy [3], sputtering [4], fracture mechanics [5-7], and electrodeposition [8] have been discussed in terms of anomalous scaling, but its physical origin remains poorly understood.

In this Letter we report the first observations of anomalous scaling in experiments of Hele-Shaw flows with quenched disorder. We consider an initially flat front of oil and air at rest, or with a small constant average velocity, in a horizontal Hele-Shaw cell with columnar disorder. The columnar quenched disorder consists of continuous copper tracks on a fibre-glass substrate in the advancing direction of growth and randomly distributed in the perpendicular direction, as can be seen in Fig. 1. In this situation, the correlation of the disorder in the advancing direction is infinite and the local motion relative to the average interface position is driven by cap-

illarity. This effect is caused by the different curvatures of the advancing front in the third dimension, depending on whether the oil is on a copper track or in the fibre-glass substrate, and is responsible for the resulting rough interface. We characterize the anomalous scaling by the presence of a vertical shift in the experimental power spectra at different times. An analysis of the *rms* width at short- and long-length scales plus a collapse of the power spectra enables an independent determination of the three exponents characteristic of anomalous scaling.

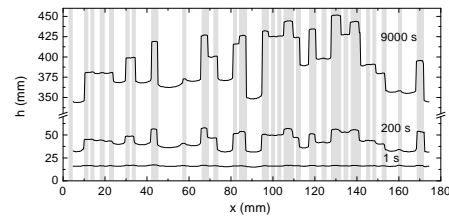


FIG. 1. Sequence of typical oil-air interfaces. The silicone oil moves upwards in the picture, and the disorder pattern is represented in grey. The experimental parameters are  $b = 0.36$  mm and  $v = 0.04$  mm/s.

We associate the anomalous roughening with the initial acceleration and subsequent deceleration of the liquid on the copper tracks, caused by capillary forces, and the coupling of the motion over tracks and over fibre-glass due to mass conservation. The anomaly effect decreases as the externally imposed average velocity increases, and disappears when the velocity is large enough to override the local acceleration and deceleration [9]. To explain the experimental results, we propose a phenomenological

model which gives global and local exponents in good agreement with the experimental exponents.

The roughening process of an initially flat interface is described in terms of the interfacial root-mean-square width  $w_l$ , measured in windows of size  $l \leq L$ . In the anomalous scaling theory [10]:  $w(l, t) \sim t^\beta$  for  $t < t_l$ ,  $w(l, t) \sim l^{\alpha_{loc}} t^{\beta^*}$  for  $t_l < t < t_x$ , and  $w(l, t) \sim l^{\alpha_{loc}} L^{\alpha - \alpha_{loc}}$  for  $t_x < t$ . The local time  $t_l \sim l^{1/z}$ , and the saturation time  $t_x \sim L^{1/z}$ . Here  $\beta$  and  $\beta^*$  are the growth exponents,  $\alpha$  and  $\alpha_{loc}$  the roughness exponents, and  $z$  the dynamic exponent. They satisfy the scaling relations  $\alpha = z\beta$  and  $\alpha - \alpha_{loc} = z\beta^*$ . Since there are five exponents and two scaling relations, we need three independent exponents to characterize the dynamics. The roughness exponents are usually determined through the power spectrum, which is less sensitive to finite size effects, and scales as  $S(k, t) = k^{-(2\alpha+1)} s_A(kt^{1/z})$ , where  $s_A$  obeys  $s_A(u) \sim u^{2\alpha+1}$  when  $u \ll 1$  and  $s_A(u) \sim u^{2\theta}$  when  $u \gg 1$ . Here  $\theta = \alpha - \alpha_{loc}$ . The anomalous scaling leads to the usual FV scaling when  $\theta = 0$  and  $\beta^* = 0$ .

The experiments have been performed in a horizontal Hele-Shaw cell,  $190 \times 550$  ( $L \times H$ ) mm<sup>2</sup>, made of two glass plates 20 mm thick. The copper tracks on the substrate are randomly distributed along  $x$ , with a filling factor  $f = 35\%$ . The tracks are  $d = 0.06 \pm 0.01$  mm high and have a lateral size of  $1.50 \pm 0.04$  mm. The distance between the top plate and the substrate defines the gap spacing  $b$ , which has been varied in the range  $0.16 \leq b \leq 0.75$  mm. We have used 4 different disorder configurations and carried out 2 identical runs per disorder configuration. A silicone oil (kinematic viscosity  $\nu = 50$  mm<sup>2</sup>/s, density  $\rho = 998$  kg/m<sup>3</sup>, and surface tension oil-air  $\sigma = 20.7$  mN/m at room temperature) was injected into one side of the cell at constant volumetric injection rate. The oil completely wets the glass plates, the substrate, and the copper tracks. The evolution of the interface at average velocity  $v$  was monitored using two CCD cameras with a resolution of 0.38 mm/pixel. Further details of the experimental set-up can be found in [11].

In Fig. 2 we present the results for the interfacial width as a function of time at long ( $l = L$ ) and short ( $l = L/128$ ) scales. We obtain clear power law dependencies that last for three decades in time, with  $\beta = 0.52 \pm 0.02$  and  $\beta^* = 0.26 \pm 0.03$  respectively. Notice that having a growth exponent  $\beta^* \neq 0$  is a sign of anomalous scaling. The temporal evolution of the power spectrum is presented in Fig. 3(a). At very short times we observe a regime with  $S(k) \sim k^{-3.4}$ . It is a super-rough transient regime created when the fluid on the tracks reaches its maximum velocity after coming into contact with the disorder. The main regime appears further on, with  $S(k) \sim k^{-2.1}$ , and a vertical shift that progressively

decreases with time and disappears at saturation ( $t \gtrsim 450$  s). The vertical shift of the power spectra is a sign of intrinsic anomalous scaling, in which the spectral exponent [2] can be identified with the local roughness exponent, so that  $\alpha_{loc} = 0.55 \pm 0.10$ .

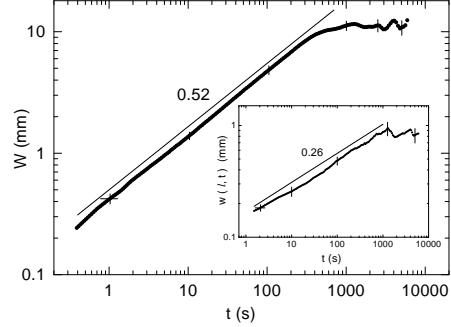


FIG. 2. Experimental determination of  $\beta$  (main plot) and  $\beta^*$  (inset). We plot  $W(t) = [w^2(L, t) - w^2(L, 0)]^{1/2}$  to minimize the influence of the initial condition. The experimental parameters are  $b = 0.36$  mm and  $v = 0.08$  mm/s.

Using the above set-up, the three independent exponents  $\beta$ ,  $\beta^*$ ,  $\alpha_{loc}$  have been obtained directly from the experiments. The other two exponents  $\alpha$ ,  $z$  can be obtained from the scaling relations. In order to verify the whole scaling, however, we prefer to determine the critical exponents by performing the best collapse of the spectra compatible with the experimental results. The collapse, presented in Fig. 3(b), leads to the following set of scaling exponents:

$$\begin{aligned} \beta &= 0.5 \pm 0.04, \quad \beta^* = 0.25 \pm 0.03, \\ \alpha &= 1.0 \pm 0.1, \quad \alpha_{loc} = 0.5 \pm 0.1, \quad z = 2.0 \pm 0.2. \end{aligned} \quad (1)$$

We have also looked into the possibility of multiscaling [12] through the scaling of the generalized correlations of order  $q$ , of the form  $\{(h(x+l, t) - h(x, t))^q\}^{1/q} \sim l^{\alpha_q}$ . Different exponents for  $\alpha_q$ :  $\alpha_2 \simeq 0.6$ ,  $\alpha_4 \simeq 0.4$ , and  $\alpha_6 \simeq 0.2$  were obtained, which confirm the existence of multiscaling in the experiment.

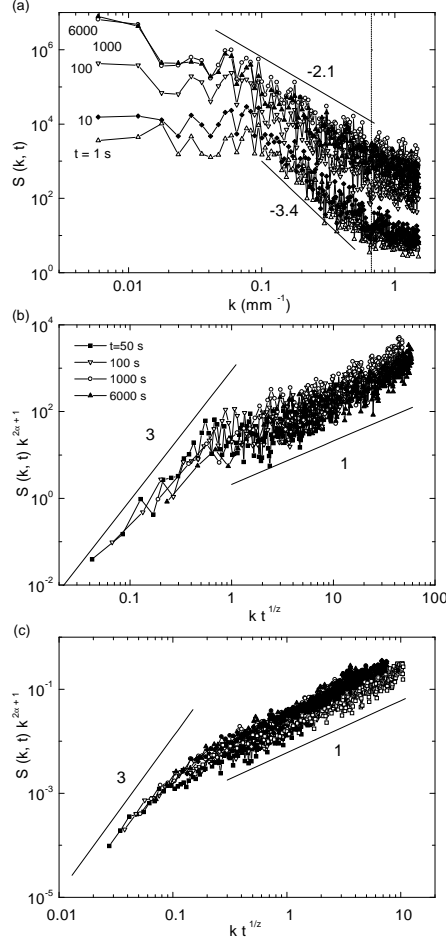


FIG. 3. (a) Temporal evolution of the power spectrum for the same experiments as Fig. 2. The vertical line gives the value of  $k$  associated with the spatial scale of the disorder. (b) Collapse of the experimental power spectra for  $t > 10$  s. (c) Collapse of the power spectra obtained from numerical simulation of the phenomenological model.

To understand the origin of anomalous scaling, we should look at interfacial dynamics in greater detail. An initially flat oil-air interface, moving at a nominal average velocity  $v$ , experiences local accelerations at those points that touch a copper track for the first time. The local velocity of these points jumps to a maximum in a characteristic time of 1 s, and then relaxes as  $t^{-1/2}$  to the nominal average velocity. The maximum veloc-

ity reached in a given track increases with track width and decreases with gap spacing. As can be observed in Fig. 4, the average velocity over copper tracks,  $v_+$ , and fibre glass substrate,  $v_-$ , follows  $v_{\pm} = v \pm (v_M - v)t^{-1/2}$ , where  $v_M$  is the maximum of the average velocity over tracks. This functionality varies slightly with gap spacing due to the increasing correlation between neighbouring tracks. However, for gap spacings above  $b, \simeq 0.6$  mm is not reached. This behaviour of different velocities over copper and fibre-glass tracks is an important ingredient for anomalous scaling. At very short times the difference in velocity is maximum, thus giving a maximum shift between spectra. Close to saturation the velocity over copper tracks and fibre-glass almost equals the nominal velocity, and the vertical shift disappears. When we inhibit the relaxation of the velocity over copper tracks by either injecting at velocities  $v > v_M$  or using large gap spacings, the anomalous scaling disappears. This scenario has been studied experimentally by exploring different gap spacings and velocities, and the results are summarized in Fig. 5, where we show a phase diagram representing the regions where the anomalous scaling is present (grey region,  $\theta \neq 0$ ) or not (white regions,  $\theta = 0$ ). The solid line represents the function  $v_M(b)$ , and the vertical line the limit between strong and weak capillary forces.

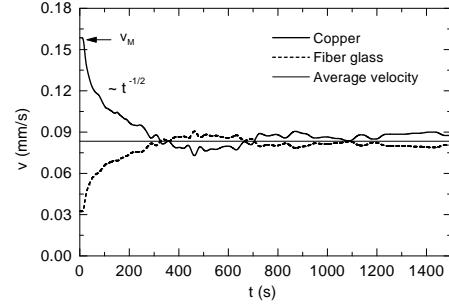


FIG. 4. Local interface velocity over copper tracks ( $v_+$ ) and over fibre-glass tracks ( $v_-$ ), for  $b = 0.36$  mm and  $v = 0.08$  mm/s.

The critical exponents of the anomalous scaling depend on gap spacing and velocity. We have seen that the anomalous exponent  $\theta$  tends to  $\theta = 0$  as we increase either the velocity or the gap spacing. This exponent is particularly sensitive to variations of the gap spacing. For  $b \gtrsim 0.6$  mm,  $\theta = 0$  at any velocity. The experimental parameters  $b = 0.36$  mm and  $v = 0.08$  mm/s, deep in the grey region of Fig. 5, give the appropriate conditions to fully characterize the anomalous scaling experimentally. Smaller gap spacings mean that the correlation length in the  $x$  direction cannot grow to scales larger than the average track width, and larger gap spacings give too

weak an anomalous scaling because the  $t^{-1/2}$  law is only obeyed on the widest tracks.

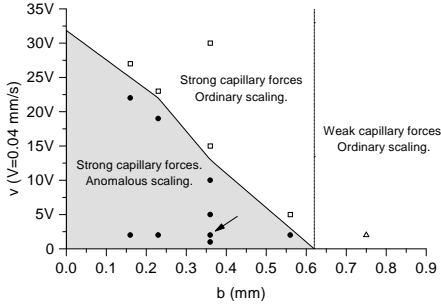


FIG. 5. Phase diagram  $v(b)$  indicating the regions where the anomalous scaling is observable. The symbols represent the different regions explored experimentally, and the arrow indicates the parameters used in the paper.

Finally, we have developed a phenomenological model based on the interplay of capillarity with a local diffusive coupling between columns that reproduces experimental behaviour. We first write an analytical model showing this interplay as

$$\partial_t h(x, t) = \partial_x D(x) \partial_x h(x, t) + v + (v_M - v) t^{-1/2} \eta(x), \quad (2)$$

, where  $\eta(x)$  is a dichotomous noise, with values  $+1$  and  $-1$ , which model the geometry of the columnar disorder. The diffusive coupling is introduced to obtain the dynamics with  $z = 2$  found in experiments, and the other two terms account for the behaviour of  $v_{\pm}$  observed experimentally. Although the term  $t^{-1/2}$  introduces some nonlocality in the model, this is essentially different from non-local models [11,13,14] introduced recently to account for mass conservation. By dimensional analysis of the simplest version ( $D = \text{constant}$ ), one obtains the same global exponents found in experiments:  $\alpha = 1$ ,  $\beta = 0.5$ ,  $z = 2$ . The local exponent  $\beta^*$  can be deduced from the evolution of the local slopes  $\partial_x h(x, t)$  [15], resulting in  $\beta^* = 0$ , so that  $\alpha_{loc} = \alpha = 1$ . Hence this model reproduces global behaviour, but not local behaviour. In order to recover local scaling, the fact that the interface is almost flat inside each track, easily observed in Fig. 1, must be introduced in our model as well as the fact that fluctuations occur only between tracks. Analytically this is imposed in Eq. 2 through an inhomogeneous diffusion coefficient  $D(x)$ . Numerically, we have introduced this effect by spatially averaging the interface inside each track once each  $n$  time steps. We thus recover interfaces that are morphologically analogous to experimental interfaces. The exponents derived

from the scaling of the power spectra shown in Fig. 3(c), and the multiscaling exponents, reproduce the values determined experimentally. It is remarkable that the simulated spectra, averaged over 50 experimental runs, and the measured spectra, averaged over only 4 experimental runs, have comparable dispersions. This is due to the lack of self-averaging in this problem with persistent disorder. In summary, our phenomenological model enables the relevant effects in the experiment to be both identified and calibrated.

In conclusion, we have presented the first experimental evidence of anomalous scaling in the dynamic roughening of a fluid interface in a Hele-Shaw cell with quenched disorder, and we have studied the experimental conditions for the appearance of the observed anomaly. The exponents  $\beta$ ,  $\beta^*$ , and  $\alpha_{loc}$  have been measured independently and their value has been refined by imposing the scaling relations through a collapse of the power spectra. Finally, we have introduced an interfacial equation which models the capillary phenomena observed in the experiment at a phenomenological level. The model reproduces both the morphology of the interfaces and the values of the anomalous scaling exponents.

We are grateful to J.M. López for fruitful discussions. The research has received financial support from the Dirección General de Investigación (MCT, Spain) under projects BFM2000-0628-C03-01 and -02. J. Soriano and J.J. Ramasco have received financial support from the Spanish Ministry of Science and the Spanish Ministry of Education respectively.

- 
- [1] P. Meakin, *Fractals, scaling and growth far from equilibrium* (Cambridge University Press, Cambridge, 1998); M. Kardar, Phys. Rep. **301**, 85 (1998); J. Krug, Adv. Phys. **46**, 139 (1997).
  - [2] J.J. Ramasco *et al.*, Phys. Rev. Lett. **84**, 2199 (2000).
  - [3] H.-N. Yang *et al.*, Phys. Rev. Lett. **73**, 2348 (1994).
  - [4] J.H. Jeffries *et al.*, Phys. Rev. Lett. **76**, 4931 (1996).
  - [5] J.M. López and J. Schmittbuhl, Phys. Rev. E **57**, 6405 (1998).
  - [6] S. Morel *et al.*, Phys. Rev. E **58**, 6999 (1998).
  - [7] S. Morel *et al.*, Phys. Rev. Lett. **85**, 1678 (2000).
  - [8] S. Huo and W. Schwarzacher, Phys. Rev. Lett. **86**, 256 (2001).
  - [9] The anomaly also decreases as the persistence of the disorder in the advancing direction is reduced, e.g. when tracks are replaced by square islands (J. Soriano, J. Ortín and A. Hernández-Machado, to be published).
  - [10] J.M. López and M.A. Rodríguez, Phys. Rev. E **54**, R2189 (1996); J.M. López *et al.*, Physica A **246**, 329 (1997).
  - [11] A. Hernández-Machado *et al.*, Europhys. Lett. **55**, 194

- (2001)
- [12] J. Krug, Phys. Rev. Lett. **72**, 2907 (1994).
- [13] V. Ganesan and H. Brenner, Phys. Rev. Lett. **81**, 578 (1998).
- [14] M. Dubé *et al.*, Phys. Rev. Lett. **83**, 1628 (1999); Eur. Phys. J. B **15**, 701 (2000); M. Dubé *et al.*, Eur. Phys. J. B **15**, 691 (2000).
- [15] J.M. López, Phys. Rev. Lett. **83**, 4594 (1999).

# Bibliography

- [Ahr 2000] M. Ahr and M. Biehl, Phys. Rev. E **62** 1773.
- [Ala-Nissila 1993] T. Ala-Nissila, T. Hjelt, J.M. Kosterlitz and O. Venäläinen, J. Stat. Phys. **72** 207.
- [Alon 1996] U. Alon, M.R. Evans, H. Hinrichsen and D. Mukamel, Phys. Rev. Lett. **76** 2746.
- [Amar 1990] J.G. Amar and F. Family, Phys. Rev. A **41** 3399.
- [Amar 1993] J.G. Amar, P.-M. Lam and F. Family, Phys. Rev. E **47** 3242.
- [Amaral 1994] L.A.N. Amaral, A.-L. Barabási and H.E. Stanley, Phys. Rev. Lett. **73** 62.
- [Amaral 1995] L.A.N. Amaral, A.-L. Barabási, H.A. Makse and H.E. Stanley, Phys. Rev. E **52** 4087.
- [Amaral 1995b] L.A.N. Amaral, A.-L. Barabási, S.V. Buldyrev, S.T. Harrington, S. Havlin, R. Sadr-Lahijany and H.E. Stanley, Phys. Rev. E **51** 4655.
- [Amaral 1998] L.A.N. Amaral and H.A. Makse, Phys. Rev. Lett. **80** 5706.

- [Bak 1987] P. Bak, C. Tang and K. Wiesenfeld, Phys. Rev. Lett. **59** 381.
- [Bak 1988] P. Bak, C. Tang and K. Wiesenfeld, Phys. Rev. E **38** 364.
- [Balakin 2000] A.S. Balakin, A. Bravo-Ortega and D. Morales, Philos. Mag. Lett. **80** 503.
- [Ballestad 2001] A. Ballestad, B.J. Ruck, M. Adamcyk, T. Pinnington and T. Tiedje, Phys. Rev. Lett. **86** 2377.
- [Barabási 1995] Albert-László Barabási and H. Eugene Stanley, *Fractal concepts in surface growth*, Cambridge University Press.
- [Barabási 1996] A.-L. Barabási, G. Grinstein and M.A. Muñoz, Phys. Rev. Lett. **76** 1481.
- [Ben-Jacob 1983] E. Ben-Jacob, N. Goldenfeld, J.S. Langer and G. Schön, Phys. Rev. Lett. **51** 1930.
- [Bianconi 1999] G. Bianconi, M.A. Muñoz, A. Gabrielli and L. Pietronero, Phys. Rev. E **60** 3719.
- [Bouchaud E. 1990] E. Bouchaud, G. Lapasset and J. Planès, Europhys. Lett. **13** 73.
- [Bouchaud E. 1993] E. Bouchaud, J. Planès, G. Lapasset and S. Navéos, Phys. Rev. B **48** 2917.
- [Bouchaud E. 1997] E. Bouchaud, J. Phys.: Condens. Matter **9** 4319.
- [Bouchaud J.P. 1993] J.P. Bouchaud, E. Bouchaud, G. Lapasset and J. Planès, Phys. Rev. Lett. **71** 2240.

- [Bruinsma 1984] R. Bruinsma and G. Aeppli, Phys. Rev. Lett. **52** 1547.
- [Buceta 2000] J. Buceta, J.M. Pastor, M.A. Rubio and F.J. de la Rubia, Phys. Rev. E **61** 6015.
- [Buldyrev 1992] S.V. Buldyrev, A.L. Barabási, F. Caserta, S. Havlin, H.E. Stanley and T. Vicsek, Phys. Rev. A **45** R8313.
- [Buldyrev 1992b] S.V. Buldyrev, A.L. Barabási, S. Havlin, J. Kertész, H.E. Stanley and H.S. Xenias, Physica A **191** 220.
- [Burgers 1974] J.M. Burgers, *The Nonlinear Diffusion Equation*, D. Reidel Publishing Company.
- [Castellano 1998] C. Castellano, M. Marsili and L. Pietronero, Phys. Rev. Lett. **80** 3527.
- [Castellano 1999] C. Castellano, M. Marsili, M.A. Muñoz and L. Pietronero, Phys. Rev. E **59** 6460.
- [Colaioni 2001] F. Colaioni and M.A. Moore, Phys. Rev. Lett. **86** 3946.
- [Csahók 1993] Z. Csahók, K. Honda and T. Vicsek, J. Phys. A: Math. Gen. **26** L171.
- [Csahók 1993b] Z. Csahók, K. Honda, E. Somfai, M. Vicsek and T. Vicsek, Physica A **200** 136.
- [Daguier 1996] P. Daguier, E. Bouchaud and G. Lapasset, Europhys. Lett. **31** 367.
- [Daguier 1996] P. Daguier, S. Hénaux, E. Bouchaud and F. Creuzet, Phys. Rev. E **53** 5637.

- [Daguier 1997] P. Daguier, B. Nghiem, E. Bouchaud and F. Creuzet, Phys. Rev. Lett. **78** 1062.
- [Das Sarma 1991] S. Das Sarma and P. Tamborenea, Phys. Rev. Lett. **66** 325.
- [Das Sarma 1992] S. Das Sarma and S.V. Ghaisas, Phys. Rev. Lett. **69** 3762.
- [Das Sarma 1994] S. Das Sarma, S.V. Ghaisas and J.M. Kim, Phys. Rev. E **49** 122.
- [Das Sarma 1996] S. Das Sarma, C.J. Lanczycki, R. Kotlyar and S.V. Ghaisas, Phys. Rev. E **53** 359.
- [Das Sarma 1997] S. Das Sarma and P. Punyindu, Phys. Rev. E **55** 5361.
- [Dasgupta 1996] C. Dasgupta, S. Das Sarma and J.M. Kim, Phys. Rev. E **54** R4552.
- [Dasgupta 1997] C. Dasgupta, J.M. Kim, M. Dutta and S. Das Sarma, Phys. Rev. E **55** 2235.
- [Delaplace 1999] A. Delaplace, J. Schmittbuhl and K.J. Måløy, Phys. Rev. E **60** 1337.
- [Desjardins 1999] P. Desjardins, T. Spila, O. Gürdal, N. Taylor and J.E. Greene, Phys. Rev. B **60** 15993.
- [Dickman 2000] R. Dickman and M.A. Muñoz, Phys. Rev. E **62** 7632.
- [Doherty 1994] J.P. Doherty, M.A. Moore, J.M. Kim and A.J. Bray, Phys. Rev. Lett. **72** 2041.

- [Dong 1993] M. Dong, M.C. Marchetti, A.A. Middleton and V. Vinokur, Phys. Rev. Lett. **70** 662.
- [Doty 1992] C.A. Doty and J.M. Kosterlitz, Phys. Rev. Lett. **69** 1979.
- [Dubé 1999] M. Dubé, M. Rost, K.R. Elder, M. Alava, S. Majaniemi and T. Ala-Nissila, Phys. Rev. Lett. **83** 1628.
- [Dubé 2000] M. Dubé, M. Rost, K.R. Elder, M. Alava, S. Majaniemi and T. Ala-Nissila, Eur. Phys. J. B **15** 701.
- [Dubé 2001] M. Dubé, M. Rost, K.R. Elder, M. Alava, S. Majaniemi and T. Ala-Nissila, Phys. Rev. Lett. **86** 6046.
- [Edwards 1982] S.F. Edwards and D.R. Wilkinson, Proc. R. Soc. Lond. A **381** 17.
- [Ernst 1994] H.-J. Ernst, F. Fabre, R. Folkerts and J. Lapujoulade, Phys. Rev. Lett. **72** 112.
- [Ertas 1992] D. Ertas and M. Kardar, Phys. Rev. Lett. **69** 929.
- [Falk 1994] J. Falk, M.H. Jensen and K. Sneppen, Phys. Rev. E **49** 2804.
- [Family 1985] F. Family and T. Vicsek, J. Phys. A **18** L75.
- [Family 1986] F. Family, J. Phys. A **19** L441.
- [Feder 1988] Jens Feder, *Fractals*, Plenum Press, New York.
- [Fineberg 1999] J. Fineberg and M. Marder, Physics Reports **313** 1.
- [Fisher 1998] D.S. Fisher, Physics Reports **301** 113.

- [Frey 1994] E. Frey and U.C. Täuber, *Phys. Rev. E* **50** 1024.
- [Ganesan 1998] V. Ganesan and H. Brenner, *Phys. Rev. Lett.* **81** 578.
- [Guilloteau 1996] E. Guilloteau, H. Charrue and F. Creuzet, *Europhys. Lett.* **34** 549.
- [Guzzo 1991] L. Guzzo, A. Iovino, G. Chincarini, R. Giovanelli and M.P. Haynes, *Astrophys. J.* **382** L5.
- [Havlin 1995] S. Havlin, L.A.N. Amaral, S.V. Buldyrev, S.T. Harrington and H.E. Stanley, *Phys. Rev. Lett.* **74** 4205.
- [He-S. 1992] S. He, G.L.M.K.S. Kahanda and P-Z. Wong, *Phys. Rev. Lett.* **69** 3731.
- [He-YL. 1992] Y.-L. He, H.-N. Yang, T.-M. Lu and G.-C. Wang, *Phys. Rev. Lett.* **69** 3770.
- [Hentschel 1991] H.G.E. Hentschel and F. Family, *Phys. Rev. Lett.* **66** 1982.
- [Hernández-M 2001] A. Hernández-Machado, J. Soriano, A.M. Lacasta, M.A. Rodríguez, L. Ramírez-Piscina and J. Ortín, *Europhys. Lett.* **55** 194.
- [Heyvaert. 1996] I. Heyvaert, J. Krim, C. van Haesendonck and Y. Bruynseraede, *Phys. Rev. E* **54** 349.
- [Hinrichsen 2000] H. Hinrichsen, *Adv. Phys.* **49** 815.
- [Horváth 1990] V.K. Horváth, F. Family and T. Vicsek, *Phys. Rev. Lett.* **65** 1388.

- [Horváth 1991] V.K. Horváth, F. Family and T. Vicsek, *J. Phys. A* **24** L25.
- [Horváth 1995] V.K. Horváth and H.E. Stanley, *Phys. Rev. E* **52** 5166.
- [Huang 1996] Z.-F. Huang and B.-L. Gu, *Phys. Rev. E* **54** 5935.
- [Huo 2001] S. Huo and W. Schwarzacher, *Phys. Rev. Lett.* **86** 256.
- [Jeffries 1996] J.H. Jeffries, J.-K. Zuo and M.M. Craig, *Phys. Rev. Lett.* **76** 4931.
- [Jensen 1995] H.J. Jensen, *J. Phys. A: Math. Gen.* **28** 1861.
- [Jeong 1996] H. Jeong, B. Kahng and D. Kim, *Phys. Rev. Lett.* **77** 5094.
- [Jeong 1999] H. Jeong, B. Kahng and D. Kim, *Phys. Rev. E* **59** 1570.
- [Jost 1998] M. Jost and K.D. Usadel, *Physica A* **225** 15.
- [Kardar 1986] M. Kardar, G. Parisi and Y.-C. Zhang, *Phys. Rev. Lett.* **56** 889.
- [Kardar 1987] M. Kardar and Y.-C. Zhang, *Phys. Rev. Lett.* **58** 2087.
- [Kertész 1989] J. Kertész and D.E. Wolf, *Phys. Rev. Lett.* **62** 2571.
- [Kessler 1991] D.A. Kessler, H. Levine and Y. Tu, *Phys. Rev. A* **43** 4551.

- [Kessler 1992] D.A. Kessler, H. Levine and L.M. Sander, Phys. Rev. Lett. **69** 100.
- [Kim 1989] J.M. Kim and J.M. Kosterlitz, Phys. Rev. Lett. **62** 2289.
- [Koplik 1985] J. Koplik and H. Levine, Phys. Rev. B **32** 280.
- [Kotrla 1992] M. Kotrla, A.C. Levi and P. Šmilauer, Europhys. Lett. **20** 25.
- [Krug 1987] J. Krug, Phys. Rev. A **36** 5465.
- [Krug 1993] J. Krug, M. Plischke and M. Siegert, Phys. Rev. Lett. **70** 3271.
- [Krug 1994] J. Krug, Phys. Rev. Lett. **72** 2907.
- [Krug 1997] J. Krug, Adv. Phys. **46** 139.
- [Kwon 1996] T.H. Kwon, A.E. Hopkins and S.E. O'Donnell, Phys. Rev. E **54** 685.
- [Labini 1998] F.S. Labini, M. Montuori and L. Pietronero, Phys. Rep. **293** 61.
- [Lai 1991] Z.-W. Lai and S. Das Sarma, Phys. Rev. Lett. **66** 2348.
- [Lam 1998] C.-H. Lam and F.G. Shin, Phys. Rev. E **57** 6506.
- [Lam 2000] C.-H. Lam and V.K. Horváth, Phys. Rev. Lett. **85** 1238.
- [Lam 2001] C.-H. Lam and V.K. Horváth, Phys. Rev. Lett. **86** 6047.

- [Langer 1980] J.S. Langer, *Rev. Mod. Phys.* **52** 1.
- [Larkin 1970] A.I. Larkin, *Sov. Phys. JETP* **31** 784.
- [Lässig 1997] M. Lässig and H. Kinzelbach, *Phys. Rev. Lett.* **78** 903.
- [Lässig 1998] M. Lässig, *Phys. Rev. Lett.* **80** 2366.
- [Lemson 1991] G. Lemson and R.H. Sanders, *Mon. Not. R. Astron. Soc.* **252** 319.
- [Leschhorn 1993] H. Leschhorn and L.-H. Tang, *Phys. Rev. Lett.* **70** 2973.
- [Leschhorn 1993b] H. Leschhorn, *Physica A* **195** 324.
- [Leschhorn 1994] H. Leschhorn and L.-H. Tang, *Phys. Rev. E* **49** 1238.
- [Leschhorn 1996] H. Leschhorn, *Phys. Rev. E* **54** 1313.
- [Leschhorn 1997] H. Leschhorn, T. Nattermann, S. Stepanow and L.-H. Tang, *Ann. Phys. (Leipzig)* **6** 1.
- [López 1996] J. M. López and M.A. Rodríguez, *Phys. Rev. E* **54** R2189.
- [López 1997] J. M. López and M.A. Rodríguez, *J. Phys. I (France)* **7** 1191.
- [López 1997b] J. M. López, M.A. Rodríguez and R. Cuerno, *Physica A* **246** 329.
- [López 1997c] J. M. López, M.A. Rodríguez and R. Cuerno, *Phys. Rev. E* **56** 3993.

- [López 1998] J. M. López and H.J. Jensen, Phys. Rev. Lett. **81** 1734.
- [López 1998b] J. M. López and J. Schmittbuhl, Phys. Rev. E **57** 6405.
- [López 1999] J. M. López , Phys. Rev. Lett. **83** 4594.
- [Makse 1995] H.A. Makse and L.A.N. Amaral, Europhys. Lett. **31** 379.
- [Makse 1995b] H.A. Makse, Phys. Rev. E **52** 4080.
- [Måløy 1992] K.J. Måløy, A. Hansen and E.L. Hinrichsen, Phys. Rev. Lett. **68** 213.
- [Mandelbrot 1977] Benoit B. Mandelbrot, *Fractals: form, chance and dimension*, W. H. Freeman, San Francisco.
- [Mandelbrot 1982] Benoit B. Mandelbrot, *The fractal geometry of Nature*, W. H. Freeman, New York.
- [Mandelbrot 1984] B.B. Mandelbrot, Passoja D.E. and Paullay A.J., Nature **308** 721.
- [Marinari 2001] E. Marinari, A. Pagnani, G. Parisi and Z. Rácz, condmat/0105158.
- [Martínez 1994] V.J. Martínez and P. Coles, Astrophys. J. **437** 550.
- [Martínez 1998] V.J. Martinez, M.J. Pons-Bordería, R.A. Moyeed and M.J. Graham, Mon. Not. R. Astron. Soc. **298** 1212.
- [Maslov 1994] S. Maslov and M. Paczuski, Phys. Rev. E **50** R643.

- [Maslov 1994b] S. Maslov, M. Paczuski and P. Bak, Phys. Rev. Lett. **73** 2162.
- [Maunuksela 1997] J. Maunuksela, M. Myllys, O.-P. Kähkönen, J. Timonen, N. Provatas, M.J. Alava and T. Ala-Nissila, Phys. Rev. Lett. **79** 1515.
- [Maunuksela 1998] J. Maunuksela, M. Myllys, J. Timonen, M. Kuittu, T. Ala-Nissila, M.J. Alava and N. Provatas, Phys. Rev. Lett. **80** 5707.
- [Meakin 1998] Paul Meakin, *Fractals, scaling and growth far from equilibrium*, Cambridge University Press.
- [Meakin 1986] P. Meakin, P. Ramanlal, L.M. Sander and R.C. Ball, Phys. Rev. A **34** 5091.
- [Medina 1989] E. Medina, T. Hwa and M. Kardar, Phys. Rev. A **39** 3053.
- [Middleton 1992] A.A. Middleton, Phys. Rev. Lett. **68** 670.
- [Moore 1995] M.A. Moore, T. Blum, J.P. Doherty and M. Marsili, Phys. Rev. Lett. **74** 4257.
- [Morel 1998] S. Morel, J. Schmittbuhl, J.M. López and G. Valentin, Phys. Rev. E **58** 6999.
- [Morel 2000] S. Morel, J. Schmittbuhl, E. Bouchaud and G. Valentin, Phys. Rev. Lett. **85** 1678.
- [Morel 2002] S. Morel, E. Bouchaud and G. Valentin, to appear in Phys. Rev. B, it can be found at condmat/0201045
- [Moser 1994] K. Moser and D. E. Wolf, J. Phys. A: Math. Gen. **27** 4049.

- [Myllys 2000] M. Myllys, J. Maunuksela, M.J. Alava, T. AlaNissila and J. Timonen, *Phys. Rev. Lett.* **84** 1946.
- [Myllys 2001] M. Myllys, J. Maunuksela, M.J. Alava, T. AlaNissila, J. Merikoski and J. Timonen, condmat/0105234, submitted to PRE.
- [Narayan 1993] O. Narayan and D.S. Fisher, *Phys. Rev. B* **48** 7030.
- [Nattermann 1991] T. Nattermann and L.-H. Tang, *Phys. Rev. A* **14** 603.
- [Nattermann 1992] T. Nattermann and H. Leschhorn, *Europhys. Lett.* **45** 7156.
- [Nattermann 1992b] T. Nattermann, S. Stepanow, L.-H. Tang and H. Leschhorn, *J. Phys. II (France)* **2** 1483.
- [Neshkov 2000] N. Neshkov, *Phys. Rev. E* **61** 6023.
- [Newman 1996] T.J. Newman and A.J. Bray, *J. Phys. A: Math. Gen.* **29** 7917.
- [Ojeda 2000] F. Ojeda, R. Cuerno, R. Salvarezza and L. Vázquez, *Phys. Rev. Lett.* **84** 3125.
- [Olami 1994] Z. Olami, I. Procaccia and R. Zeitak, *Phys. Rev. E* **49** 1232.
- [Olami 1995] Z. Olami, I. Procaccia and R. Zeitak, *Phys. Rev. E* **52** 3402.
- [Paczuski 1996] M. Paczuski, S. Maslov and P. Bak, *Phys. Rev. E* **53** 414.

- [Palasantzas 1994] G. Palasantzas and J. Krim, *Phys. Rev. Lett.* **73** 3564.
- [Pang 1997] N.-N. Pang and N.Y. Liang, *Phys. Rev. E* **56** 1461.
- [Parisi 1992] G. Parisi, *Europhys. Lett.* **17** 673.
- [Pimpinelli 1998] Alberto Pimpinelli and Jacques Villain, *Physics of crystal growth*, Cambridge University Press.
- [Plischke 1984] M. Plischke and Z. Rácz, *Phys. Rev. Lett.* **53** 415.
- [Punyindu 1998] P. Punyindun and S. Das Sarma, *Phys. Rev. E* **57** R4863.
- [Ramanathan 1998] S. Ramanathan and D.S. Fisher, *Phys. Rev. B* **58** 6026.
- [Ramasco 2000] J.J. Ramasco, J.M. López and M.A. Rodríguez, *Phys. Rev. Lett.* **84** 2199.
- [Roux 1994] S. Roux and A. Hansen, *J. Phys. I (France)* **4** 515.
- [Rubio 1989] M.A. Rubio, C.A. Edwards, A. Dougherty and J.P. Gollub, *Phys. Rev. Lett.* **63** 1685.
- [Sahimi 1998] M. Sahimi, *Physics Reports* **306** 213.
- [Scaramella 1998] R. Scaramella, L. Guzzo, G. Zamorani, E. Zucca et al., *Astron. Astrophys.* **334** 404.
- [Schmittbuhl 1994] J. Schmittbuhl, S. Roux and Y. Berthaud, *Europhys. Lett.* **28** 585.
- [Schmittbuhl 1995] J. Schmittbuhl, J.P. Vilotte and S. Roux, *Phys. Rev. E* **51** 131.

- [Schmittbuhl 1997] J. Schmittbuhl and K.J. Måløy, Phys. Rev. Lett. **78** 3888.
- [Simonsen 1998] I. Simonsen, A. Hansen and O.M. Nes, Phys. Rev. E **58** 2779.
- [Šmilauer 1994] P. Šmilauer and M. Kotrla, Phys. Rev. B **49** 5769.
- [Sneppen 1992] K. Sneppen, Phys. Rev. Lett. **69** 3539.
- [Sneppen 1993] K. Sneppen and M.H. Jensen, Phys. Rev. Lett. **70** 3833.
- [Sneppen 1993b] K. Sneppen and M.H. Jensen, Phys. Rev. Lett. **71** 101.
- [Soriano 2002] J. Soriano, J.J. Ramasco, M.A. Rodríguez, A. Hernández-Machado and J. Ortín, submitted to Phys. Rev. Lett.
- [Stanley 1971] H. Eugene Stanley, *Introduction to phase transitions and critical phenomena*, Oxford Science Publications.
- [Stauffer 1994] Dietrich Stauffer and Amnon Aharony, *Introduction to percolation theory*, Taylor & Francis Ltd (UK).
- [Stepanow 1997] S. Stepanow, Phys. Rev. E **55** R4853.
- [Sun 1989] T. Sun, H. Guo and M. Grant, Phys. Rev. A **40** 6763.
- [Szabó 2001] G.J. Szabó and M.J. Alava, condmat/0109162.
- [Tamborenea 1993] P.I. Tamborenea and S. Das Sarma, Phys. Rev. E **48** 2575.

- [Tang 1992] L.-H. Tang and H. Leschhorn, Phys. Rev. A **45** R8309.
- [Tang 1993] L.-H. Tang and H. Leschhorn, Phys. Rev. Lett. **70** 3832.
- [Tang 1995] L.-H. Tang, M. Kardar and D. Dhar, Phys. Rev. Lett. **74** 920.
- [Thompson 1994] C. Thompson, G. Palasantzas, Y.P. Feng, S.K. Sinha and J. Krim, Phys. Rev. B **49** 4902.
- [Tong 1994] W.M. Tong, R.S. Williams, A. Yanase, Y. Segawa and M.S. Anderson, Phys. Rev. Lett. **72** 3374.
- [Vicsek 1989] Tamás Vicsek, *Fractal growth phenomena*, World Scientific.
- [Vielva y Herranz 2002] D. Herranz y P. Vielva,  
*El caso del aceite de ricino*,  
<http://www.ifca.unican.es/~herranz/ricino.html>.
- [Villain 1991] J. Villain, J. Phys. I (France) **1** 19.
- [Weinberg 1990] Steven Weinberg, *The discovery of subatomic particles*, Penguin Science Books.
- [Witten 1981] T.A. Witten Jr. and L.M. Sander, Phys. Rev. Lett. **47** 1400.
- [Wolf 1987] D.E. Wolf and J. Kertész, Europhys. Lett. **4** 651.
- [Wolf 1990] D.E. Wolf and J. Villain, Europhys. Lett. **13** 389.
- [Wu 1999] K.K.S. Wu, O. Lahav and M.J. Rees, Nature (London) **397** 225.

- [Yan 1992] H. Yan, Phys. Rev. Lett. **68** 3048.
- [Yang 1994] H.-N. Yang, G.-C. Wang and T.-M. Lu, Phys. Rev. Lett. **73** 2348.
- [You 1993] H. You, R.P. Chiarello, H.K. Kim and K.G. Vandervoort, Phys. Rev. Lett. **70** 2900.
- [Zabolitzky 1986] J. Zabolitzky and D. Stauffer, Phys. Rev. A **34** 1523.
- [Zhang-J. 1992] J. Zhang, Y.-C. Zhang, P. Alstrøm and M.T. Levinsen, Physica (Amsterdam) **189A** 383.
- [Zhao 2000] Y.-P. Zhao, J.B. Fortin, G. Bonvallet, G.-C. Wang and T.-M. Lu, Phys. Rev. Lett. **85** 509.
- [Zik 1997] O. Zik, E. Moses, Z. Olami and I. Webman, Europhys. Lett. **38** 509.